f the CERAMIC SOCIETY of Japan, International Edition 第99集 第1150号 平成3年5月25日発行(毎月1回25日発行) ISSN 0912-9200

)urnal of the CERAMIC SOCIETY of
ıpan,
ternational Edition
ol.99 May 1991

8 Papers from Nippon Seramikkusu Kyokai Gakujutsu Ronbunshi, Vol.99 No.5 1991

N SERAMIKKUSU KYOKAI GAKUJUTSU RONBUNSHI Vol.99 1991

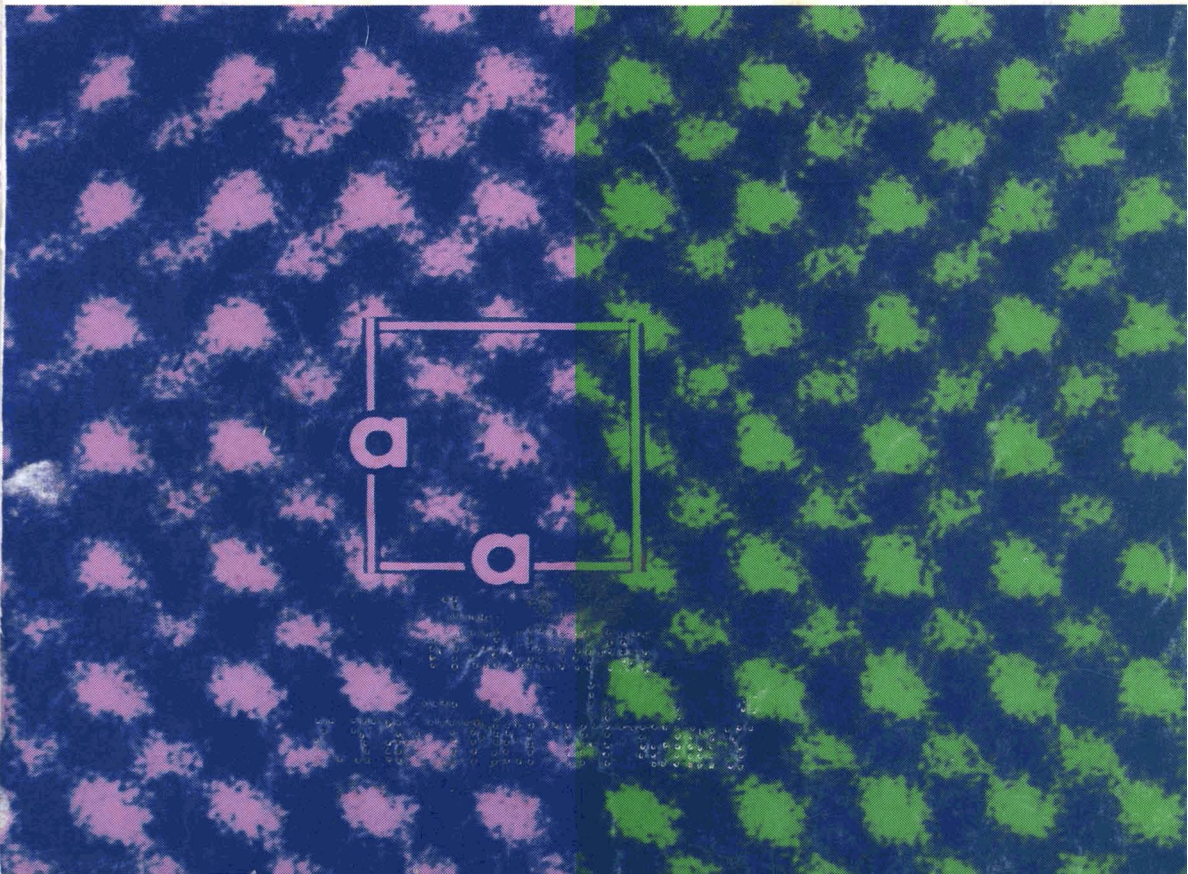

Journal of Ceramic Society of Japan, *International Edition*

Vol.99 No.5
May 1991

Published Monthly by
FUJI TECHNOLOGY PRESS LTD.
7F Daini Bunsei Bldg.
11-7, Toranomon 1-chome
Minato-ku, Tokyo 105, Japan
Tel:81-3-3508-0051
Fax:81-3-3592-0648

One year subscription
Air Mail ¥200,000

CONTENTS

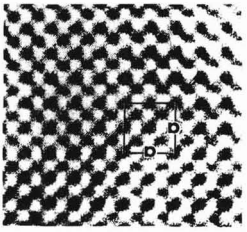

Cover:

This picture shows a high-resolution structure image of zirconia (ZRO_2) projected along the a-axis of a cubic lattice (a=5.1). As indicated by arrowheads in the micrograph, both zirconium (Zr) and oxygen (O) atom positions appear as strong and weak dark dots, respectively. This is the first electron microscope data in which individual oxygen positions in inorganic compounds can be directly observed as weak dark dots.

The microgram was obtained by the ultra-high-resolution, high-voltage electron microscope (Model: H-1500) developed in 1990 as NIRIM's second high-voltage electron microscope. The device has the world's highest resolution of 1.0Å, which was achieved by employing operating and applicable voltages of 1300kV and 1500kV, respectively. A very low spherical aberration coefficient for the objective (C_s=1.85mm at 1300kV) was realized by computer-aided design of the electron-magnetic lens system. This new apparatus permits the imaging of not only metal atoms but also light atoms (such as oxygen) in many inorganic materials by means of high-resolution electron microscopy.

Papers, Letters and Notes

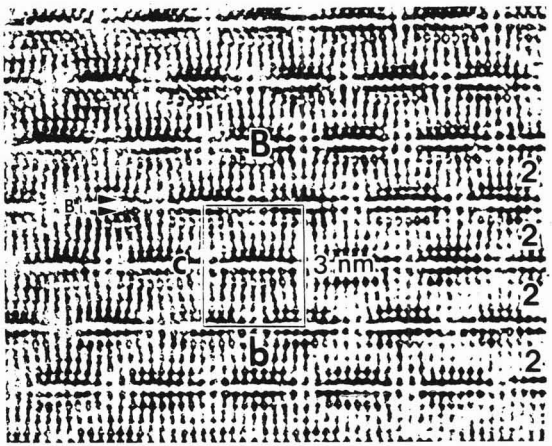

High resolution electron microscope photograph of the modulation doped structure of $Bi_2Sr_2CaCu_2O_y$ (T_c=80K) in the [100] direction. Figures at right side indicate number of copper layers, symbol B indicates bismuth rich region.

Formation of the High-Tc Phase in Superconducting Bi-Sr-Ca-Cu-O Films Fabricated from Metal Alkoxides

Shingo Katayama and Masahiro Sekine

Colloid Research Institute
350-1 Ogura, Yahata-higashi-ku, Kitakyushu-shi, 805 Japan

The formation of the high-Tc phase in Bi-Sr-Ca-Cu-O films fabricated using metal alkoxides has been investigated. Pb-doping, an addition of excess Ca and Cu, change of heating and cooling rates and firing under low oxygen partial pressure were studied to increase the volume fraction of the high-Tc phase. The pb-doping and firing under low oxygen partial pressure were not effective, but the addition of a proper amount of excess Ca and Cu under the firing condition at high heating and cooling rates was effective. The film with a nominal composition of $Bi_2Sr_2Ca_3Cu_4O_x$ fired at 850°C for 48h in air at heating and cooling rates of 30°C/min showed superconductivity with Tc(onset)=125K and Tc(zero)=115K.

[Received October 19, 1990; Accepted January 24, 1991]

Key-words: Superconductor, Metal alkoxide, Bi-Sr-Ca-Cu-O film, High-Tc phase, Excess Ca and Cu, Heating rate, Cooling rate

1. Introduction

Since the discovery of high-Tc superconductivity in the Bi-Sr-Ca-Cu-O system,[1] a lot of research has been carried out to fabricate Bi-Sr-Ca-Cu-O films using a variety of methods. This system has two superconducting phases with Tc ~80K and to ~110K, called the low-Tc phase ($Bi_2Sr_2Ca_1Cu_2O_x$) and the high-Tc phase ($Bi_2Sr_2Ca_2Cu_3O_x$), respectively. However, it is extremely difficult to synthesize the high fraction of the high-Tc phase. Currently, several methods, such as the partial substitution of Pb for Bi,[2,3] an addition of excess Ca and Cu,[4,5] and heating under low oxygen partial pressure[6] were reported to be effective for increasing the volume fraction of the high-Tc phase.

Some attempts have been made to fabricate Bi-Sr-Ca-Cu-O films by the sol-gel method,[7~10] because of advantages for obtaining "shaped" ceramics such as bulks, films, and fibers, as well as pure and homogenous products at a relatively low sintering temperature. In the fabrication of Bi-Sr-Ca-Cu-O films using this method, however, the low-Tc phase has been mainly obtained without a detailed investigation for increasing the volume fraction of the high-Tc phase.[7~9]

In our previous works,[11,12] we reported on the preparation of a mixed alkoxide solution in the Bi-Sr-Ca-Cu-O system and the fabrication of Bi-Sr-Ca-Cu-O films with the nominally ideal composition of high-Tc phase (Bi:Sr:Ca:Cu=2:2:2:3). The nominal composition of $Bi_2Sr_2Ca_2Cu_3O_x$ provided the low-Tc phase film with a trace amount of the high-Tc phase. The present paper describes an extensive study regarding nominal compositions and firing conditions to increase the volume fraction of the high-Tc phase in the fabrication of Bi-Sr-Ca-Cu-O films using metal alkoxides.

2. Experimental Procedure

The starting materials used for preparing Bi(Pb)-Sr-Ca-Cu-O films were $Bi(O\text{-}iC_3H_7)_3$, $Pb(OiIC_3H_7)_2$, $Sr(OC_2H_5)_2$, $Ca(OC_2H_5)_2$, and $Cu(OCH_3)_2$. $Bi(O\text{-}iC_3H_7)_3$ and $Pb(O\text{-}iC_3H_7)_2$ were commercially obtained (High Purity Chemicals Co.). $Sr(OC_2H_5)_2$ and $Ca(OC_2H_5)_2$ were prepared by reaction of the corresponding metal with ethanol, and an ethanol solution of these alkoxides was used as the starting solution. $Cu(OCH_3)_2$ was synthesized by reacting $CuCl_2$ in methanol with $KOCH_3$.[13] Commercially available 2-dimethylaminoethanol (Kanto Chemical Co.) as a modifier of $Cu(OCH_3)_2$ was used without further purification. Ethanol as a solvent was dried over $Mg(OC_2H_5)_2$ and distilled.

Figure 1 shows the procedure for fabricating Bi-Sr-Ca-Cu-O films. $Cu(OCH_3)_2$ was modified using 2-dimethylaminoethanol in ethanol at the molar ratio of $Cu(OCH_3)_2$ to 2-dimethylaminothanol of 1:2 to make it soluble.[14] For the addition of Pb to the Bi-Sr-Ca-Cu-O system, a desired amount of $Pb(O\text{-}iC_3H_7)_2$ was dissolved into the above solution. $Bi(O\text{-}iC_3H_7)_3$ was completely dissolved in an ethanol solution of $Sr(OC_2H_5)_2$ and $Ca(OC_2H_5)_2$ by the formation of a double alkoxide of Bi with Sr and Ca.[11,12] Both solutions obtained by the above methods were mixed to obtain an alkoxide solution (0.5-0.7 mol-alkoxide/*l*) at a desired molar ratio of Bi(:Pb):Sr:Ca:Cu. This alkoxide solution was dip-coated on the surfaces of a single crystal MgO(100) substrate at a draw-up speed of 3mm/sec in a nitrogen atmosphere. The coated substrates were subsequently heated at 200°C for 5min in air. This process of coating and heating was repeated 15 times to increase the film thickness. Finally, the films were fired

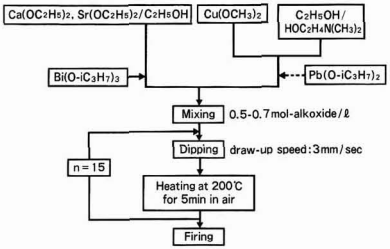

Fig. 1. Procedure for fabricating Bi-Sr-Ca-Cu-O films.

under various conditions using an electric furnace. The fired films consisted of Bi-Sr-Ca-Cu-O phases with a preferred orientation to the c-axis perpendicular to the substrate.

The crystal structures of the films were examined employing the X-ray diffraction method (Rigaku Co.) using CuKα radiation with a monochrometer. To determine the film morphology and composition, scanning electron microscopy (SEM) and energy dispersive X-ray (EDX) analysis were performed using a JSM-840A (JEOL Ltd.) with QX200J (Link Analytical Ltd.). The electrical resistivity of the films was measured by the conventional four-probe method.

3. Results

3.1 Pb-doping of the Bi-Sr-Ca-Cu-O films

Films with a nominal composition of $(Bi_{0.7}Pb_{0.3})_2Sr_2Ca_2Cu_3O_x$ and $Bi_2Pb_{0.6}Sr_2Ca_2Cu_3O_x$, which are substitution- and addition-type compositions, respectively, were fired at 850°C for 48h in air at heating and cooling rates of 30°C/min. The effects of Pb-doping on the kinds of resulting phases and properties were investigated using the films.

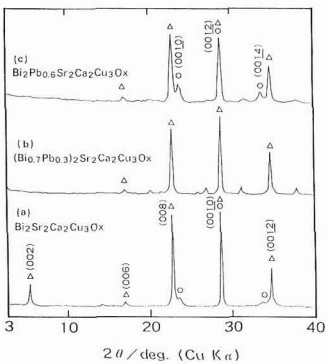

Fig. 2. X-ray diffraction patterns of films with a nominal composition of (a) $Bi_2Sr_2Ca_2Cu_3O_X$, (b) $(Bi_{0.7}Pb_{0.3})_2Sr_2Ca_2Cu_3O_X$ and (c) $Bi_2Pb_{0.6}Sr_2Ca_2Cu_3O_X$. The films fired at 850°C for 48h in air at heating and cooling rates of 30°C/min.
○: high-T_c phase, △: low-T_c phase

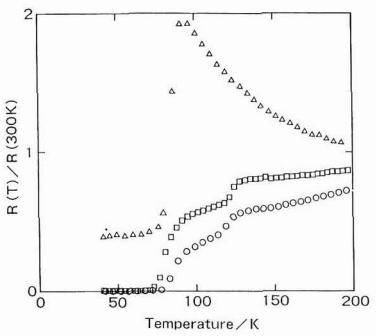

□: $Bi_2Pb_{0.6}Sr_2Ca_2Cu_3O_X$, △: $(Bi_{0.7}Pb_{0.3})_2Sr_2Ca_2Cu_3O_X$,
○: $Bi_2Sr_2Ca_2Cu_3O_X$

Fig. 3. Temperature dependence of electrical resistance normalized to that at 300K for films with a nominal composition of $Bi_2Sr_2Ca_2Cu_3O_X$, $(Bi_{0.7}Pb_{0.3})_2Sr_2Ca_2Cu_3O_X$ and $Bi_2Pb_{0.6}Sr_2Ca_2Cu_3O_X$. The films fired at 850°C for 48h in air at heating and cooling rates of 30°C/min.

The X-ray diffraction patterns of the Pb-doped films and Pb-undoped film are shown in **Fig. 2**. As shown in Fig. 2(a), the X-ray diffraction pattern of the Pb-undoped film with a nominal composition of $Bi_2Sr_2Ca_2CuO_x$, which was the stoichiometric composition of the high-Tc phase, exhibited the low-Tc phase as a main phase with a slight amount of the high-Tc phase. The X-ray diffraction pattern of the Pb-doped film with a nominal composition of $(Bi_{0.7}Pb_{0.3})_2Sr_2Ca_2Cu_3O_x$ comprised mainly the low-Tc phase with unknown peaks (Fig.2(b)). In the nominal composition of $Bi_2Pb_{0.6}Sr_2Ca_2Cu_3O_x$, the volume fraction of the high-Tc phase increased slightly, compared with the Pb-undoped film, although the low-Tc phase was mainly formed as shown in Fig.2(c).

The temperature dependences of electrical resistance normalized to that at 300K for the Pb-doped films and Pb-undoped film are shown in **Fig. 3**. The film with a nominal composition of $(Bi_{0.7}Pb_{0.3})_2Sr_2Ca_2Cu_3O_x$ exhibited semiconducting behavior above 85K and a drop of resistance from 85 to 70K followed by a constant resistance below 70K. This behavior means that the superconducting phase is divided by the non-superconducting phase which makes the constant resistance below 70K. This was supported by the observation of the microstructure using SEM. In this film, needle-like crystals with a length of ~100μm divided the superconducting phase consisting of plate-like crystals with size of ~10μm, whereas other films were composed of plate-like crystals without a needle-like crystal. The resistance of the film with a nominal composition of $Bi_2Pb_{0.6}Sr_2Ca_2Cu_3O_x$ started to drop at around 125K, and dropped subsequently to zero resistance over the temperature range of 50K, but no increase in Tc(zero) was observed.

Although the presence of Pb in the Pb-doped films before firing was confirmed by EDX, the EDX spectra of the fired films showed no peaks corresponding to Pb. This suggests that Pb doped in the as-coated films evaporates easily during firing. Therefore, Pb-doping was not effective for increasing the volume fraction of the high-Tc phase in the film. The evaporation of Pb from the film with a nominal composition of $(Bi_{0.7}Pb_{0.3})_2Sr_2Ca_2Cu_3O_x$ results in the significant change of composition from that of the high-Tc phase, so that the unknown phase appeared.

3.2 Addition of excess Ca and Cu on Bi-Sr-Ca-Cu-O films

The films with a nominal composition of $Bi_2Sr_2Ca_3Cu_4O_x$ and $Bi_2Sr_2Ca_4Cu_5O_x$ containing excess amounts of Ca and Cu were fired at 850°C for 48h in air at heating and cooling rates of 30°C/min. **Figure 4** shows the X-ray diffraction patterns of these films and that of the film with a nominal composition of $Bi_2Sr_2Ca_2Cu_3O_x$. Although the high-Tc phase was not obtained and the low-Tc phase was observed with a small amount of $Bi_2Sr_2CuO_x$ in the nominal composition of $Bi_2Sr_2Ca_4Cu_5O_x$(Fig.4(c)), the film with a nominal composition of $Bi_2Sr_2Ca_3Cu_4O_x$ had the high-Tc phase as a main phase as shown in fig. 4(b). In this method, the addition of a proper amount of excess Ca and Cu was effective for increasing the volume fraction of the high-Tc phase.

The temperature dependences of electrical resistance nor-

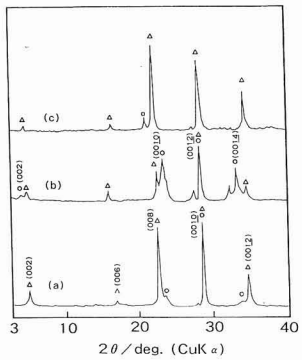

Fig. 4. X-ray diffraction patterns of films with a nominal composition of (a) $Bi_2Sr_2Ca_2Cu_3O_X$, (b) $Bi_2Sr_2Ca_3Cu_4O_X$ and (c) $Bi_2Sr_2Ca_4Cu_5O_X$. The films fired at 850°C for 48h in air at heating and cooling rates of 30°C/min.
○: high-Tc phase, △: low-Tc phase, ❑: $Bi_2Sr_2CuO_X$.

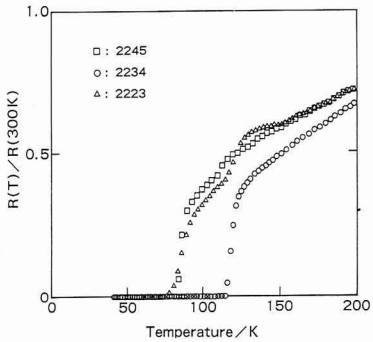

Fig. 5. Temperature dependence of electrical resistance normalized to that at 300K for films with a nominal composition of $Bi_2Sr_2Ca_2Cu_3O_X$, $Bi_2Sr_2Ca_3Cu_4O_X$ and $Bi_2Sr_2Ca_4Cu_5O_X$. The films fired at 850°C for 48h in air at heating and cooling rates of 30°C/min.

malized to that at 300K for films with a nominal composition of $Bi_2Sr_2Ca_2Cu_3O_x$, $Bi_2Sr_2Ca_3Cu_4O_x$, and $Bi_2Sr_2Ca_4Cu_5O_x$ are shown in **Fig. 5**. The film with a nominal composition of $Bi_2Sr_2Ca_4Cu_5O_x$ had a slight drop in resistance corresponding to the high-Tc phase around 110K. Although the X-ray diffraction pattern of the film with a nominal composition of $Bi_2Sr_2Ca_3Cu_4O_x$ exhibited the high-Tc and low-Tc phases, this film had a single drop transition in the resistance with Tc(onset)=122K and Tc(zero)=115K corresponding to the high-Tc phase. The single step transition is attributable to the presence of high-Tc phase having a continuous superconducting path.

The SEM photographs of surface morphology for the films with a nominal composition of $Bi_2Sr_2Ca_2Cu_3O_x$, $Bi_2Sr_2Ca_3Cu_4O_x$, and $Bi_2Sr_2Ca_4Cu_5O_x$ are shown in **Fig.6**. The film with a nominal composition of $Bi_2Sr_2Ca_2Cu_3O_x$ was composed of plate-like grains of several μm as shown in Fig.6(a). This is consistent with the X-ray diffraction pattern shown in Fig.4(a) where the texture is developed. The film with a nominal composition of $Bi_2Sr_2Ca_3Cu_4O_X$. (Fig.6(b)) had large plate-like gains of 20-30μm as well as particles of a few μm scattered on the grains. The particles on the grains were confirmed to contain Ca and Cu by EDX analysis. Consequently, excess Ca and Cu were considered to concentrate as the form of Ca-Cu-O particles. The particles were non-superconducting, but did not affect the superconductivity of the film because they were only on the surface of the continuous superconducting phase. The SEM photograph of the film with a nominal composition of $Bi_2Sr_2Ca_4Cu_5O_X$ gave evidence of remarkable melting as shown in Fig.6(c). These results indicate that the melting point in the Bi-Sr-Ca-Cu-O system decreases as the Ca content increases, as described by Tsuchiya et al.[15]

The Pb-doping into the film with a nominal composition of $Bi_2Sr_2Ca_3Cu_4O_X$ was found not to increase the volume fraction of the high-Tc phase. Therefore, the film with a nominal composition of $Bi_2Sr_2Ca_3Cu_4O_X$ was treated under various conditions in order to increase the amount of high-Tc phase in the following sections.

3.3. Effects of Heating and Cooling Rates on Resultant Phases

The films with a nominal composition of $Bi_2Sr_2Ca_3Cu_4O_X$ were fired at 850°C for 48h in air at (a) heating rate (h.r.)=30°C/min and cooling rate (c.r.)=30°C/min, (b) h.r.=30°C/min and c.r.=2°C/min, and (c) h.r.=2°C/min and 30°C/min. The X-ray diffraction patterns of these films are shown in **Fig.7**. Although the diffraction profile of the film

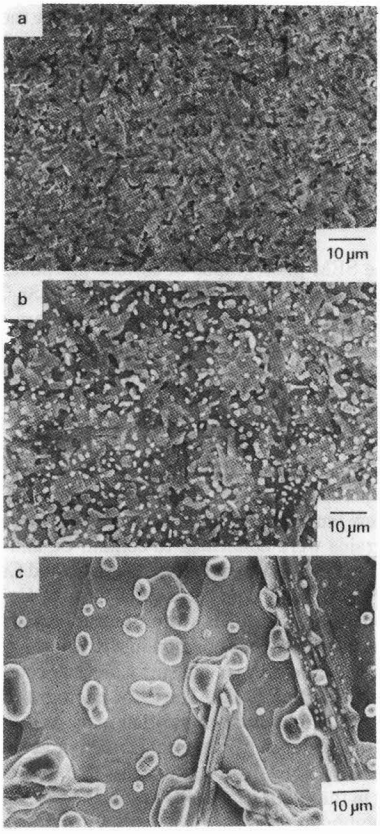

Fig. 6. SEM photographs of surface morphology for films with a nominal composition of (a) $Bi_2Sr_2Ca_2Cu_3O_X$, (b) $Bi_2Sr_2Ca_3Cu_4O_X$ and (c) $Bi_2Sr_2Ca_4Cu_5O_X$. The films fired at 850°C for 48h in air at heating and cooling rates of 30°C/min.

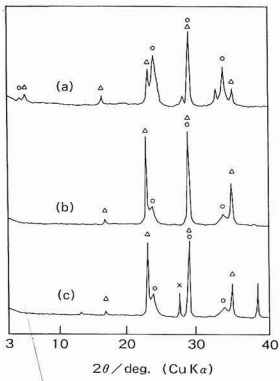

Fig. 7. X-ray diffraction patterns of films fired at 850°C for 48h in air at (a) h.r.=30°C/min and c.r.=30°C/min, (b) h.r.=30°C/min and c.r.=2°C/min and (c) h.r.=2°C/min and c.r.=30°C/min. Nominal composition of the film was $Bi_2Sr_2Ca_3Cu_4O_X$.
○: high-T_c phase, △: low-T_c phase, ×: Ca_2CuO_3

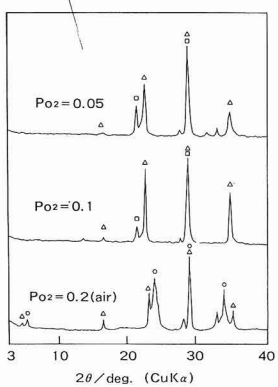

Fig. 8. X-ray diffraction patterns of films fired at 850°C for 48h under P_{O_2}=0.2(air), 0.1 and 0.05atm at heating and cooling rates of 30°C/min. Nominal composition of the film was $Bi_2Sr_2Ca_3Cu_4O_X$.
○: high-T_c phase, △: low-T_c phase, ❑: $Bi_2Sr_2CuO_X$

fired at (a) h.r.=30°C/min and c.r.=30°C/min showed a favorable formation of the high-Tc phase as shown in Fig.7(a), the film fired at (b) h.r.=30°C/min and c.r.=2°C/min mainly contained the low-Tc phase accompanied by the high-Tc phase(Fig.7(b)). This means that a part of the high-Tc phase changes into the low-Tc phase during slow cooling, as described by Hayashi et al..[16] In the film fired at (c) h.r.=2°C/min and c.r.=30°C/min, the low-Tc phase was produced as a main phase with the formation of Ca_2CuO_3 as shown in Fig.7(c). Since a large amount of Ca_2CuO_3 is easily formed during slow heating, the latter is not effective for the formation of the high-Tc phase. Consequently, the fast heating and cooling effectively act to increase the volume fraction of the high-Tc phase when the film is formed from the nominal composition including excess Ca and Cu.

3.4. Phases Formed at Low Oxygen Partial Pressure

The films with a nominal composition of $Bi_2Sr_2Ca_3Cu_4O_X$ were fired at temperatures between 800 and 850°C for 48h under oxygen partial pressures (Po_2) of 0.1 and 0.05 atm at heating and cooling rates of 30°C/min. The X-ray diffraction patterns of films fired under Po_2=0.2 (air), 0.1 and 0.05atm are shown in **Fig.8.** When the films were fired under an oxygen partial pressure lower than Po_2=0.2atm, both $Bi_2Sr_2CuO_X$ and the low-Tc phase were formed without any high-Tc phase. The X-ray diffractions of $Bi_2Sr_2CuO_X$ increased as the oxygen partial pressure decreased from 0.1 to 0.05atm. The remarkable melting on the film surface of under lower oxygen partial pressure was observed using SEM. The X-ray diffraction patterns of films fired at 800, 830, and 850°C for 48h under P_{o2}=0.05atm are shown in **Fig.9**. Although the fraction of $Bi_2Sr_2CuO_X$ decreased as the firing temperature decreased from 850 to 830°C, the high-Tc phase was not observed. At the low firing temperature of 800°C(Fig.9(a)), the film did not melt nor include any $Bi_2Sr_2CuO_X$. The films fired under P_{o2}=0.1atm gave X-ray diffraction results similar to those in Fig.9.

The lower oxygen partial pressure lowered the melting point of the system as reported by the previous papers,[15,17,18] but no high-Tc phase was produced.

4. Discussion

Although the Pb-doping technique has been effectively used to increase the volume fraction of the high-Tc phase, especially in bulks,[2,3] this technique in the films fabricated using metal alkoxides was not effective because of the evaporation of doped Pb in the firing process. The losses of doped Pb in films are apparently larger than that in bulks, since the exposed surface area-to-volume ratio is higher for film than bulk.[19]

There are other techniques to obtain a large amount of the high-Tc phase. When the firing was carried out at high heating and cooling rates, an addition of excess Ca and Cu (Bi:Sr:Ca:Cu=2:2:3:4) had a significant effect on the increase of the high-Tc phase in the films fabricated using metal alkoxides. However, when a large amount of Ca and Cu (Bi:Sr:Ca:Cu=2:2:4:5) was added, the melted phase was observed and the high-Tc phase was not obtained. Also in

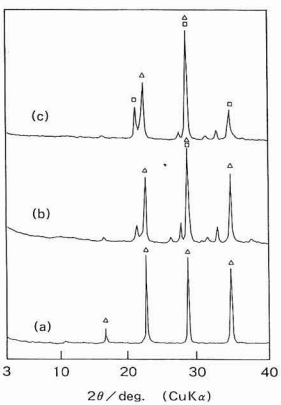

Fig. 9. X-ray diffraction patterns of films fired at (a) 800°, (b) 830° and (c) 850°C for 48h under P_{O_2}=0.05atm at heating and cooling rates of 30°C/min. Nominal composition of the film was $Bi_2Sr_2Ca_3Cu_4O_X$.
△: low-T_c phase, ❑: $Bi_2Sr_2CuO_X$

the case of firing under lower oxygen partial pressure (Po_2<0.2atm), melting occurred and no high-Tc phase was synthesized. Upon melting, $Bi_2Sr_2CuO_X$ was formed and no high-Tc phase was produced under the conditions of the nominal composition of $Bi_2Sr_2Ca_4Cu_5O_X$ as well as the firing at lower oxygen partial pressure. These phenomena are consistently explained by considering the formation of the high-Tc phase by the diffusion of Ca and Cu into the initially formed low-Tc structure.[20,21] However, the marked melting destroys the structure of the low-Tc phase and prevents the formation of the high-Tc phase. Also, a part of the low-Tc phase is suggested to melt and decompose into $Bi_2Sr_2CuO_x$.[18,22] It is thought that in the nominal composition of $Bi_2Sr_2Ca_3Cu_4O_X$, the structure of the low-Tc phase was preserved and the high-Tc phase was formed by diffusion of Ca and Cu into the low-Tc phase. Although the film was fired below 850°C under lower oxygen partial pressure in order to avoid the decomposition and melting of the low-Tc phase, the high-Tc phase was not obtained. The structure of the low-Tc phase can be kept at low temperature, but the formation of the high-Tc phase is extremely slow because the diffusion coefficient exponentially decreases with decreasing temperature.

Furthermore, high heating and cooling rates should be employed to yield a high fraction of the high-Tc phase. This is possibly explained as follows. The low heating rate results in the growth of large Ca-Cu-O crystals including Ca and Cu as diffusion elements, and the small area of the interface between the low-Tc phase and Ca-Cu-O crystal is formed. At the high heating rate, however, a number of small Ca-Cu-O crystals are precipitated and the area of the interface between the low-Tc phase and Ca-Cu-O crystal becomes larger. The large interface for the diffusion of Ca and Cu into the low-Tc phase accelerates the formation of the high-Tc phase. During slow cooling, part of the high-Tc phase decomposes into the low-Tc phase and Ca-Cu-O possibly because the high-Tc phase is metastable at low temperature.[16] Therefore, a high cooling rate is required to prevent the decomposition of the high-Tc phase during cooling. Therefore, the nominal composition of proper excess amounts of Ca and Cu (Bi:Sr:Ca:Cu=2:2:3:4:) should be adopted for increasing the volume fraction of the high-Tc phase, because a large amount of the diffusion species can be formed and the structure of the low-Tc phase can be kept without melting. Furthermore, high heating and cooling rates should be employed to avoid the growth of Ca-Cu-O phase and the decomposition of the high-Tc phase, respectively. In the fabrication of films using metal alkoxides, it is possible to produce a high fraction of high-Tc phase without Pb-doping by carefully controlling the composition and firing conditions.

5. Conclusions

The effects of Pb-doping, the addition of excess Ca and Cu, various heating and cooling rates, and firing under low oxygen partial pressure were investigated to increase the volume fraction of the high-Tc phase in Bi-Sr-Ca-Cu-O films fabricated using metal alkoxides.

1) Pb-doping was not effective for increasing the volume fraction of the high-Tc phase because of the evaporation of doped Pb.
2) When firing at high heating and cooling rates, the nominal composition of excess Ca and Cu (Bi:Sr:Ca:Cu=2:2:3:4) effectively increased the volume fraction of the high-Tc phase. This film showed superconductivity with Tc(onset)=125K and Tc(zero)=115K.
3) Although the low oxygen partial pressure lowered the melting point, the high-Tc phase was not obtained.

Acknowledgments

The authors would like to thank the Japan Technology Center for its financial support for the "Research and development of production technology of high performance ceramics with a controlled colloidal solution as a precursor". The authors would also like to express their gratitude to Miss Akiko Kamimura for her experimental support.

References:

1) H. Maeda, T. Tanaka, M. Fukutomi and T. Asano, Jpn. J. Appl. Phys., 27(2), L209-10(1988)
2) M. Takano, J. Takada, K.Oda, H.Kitaguchi, Y.Miura, Y. Ikeda, Y.Tomii and H.Mazaki, Jpn. J. Appl. Phys., 27(6), L1041-43 (1988)
3) T. Hatana, K. Aota, S.Ikeda, K. Nakamura and K. Ogawa, Jpn. J. Appl. Phys. 27(11), L2055-58(1988)
4) A. Sumiyama, T. Yoshitomi, H. Endo, J. Tsuchiya, N. Kijima, M. Mizuno and Y. Oguri, Jpn. J. Appl. Phys., 27(4), L542-44(1988)
5) N. Kijima, H. Endo, J. Tsuchiya, A. Sumiyama, M. Mizuno and Y. Oguri, Jpn. J. Appl. Phys., 27(5), L821-23(1988)
6) U. Endo, S. Koyama and T. Kawai, Jpn. J. Appl. Phys., 27(8), L1476-79(1988)
7) T. Kobayashi, K. Nomura, F. Uchikawa, T. Masushi and Y. Uehara, Jpn. J. Appl. Phys., 27(10), L1880-82(1988)
8) S. Hirano, T. Hayashi and H. Tomonaga, Jpn. J. Appl. Phys., 29(1), L40-42 (1990)
9) H. Zhuang, H. Kozuka, T. Yoko and S. Sakka, Jpn. J. Appl. Phys., 29(7), L1107-10(1990)
10) K. Tanaka, A. Nozue and K. Kamiya, J. Mater. Sci. 25, 3551-56(1990)
11) S. Katayama and M. Sekine, J. Mater. Res. 6(1), 36-41(1990)
12) S. Katayama and M. Sekine, "Better Ceramics Through Chemistry IV" edited by C.J. Brinker, D.E. Clark, D.R. Ulrich and B.J.J. Zelinsky, Mater. Res. Soc. Proc. 180, Pittsburgh, PA, 1990, P.873-6.
13) J.V. Singh, B.P. Baranwal and R.C. Mehrotra, Z. anorg. allg. Chem., 477, 235-40 (1981)
14) S. Katayama and M. Sekine, J. Mater. Res. 5(4), 683-90 (1990)
15) J. Tsuchiya, H. Endo, N. Kijima, A. Sumiyama, M. Mizuno and Y. Oguri, Jpn. J. Appl. Phys., 28(11), L1981-21(1989)
16) Y. Hayashi, H. Kogure and Y. Gondo, Jpn. J. Appl. Phys., 28(12), L2182-84(1989)
17) U. Endo, S. Koyama and T. Kawai, Jpn. J. Appl. Phys., 27(8), L1476-79(1989)
18) K. Aota, H. Hattori, T. Hatano, K. Nakamura and K. Ogawa, Jpn. J. Appl. Phys., 28(12), L2196-99(1989)
19) S.K. Dew, N.R. Osborne, P.J. Mulhern and R.R. Parsons, Appl. Phys. Lett. 54(19), 1929-31(1989)
20) D. Shi, M. Tang, K. Vandervoort and H. Claus, Phys. Rev. B 39(13), 9091-8(1989)
21) D. Shi and M.S. Boley, J.G. Chen, M. Xu, K. Vandervoort, J. Akujieze and C. Segre, Appl. Phys. Lett. 55(7), 699-707(1989)
22) T. Maruyama and S. Higashi, Jpn. J. Appl. Phys. 28(4), L624-7(1989).

This article appeared in English in Nippon Seramikkusu Kyokai Gakujutsu Ronbunshi (Japanese version), Vol.99, No.5, 1991.

Effects of Rare Earth Oxide Addition on the Sintering of Mullite

Takashi Mitamura, Hidehiko Kobayashi, Noboru Ishibashi and Tokuji Akiba*

Department of Applied Chemistry, Faculty of Engineering, Saitama University
255 Shimo-ohkubo, Urawa-shi, Saitama 338, Japan
* Research and Development Division, Chichibu Cement Co. Ltd.
5310 Mikajiri, Kumagaya-shi, Saitama 360, Japan

Effects of various kinds of rare earth oxides (Y_2O_3, Er_2O_3, Sm_2O_3, La_2O_3 and CeO_2) addition on the sintering of mullite and the precipitation behavior of secondary phases in the mullite sintered bodies were investigated. The sintering of the mullite compacts, to which a small amount of these rare earth oxides was added, was performed at 1500° to 1600°C. The morphologies of the rare earth silicates precipitated and remained on the grain boundaries of the sintered bodies could be classified into three categories, i.e., crystalline, glassy and decomposed substances, depending upon the kinds of rare earth oxide added. The microstructures of the mullite sintered bodies changed as the amount of the additives varied. The three point bending strength of the sintered mullite increased with the addition of 0.5wt% of Y_2O_3 or CeO_2. On the other hand, an excessive amount of these additives would result in the decrease of three point bending strength. It was found that the maximum value of three point bending strength was evidently related to the melting point of the secondary phases existing in the sintered bodies of mullite.

[Received May 21, 1991; Accepted January 24, 1991]

Key-words: Mullite, Rare earth oxide, Y_2O_3, Sm_2O_3, La_2O_3, CeO_2, Silicate, Three point bending strength

1. Introduction

Being among the few substances which have excellent properties for high-temperature structural materials, mullite ($3Al_2O_3 \cdot 2SiO_2$), a kind of composite oxide ceramic, has been studied very extensively.[1,2] The most dominant trend in such conventional studies was toward higher purities of powders and sintered products to extract full properties for high-temperature structural materials. Recently, for the purpose of increasing the thermal shock resistance or decreasing thermal expansion of mullite itself, new studies have been emerging to produce low-thermal-expansion and low-permittivity boards from materials prepared by adding traces of oxides to high-purity mullite, which can be sintered at lower temperatures than for conventional mullite.[3-9]

For instance, Ushifusa et al. have been studying the effect of adding rare earth oxides other than CeO_2 to mullite synthesized by an electromelting or sol-gel method.[3-5] According to them, the rare earth oxides added react with mullite or silica slightly contained in mullite, producing rare earth silicates. Thus, it is reported that sintering proceeds at lower temperatures than with conventional mullite and that sintered products made by adding Y_2O_3 in particular have 3-point bending strengths of 270 to 280MPa (from room temperature to 1200°C) and dielectric constants of 6.1 to 9.4.[3-5] For the effect of adding MgO in manufacturing sintered blocks of mullite by the reaction between Al_2O_3 and SiO_2, Hashimoto et al. report that the MgO added reacts with Al_2O_3 or SiO_2, producing cordierite or spinel, which enables the coefficient of thermal expansion and the dielectric constant to be controlled, while improving sinterability.[7]

Thus, it is already known that slightly adding alkaline earth metal oxides or rare earth oxides in mullite sintering causes mullite sintering to be promoted, or the sintering characteristics of mullite to be changed, by products such as silicates, aluminates and aluminosilicates of reactions between added oxides and mullite. Details, however, remain unknown. The grain size, composition and manufacture of mullite powder as the starting material differ from report to report and there are no systematic reports on overall additives in the same family.

Slightly adding rare earth oxides (Y_2O_3, Er_2O_3, Sm_2O_3, La_2O_3 and CeO_2) to powdered mullite, we investigated the effects of the mode of second phase and the mechanical properties at high temperature on the sinterbility of mullite.

2. Experimental Procedure

2.1. Preparation of Samples

Powder samples were prepared by adding Y_2O_3, Er_2O_3, Sm_2O_3, La_2O_3 and CeO_2 at specified weight ratios (0.2 to 10wt%) in terms of mullite weight to commercial powdered mullite (MP-20 made by Chichibu Cement, mean grain size 1μm, purity 99.9%, Al_2O_3 content 71.8wt%), wet mixing them together with ethanol and mullite balls in plastic pots for 24h and drying them. The purity and the mean grain size of all the powdered rare earth oxides were 99.9% and 2 to 3μm respectively.

2.2. Preparation of Sintered Blocks

The prepared powder samples were classified by passing them through a 100 mesh screen and molded under a single-axis pressure of 500kg/cm^2 into bars about 5.0×7.2×52.4mm. The moldings were then calcined in air at 800°C for 1h and sintered at 1400° to 1600°C for 2h using a heating/cooling rate of 4°C/min.

2.3. Analysis and Property Evaluation of Sintered Samples

To evaluate the sintering characteristics of the sintered

samples manufactured as above, their densities were measured under the Archimedean method, linear coefficients of contraction measured with a micrometer, crystal phases identified by an X-ray diffraction test and surfaces observed for element analysis etc. by using TEM, SEM and EDX. Also, sintered samples were mirror polished and their 3-point bending strengths were measured at room temperature, 1200°C and 1300°C with a span of 30mm and a crosshead speed of 0.5mm/min.

3. Results

3.1. Effect of Slight Rare Earth Oxide Additives on Sintering Characteristics of Mullite

Figure 1 shows the relation between bulk density and sintering temperature of sintered mullite samples with rare earth oxides added by 2wt%. The bulk density of mullite only was 2.75g/cm^3 after 2h sintering at 1600°C. Sintering proceeded only by 86.5% on the assumption that the theoretical density of mullite is 3.18g/cm^3. On the other hand, the bulk densities of sintered samples with rare earth oxides added were around 3.1g/cm^3 at 1500°C, proving that their sintering proceeded at lower temperatures than for mullite only.

We investigated the relation between bulk density and earth oxide content of the samples sintered at 1500°C and 1600°C. **Figures 2** and **3** show the data with additives Y_2O_3 and CeO_2. With Y_2O_3 addition, the bulk densities for 1500°C remain constant at 3.10g/cm^3 in the additive content range above 2wt% and those for 1600°C are nearly constant at 3.12g/cm^3 in the additive content range above 0.5wt%. Within the test range, the bulk densities of sintered samples were not affected by excessive addition (up to 10wt%) of Y_2O_3. With CeO_2 addition, on the other hand, the bulk densities for 1500°C stand constant at 3.11g/cm^3 in the additive content range above 3wt% and those for 1600°C stand nearly constant at 3.11g/cm^3 in the additive content range above 1wt%.

Figure 4 shows the X-ray diffraction patterns of sintered mullite samples with rare earth oxides added by 5 or 10wt%. With Y_2O_3 or Er_2O_3 added, diortho-silicates $Y_2Si_2O_7$ or $Er_2Si_2O_7$ were found respectively in addition to the matrix mullite phase. With Sm_2O_3 addition, diortho-silicate $Sm_2Si_2O_7$ was detected as the second phase but oxyorhot-silicates Sm_2SiO_5 and Sm_2O_3 were also detected, which was somewhat different from the results of Y_2O_3 or Er_2O_3 addition. With La_2O_3 addition, unlike with Y_2O_3 or Er_2O_3 addition, no rare earth silicate phases were discovered but the background of the X-ray diffraction pattern showed a broad swell at around $2\theta=20°$ to 30°, proving that there was some vitreous phase other than the matrix mullite phase.

Believing that firing mullite with IIIa family oxides added produced a low-melting point vitreous phase which promoted sintering, Ushifusa et al. discovered the production of composite IIIa oxides and SiO_2.[3] Preparing samples with 3wt% Y_2O_3 by rapidly cooling (from firing at 1600°C), we checked them for vitreous phases. The results are shown in **Fig.5**. Submitting the arrowed part in the TEM photograph to electron beam diffraction analysis, we found that an amorphous vitreous phase existed on grain boundaries. This suggests that rare earth silicate phases were produced in reactions with the mullite phase or vitreous phases slightly existing therein.

We also applied EDX element analysis to additives in the microstructures of sintered mullite samples. **Figure 6** shows SEM photographs at measurement points of EDX analysis on grain boundaries. With 3wt% Y_2O_3 addition, Y was found in grains, on grain boundaries and at triple points as shown in **Table 1**. These results suggested that in firing at 1500° and 1600°C, mullite sinterability was improved by viscous fluidity of diortho-silicates.

With CeO_2 addition, only the CeO_2 phase was found in addition to the mullite phase. EDX element analysis of Ce in the microstructures of sintered samples discovered, as shown in Table 1, that Ce was largely concentrated on grain boundaries and at triple points. This, together with the results of XRD, suggests that Ce exists as CeO_2. Crystal and vitreous phases of rare earth silicates, as found with

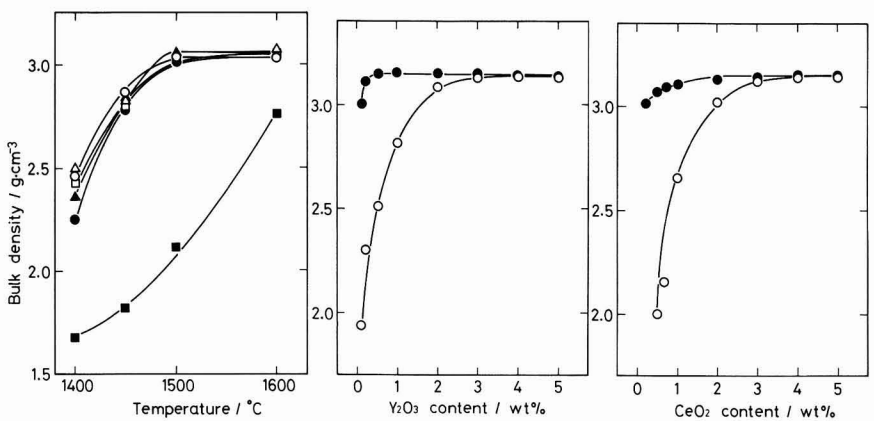

Fig. 1. Relation between bulk density and sintering temperature for the samples with 2wt% of various rare earth oxides. ○: Y_2O_3, △: Sm_2O_3, □: Er_2O_3, ●: La_2O_3, ▲: CeO_2, ■: no add.

Fig. 2. Effect of Y_2O_3 content on the bulk density of mullite. ○: 1500°C, ●: 1600°C.

Fig. 3. Effect of CeO_2 content on the bulk density of mullite. ○: 1500°C, ●: 1600°C.

addition to other rare earth oxides, were not found with CeO_2.

Now it was discovered that with a slight addition of rare earth oxides, mullite sintering proceeded at relatively low temperatures and that the mode of the second phase in sintered products differs with the kind of rare earth oxide.

3.2. Microstructures of Sintered Mullite

We manufactured sintered samples by firing at 1600°C for 2h mullite blocks containing Y_2O_3 by 0.5wt%, or Y_2O_3, Er_2O_3, Sm_2O_3, La_2O_3 or CeO_2 each by 3wt%. **Figure 7** shows SEM photographs of their thermal etched surfaces.

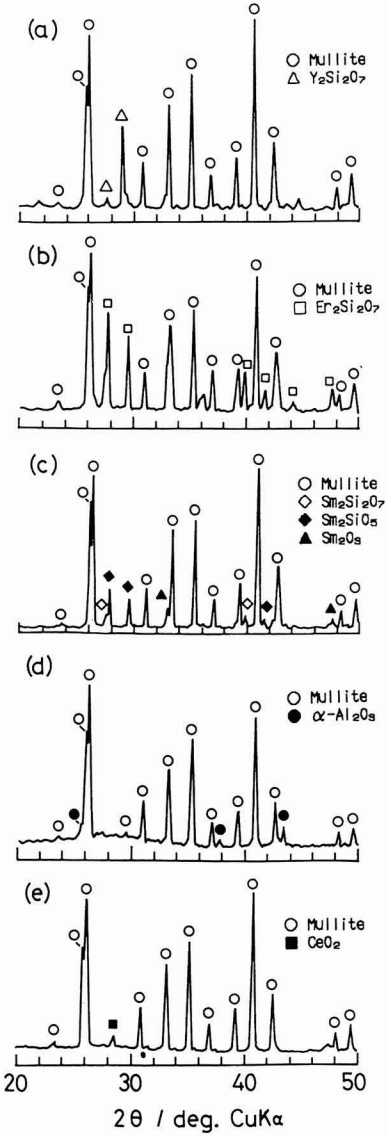

Fig. 4. XRD patterns of the samples with various rare earth oxides sintered at 1500°C.
(a) 5wt% Y_2O_3, (b) 10wt% Er_2O_3, (c) 5wt% Sm_2O_3, (d) 10wt% La_2O_3 and (e) 5wt% CeO_2

Crystal grains in the sintered sample with 0.5wt% Y_2O_3 were isometric and there were few remaining pores. The sintered samples with 3wt% rare earth oxide each had columnar crystal grain growth and remaining pores.

From the X-ray diffraction patterns and electron beam diffraction patterns for grain boundaries shown in Figs.4 and 5, we ascribed the columnar growth of crystal grains in sintered samples with rare earth oxides added to sintering based on the viscous fluidity of composite oxides of rare earth oxides and SiO_2.

3.3. Mechanical Properties of Sintered Mullite

3.3.1. 3-Point Bending Strengths of Sintered Mullite at Room Temperature

Figures 8 and **9** show the relations between 3-point bending strength at room temperature and Y_2O_3 or CeO_2 content for differing firing temperatures. With both firing temperatures 1500° and 1600°C, the 3-point bending strengths in-

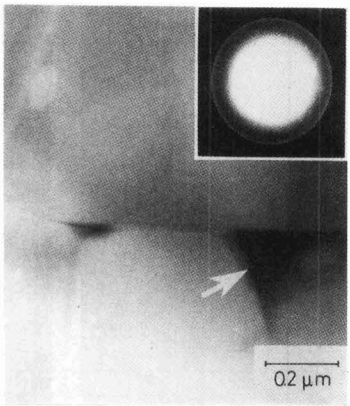

Fig 5. TEM photograph and electron diffraction pattern of the 3wt% Y_2O_3-mullite.

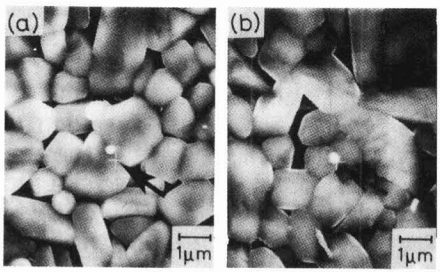

Fig. 6. SEM photographs of the fractured surface of (a) 3wt% Y_2O_3-mullite and (b) 3wt% CeO_2-mullite. Arrow indicates analytical point at the grain boundary.

Table 1. Result of EDX analysis at various points of the mullite sintered body with 3wt% of additive.

Additives	Grain (atom wt%)	Grain boundary (atom wt%)	Triple point (atom wt%)
3wt% Y2O3	0.99	1.22	1.64
3wt% CeO2	0.38	1.14	1.25

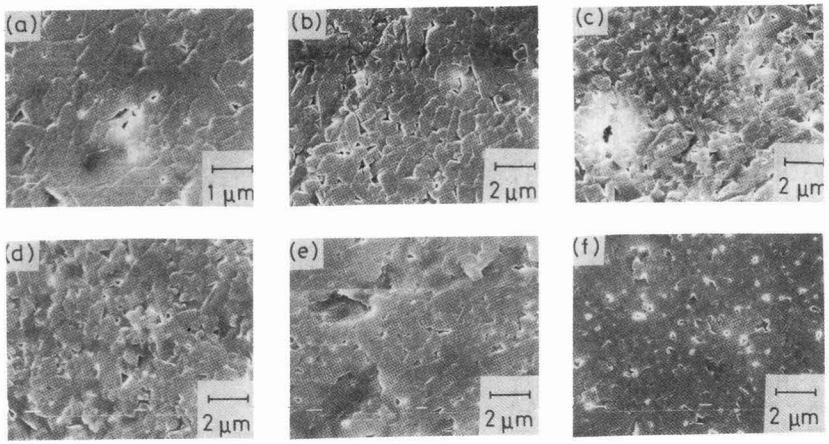

Fig. 7. SEM photographs of the samples with various rare earth oxides sintered at 1600°C. (a) 0.5wt% Y_2O_3, (b) 3wt% Y_2O_3, (c) 3wt% CeO_2, (d) 3wt% Sm_2O_3, (e) 3wt% Er_2O_3 and (f) 3wt% La_2O_3.

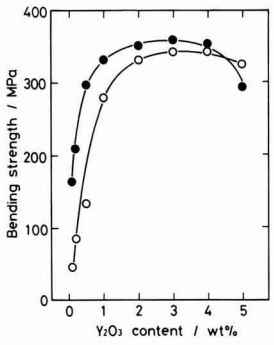

Fig. 8. Bending strength at room temperature as a function of Y_2O_3 content. ○: 1500°C, ●: 1600°C

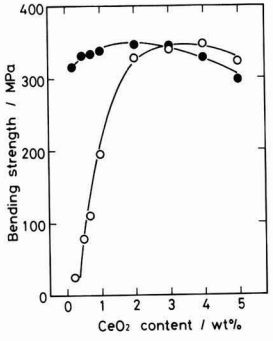

Fig. 9. Bending strength at room temperature as a function of CeO_2 content. ○: 1500°C, ●: 1600°C

creased in relation to increases in bulk densities of sintered samples due to increases in oxide contents. In the additive content range in which the bulk densities of sintered samples are constant, however, the 3-point bending strengths decreased as the additive contents increased. This behavior of 3-point bending strengths of sintered blocks in relation to additive contents can be explained by the fact that increasing the contents of oxide additives in the range in which bulk densities are constant caused columnar crystal grain growth in the sintered materials, promoting pores.

3.3.2. 3-Point Bending Strengths of Sintered Mullite at High Temperatures

Table 2 shows the 3-point bending strengths at 1200° and 1300°C of sintered samples manufactured by adding Y_2O_3 by 0.5wt% and firing at 1600°C for 2h. It also shows the value at room temperature for comparison. The 3-point bending strength of Y_2O_3 contained sintered mullite showed a peak of about 420MPa at 1200°C and then rapidly decreased to about 220MPa at 1300°C. At 1400°C, the test samples showed creep deformations. Concerning such behavior of 3-point bending strengths of sintered mullite at high temperatures, Kumazawa et al. report that sintered mullite richer in silica than stoichiometric compositions have a 3-point bending strength peak at 1300°C due to a decrease

Table 2. Relation between testing temperature and 3-point bending strength of the mullite with 0.5wt% Y_2O_3 sintered at 1600°C for 2h.

Additive	3-point bending strength (MPa)		
	R.T.	1200°C	1300°C
0.5wt% Y_2O_3	326	428	219

in the viscosity of the vitreous phase on grain boundaries.[10] Ismail et al. also report that sintered mullite with 0.3wt% MgO shows a 3-point bending strength peak at 1000°C, which can be ascribed to the vitreous phase in the sintered mullite.

4. Discussion

4.1. Sinterability of Mullite Slightly Containing Rare Earth Oxides Other than CeO_2

As to slight Y_2O_3 addition having an effect on the sintering of mullite synthesized under an electromelting or sol-gel method, Ushifusa et al. report that an oxyort silicate phase of Y_2SiO_5 was detected as the second phase in sintered mullite with Y_2O_3.[3,6] According to these researchers, in the

sintered products made from powdered mullite (Al_2O_3 content 78.0wt%, mean grain size d_{50}=3.3μm) under an electromelting method, the Y_2SiO_5 phase was detected with Y_2O_3 contents above 5.5mol% and in those made from powdered mullite (Al_2O_3 content 72.0wt%, mean grain size d_{50}=1.0μm) under a sol-gel method, a trace of the Y_2SiO_5 phase was found with Y_2O_3 contents above 8.9mol%. Thus, they pointed out that the Y_2O_3 content range which allows the Y_2SiO_5 phase to be detected varies with grain size, composition of mullite powder, and synthesis conditions.

Differing mullite powder synthesis conditions may vary the production of the second phase. In the sintered samples made by adding Y_2O_3 to be powdered mullite used in the present test, a diortho-silicate phase of $Y_2Si_2O_7$, not $Y_2Si_2O_5$, was found and with Y_2O_3 contents above 5wt%, an α-Al_2O_3 phase was also slightly detected. Considering that in the sintering of the mullite powder SiO_2 was freed very little, this may due to the consequent production of $Y_2Si_2O_7$ in the reaction between additive Y_2O_3 and mullite, causing the mullite composition to be changed beyond the solid-dissolution limit, which resulted in α-Al_2O_3 being freed. Thus, we assumed that additive Y_2O_3 reacted not only with the SiO_2 phase slightly remaining in the mullite powder initially used but also with mullite, causing SiO_2-rich Y_2SiO_7, rather than Y_2SiO_5, to be produced. That which occurs with Y_2O_3 addition is also true with Er_2O_3 addition to the mullite phase. With Sm_2O_3 addition, however, it is assumed that the effect on the reaction with mullite was so small that as the additive content increased, SiO_2-poor Sm_2SiO_5 was also produced.

4.2. Sinterability of CeO_2 Content Mullite

Much is still unknown about the reaction between CeO_2 and SiO_2 in air or an oxidizing atmosphere. Bonder reports that while SiO_2 reacts with rare earth oxides in an oxidizing atmosphere, producing rare earth silicates, CeO_2 reacts with SiO_2 only in a reducing atmosphere and never in an oxidizing atmosphere.[12] Felsche et al. report that cerium silicates are unstable in a low-temperature oxidizing atmosphere.[13] Babini et al. report that in sintered products made by adding CeO_2 to Si_3N_4 and hot pressing in a nitrogen atmosphere, $Ce_2Si_2O_7$ is produced, which is decomposed into CeO_2 and SiO_2 when the sintered products are oxidized at a temperature above 1650K (about 1377°C).[14,15] Their report suggests that cerium silicate is hardly produced in the reaction between CeO_2 and SiO_2 in air or an oxidizing atmosphere.

Studying the effect of CeO_2 addition to alumino-silicate refractory, O'Brien et al. have recently detected by XRD $Ce_2Si_2O_7$ and Ce_2SiO_5 in the samples made by firing a 1550°C for 5h in air or a nonoxidizing atmosphere and then rapidly cooling. They have also reported that CeO_2 and α-cristobalite were detected in the samples annealed at 1300°C for 8h after firing at 1550°C for 5h and cooling for 2.5h to 1300°C.

These findings show that the production and stability of cerium silicates from reactions between CeO_2 and SiO_2 in air depend greatly on test conditions. In accordance with the knowledge above (on condition that the report by O'Brien et al. is supported), the improved sinterability of sintered mullite by CeO_2 addition can possibly be ascribed to the reaction between CeO_2 and mullite and subsequent sintering based on the viscous fluidity of cerium silicate at about 1500° to 1600°C. Cerium silicate was not detected in the XRD pattern shown in Fig.4; this may be because the heating/cooling rate was relatively low: 4°C/min, which allowed the cerium silicate to be decomposed into CeO_2 and amorphous SiO_2. If Bonder's report is supported, the separation of SiO_2 from mullite is promoted by CeO_2 addition and sintering occurs due to the viscous fluidity of free SiO_2, while a cerium silicate phase is hardly produced from the reaction between CeO_2 and SiO_2. Thus, the improved sinterability of mullite by CeO_2 addition can be explained by either O'Brien's or Bonder's opinion. At any rate, the sintering of mullite with CeO_2, as with other rare earth oxide additives, is certainly promoted by viscous fluidity.

Table 3. Relation between the temperature indicating a maximum 3-point bending strength of various mullite sintered bodies and the melting point of those secondary phases.

Secondary phase	Melting point (°C)	Maximum temp. (°C)
SiO_2 (Cristobalite)	1728	1300
$Y_2Si_2O_7$	1660-1775	1200
Cordierite	1460-1470	1000

4.3. Relation between High-Temperature 3-Point Bending Strength and Silicate Phases

Generally, the viscosity of a substance is closely related to the melting point of the substance and we can assume that with a certain level of viscosity, the higher the melting point of a substance, the higher the temperature at which that substance shows viscosity. Utilizing this fact, we investigated, using glass-rich, MgO-added and Y_2O_3- added sintered mullite samples, the relation between measured temperatures which caused 3-point bending strengths to peak and the melting points of the vitreous phase (taken as a cristobalite phase) and the cordierite and $Y_2Si_2O_7$ phases of silicate as second phases respectively in the three groups of sintered samples.[17-20] The results are shown in **Table 3**. The lower the melting point of the second phase, the lower the measured temperature which gave a 3-point bending strength peak. Thus, as one of the reasons why 3-point bending strength peaks, we can possibly point out decreases in viscosity due to silicate as the second phase produced in sintered products. In other words, the lower the melting point of the second phase contained in the sintered mullite, the more the measured temperature shifts toward the low-temperature side, which gives the peak of 3-point bending strength.

5. Conclusion

The sintering of mullite materials with each of several rare earth oxides added by 0.2 to 10wt% proceeded at relatively lower temperatures of 1500° to 1600°C. This is because the additive rare earth oxides reacted during sintering with mullite or silica slightly contained in mullite, producing rare earth silicates which have lower melting points than that of mullite. The rare earth silicates produced remained in different forms which can be classified into crystal, vitreous and decomposed.

The microstructures of sintered mullite samples varied with the content of added rare earth oxides. With a higher additive content, as rare earth silicate phases were produced, sintering based on viscous fluidity proceeded, producing

columnar mullite crystals and more pores. While slightly adding Y_2O_3 or CeO_2 improved the sinterability of mullite and increased 3-point bending strength, an ample addition of these additives caused the 3-point bending strength to decrease. The 3-point bending strength of sintered mullite with 0.5wt%Y_2O_3 added peaked to around 420MPa at 1200°C, which was a similar trend to those with MgO addition or the slight existence of a vitreous phase. With these systems, we discovered that the measured temperatures which gave peaks of 3-point bending strength were related to the melting points of the second phases in sintered samples.

References:

1) Mullite, ed. by S. Somiya, Uchida Rokakuho (1985).
2) Mullite 2, ed. by S. Somiya, Uchida Rokakuho (1987).
3) N. Ushifusa, and S. Ogihara: Seramikkusu Ronbunshi, 97, 690-98 (1989).
4) N. Ushifusa: JP. 63-60153.
5) N. Ushifusa: JP. 62-60154.
6) T. Kurihara, M. Horiuchi, A. Kuribayashi, Y. Takeuchi, and S. Wakabayashi: Ms. for 1989 Annual convention of Ceramics Society of Japan, p.486.
7) K. Hashimòto, and K. Niwa: Yogyo-Kyokai-Shi, 95, 1037-39 (1987).
8) T. Mori, N. Kosugi, and Y. Kubota: Ms. for 1989 Annual convention of Ceramics Society of Japan, p.8.
9) K. Hayashi, S. Kanzaki, Y. Ohashi, and T. Nagaoka: Ms. for 1989 annual convention of Ceramics Society of Japan, P.9.
10) T. Kumazawa, S. Kanzaki, S. Ohta, and H. Tabata: Yogyo-Kyokai-Shi, 96, 85-91 (1988).
11) M.G.M.U. Ismail, H. Tsumatori and Z. Nakai, J. Mater. Sci. (submitted).
12) I.A. Bonder, Ceram. Int., 8, 83-89 (1982).
13) J. Felsche and W. Hirsiger, J. Less-Common Met., 18, 131-37 (1969).
14) G.N. Babini, A. Bellosi and P. Vincenzini, Ceram. Int., 6, 150-52 (1980).
15) G.N. Babini, A. Bellosi and P. Vincenzini, Ceram. Int., 7, 78-86 (1981).
16) M.H. O'Brien and M. Akinc, J. Am. Ceram. Soc., 72, 896-904 (1989).
17) S. Kanzaki, T. Kurihara, S. Iwai, M. Ohashi, and H. Tabata: Yogyo-Kyokai-Shi, 95, 1213-18 (1987).
18) N.A. Toropov and I.A. Bondar, Izv. Akad. Nauk SSSR, Otd. Khim. Nauk, 4, 544-50 (1961).
19) A. Nukui: Ceramics, 20, 266-73 (1985).
20) W. Schreyer and J.F. Schairer, J. Petrol., 2, 324-406 (1961).

This article is a full translation of the article which appeared in Nippon Seramikkusu Kyokai Gakujutsu Ronbunshi (Japanese version), Vol.99, No.5, 1991.

Creep in Mullite Ceramics Containing Zirconia

Masahiro Ashizuka, Takeshi Honda* and Yoshitaka Kubota**

Kyushu Institute of Technology, Department of Materials Science and Engineering
1-1, Sensui-cho, Tobata-ku, Kitakyushu-shi, 804 Japan
*Graduate student, Kyushu Institute of Technology
1-1, Sensui-cho, Tobata-ku, Kitakyushu-shi, 804 Japan
**Tosoh Corporation, Advanced Materials Laboratory
2743, Hayakawa, Ayase-shi, 252 Japan

The creep deformation in 72wt%Al_2O_3-mullite (72A), 74wt%Al_2O_3-mullite (74A) and those containing 10vol%ZrO_2 (72A-10Z and 74A-10Z, respectively) has been studied. Stress exponent n's for creep in 72A-10Z and 74A-10Z were 1.1 to 1.2 and 1.0 to 1.2, respectively, slightly smaller than those in 72A (1.2 to 1.3) and 74A (1.3 to 1.5). Activation energies for creep in 72A-10Z and 74A-10Z were 157 and 158 kcal/mol, respectively, slightly smaller than those in 72A and 74A (171 and 169kcal/mol, respectively). Creep rate in 74A was increased more than that in 72A by addition of 10vol%ZrO_2. It was estimated that the enhanced creep rate of mullite ceramics by the addition of ZrO_2 was ascribed to the relaxation of the stress at grain boundary triple points by the creep deformation of ZrO_2 grains.
[Received August 9, 1990; Accepted December 14, 1990]

Key-words: Creep, Mullite, SiO_2-Al_2-O_3 ceramics, Zirconia, Grain boundary sliding, Stress exponent, Activation energy

1. Introduction

Because of its small coefficient of thermal expansion and small strength degradation at high temperature, mullite ($3Al_2O_3$-$2SiO_2$), an oxide, is hopeful as a high-temperature structural material.[1,2] Measuring creeps in mullite ceramics with the composition of 71, 74 and 78 wt% Al_2O_3 at 1350° to 1500°C, we already reported that in 74wt%Al_2O_3 mullite, creep deformation rates were very low even at 1400°C.[3] Further, studying the effect of grain size on creep rates in 71, 72 and 74wt%Al_2O_3 mullites, we concluded that primary creep deformation mechanism were grain boundary sliding for the 74wt%Al_2O_3 system; diffusion in the vitreous phase on grain boundaries for the 71wt%Al_2O_3 system; and the mixed one of the above for the 72wt%Al_2O_3 system.[4]

As appeared in the previous paper, mullite ceramics have excellent creep resistance and a high bending strength above 200MPa even at high temperatures around 140° to 1500°C. At room temperature, however, a rather low strength around 300 to 400MPa and a low fracture toughness around 2MPam$^{1/2}$ are exhibited. To improve its mechanical properties, zirconia (ZrO_2) is added.

Measuring in the strength of mullite ceramics containing ZrO_2, Kubota et al. reported that room-temperature strength was improved from 400 to 500MPa.[5,6] Measuring creeps of 72 and 74wt%Al_2O_3 mullite systems containing 10vol%ZrO_2, we studied creep characteristics of zirconia reinforced mullite ceramics by comparing them with data without ZrO_2.

2. Experimental Procedure

To manufacture specimens for creep measurement, mullite powders with the composition of 72 and 74 wt% Al_2O_3 and these containing 10 vol% ZrO_2 were used. These powder were pressed uniaxially at 20 MPa and were compacted isostatically at 250 MPa. Their compacted specimens were sintered for 4th at 1600°C for specimens containing ZrO_2 and at 1650°C for ones without ZrO_2. Their sintered specimens were cut into the rectangular bars of 3mm by 4mm by 40mm. Creep was measured by a 4 point bending method. Four point equipment and loading rod are made of mullite ceramics. The stress was applied by a balance method and the deflection was measured by a dirrential transformer. All measurements were carried in air. The average grain sizes were measured by a linear intercept method.

3. Results and Discussion

3.1. Microstructures

Figure 1 shows the microstructures of ZrO_2 added mullite ceramic samples. Those of 72A and 74A were shown previously.[4] The microstructure of 72A-10Z has ZrO_2 particles distributed on grain boundaries in the matrix containing fine isotropic and rod-like crystals together. That of 74A-10Z also had ZrO_2 particles distributed on grain boundaries in the matrix but the matrix consisted of isotropic

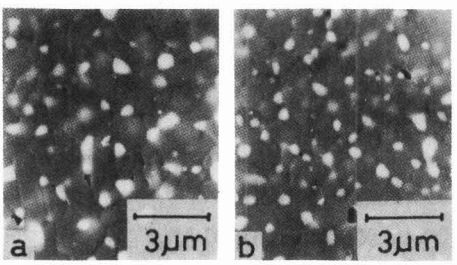

Fig. 1. Microstructures of mullite ceramics (chemically etched by 1%HF aqueous solution at 0°C). (a) 72wt%Al_2O_3-10ZrO_2(72A-10Z) and (b) 74wt%Al_2O_3-10ZrO_2(74A-10Z)

crystals only. The mean grain sizes in the matrices of the 4 types of specimens used in the present study were obtained as follows: 1.3 and 2.4μm for 72A and 74A respectively. The microstructures of 72A-10Z and 74A-10Z had tetragonal ZrO_2 distributed on the grain boundaries in the mullite matrices and the mean grain sizes of the mullite matrix and ZrO_2 were 2.0 and 1.0μm respectively for 72A-10Z and 2.3 and 0.8μm respectively for 74A-10Z.

3.2. Creep Measurement

Figure 2 shows changes of deflection with time for 74A and 74A-10Z under a stress of 35.7MPa at 1400°C. Although the time dependence of the deflection for the specimen containing ZrO_2 are greater, the variations for both materials show a similar trend; and as reported previously, a transition creep region is followed by a steady creep region.

The following relation exists between strain rate ε and stress σ in the steady creep zone:[8]

$$\dot{\varepsilon} = \frac{ADGb}{kT}\left(\frac{b}{d}\right)^m\left(\frac{\sigma}{G}\right)^n \quad \ldots\ldots\ldots\ldots\ldots (1)$$

where

A : constant
D : coefficient of diffusion
G : shear modulus
b : Burger's vector
d : grain size
σ : applied stress
m : grain size exponent
n : stress exponent
k : Boltzmann's constant
T: absolute temperature

The diffusion coefficient D is given by:

$$D = D_0 \exp(-Q/RT) \quad \ldots\ldots\ldots\ldots\ldots (2)$$

where

D_0 : frequency factor
Q : activation energy of creep
R : gas constant

Exponents m and n in equation (1) are related to creeping mechanisms. Since measurement in the present study is with only 1 grain size, equation (1) can be simplified as

$$\dot{\varepsilon} = B\sigma^n \quad \ldots\ldots\ldots\ldots\ldots\ldots (3)$$

where B is a constant if the temperature is constant. In addition, bending stress σ and straining rate $\dot{\varepsilon}$ in 4-point bending tests needed when reducing measured data in equation (1) or (3) were calculated, in the same way as in the previous reports, from loads and load point deflection rate under the analysis method by Hollenberg et al.[9]

One example of time dependence in the deflection at the loading point under a constant load is shown in Fig.2. Such relations were measured at temperatures between 1300° and 1500°C and on the basis of the data obtained, the relation between stress σ and straining rate ε was obtained. The results are shown in **Figs.3** through **6**. Figs.3 and 4 show the relation between creep rate and appllied stress for 72wt%Al_2O_3 mullite (72A) and 72wt%Al_2O_3 mullite containing 10vol%ZrO_2 (72A-10Z) respectively. The data for

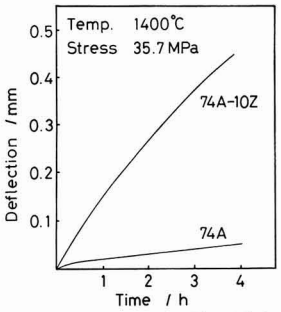

Fig. 2. Typical creep curves for 74wt%Al_2O_3-mullite(74A) and 74wt%Al_2O_3-mullite containing 10vol%ZrO_2(74A-10Z).

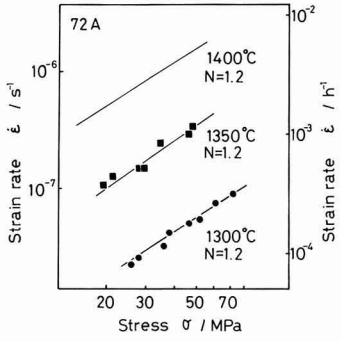

Fig. 3. Relation between creep rate ε and applied stress σ for 72wt%Al_2O_3-mullite ceramics (72A). The line for 1400°C is from reference 4.

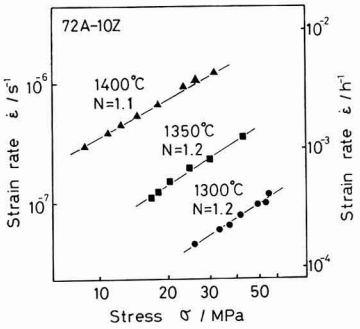

Fig. 4. Relation between creep rate and applied stress σ for 72wt%Al_2O_3-mullite containing 10vol%ZrO_2(72A-10Z).

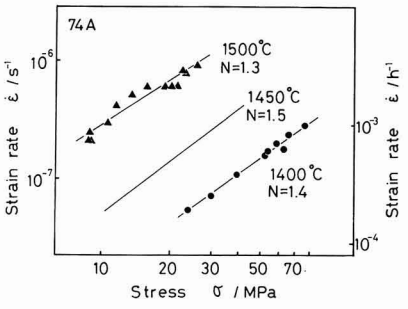

Fig. 5. Relation between creep rate and applied stress σ for 74wt%Al_2O_3-mullite ceramics (74A). The line for 1450°C is from reference 4.

72A at 1400°C in Fig.3 was taken from the previous report.[4] From the gradients of the lines, the stress exponent n for 72A was 1.2 to 1.3 (including n=1.3 for grain size of 2.1μm in previous report[4]), while the n value for 72A-10Z containing 10 vol% ZrO_2 was 1.1 to 1.2. Figs.5 and 6 show the relation for 74wt%Al_2O_3 mullite (74A) and 74wt%Al_2O_3 mullite containing 10vol%ZrO_2(74A-10Z) respectively. The data of 1450°C in Fig.5 was taken from the previous report.[4] Stress exponent n (obtained from the gradients) was 1.3 to 1.5 for 74A and 1.0 to 1.2 for 74A-10Z (with 20vol%ZrO_2). Generally, n is smaller for mullite containing ZrO_2 than for mullite without ZrO_2. Adding ZrO_2 to both 72A and 74A, n values decrease until 1.0 to 1.2. That is, n value becomes close to 1 exhibiting diffusion creep.

Figure 7 shows the relation between creeping rate and temperature at a constant applied stress of 40MPa. The relative positions of the straight lines show that adding 10vol%ZrO_2 to 74wt%Al_2O_3 mullite (74A-10Z) causes the creeping rate to rise greatly. On the other hand, adding 10vol%ZrO_2 to 72wt%Al_2O_3 mullite (72A-10Z) does likewise but only slightly. However, when comparing creep rates, we should consider that the grain size (1.3μm) of the 72A matrix is smaller than that (2.0μm) of the 72A-10Z matrix. Referring to the results in the previous paper, we converted the creep rate in 72A at 1400°C into the value at the grain size of 2.0μm, which is shown by the x mark in the figure.[4] Comparing the data at the same grain size level,

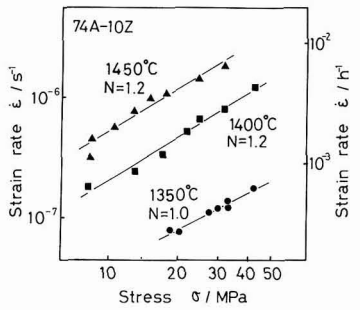

Fig. 6. Relation between creep rate and applied stress σ for 74wt%Al_2O_3-mullite containing 10vol%ZrO_2(74A-10Z).

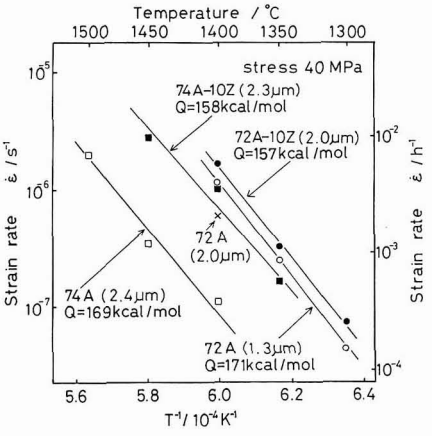

Fig. 7. Arrhenius plots for creep deformation rate of mullites and ZrO_2-containing mullites. The data of mark ö is from reference 4. The number in parentheses shows the grain size of mullite matrix.

we find that adding ZrO_2 to 72A causes the creep rate to increase but the magnitude of the increase is not so much as ZrO_2 addition to 74A.

From the gradients of the straight lines in Fig.7, activation energies can be obtained as 157kcal/mol for 72A-10Z and 158kcal/mol for 74A-10Z, in contrast to 171 and 169kcal/mol for 72A and 74A respectively. Thus, with both 72A and 74A, a 10vol%ZrO_2 addition causes activation energy to decrease a little.

Next, the ceep deformation mechanism of the mullite ceramics containing ZrO_2 was considered in connection with previous paper.[3,4] The results in the previous papers can be summarized as follows:

1) There is a vitreous phase on grain boundaries in 72A mullite. This facilitates grain boundary sliding, allows diffusion via the vitreous phase on grain boundaries and also facilitates creep deformation.[4]
2) There is no vitreous phase on grain boundaries in 74A mullite. This means that there is no mechanism that relaxes stress concentration on triple points of grain boundaries due to grain boundary sliding. Consequently, creep rates become low.
3) In 78A mullite, there is no vitreous phase on grain boundaries but Al_2O_3 distributed near triple points of grain boundaries. Stress concentration near triple points of grain boundaries due to grain boundary sliding is relaxed by the deformation of Al_2O_3 particles. Consequently, creep rates become higher than that in 74A.[3]

The microstructure of mullite ceramics containing ZrU_2 is shown in Fig.1. ZrU_2 is not homogenized in mullite but distributed on grain boundary. From SEM observation of microstructure, on the other hand, as already reported, it can be assumed that 78A is regarded as 74A mullite with Al_2O_3 particle dispersed in its matrix. That is, 74A-10Z used in this study may be regarded as the mullite that Al_2O_3 particles dispersed in 78A mullite are replaced with ZrU_2 particles. Therefore, the creep mechanism in the 74-10Z can be considered in comparison with term (3) in above summary.

Further, the diffusion conefficient of oxygen and Zr in zirconia ceramics and the activation energy for creep of zirconia ceramics. Since the diffusion coefficient of pure ZrO2 has not been measured, activation energies of oxygen and Zr diffusion in zirconia ceramics containing a stabilizer CaO or MgO are shown below. For activation energy for oxygen, Oishi et al. report 15kcal/mol for a 12mol%MgO-ZrO2 system and 19.1kcal/mol for a 15mol% CaO-ZrO_2 system.[10] For activation energy of Zr diffusion, Rhodes et al. report 92.5kcal/mol for 12 and 16mol%CaO-ZrO_2 systems and Oishi et al. report 90.2kcal/mol for 16mol%CaO-84mol%$(Zr_{1-x}Hf_x)O_2$, 91.1kcal/mol for 14MgO-86mol%$(Zr_{1-x}Hf_x)O_2$ and 93.5kcal/mol for 16mol%Y_2O_3-84mol%$(Zr_{1-x}Hf_{xD})O_2$.[11,12]

As with diffusion, no creeps for pure ZrO_2 have been measured. For creep activation energy, P. E. Evans reports 86kcal/mol for 6mol%Y_2O_3-ZrO_2(grain size: 17μm) and St-Jacques and Angers report 94kcal/mol for 18mol%CaO-ZrO_2 (grain size: 7 to 29μm).[13,14] Wakai et al. prove that if grain size is as small as 0.3μm, the phenomenon of superplasticity are observed in 3mol%Y_2O_3-ZrO_2 and report 140kcal/mol as creep activation energy.[15] The values estimated by converting creeping rates obtained in these reports into ones with the ZrO_2 grain size 0.8 to 1.0μm in the present study are larger than those for 74A composed of mullite only.

As shown by the comparison of diffusion and creep activation energies above, except for the results by Wakai et al. (who observed the phenomenon of superplasticity), creep activation energy is close to activation energy for Zr diffusion in zirconia ceramics (about 90kcal/mol). This suggests that activation energy for creeping rates in ZrO_2 ceramics at 1300° to 1450°C is smaller than that with the matrix composed of mullite only (74A) and that the n value is close to 1.

The tensile surface after creep test for 4h at 1400°C for 72A-10Z and at 1450°C for 74A-10Z were observed by SEM. However, their grain boundaries were not clear and cavities were not observd.

To consider the results described above, it is estimated that the stress concentration occurred at triple point of grain boudnary by grain boundary sliding is relaxed by diffusion creep responsible for the deformation of ZrO_2 particles in 74A containing 10vol%ZrO_2 (74A-10Z). That is, it is concluded that this causes the creep deformation rate to enhance, activation energy to decrease and the n vaue to approach 1. On the other hand, the creep deformation rate of the 72A is originally high. This may be the reason why adding ZrO_2 to 72A does not cause the creep deformation rate to enhance as much as in 74A.

4. Conclusion

Measuring creeps in 72 and 74wt%Al_2O_3 mullite ceramics (72A and 74A) and ZrO_2 reinforced mullite ceramics by adding 10vol%ZrO_2 each to 72A and 74A (72A-10Z and 74A-10Z), we reached the following conclusions:

1) Stress exponent indices for creep deformation were 1.2 to 1.3 and 1.1 to 1.2 for 72A and 72A-10Z respectively and 1.3 to 1.5 and 1.1 to 1.2 for 74A and 74A-10Z respectively. Thus, adding ZrO_2 to mullite ceramics caused stress exponent n to decrease.
2) Activation energies for creep deforamtion were 171 and 157kcal/mol for 72A and 72A-10Z respectively and 168 and 158kcal/mol for 74A and 74A-10Z respectively. Thus, ZrO_2 addition caused the activation energies for creep of 72A and 74A to decrease.
3) ZrO_2 addition to 74A caused the creep rate to increase more than did ZrO_2 addition to 72A.
4) Creep rates in ZrO_2-toughened mullite ceramics are higher than in mullite-single phase ceramics. This is possibly because stress concentration on triple points of grain boundaries due to grain boundary sliding is relaxed by deformation of ZrO_2 particles.

Acknowledgements

We express our thanks to T. Okuno (graduate student), K. Tsutsumi, H. Ito and M. Oshita (undergraduate students) at the Engineering Dept. of Kyushu Institute of Technology for helping us pursue our study.

References:

1) S. Somiya: Materials Series: Mullite, Uchida Rokakuho, 1985, pp.1-11.
2) T. Kawanami: New Materials Series: Mullite, ed. by S. Somiya, Uchida Rokakuho, 1985, pp.123-135.
3) M. Ashizuka, T. Okuno, and Y. Kubota: Seramikks Ronbunshi, 97, 662-68, (1989).
4) M. Ashizuka, T. Honda, and Y. Kubota: Seramikks Ronbunshi, 99, 292-295, (1991).
5) Y. Kubota and H. Takagi, Proc. Brit. Ceram. Soc., 37, 179-188 (1986).
6) Y. Kubota and H. Takagi, "New Materials Series: Mullite", ed. by S. Somiya, Uchida Rokakuho, 1987, pp.105-118.
7) R. L. Fullman, Trans. AIME, 197, 447-452 (1953).
8) T. G. Langdon, Deformation of Ceramic Materials, ed.by R. C. Bradt and R. E. Tressler, Plenum Press, New York(1974), pp.101-126.
9) G. W. Hollenberg, G. R. Terwilliger and R. S. Gordon, J. Amer. Ceram. Soc., 54, 196-199 (1971).
10) Oishi, Ando, M. Akiyama: Journal of chemical Society of Japan, 1445-1453 (1981).
11) W. . Rhode and R. E. Carter, J. Amer. Ceram. Soc., 49 244-249.
12) Y. Sakka, Y. Oishi and K. Ando, J. Mater. Sci., 17, 3101-3105 (1982).
13) P. E. Evans, J. Amer. Ceram. Soc., 53, 365-369 (1970).
14) St-Jacques and Angers, J. Amer. Ceram. Soc., 55, 571-574 (1972).
15) F. Wakai, S. Sakaguchi and Y. Matsuno, Advanced Ceramic Materials, 1, 257-263 (1986).

This article is a full translation of the article which appeared in Nippon Seramikkusu Kyokai Gakujutsu Ronbunshi (Japanese version), Vol.99, No.5, 1991.

A Theory of Non-Destructive Inspection Based on Fracture Mechanics and Fracture Statistics

Koichi Kitakami, Yohtaro Matsuo* and Shiushichi Kimura*

Canon Inc., Information Systems Research Center,
890-12 Kashimada, Saiwai-ku Kawasaki-shi, Kanagawa, 211 Japan
*Tokyo Institute of Technology, Faculty of Engineering, Department of Inorganic materials
2-12-1, Ookayama, Meguro-ku, Tokyo 152

The proof-test and non-destructive inspection (N.D.I.) are used to assure the reliability of structural ceramics. Especially, the proof-test has widely been applied to guarantee the safety of the structural materials. On the other hand, N.D.I. is not yet adopted independently, because of no available theoretical analysis.
In this paper, the statistical theory and effective execution method of N.D.I. are presented. By calculating the flaw-size distributions for uni-axial tensile stress field after N.D.I., the effect of screening-size (d_p) is analyzed theoretically. It is proposed that the stress field in N.D.I. must be the same as the stress field in real loading.
[Received August 30, 1990; Accepted March 22, 1991]

Key-words: Non-destructive inspection, Structural ceramics, Weibull statistics, Flaw-size-distribution, Stress distribution

1. Introduction

Fine ceramics are attracting interest in extensive fields because of their excellent properties, with various material design and reliability evaluation being adopted in applications. In particular, in use for structural materials, proof tests are said to be effective to guarantee minimum strength or life; some studies and applications have already been reported.[1-4] On the other hand, there are some drawbacks such as the proof tests requiring much time and labor. Moreover, load applied in the proof test may cause some degradation in the remaining samples. There used to be a restriction in that minimum strength or life obtained from proof tests were only effective in cases under the same load as the proof tests, but this point is being cleared up thanks to work by Hamanaka et al.[4] However, some other problems are still unsolved as stated above.

Another reliability evaluation is non-destructive inspection (N.D.I.). In N.D.I., information on the size distribution of flaws causing failure is quite important, and yet theoretical studies in this area have been few. The authors have so far reported statistical theories[5,6] on fracture locations based on a competing risk theory, and deduced the flaw-size distribution at fracture origin and strength distribution in a 3-point bendig stress field after screening with the help of the above reported theories, and compared them with the results of experiments on hot-pressed silicon nitride to prove the effectiveness of the theory.[7]

On the other hand, the authors have studied hot-pressed silicon nitride to investigate various properties of the flaw-size distribution at fracture origin, namely the influences of stress gradient in materials, shape parameters, the volume of materials, and fracture toughness.[8] Among these, in an analysis on the stress gradient dependence of the flaw-size distribution, the size distribution in the 3-point bending stress field was compared with that in the uni-axial uniform tensile stress field to find that the former in the presence of stress gradient is shifted to the lower side by 20μm more than the latter.

In the evaluation of the strength property of ceramic materials, the 3-point bending test is commonly used to measure fracture stress or the geometry of fracture origins. From the viewpoint of the theoretical establishment of N.D.I. along with efficient use of test data, the construction of a theory is awaited which can predict the flaw-size distribution at fracture origin and fracture stress distribution when specimens after screening based on the flaw-size distribution obtained from the above-stated 3-point bending tests are exposed to other conditions such as uni-axial uniform tensile stress.

This paper is intended to contribute to the establishment of N.D.I. theories and discusses that a screening size d_p cannot be determined without depending on a stress condition, through the theoretical analysis of influences of the screening size d_p on the size distribution of fracture source defects after screening under uni-axial uniform stress. Moreover, the paper describes the importance of identifying regions for screening in the presence of stress distribution in specimens, and proposes a new, efficient screening method considering the identification of these regions.

2. Flaw-Size Distribution at Fracture Origin

In the following discussion, only an internal flaw (i=1) is conceived as well as a penny shape for a crack model for simplification. When fracture stress σ_c (perpendicular to a crack plane) at a fracture location and the diameter d_c of a crack at the location are expressed as follows:

$$K_{IC} = \frac{2}{\pi}\sigma_c\sqrt{\pi d_c/2} \quad \cdots\cdots\cdots\cdots\cdots (1)$$

where K_{IC} is fracture toughness; the probability density function of crack size at fracture $h_T(dc)$ and its distribution function $H_T(dc)$ under uni-axial uniform tensile stress are determined by the following formulas[8]:

$$h_T(d_c) = \left(\frac{m_1}{2}\right) V \left(\sqrt{\frac{\pi K_{IC}}{2\sigma_{01}}}\right)^{m_1} d_c^{-(m_1+2)/2} \cdot \exp\left\{-V\left(\sqrt{\frac{\pi K_{IC}}{2\sigma_{01}}}\right)^{m_1} d_c^{-m/2}\right\} \quad \cdots\cdots (2)$$

and,

$$H_T(d_c) = \exp\left\{-V\left(\sqrt{\frac{\pi K_{IC}}{2\sigma_{01}}}\right)^{m_1} d_c^{-m_1/2}\right\} \quad \cdots\cdots (3)$$

where

m_1: shape parameter

σ_{01}: scale parameter

V: the volume of a specimen.

Moreover, the probability density function of the crack size under 3-point bending stress (**Fig.1**) is[6]:

$$h_B(d_c) = \int_{y_t}\int_{x_t} h_B(d_c, x, y)\, dxdy,$$

$$h_B(d_c, x, y) = b \cdot m_1 \left(\sqrt{\frac{\pi K_{IC}}{2\sigma_{01}}}\right)^{m_1} \cdot d_c^{-(m_1+2)/2} \cdot \exp\left[-V_{e0}\left\{\sqrt{\frac{\pi}{2}}\frac{K_{IC}}{\sigma_{01}}\frac{Lh}{x(h-y)\sqrt{d_c}}\right\}^{m_1}\right],$$

$$V_{e0} = \frac{2bLh}{(m_1+1)^2} \quad \cdots\cdots (4)$$

where

V_{eO}: dimensionless effective volume

b, h, and L: specimen size.

In this case, it is necessary that numerical integration be performed over the entire region in terms of fracture location variables (x,y) to obtain peripheral distribution regarding the diameter d_c of a fracture source crack.

Figure 2 shows the examples of the probability density function of flaw size under uni-axial uniform tensile and 3-point bending stress described above. The values of used parameters (**Table 1**) were estimated applying a multi-step maximum likelihood method[10] with the measurements of 3-point bending tests of silicon nitride conducted by Ito et al..[9] The figure also includes data when the volume was varied against each stress condition (volume V = 45, 90, 180mm^3). It is clear that the flaw-size is smaller under 3-point bending with stress gradient in the material than under uni-axial uniform tension.

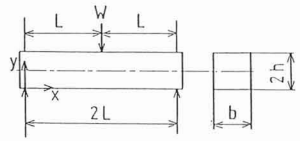

Fig. 1. The coordinate systems in the three-point bending test.

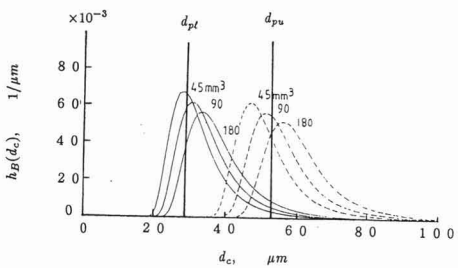

Fig. 2. Probability density function of flow-size. d_{pl} and d_{pu} are screening-size from three-point bending and from uniaxial tension, respectively.

3. Proposition to N.D.I

This chapter states analysis using the probability density function of flaw-size introduced in the previous chapter. In this case, flaw detection probability is assumed to be 100 percent.

3.1. Flaw-Size Distribution After Screening

An earlier report[7] described that the flaw size distribution at fracture origin is expressed in the following formula using probability density function stated in Chapter 2. Under uni-axial uniform tensile stress:

$$H_{Ta}(d_c) = \frac{\int_0^{d_c} h_T(d_c)dd_c}{\int_0^{d_p} h_T(d_c)dd_c}, \quad (0 \le d_c < d_p)$$

$$= \frac{\exp\left\{-V\left(\sqrt{\frac{\pi}{2}}\frac{K_{IC}}{\sigma_{01}}\right)^{m_1} d_c^{-m_1/2}\right\}}{\exp\left\{-V\left(\sqrt{\frac{\pi}{2}}\frac{K_{IC}}{\sigma_{01}}\right)^{m_1} d_p^{-m_1/2}\right\}} \quad \cdots\cdots (5)$$

under 3-point bending stress:

$$H_{Ba}(d_c) = \frac{\int_0^{d_c} h_B(d_c)dd_c}{\int_0^{d_p} h_B(d_c)dd_c}, \quad (0 \le d_c < d_p) \quad \cdots\cdots (6)$$

where d_p is a screening size.

3.2. Discussion on Determination of Screening Size

This chapsection shows that the determination of screening size and classification of specimen groups without considering stress conditions might fail to obtain effective N.D.I results as long as tests are conducted with a finite number of specimens, from the following viewpoints.

3.2.1. Screening on Left Foot of Flaw-Size Distribution

Out of the above-stated flaw-size distributions after screening, the first discussion deals with that involving different screening size d_p regarding a theoretical distribution (Equation (5)) under uni-axial uniform tensile stress. **Figure 3** presents flaw-size distribution (silid line) for V=90mm^3 together with distribution after screening expressed by Eq.(5) (dotted line), in which screening size d_p was varied in the range of 30 to 70μm. The figure clearly shows that as screening size decreases the distribution after screening shifts to the region with smaller flaw-size, and at

Table 1. Weibull parameters and fracture toughness of Si_3N_4 .

$\hat{m}_1$	$\hat{\sigma_{01}}$ (MPa)	$\hat{K_{IC}}$ (MPa $\sqrt{m}$)
15.79	959.9	4.06

the same time the peak value of the distribution (mode) increases. The especially noteworthy point is that when screening size is set near the left foot of the distribution before screening, a sharp peak appears on the spot where the probality was almost zero before screening (Fig.3(a)). However, in the practical case of N.D.I with a group having a finite number of specimens, results are different from those as in Fig.3. That is, when screening is carried out near the left foot of flaw-size distribution, almost all specimens are to be excluded leading to meaningless inspection. The following case is taken as an example. In N.D.I with a finite number of specimens, screening size is determined according to flaw-size distribution under 3-point bending stress; these specimens undergo screening based on this screening size, and then specimens clearing the criteria are subjected to uni-axial uniform tensile stress. Under 3-point bending stress a region to act as a fracture source is virtually limited to a small portion near a maximum stress point, so that the size of a flaw to become a fracture source is about 20μm smaller than under uni-axial uniform tensile stress (Fig.2). Therefore, in some cases, the screening size d_{pl} is determined at the left foot of flaw-size distribution under uni-axial uniform tensile stress. Under uni-axial uniform tensile stress the possible region to become a fracture source extends to the entire specimen requiring scanning throughout the inside, and yet as in Fig.2 a defect greater than d_{pl} is present in each specimen with high probability so that almost all specimens will fail.

3.2.2 Screening at Right Foot of Flaw-Size Distribution

In contrast to the discussion in 3.2.1, the case is examined where screening is performed with d_{pu} shown in Fig.2. This is to determine screening size d_{pu} on the basis of flaw-size distribution under uni-axial uniform tensile stress, screen a finite number of specimens according to this screening size d_{pu}, and expose the specimens clearing the criteria to 3-point bending stress.

The size of flaws at fracture origins under 3-point bending stress detected as a result of the above process will be less than d_{pu} as clearly shown in Fig.2, leaving almost all specimens without exclusion. Also in simulation with a theoretical distribution for an infinite number of specimens, a flaw size distribution after screening at d_p=70μm near the right foot of a flaw size distribution before screening mostly overlaps the latter, and the effect by screening is virtually negligible (Fig.3(g)). Consequently, when screening is carried out with greater size than the right foot of the flaw size distribution before screening, the flaw-size distribution is evidently not improved at all.

4. Effective Screening

The previous section (3.2) described that as long as N.D.I is conducted with a finite number of specimens, a universal screening size independent of load stress conditions for specimens cannot be determined. That is, effective screening for specimens is available only in the case where the stress condition during N.D.I is the same as that in practice. Meanwhile, it is common experience for a different load stress mode for a specimen to lead to the different location

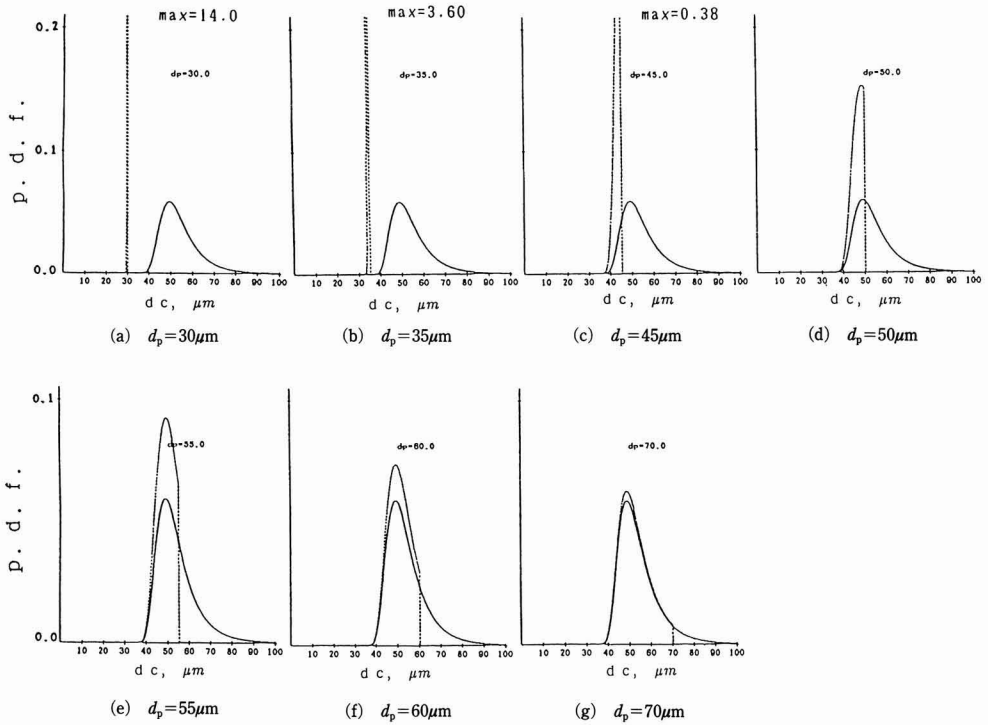

Fig. 3. Effects of screening-size (d_p); solid lines: probability density functions of flaw-size, dotted lines: probability density functions of flaw-size after screening.

of a fracture origin. This chapter is intended to indicate that a region for screening can be effectively reduced by elucidating the above fact from the stand-point of statistics coupled with information on the distribution of fracture location,[5,6] as well as to propose a new screening method effective for specimens. The procedures of the new method are stated as follows taking the condition of 3-point bending stress as an example.

When stress gradient is present in the specimen, regions which can become a fracture origin are limited to a certain portion of the specimen. The potential region varies with the kind of stress gradient and specimen size, while the probability theory for fracture location established and expanded by the authors[5,6] can estimate the possible region to become a fracture source based on knowledge such as the kind of stress gradient and the geometry of specimens, so that the region to be scanned in N.D.I can be determined with the backing of statistical fracture theory. For example, the distribution of fracture location under 3-point bending stress in Fig.1 is expressed by the following formula with regard to the x and y directions in the figure.[5,6]

$$s(x) = \frac{m_1 + 1}{L}\left(\frac{x}{L}\right)^{m_1} \quad \cdots\cdots\cdots\cdots\cdots (7)$$

$$u(y) = \frac{m_1 + 1}{h}\left(\frac{h - y}{h}\right)^{m_1} \quad \cdots\cdots\cdots\cdots\cdots (8)$$

It was confirmed that these two theoretical distributions were in good agreement with numerous measurements (403 pieces)[9] of 3-point bending tests on hot-pressed silicon nitride.[5,6] When a region where a fracture source is present with high probability is determined using the formulas (7) and (8), it becomes the region for scanning (Generally it is restricted to a small triangle around a maximum stress point, thus greatly reducing a region to be detected).[11]

That is, in the presence of stress gradient, a region as a possible fracture source is determined with the above theoretical formulas; only this region is subjected to scanning according to screening size adopted beforehand in order to classify specimens, thereby assuring effective and sufficient screening. Additionally, scanning by this technique can be limited to the required area, which provides savings in time and costs.

5. Conclusion

This paper first described a simulation concerning how the flaw-size distribution at fracture origin after screening behave when a screen size d_p is varied for the flaw-size distribution under uni-axial uniform tensile stress. Then it indicated that there is a difference in results between screening based on theoretical distribution and actual screening with a finite number of specimens. In so far as N.D.I is conducted with a finite number of specimens, the screening size d_p cannot be determined without depending on a stress condition. Moreover, the paper stated that a comparison between the flaw-size distribution under 3-point bending stress and one under uni-axial uniform stress shows that the determination of a region to be scanned is very important when stress gradient is present in the specimen. Finally, the authors proposed a method of achieving this by estimating the distribution of fracture location, and showed that it is efficient to adopt a new screening method considering information on fracture location.

References:

1) Wiederhorn, S.M., in Fracture Mechanics of Ceramics, 2(1974), 613.
2) Y. Matsuo, J. Soc. Mat., Sci. Japan 33-370 (1984), p.857.
3) Hamanaka, Hashimoto, Ito and Watabe, Trans. JSME, 52-481, A(1986), 2187.
4) Hamanaka, Ezumi, Suzaki and Sugiyama, Trans. JSME, 56-523, p.462 A(1990).
5) Y. Matsuo and K. Kitagami, Trans. JSME 51-471, A(1985), 2575.
6) Y. Matsuo and K. Kitakami, in Fracture Mechanics of Ceramics, 7(1986),p.223.
7) Y. Matsuo, K. Kitakami and S. Kimura, J. Mater. Sci., 22(1987), p.2253.
8) Y. Matsuo, K. Kitakami and S. Kimura, Yogyo-Kyokai-shi, 94(8) (1986), p.711
9) Ito, Sakai, Ito, J. Soc. Mat. Sci. Japan 30-337 (1981), p.1019.
10) Murata, Matsuo, Miyagawa, Kitagami, Trans. JSME, 52-473, A(1986) p.27.

This article is a full translation of the article which appeared in Nippon Seramikkusu Kyokai Gakujutsu Ronbunshi (Japanese version), Vol.99, No.6, 1991.

Effect of SrO Addition on Growth and Electrical Properties of $PbTiO_3$ Single Crystals

Satoshi Fujii, Yosohiro Sugie, Yuusuke Takahashi and Masafumi Kobune*

Department of Applied Chemistry, Faculty of Engineering, Himeji Institute of Technology
2167, Shosha, Himeji-shi, 671-22 Japan
* Engineering for Production Course, Graduate School, Himeji Institute of Technology
2167 Shosha, Himeji-shi, 671-22 Japan

$PbTiO_3$ single crystals with SrO additive (wt%) were grown by a flux cooling technique. The electrical measurements were carried out by using as-grown crystals of $PbTiO_3$ with 0.4wt% SrO. In summary, (1) The addition of SrO remarkably effected the crystal size and the yield of $PbTiO_3$. Especially, it was available for improving the crystal perfection of $PbTiO_3$. (2) The resulting crystals was platelet (1.6×1.6×0.2mm) in shape and yellow-brown with highly transparent. (3) According to the X-ray diffraction, little change of axial ratio c/a was observed with increasing SrO content. (4) The Arrhenius plot of σ_{dc} indicated that the conductivities were represented as the following equations; $\sigma=3.1\times10^3\exp(-0.2/kT)$ [25 to 150°C], $\sigma=3.1\times10^3\exp(-1.5/kT)$ [150 to 500°C]. (5) Above 300°C, non-ohmic behavior was observed in the I-V characteristic curves. And the threshold value V_N decreased with increasing temperature.

[Received September 13, 1990; Accepted January 24, 1991]

Key-words: $PbTiO_3$ single crystal, Flux cooling technique, SrO, Conductivity, I-V characteristics

1. Introduction

Lead titanate ($PbTiO_3$) is a highly dielectric substance having a perovskitic structure. Because of its high Curie temperature: about 495°C and excellent pyroelectric characteristics, it is noted as a material for pyroelectric infrared sensor elements.[1,2]

Single crystals of $PbTiO_3$ are usually grown by a flux cooling method using PbO as flux. Under this method, however, it is generally difficult to obtain highly perfect single crystals because PbO as a component of the crystal evaporates during crystal growth, causing heavy lead deficiency in crystals. In our studies on the growth of single crystals of $PbTiO_3$, we have proved that highly perfect single crystals can be obtained by growing crystals with an additive MgO, which is solid dissolved in substitution for Pb.[3,4] MgO addition was certainly effective in promoting the growth and raising the perfection of crystals but increasing its content caused the axial ratio (c/a) of $PbTiO_3$ crystals to decrease. This can be explained by the smaller (about half), Mg ion radius than that of Pb. Thus, we considered that such crystal axial ratio decreases can be reduced by using, instead of Mg ions, Sr ions which are comparable in size with Pb ions.

Therefore, using SrO as an additive, we tried to grow single crystals of $PbTiO_3$ with Si ions solid dissolved. We also studied the electrical properties of the single crystals thus obtained in comparison with those of single crystals obtained by adding MgO.[5]

2. Experimental Method

2.1. Starting Materials and Flux

The starting materials were prepared by mixing and pulverizing fine $PbTiO_3$ powder (99.9% made by Yamanaka Semiconductor) and $SrCO_3$ powder (guaranteed grade made by Nakarai Resk Co.) at ratios: $SrO/(PbTiO_3+SrO) = 0.1$ to 0.5wt% and firing each mix at 1450°C for 1h in a capped 50ml platinum crucible. The powders thus obtained were further pulverized below 200 mesh and were identified as a $PbTiO_3$ phase by an X-ray diffraction method.

For the flux, we used PbO powder (guaranteed, made by Nakarai Tesk Co.).

2.2. Growing of Single Crystals

Each starting material and the flux were mixed together at a material-flux weight ratio of 0.339, pulverized and charged in a capped platinum crucible (50ml). Then the charge was heated in a vertical electric furnace to 1100°C at a rate of 200°C/h, held there for 10h and then cooled slowly, 10°C/h, down to room temperature. The grown crystals were treated with diluted nitric acid to dissolve flux, filtered, then washed and dried for a full day in a 50°C thermostatic drier. Thus, the final crystals were obtained.

2.3. Identification and Observation of Grown Crystal

We identified the crystals obtained using a powder X-ray diffracting system. To observe crystals, we used a scanning electron microscope (SEM).

We obtained lattice constants at room temperature of the grown crystals from the (002) and (200) diffraction lines of $PbTiO_3$ under a powder X-ray diffraction method using a high-purity silicon powder (99.9%) as an internal standard and calculated axial ratios (c/a).

We determined the composition of the grown crystals by treating samples under an ICP analysis method.

2.4. Measurement of Electrical Properties

2.4.1. Measuring Instruments

Using the same system as reported by Kobune et al., we measured electrical properties in air by vapor fusing the platinum electrodes on both sides vertical to the c-axis of the grown crystal.[5] We controlled the temperature of the

electric furnace in the range from room temperature to 500°C by using a program regulator (UP30) made by Yokogawa Denki. To measure temperatures, we used chromel-alumel thermocouples. The lead wires and the electrodes in the furnace were made of platinum. Using a microammeter (R8340A) made by Advantest Co., we measured currents while controlling impressed voltage by using a personal computer (PC-98901F).

2.4.2. Measurement of Current-Voltage Characteristics: σ_{dc}, U_a and E_H

Impressing a DC voltage on a highly dielectric substance causes current I to decrease hourly, I being given by

$$I = I_{sp} + I_a + I_d \quad \ldots\ldots\ldots\ldots\ldots\ldots (1)$$

where,

I: observed current

I_{sp}: instantaneous charging current

I_a: absorption current

I_d: equilibrium leakage current.

To prevent sample fracture due to rapid temperature variations in current measurement, we heated the furnace to the specified temperature at a rate of 5°C/min and then held the temperature constant until the current reached the equilibrium leakage current mentioned above. From impressed voltage V and equilibrium leakage current I_d, electrical conductivity σ_{dc} (ohm^{-1}-cm^{-1}) was obtained as follows:

$$R = I_d/V$$

$$\sigma_{dc} = D/R \cdot S \quad \ldots\ldots\ldots\ldots\ldots\ldots (2)$$

Table 1. Experimental data on the $PbTiO_3$ single crystals as a function of SrO content.

Condition:

Starting material/Flux = 0.339 (weight ratio),

Heating rate = 200°C/h,

Soaking temperature = 1100°C, Soaking time = 10h,

Cooling rate = 10°C/h

No.	Quantity of SrO (wt%)	Yield (%)	Max.crystal size (mm)	Sieving analysis(%) ~3.0 (mm)	3.0~2.8 (mm)	2.8~2.0 (mm)	2.0~1.0 (mm)	1.0~ (mm)
1	0	64.3	5.5×5.5×1.3	88.7	6.0	8.1	6.6	–
2	0.1	55.8	–	20.1	16.4	20.7	38.4	4.2
3	0.2	60.0	5.0×5.0×0.8	2.9	8.5	4.7	31.9	29.6
4	0.3	54.1	2.5×2.5×0.4	–	–	–	15.9	84.1
5	0.4	50.5	1.6×1.6×0.2	–	–	–	9.5	90.5
6	0.5	50.1	1.0×1.0×0.2	–	–	–	0.3	99.7

where D is the thickness (cm) of the sample and S is the cross-sectional area (cm^2) vertical to the c-axis of the sample. Raising the impressed voltage stepwise at a constant temperature, we measured equilibrium leakage currents and obtained a current-voltage curve.

In general, between σ_{dc} and T is the Arrhenian relation given by

$$\sigma_{dc} = \sigma_0 \exp(-U_a/kT) \quad \ldots\ldots\ldots\ldots (3)$$

where σ_0 is the value of σ_{dc} at an infinite temperature, k is Boltzmann's constant (eV) and T is absolute temperature (K).[6] We calculated apparent activation energy U_a(eV) by putting σ_{dc} into equation (3).

With the present samples, as described later, currents conform to Ohm's law in low field ranges but grow nonlinearly beyond Ohm's law in high field ranges. With the impressed voltage at the start of the current growth defined as V_H, E_H was obtained by dividing V_H by the thickness of the sample.

3. Results and Review

3.1. Growing of $PbTiO_3$ Single-Crystals with SrO Added

3.1.1. Effect of SrO Addition

When SrO was added by more than 0.6wt% in a preliminary test, grainy crystals with indefinite crystal orientation were obtained. So, we limited SrO content to 0.5wt% in the main test.

While varying the SrO content in the range of 0.1 to 0.5wt%, we grew crystals under the test method in 2.2. The results are shown in Table 1. As the SrO content increased, crystal size decreased. As for yields, No.1 without SrO ranked top. In terms of crystal perfection, Nos.5 and 6 were particularly good. In summary, the effect of additive SrO was negative for crystal size and yield and positive for crystal perfection.

3.1.2. Identification and Observation of Grown Crystals

Figure 1 shows SEM photographs of grown crystals Nos.1, 3 and 5. As the SrO content increases, the perfection of crystal contours rises. In addition, No.1 was dark green, Nos.2 to 4 were opaque brown and Nos.5 and 6 were highly transparent yellowish brown. All these products were identified as $PbTiO_3$ by powder X-ray diffraction analysis. **Figure 2** is the photograph of a reflection Loue spot for crystal

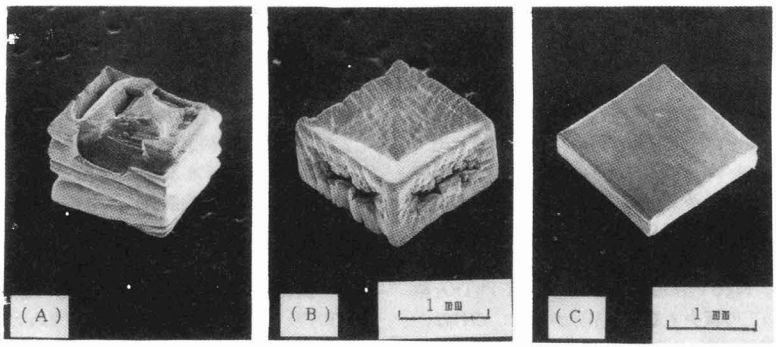

Fig. 1. SEM photographs of $PbTiO_3$ single crystals. Added SrO: (A) 0wt%, (B) 0.2wt% and (C) 0.4wt%.

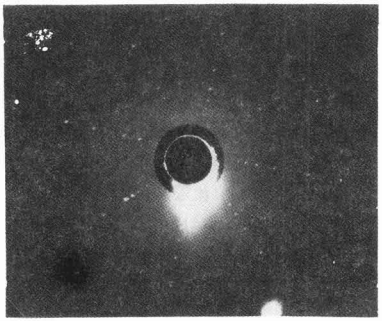

Fig. 2. Laue diffraction pattern of $PbTiO_3$ single crystal (SrO = 0.4wt%).

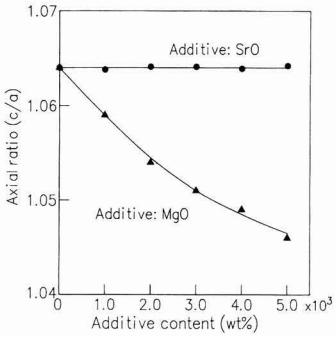

Fig. 3. Axial ratio of lattice constant vs amount of added SrO on $PbTiO_3$ single crystals.

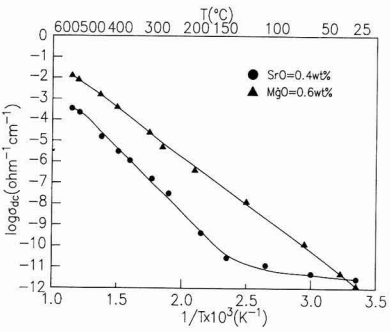

Fig. 4. σ_{dc} of $PbTiO_3$ single crystals as a function of temperature.

No.5 (SrO=0.4wt%). The incident X rays are vertical to the (001) face and definite symmetrical points are shown. From the spread of diffraction spots shown in the photograph, it was also proved that the sample was a single crystal with very little distortion. Through ICP analysis of crystal components, we detected Sr in all crystals obtained by adding SrO and identified the composition of the crystal obtained by adding 0.4wt% SrO as SrO: 0.393±0.001wt%, PbO: 74.471wt% and TiO_2: 25.512wt%, which proved that all SrO added was solid dissolved.

3.1.3. Lattice Constants and Axial Ratios

We measured the lattice constants of the crystals obtained and examined variations in axial ratios for SrO contents. The results are shown in **Fig.3**. The lattice constants of the $PbTiO_3$ crystals obtained without SrO addition were a=3.903±0.005A and c=4.153±0.008A, making an axial ratio (c/a) of 1.064. As the additive content increases, the axial ratio of the crystals obtained with additive MgO decreases.[4] With the crystals obtained by adding SrO, there are no such changes in axial ratio. This may be because Sr ions are solid dissolved in place of Pb ions at site A, causing no changes in lattice constants and axial ratio because of little difference in radius between solid dissolved Sr ions and Pb ions.

In summary, as for conditions for SrO addition, No.5 is considered best in terms of crystal size and perfection. Thus, for the following test of measuring electrical properties, we used single crystals No.5 obtained by adding SrO by 0.4wt% and compared the results with those for single crystals obtained by adding MgO by 0.6wt%.[5]

3.2. Electrical Properties

3.2.1. Temperature Dependency of Electrical Conductivity σ_{dc}

We measured σ_{dc} of sample No.5 and crystals with MgO solid dissolved. The results are shown by Arrhenius plotting in **Fig.4**. While the plotting for the crystals with MgO solid dissolved is nearly linear, that for the present sample is nonlinear and lower than the other in a wide temperature range. The temperature characteristics of σ_{dc} of the present sample can be divided into three at 150° and 500°C, appearing highly linear but with a different gradient in each section. The section from room temperature to around 150°C is generally called a low-temperature zone, in which σ_{dc} is reportedly heavily affected by impurities in crystals.[7] With the crystals in the present study, σ_{dc} in this zone is very low, below 10^{-11}, suggesting that a trace of Sr ions solid dissolved in crystals makes the crystals highly resistant. The variations in the gradient at around 500°C, on the other hand, suggest that since the Curie point of $PbTiO_3$ is at around 495°C, changes in crystal structure due to phase transition have an effect on σ_{dc}.

3.2.2. Apparent Activation Energy U_a

From the gradients of the line for the zones in Fig.4, we calculated U_a of the present sample as 0.2eV for the zone 25° to 150°C, 1.5eV for the zone 150° to 500°C and 0.6eV for the zone above 500°C. **Table 2** shows electrical constants for the single crystals of $PbTiO_3$ obtained by adding MgO or SrO. U_a is related with the types and mobility of carriers. In low U_a ranges, variations in the types and mobility of carriers are so small that the resistance of crystals is hardly affected by temperature variations. This proves, as shown by the U_a values in the table, that in low temperature ranges, the present sample is stabler than the crystals with MgO solid dissolved. In addition, resistivity

Table 2. Additive content, ρ, $\sigma=\sigma_0\exp(-U_a/kT)$, U_a and applied temperature range for various $PbTiO_3$ single crystals.

Quantity of	ρ		Direct current conductivity		
Addtive	R.T.	600℃	$\sigma=\sigma_0\exp(-U_a/kT)$	U_a	Temp. range
(wt%)	(Ω·cm)	(Ω·cm)	($\Omega^{-1}\cdot cm^{-1}$)	(eV)	(℃)
MgO=0.5	5.3×10^{11}	53	$\sigma=3.1\times10^{3}\exp(-0.9/kT)$	0.9	25～600
MgO=0.6	8.9×10^{11}	49	$\sigma=3.4\times10^{3}\exp(-0.9/kT)$	0.9	25～600
SrO=0.4	3.5×10^{11}	2880	$\sigma=3.1\times10^{3}\exp(-0.2/kT)$	0.2	25～150
			$\sigma=3.1\times10^{3}\exp(-1.5/kT)$	1.5	150～500
			$\sigma=3.1\times10^{3}\exp(-0.6/kT)$	0.6	500～600

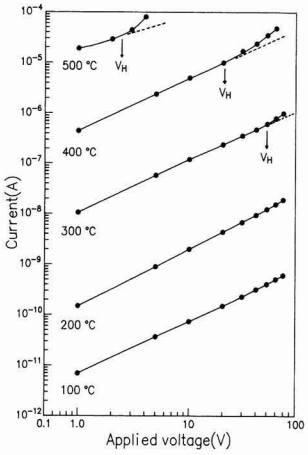

Fig. 5. *I-V* characteristics of $PbTiO_3$ single crystal (SrO = 0.4wt%).

ρ of the present sample was about half of the value for the crystals with MgO at room temperature but about 60 times at 600°C.

3.2.3. Current-Voltage Characteristics

Figure 5 shows the current-voltage characteristics measured with sample No.5. Within the measurement range, the currents at 100°and 200°C conform to Ohm's law. At temperatures 300°C and above, the measurement range is divided into two, between which currents behave differently.[8] Range 1 is on the lower field side in which currents conform to Ohm's law. Range 2 is on the higher field side in which currents grow nonlinearly from Ohm's law. The V_H values of the sample were 50V at 300°C, 20V at 400°C and 2.5V at 500°C. The maximum voltage impressed in the test was 70V. Range 2 was not observed at temperatures 200°C and below. To observe range 2 at such temperatures, it seems necessary to impress a considerably high voltage.

3.2.4. Dielectric Breakdown Current E_H

To evaluate electrical insulation capacity, E_H, the value of V_H divided by the thickness of the sample, must be obtained. **Figure 6** shows E_H values at several temperatures for the present sample and the crystals with MgO solid dissolved. The E_H values for the present sample are higher than for the crystals with MgO solid dissolved. This suggests that the solid dissolution of Sr ions is effective for electrical insulation.

From the above, to apply single crystals of the present sample (SrO=0.4wt%) to elements for pyroelectric infrared detectors, an effective method for polarization may be slow cooling with a DC field about 100V/cm impressed in a temperature range from a point (about 500°C) above T_c to room temperature. This method of polarization prevents thermal breakdown of samples, permitting yields to be increased.

4. Conclusion

We grew single crystals of $PbTiO_3$ with different SrO contents by a flux cooling method and examined the electrical properties of grown crystals. The results can be summarized as follows:

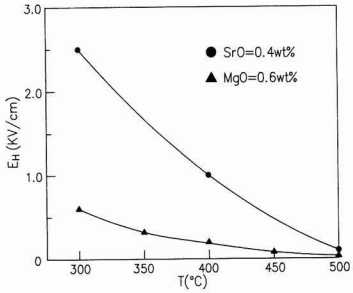

Fig. 6. Temperature dependence of E_H for $PbTiO_3$ single crystals.

1) The effect of SrO addition was found on the size and yield of crystals and was particularly prominent on higher perfection of crystal structures.
2) With an SrO content of 0.4wt%, the grown $PbTiO_3$ crystals were highly transparent yellowish brown single crystals. The maximum size of the crystals was 1.6×1.6×0.2mm of a plate crystal.
3) There were no variations in lattice constants and axial ratio in relation with variations in SrO content.
4) The electrical conductivity of the crystals with 0.4wt% SrO added was affected by solid dissolved Sr ions in the temperature range from room temperature to 150°C toward the higher side of crystal resistance. In the temperature range from room temperature to 500°C, Arrhenian plotting of σ_{dc} could be divided into two zones, each of which shows high linearity. The U_a and σ values were 0.2 and $3.1\times10^3\exp(-0.2/kT)$ respectively in the range: 25° to 150°C and 1.5 and $3.1\times10^3\exp(-1.5/kT)\Omega^{-1}\cdot255cm^{-1}$ respectively in the range: 150° to 500°C. At temperatures 300°C and above, the current-voltage characteristics were ohmic, having a certain threshold. The solid dissolution of SrO was also favorable for electrical insulation.

Acknowledgements

We express our thanks to M. Iwasaki, ass. professor at the Metallic Materials Engineering Div. of Himeji Institute of Technology, and to Mr. Kasamatsu at the Analysis Center of Tateho Chemical Industry, for with reflection Laue Photographs and ICP analysis respectively.

References:

1) I. Ueda, S. Kobayashi, and K. Ikegami: National Tech Report, 18, 413-25 (1972).
2) N. Ichinose, Y. Hirano, N. Nakamoto and Y. Yamashita, Japan. J. Appl. Phys., 24, 463-65 (1985).
3) M. Kobune, and C. Sakamoto: Yougyo Kyoukai-shi, 95, 1053-58 (1987).
4) M. Kobune, C. Sakamoto, S. Fujii, and Y. Sugie: Nippon Scramikkusu Kyokai Gakujutsu Robunshi, 96, 935-41 (1988).
5) M. Kobune, K. Amagawa, H. Nakayama, and M. Onoda: Nippon Scramikkusu Kyokai Gakujutsu Robunshi, 97, 954-59 (1989).
6) Denki Gakkai, Yudentai Genshoron, Ohm-sha (1973), pp.205.
7) Denki Gakkai, Yudentai Genshoron, Ohm-sha (1973), pp.208.
8) Denki Gakkai, Yudentai Genshoron, Ohm-sha (1973), pp.294.

This article is a full translation of the article which appeared in Nippon Seramikkusu Kyokai Gakujutsu Ronbunshi (Japanese version), Vol.99,

Sintering of Alumina-Silicon Nitride Whisker Composites and Their Properties

Nobuyuki Tamari, Takahiro Tanaka, Isao Kondoh and Saburoh Kose

Government Industrial Research Institute
Osaka, 1-8-31, Midorigaoka, Ikeda-shi 563

Composite ceramics of α-alumina mixed with up to 40vol% β-silicon nitride whisker were fabricated by hot-pressing at 1400°-1700°C under 30MPa for 30 min. The properties (bending strength, fracture toughness, thermal shock resistance, and oxidation resistance etc.) of the hot-pressed bodies were investigated. Dense alumina-Si_3N_4 whisker composite ceramics were obtained in the region of whisker contents up to 30vol% at the sintering temperatures above 1600°C. The composite mixed with 20vol% whisker and fired at 1600°C showed the highest bending strength (about 610MPa), which is lower than the maximum strength of alumina (about 630MPa). These composites had more excellent high temperature strength, hardness and thermal shock resistance than monolithic alumina. The fracture toughness (about 4.7MPam$^{1/2}$) of a composite with a whisker content of 30vol% was 1.7 times as large as that of monolithic alumina. The weight gain by oxidation at 1400°C increased with increasing oxidation time and whisker content, but decrease in strength was not observed after oxidation.

[Received September 20, 1990; Accepted January 24, 1991]

Key-words: Alumina, Silicon nitride whisker, Composite ceramics, Sintering, Properties

1. Introduction

Recently, composite technology using fibers and whiskers has increasingly been studied as a means to improve the toughness of ceramics and thus overcome the biggest problem in their structural application. Improvements in the strength and toughness of ceramics have been recognized in composites of alumina mixed with silicon carbide whiskers, and applications such as in cutting tools are being studied.[1-8] The authors previously reported[9] that by replacing silicon carbide whiskers with silicon nitride whiskers, it was possible to obtain dense whisker composites at such low sintering temperature as 200-300°C, improving the toughness by around 50% with the mixture of 20wt%(25vol%).

This report deals with the study of the effect of sintering temperature and whisker amount on the densification of Alumina-silicon nitride (Si_3N_4) whisker composite, and properties (mechanical properties, thermal expansion, thermal shock resistance, and oxidation resistance, of the resulting composites.

2. Experimental Procedures

2.1. Materials and Their Preparation

For Alumina powder, we used α-type TAIMICRON-TM-DAR(average grain size: 0.2μm) made by Taimei Chemical (Japan), and for Si_3N_4 whiskers, SN-WB (β type, dia.: about 1μm, length: 10-30μm) made by Ube Industries, (Japan).

These two materials were mixed and dispersed for 24 hours in ethanol by a wet-type ball mill, and after being dried they were passed through a sieve of 16 mesh (opening dia.: 1mm) to become the materials for the composites. The mixing ratios of whiskers were 10, 20, 30 and 40vol%.

2.2. Sintering

Sintering was carried out by the hot pressing method. The mixed source materials were filled in a graphite frame mold, and after applying the given pressure, the temperature was increased to the required level at a rising speed of around 70°C/min After being held for the given time, pressure was released and the materials were left for cooling. The sintering conditions were 1400-1700°C, 30MPa, and 30min for the retention time. The sintered products thus obtained were plates of about 20×40×5mm.

2.3. Measurement of the Composite Properties

Sintered plates thus obtained were ground by a diamond wheel of #200, and measured for their bulk density by the water immersion method.

Test pieces of 3×4mm cross section were prepared for the strength test, with the tension sides finished by a #800 diamond wheel. The test was carried out by the three-point bending method under the conditions of 30mm span and 0.5mm/min of load applying speed. The high-temperature test was carried out after keeping the specimen at that temperature for 10min in air.

Hardness was measured by a Vickers-type hardness tester under the conditions of 98N and 30min. The elastic modulus was measured by the bending resonance method on a specimen of 1×4×40mm after the JIS R 1602.

Fracture toughness was tested by the IF method after the JIS R 1607 under the conditions of 98N and 30min on the specimen with their surfaces mirror-finished by diamond pastes of 1μm.

The specimen was cut to the size of 3×4×20mm with its longitudinal direction vertical to the axis of the hot press. Thermal expansion was measured by heating this specimen in air to 1300°C at a rising rate of 10°C/min. with alumina as the standard piece. The thermal shock resistance test was carried out by heating the specimen of 3×4×40mm to the given temperature, and dropping them into water of 0°C, and then the strength was measured at room temperature. The oxidation resistance test was done in air on the

specimen of 3×4×40mm at 1400°C.

2.4. Observation on the Structure of Composites

In order to observe the grain of alumina in matrix in the sintered composites, the specimen was etched for 30sec in boiling phosphoric acid, and was observed through a scanning-type electron microscope (SEM). The preferred orientation of the whiskers in the composites was observed on an SEM, after removing the alumina matrix grains by etching the specimen for 5min in boiling phosphoric acid.

3. Results and Discussion

3.1. Sintering behavior and Strength at Room Temperature

Figure 1 shows the effects of the sintering temperatures and the content of whiskers on the densification of the composites. X-ray diffraction indicated that no reaction had taken place between α-alumina and β-Si_3N_4 under these sintering conditions. Here the value of the relative density is shown in the ratio of the bulk density against the theoretical density of simple mixture of alumina and Si_3N_4. Although the non-added alumina is not covered in Fig.1, we obtained the dense products by hot pressing at 1300°C; the relative density steadily decreased as the whisker content increased. At 1600 and 1700°C, dense composites were obtained with up to 30vol% of whisker content, and the relative density was around 97% even in 40vol% of the whisker content.

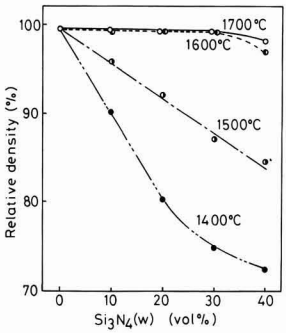

Fig. 1. Effects of sintering temperature and whisker content on densification of alumina-Si_3N_4 whisker composite.

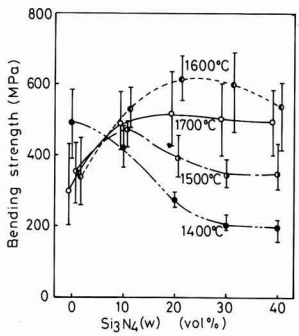

Fig. 2. Effects of sintering temperature and whisker content on the room temperature bending strength of alumina-Si_2N_4 whisker composite.

Figure 2 shows the bending strength of the specimen used for Fig.1 at room temperature. At the sintering temperature of 1400°C, the strength decreased steadily along with the increase in whisker content, due to the decrease in density. At 1500°C, the density decreased along with the increase in the whisker content as shown in Fig.1, but the strength of whisker composites was higher than or similar to non-added alumina, probably due to the effect of whisker composition. This phenomenon was also observed in the B_4C-SiC whisker system[10]. At 1600 and 1700°C, the strength showed a maximum value at 20vol% whisker content; the composite sintered at 1600°C showed the largest strength value (610MPa). This value is almost the same for composites of 25vol% whisker content in the previous report.[9] However, the value fell short of 630MPa, the maximum value of the strength of alumina sintered at 1300°C with no additive.

Figure 3 shows the SEM photos covering the etched surfaces of the alumina and the composite of 30vol% whisker content, both sintered at 1600°C. In the case of alumina, the alumina grains grew to 8μm, but remained at 3μm in the composite. This leads us to presume that the increase in strength of the dense composite along with the increase in whisker content may imply the fact that the addition of whisker inhibits the grain growth of alumina. Furthermore, a factor for the tendency to lower the strength with the increase of whisker content may be the influence of the residual tensile stress in the alumina matrix after sintering, because the thermal expansion coefficient of the alumina as the matrix is larger than that of Si_3N_4 (8.1×10^{-6}/K for alumina, while 3.4×10^{-6}/K for Si_3N_4).

The following experiments are the results on the composites sintered at 1600°C, unless otherwise mentioned.

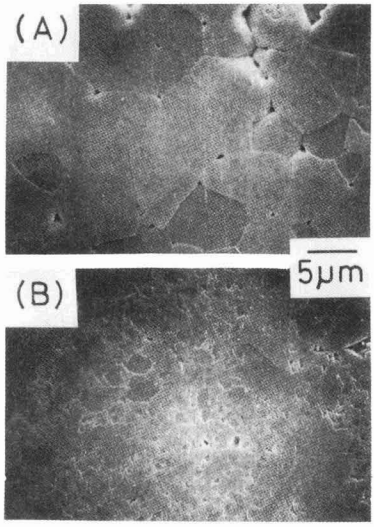

Fig. 3. Scanning electron micrographs of the chemically etched surfaces of monolithic alumina, (A), and alumina-20vol% Si_3N_4 whisker composite, (B), fired at 1600°C.

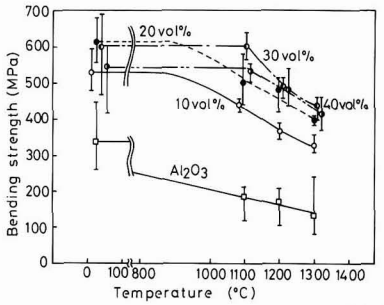

Fig. 4. High temperature bending strength of monolithic alumina and alumina-Si_3N_4 whisker composite.

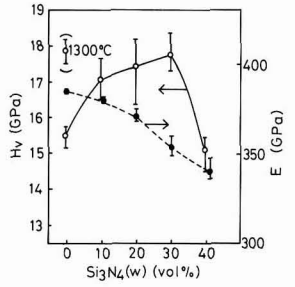

Fig. 5. Effect f whisker content on the Vickers hardness and elastic modulus.

3.2. Strength at High Temperature

Figure 4 indicates the bending strength at high temperature on the composites sintered at 1600°C. The bending strength at high temperature of alumina decreased to about 60% at 1100°C, and about 40% at 1300°C, of the strength at room temperature. Although Fig.4 does not cover the alumina sintered at 1300°C which showed the highest strength at room temperature among the alumina, the strength at 1100°C was down to 290MPa, about 45% of the strength at room temperature. On the other hand, in composites of 10 and 20vol% whisker content, a slight decrease in the strength was observed starting from 1100°C, although the strength at 1100°C for the composites with 30 and 40vol% whisker contents was almost the same as the strength at room temperature. The strength at 1300°C increased as the whisker content increased, and composites of 30 and 40vol% retained about 75% of the strength at room temperature. Thus the small decrease in the high temperature strength of the composites is considered to be caused by the decrease in SCG (slow crack growth), as the slippage at the grain boundary, the cavity growth and the cavity linkage are inhibited. This is thought to be the cause for the decreased alumina strength at high temperature, as has been pointed out for alumina-silicon carbide powder system by Niihara et al.[11].

3.3. Hardness and Elastic Modulus

Figure 5 indicates the influence of whisker contents to the Vickers hardness and elastic modulus of the composites sintered at 1600°C. Here, we included in the figure the hardness of alumina sintered at 1300°C for comparison. The hardness increased as the whisker content increased, and was as high as 17.7GPa, the maximum value, at 30vol%. The value was slightly less than the value (17.9GPa) for the monolithic alumina sintered at 1300°C, as the same can be said for the strength at room temperature. Elastic modulus, on the other hand, decreased as the whisker content increased, due to the smaller modulus of elasticity for Si_3N_4 than alumina.(Si_3N_4: 275GPa, alumina: 385GPa)

3.4. Fracture Toughness

Figure 6 points to the effect of whisker content on the fracture toughness measured by the IF method. The value of the toughness of monolithic alumina was 2.8MPam$^{1/2}$. When whiskers were added, the value of the fracture toughness increased so much so that with 30vol% content, the value increased by around 1.7 times of monolithic alumina, that is, 4.7MPam$^{1/2}$. With 40vol%, the value of the fracture toughness showed a tendency to decrease, probably due to low density. The authors added Si_3N_4 whiskers to Mullite, and obtained, with 40vol% whisker content, more than double the value in fracture toughness of pure Mullite.

Figure 7 shows the status of crack development from corners of Vickers indentation in the alumina and 30vol% whisker composite. In both cases, cracks tended to meander but more for alumina than for composites. This suggests that the tendency for whiskers causing meandering of cracks is not the reason for the improvement on the toughness of

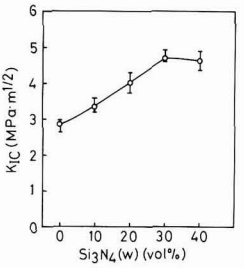

Fig. 6. Effect of whisker content on the fracture

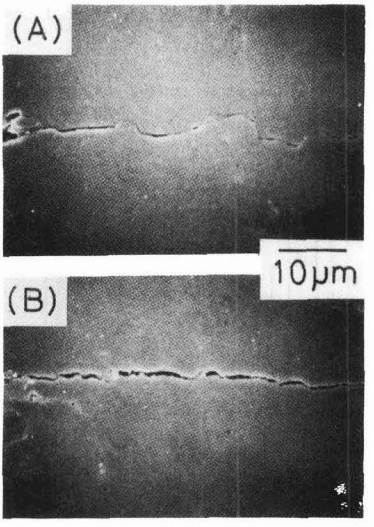

Fig. 7. Crack propagation from corner of Vickers indentation in monolithic alumina, (A), and alumina–Si_3N_4 whisker composite with 30vol% whisker, (B).

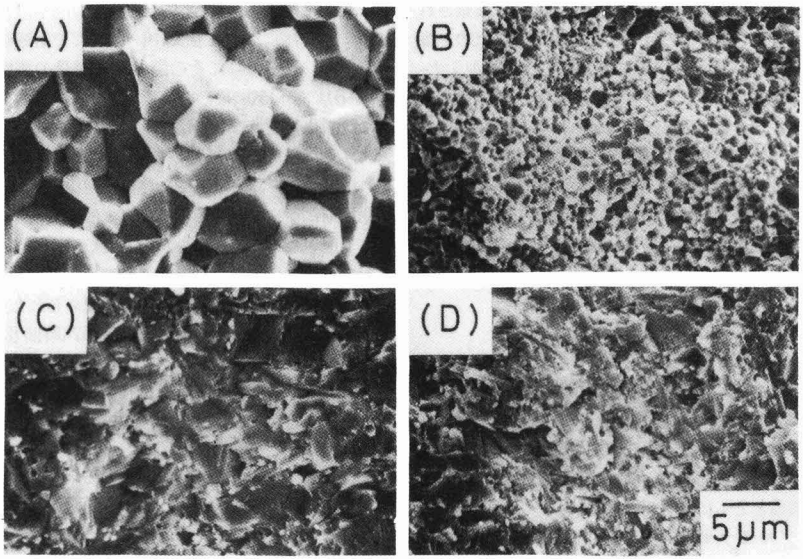

Fig. 8. Fractured surfaces of monolithic alumina, (A) and (B), and alumina-Si_3N_4 whisker composites with 20vol%, (C), and 30vol%, (D). Sintering temperature; (A), (C), (D): 1600°C, (B): 1300°C.

the whisker composites. **Figure 8** shows the fractured surfaces of the alumina and the composites of 20 and 30vol% of whisker contents, sintered at 1600 and 1300°C. As was observed in the previous report, alumina had fractures at the boundary of alumina grains in either sintering temperature, while the dense composites had fractures through the alumina grains, irrespective of the whisker contents.[9] The pull-out of the whiskers is thought to be another mechanism for improving toughness of the whisker composites. In this composite, the whisker is fractured at the fracture plane of the matrix, and no remarkable pull-out of the whiskers was observed. Accordingly, the improvement in the toughness of this whisker is thought not to be caused by the pull-out of the whiskers. A factor in the improvement of the toughness through the whisker composition may be attributed to their requirement for more fracture energy than the alumina, as the result of fractures taking place through the alumina grain for the whiskers against at the grain boundary for alumina.[9] Furthermore, it is conceivable that the toughness becomes greater as the whisker content increases, probably reflecting the fact that the fracture energy is larger for Si_3N_4 whisker than the fracture energy through the alumina grains, in addition to the difference in the fracture mechanism of alumina matrix.

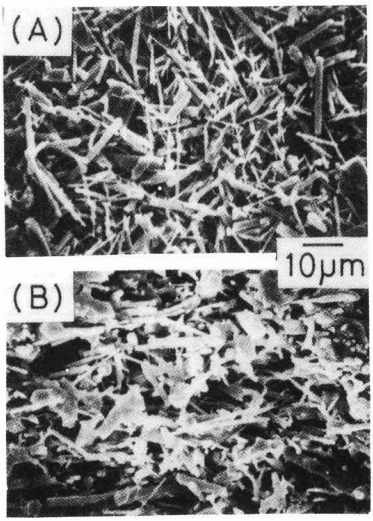

Fig. 9. Surfaces of alumina-Si_3N_4 whisker composite treated with a boiling phosphoric acid normal, (A), and parallel, (B), to hot-pressing axis.

3.5. The Effects of Preferred Orientation of Whisker on Mechanical Properties

Figure 9 shows the SEM photos of the composites with alumina matrix removed by boiling phosphoric acid. While the Si_3N_4 whisker was oriented at random in the normal plane to the hot-pressing axis, more whiskers were oriented vertically to the hot-pressing axis in the parallel plane to the hot-pressing axis. This was probably caused by the fact that the contraction to one axis during the hot-pressing oriented the whiskers predominantly vertically to the hot-pressing axis. There are some reports in the Alumina-SiC whisker system and Mullite-Si_3N_4 systems that anisotropy was observed in the mechanical properties of the composites, because of the preferred orientation of whiskers within these composites.[4,12] Therefore, we observed mechanical properties with surface normal and parallel to hot-pressing axis in Alumina-Si_3N_4 composites of 30vol% whisker contents, and the results are listed in **Table 1**. This composite also showed higher values in bending strength, fracture toughness and hardness in the normal plane to the hot-pressing axis than the parallel plane. And the Weibull modulus generally used as a guideline for the reliability of the materials also tended to show a higher value in the normal plane.

3.6. Thermal Expansion and Thermal Shock Resistance

The measurement of the thermal expansion on the materials up to 40vol% of Si_3N_4 whisker content showed that in every specimen the thermal expansion curve is almost linear from the room temperature up to 1300°C. Since the thermal expansion co-efficient of Si_3N_4 was smaller than that of alumina as stated in Section 3.1, the thermal expansion co-efficient of this composite became smaller with the increase in the whisker content, as shown in **Fig.10.**

Figure 11 indicates the results of the thermal shock resistance tests on alumina and the composite of Si_3N_4 whisker with 30vol% contents. In alumina the strength deteriorated from the temperature difference of 200K. On the other hand, the strength of the composite improved up to 300K of the critical temperature difference, having been influenced by the small thermal expansion co-efficient of the composite as shown in Fig.10, and the marked improvement in the toughness as noted in Section 3.4.

3.7. Oxidation Resistance

An oxidation resistance test was carried out in air at 1400°C. **Figure 12(A)** indicates the increase of weight by oxidation and **Fig.12(B)** indicates the measured strength after the test. Weight increased with increase in oxidation time and Si_3N_4 whisker content. The behavior of the oxidation showed that the oxidation speed tended to be slightly slow in any composites up to the initial 12 hours, but accelerated parabolically thereafter. This suggests that the oxidation mechanism is controlled predominantly by the diffusion. No deterioration in the strength after the oxidation test was observed in either composite, but on the contrary there were some instances where the strength increased after the oxidation.

Figure 13 shows the SEM photos covering the surfaces of the specimen on the composites of 40vol% whiskers after oxidizing i.e. heating for 24 hours and 360 hours. There are drip-type reaction products spotted on the surface of the specimen similar to the oxidized Mullite-Si_3N_4 whisker composite, and as the oxidation took longer these drips became larger.[13] The size of these drips became larger as the whisker content increased. This leads us to think that the size of the drip has almost no effect on the strength after oxidation.

In X-ray diffraction, we recognised a large peak of Mullite-SiC whisker in addition to those of α-alumina and β-Si_3N_4 on the oxidized specimen surface, regardless of the whisker content. This points to the following reaction taking place during this oxidation process:

$$2/3Si_3N_4 + 2O_2 \rightarrow 2SiO_2 + 4/3N_2 \quad \ldots\ldots (1)$$

$$3Al_2O_3 + 2SiO_2 \rightarrow 3Al_2O_3 + 2SiO_2 \quad \ldots\ldots (2)$$

Table 1. Mechanical properties of alumina-30vol% Si_3N_4 whisker composites with surface normal and parallel to hot-pressing axis.

	Normal to hot-pressing axis	Parallel hot-pressing axis
Bending strength (MPa)	600	553
Weibull modulus (n=20)	12.3	8.7
K_{IC}(MPa $m^{1/2}$)	4.7	4.2
H_V(GPa)	17.8	17.3

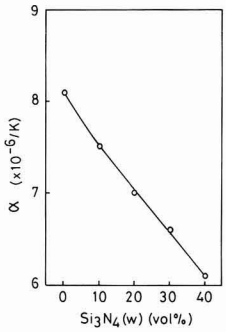

Fig. 10. Thermal expansion coefficient, α of alumina-Si_3N_4 whisker composite.

4. Conclusion

After studing the sintering by hot pressing of composite ceramics of alumina-Si_3N_4 whiskers, and observing various properties of the composites, we learned the following:

1) We can obtain considerably dense Alumina-Si_3N_4 composites with up to 30vol% of whisker content by hot

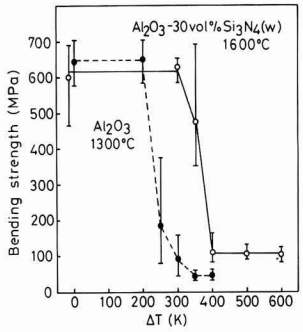

Fig. 11. Bending strength of monolithic alumina and alumina-Si_3N_4 whisker composite with 30vol% whisker after water quenching.

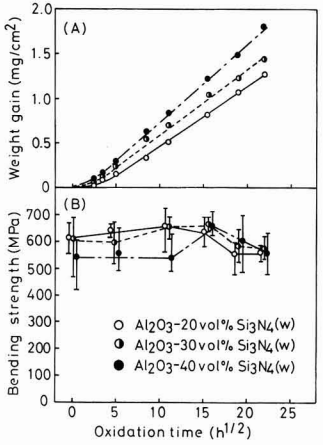

Fig. 12. Weight gain, (A), and bending strength, (B), of alumina-Si_3N_4 whisker composite after heating at 1400°C in air.

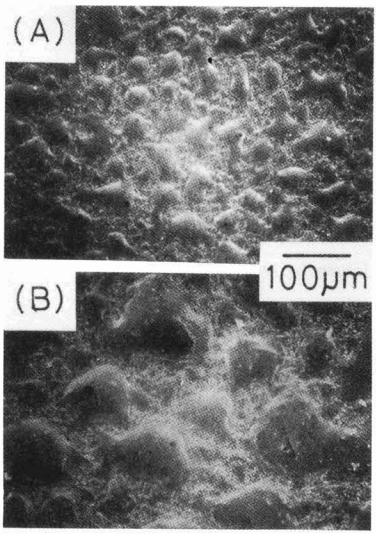

Fig. 13. Appearance of surface of alumina-Si_3N_4 whisker composite with 40-vol% whisker after heating for 24h, (A), and 360h, (B), at 1400°C in air.

pressing at sintering temperature of 1600 and 1700°C.

2) The composite with 20vol% whisker content sintered at 1600°C showed the highest strength at room temperature, about 610MPa, but the value could not exceed the highest value (630MPa) of alumina.
3) The composites with 30 and 40vol% of whiskers had the largest high-temperature strength, and the deterioration from room temperature strength was about 30%.
4) The fracture toughness in composites of 30vol% content was improved up to 4.7MPam$^{1/2}$, about 1.7 times that of alumina, due to the different fracture process.
5) Weight by oxidation increased with the increase in oxidation time and whisker content, but no deterioration of strength was noted after the oxidation.

References:

1) G.C. Wei and P.F. Becher, Am. Ceram. Soc. Bull., 64, 298-304 (1985)
2) J. Homeny, W.L. Vauchn and M.K. Ferber, ibid., 66. 333-38 (1987)
3) M.Karpman and J.Clark, Composites, 18, 121-24 (1987)
4) T.Yamamoto, M.Asano, K.Ueno, N.Tamari, Funtai-oyobi-Funmatsu-Yakin, 36, 859-64 (1989)
5) S.Ito, M.Watanabe, M.Matsubara and Y.Matsuo, J. Am. Ceram. Soc., 72, 1880-84 (1989)
6) P.F. Becher, P.Angelini, W.H. Warwick and T.N. Tiegs, ibid., 73, 91-96 (1990)
7) J.Homeny and W.L. Vaughn, ibid., 73, 394-402 (1990)
8) P.H. McCluskey, R.K. Williams, R.S. Graves and T.N. Tiegs, ibid., 73, 461-64 (1990)
9) I.Kondo, M.Asahina, N.Tamari, Seramikkusu-Ronbunsi, 97, 1424-27 (1989)
10) N.Tamari, H.Kobayasi, T.Tanaka, I.Kondo, S.Oze, ibid., 98, 1159-63 (1990)
11) K.Niihara, A.Nakahira, T.Uchiyama and T.Hirai, "Fracture Mechanics of Ceramics 7," Plenum Press (1986) pp. 103116
12) N.Tamari, T.Tanaka, I.Kondo, S.Oze, Serammikusu-Ronbunsi, 99, 89-93 (1991)
13) K.Nakamura, T.Kumasawa, N.Azuma, S.Kanzaki, ibid., 97, 976-79 (1989)

This article is a full translation of the article which appeared in Nippon Seramikkusu Kyokai Gakujutsu Ronbunshi (Japanese version), Vol.99, No.5, 1991.

6H→3C-SiC Transformation in SiC-TiN Powder Mixture at High Temperature

Hidehiko Tanaka, Shunji Takekawa and Masayuki Tsutsumi

National Institute for Research in Inorganic Materials
1-1 Namiki, Tsukuba-shi, 305 Japan

A 6H→3C transformation, which does not commonly occur at high temperature, was observed in SiC. A 6H-SiC and TiN powder mixture was hot-pressed in a flowing Ar atmosphere. The starting 6H-SiC powder was completely transformed to 3C polytype above 2200°C, although 3C-SiC was not stable at this temperature. It was found that coexistence of N was essential for this 6H→3C transformation, and a small amount of Ti was detected in the transformed SiC grain. The results suggest that a solution of N or TiN in the SiC grain would transform the 6H - SiC to the 3C form.
[Received October 3, 1990; Accepted January 24, 1991]

Key-words: Silicon carbide, Titanium nitride, Transformation, 6H-SiC, 3C-SiC

1. Introduction

More than 50 polymorph of SiC are known so far. More common polymorph are cubic 3C, hexagonal 2H, 4H, and 6H, and rhombohedral 15R. The 3C phase is referred to as the β type, and all of the hexagonal phases as the α type. The α type is stable at 2000°C or more, and the 3C system starts to appear at lower temperature and becomes unstable at high temperature. The 3C-SiC phase, therefore, transforms itself into the α type at high temperature.

The SiC powder as the starting material assumes the 6H (α) or 3C (β). The SiC material from the 3C-SiC powder, stable at low temperature, consists of plate- or rod-shaped grains of high aspect ratio. The 6H-SiC sintered material, on the other hand, consists of spherical grains. The former is slightly higher in mechanical strength than the latter.[1,2] It should be noted, however, that 3C-SiC powder tends to be transformed into the α when sintered at high temperature. This transformation will be accompanied by abnormal grain growth, which degrades sinterability and lowers the density and mechanical properties of the material.[3] The 3C→α phase transformation occurring at high temperature, therefore, is a phenomenon which must be carefully controlled, when highly functional SiC materials are produced.

It was found in this study that the 6H-SiC powder is transformed into the 3C system when mixed with a metallic nitride and treated at around 2200°C, which is contrary to the accepted concept of the phase transformation phenomenon,[4] and may be applicable to controlling the sinter structures. The metallic nitrides found to promote the 6H→3C phase transformation are TiN, ZrN and VN. This article discusses the reversed phase transformation into the 3C from the 6H-SiC powder in the presence of TiN at high temperature.

2. Experimental Procedure

The starting materials were 6H-SiC powder (Showa Denko, DU, A-1) and TiN powder (Nippon Shin-Kinzoku). The SiC powder had average particle size of 0.43μm, and contained 0.35wt% of C, 0.44wt% of SiO_2, 0.02wt% of Fe and 0.01wt% of Al as the impurities. The TiN powder, on the other hand, had average particle size of 1 to 1.5μm, and contained 2.0wt% of C, 2.5wt% of O, and 0.1wt% of Fe as the impurities; (these analytical results are the catalog values). These starting powders were ball-milled with SiC balls, and then hot-pressed in a graphite die at 20MPa and 1900° to 2300°C in an Ar atmosphere.

The sintered SiC-TiN samples were analyzed by powder X-ray diffraction method, SEM and EDS (energy dispersion type X-ray spectroscopy) to observe the structure, and by EPMA to identify the elements present as the solid solutions. The powder X-ray diffraction analysis was used to determine the precise lattice constants of the transformed SiC system and to quantitatively analyze the 3C→6H phase transformation. The lattice constants of the SiC and TiN were measured using CuK_α radiation of 40kV and 50mA by the step-scanning method at intervals of 0.01° for 4 sec from 30° to 150°, where the 3C-SiC and TiN lattice constant was determined by the least square method from 10 of 3C-SiC and TiN lattice plane distances each corrected with Si as the internal standard. Both 3C-SiC and TiN were the cubic system, zinc blend and rock salt structure, respectively. The 4H-, 6H-, 15R- and 3C-SiC types present in the sample were quantitatively analyzed using the method proposed by Ruska[5] from the X-ray diffraction patterns produced under the same conditions above and amount of transformation to β-type was determined. The Ruska method tries to determine the content of each polymorph from the theoretical strength of the powder X-ray diffraction peaks of the 3C-, 4H-, 6H- and 15R-SiC types, corrected by the experimental results. In this study, no 4H was detected, and quantity of the 15R was negligibly small.

3. Results

3.1. Transformation of 6H-SiC into 3C System

The powder X-ray diffraction analysis of the SiC powder as the starting material showed only diffraction lines relevant to the 6H. No other α polytype was detected. It should be noted, however, that the diffraction lines of the 6H and 3C polytype overlap each other, and the Ruska method determined that their contents were 91% and 9%, respectively.

The 6H-SiC powder was hot-pressed, after having been

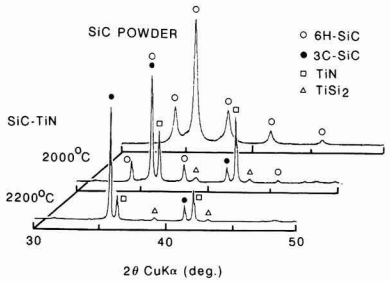

Fig. 1. 6H to 3C-SiC transformation in SiC-TiN powder mixture. The X-ray diffraction patterns of the hot-pressed powder (SiC 80vol%-TiN 20vol%) show that the 6H-SiC transformed completely to the 3C form at 2200°C.

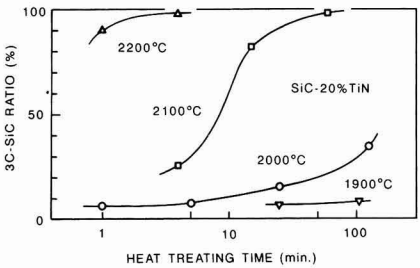

Fig. 2. Time and temperature dependence of 6H→ 3C-SiC transformation in SiC-TiN powder.

mixed with 5 to 80mol% of the TiN powder. The mixture was not completely densified by the hot-pressing process at 2300°C, though shrinkage started to appear around 1600°C. The final density was around 70% of the theoretical level.

The 6H-SiC powder was completely transformed into the 3C phase, when thermally treated at 2200°C or more. **Figure 1** presents the X-ray diffraction patterns of the 6H-SiC and the SiC/TiN mixture (TiN: 20mol%) as the starting powders, thermally treated at 2000° and 2200°C. The phase transformation proceeded to only a limited extent at 2000°C, but the 6H phase was completely transformed into the 3C phase at 2200°C.

Thus, the 6H→3C transformation greatly depended on treatment temperature. **Figure 2** shows the effects of heat-treatment time on extent of the phase transformation of the hot-pressed samples, which were heated at 53°C/min to a given temperature at which they were held for a given time. The phase transformation proceeded rapidly at 2200°C, moderately at 2100°C, and insignificantly at 2000°C and at 1900°C. The activation energy associated with phase transformation rate, determined from the results shown in Fig.2, was 1373kJ/mol.

3.2. Changes in Lattice Constants of SiC and TiN during Heat-Treatment Process

It was found that the phase transformation of SiC also depended on impurities present. Therefore, the changes in lattice constants as a result of dissolution of Ti were investigated. **Figure 3** shows the effects of SiC/TiN mixing ratio on the lattice constants a_0 of SiC and TiN. Accuracy of the measurement, taking the lattice constant of SiC as an example, was approximately 0.0001 for the a_0 = 4.3589 (ASTM29-1129) of the pure 3C-SiC phase. The hot-pressed 3C-SiC sample showed the lattice constant almost the same as that relevant to the single SiC phase. The lattice constant tended to decrease gradually as TiN content increased, but it was difficult to consider that this resulted from dissolution of another element.

On the other hand, TiN increased significantly in lattice constant, when combined with SiC; lattice constant of the TiN/SiC (5%/95%) mixture was a_0 = 4.3274, compared with a_0 = 4.2417 of TiN. This resulted from dissolution of carbon, as discussed later.

3.3. Dissolution of Ti in Structures and SiC Particles

Figure 4 presents the photographs of the fracture and polished faces of the sample, the mixed powder of SiC (20%) and TiN (80%) treated at 2300°C for 15min. As shown, SiC was completely transformed into the 3C phase. The SEM-EDS analysis indicated that the gray particles in **Fig.4(a)** represented SiC. The white portions in the figure consisted of two types of particles, the brighter one representing the $TiSi_2$ and the other parts Ti, C and N were detected. Then it was judged that carbon was dissolved in TiN. The TiN-TiC dissolution relationship is already known for all proportions.[6]

Ti and N might be dissolved in the 3C-SiC phase. **Figure 5** is the EDS photograph taken to confirm the presence of Ti within the 3C-SiC particles. The analysis of the fracture face of SiC detected small quantities of Ti. This was confirmed also by EPMA analysis. In other words, the analysis of the 18 particles of 3C-SiC in the heat-treated sample indicated that the average concentration of Ti in the particles was 0.2wt%.

It was also found that $TiSi_2$ was formed by the heat treatment, as shown in Fig.1, resulting from the reactions between SiC and TiN.

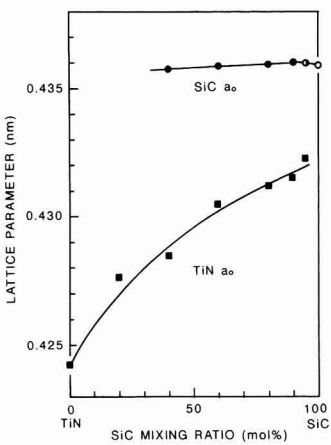

Fig. 3. Lattice parameters, a_0, of the transformed 3C-SiC and Ti(N, C) in hot-pressed SiC-TiN powders. The powders were hot-pressed at 2300°C. The lattice parameter of 3C-SiC, a_0, decreased very slightly with the increase in the content of TiN. The a_0 of TiN increased with the increase in the SiC content. The Ti(N, C) solid solution was formed by the reaction of SiC and TiN. In the sample 95%SiC-5%TiN (○ in the figure), the transformation was not completed.

4. Discussion

Thermal stability of the SiC polymorphisms has been studied fairly extensively. Knippenberg discusses that the 3C is quasi-stable, and the stable phases are the 2H at low temperature and 6H at high temperature above 2000°C.[7]

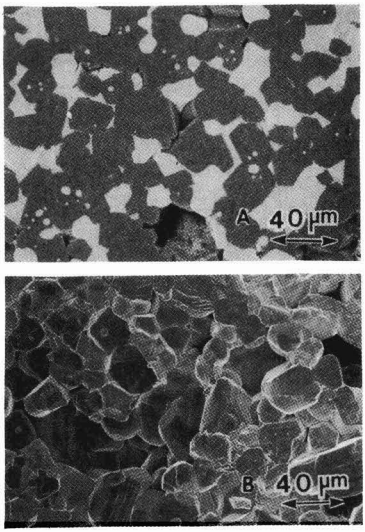

Fig. 4. Microstructure of SiC-TiN (20%), which was hot-pressed at 2300°C, (a) polished surface and (b) fracture surface. EDS analysis revealed that the sample consisted of 3C-SiC Ti(N, C) and $TiSi_2$ grains.

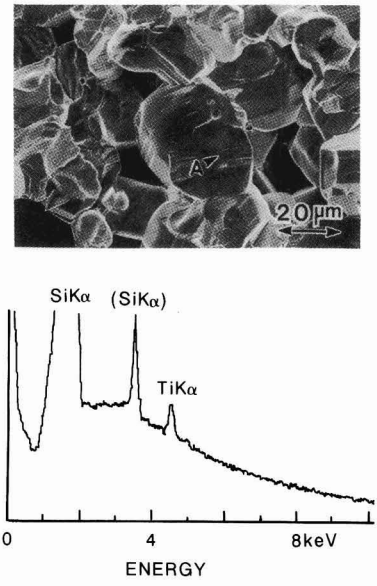

Fig. 5. EDS analysis of Ti solution in the 3C-SiC grain. Ti was detected on the fracture surface of SiC(position A). The average amount of the Ti solution in SiC was 0.2wt%. The SiC-TiN(20%) sample was hot-pressed at 2300°C.

Inomata et al., on the other hand, have discussed based on the detailed experimental results that (1) the 3C tends to predominate at 1700°C or below, (2) the 4H, 9T and 21R systems appear as temperature increases (the 9T and 21R systems are known for their long period) and (3) the 6H and 15R are the stable phases at 2000°C or above.[8] A number of other researchers have synthesized the single crystal SiC using various methods, such as sublimation,[9,10] separation from the molten Si,[8,11,12] and chemical vapor deposition,[13] presenting essentially the same results as above, as far as thermal stability of the polymorph is concerned. The 3C-SiC system is no longer stable at 2000°C or more, and is transformed mainly into the 6H system, when heated to the above temperature.[14]

Thermal stability of the polymorphisms are also sensitive to the presence of impurities. Al stabilizes the 4H polytype.[15-17] The 3C system in the B-containing sinter is transformed into the α type (mainly, the 6H and 15R polytype), the transformation being accompanied with growth of the grains.[16,18] It is also known that the 3C polytype will appear and the 6H→3C phase transformation can proceed even at high temperature, when nitrogen atoms are dissolved in SiC.[19-22] Kieffer et al. found that the 6H-SiC is transformed into the 3C, when heated at 2500°C and 30 atms in a nitrogen atmosphere, clarifying that nitrogen is dissolved in the transformed SiC phase.[21] Jepps et al. treated the reaction-sintered 6H-SiC containing Si at 2250°C and 30 atms in a nitrogen atmosphere, to find that the 6H-3C phase transformation proceeded.[22] Thus, the 6H -3C phase transformation needs the presence of high-pressure nitrogen.

The results of this study are the same as those of Kieffer et al. and Jepps et al. in that the 6H-3C phase transformation is affected by nitrogen, but differ in the treatment conditions; nitrogen is added in the form of metallic nitride and atmosphere gas is Ar at 1 atm. The formation of $TiSi_2$ in the thermally treated sample indicates that TiN, for example, reacts with SiC to form N_2:

$$2SiC + 3TiNT \rightarrow iSi_2 + 2Ti(N, C) + 1/2N_2$$

part of which is dissolved in SiC.

The experiments were conducted to investigate the effects of nitrogen, in which the 6H-SiC powder and the 6H-SiC/$TiSi_2$ mixture were thermally treated in an Ar or N_2 atmosphere, as described in **Table 1**. The treated polymorphisms were analyzed by X-ray diffractiometry.

It was found, as a result, that no phase transformation of the 6H-SiC was observed in an Ar atmosphere, the phase transformation into the 3C occurred to some extent in a N_2 atmosphere, and the phase transformation proceeded completely even at 1 atm in a N_2 atmosphere, in the presence of $TiSi_2$. There is no direct evidence to indicate dissolution of N in SiC; nevertheless, however, there will be little doubt that the 3C→6H phase transformation is accelerated in the presence of nitrogen at high temperature. Furthermore, the

Table 1. 6H→ 3C-SiC transformation induced in hot-pressed 6H-SiC and 6H-SiC + $TiSi_2$ powder.

Sample powder	Hot-Pressing Temp. (°C)	Time (min)	Atoms-phere	Content of polytypes(%) 3C	6H	15R
6H-SiC as received			-	9	91	0
6H-SiC	2300	x 15	Ar	12	80	8
6H-SiC	2300	x 15	N_2	38	56	6
6H-SiC+$TiSi_2$	2300	x 15	Ar	19	81	0
6H-SiC+$TiSi_2$	2300	x 15	N_2	98	2	0

EDS and EPMA analysis confirmed dissolution of Ti in the SiC grains. It is therefore considered that dissolution of N in SiC is responsible for the 6H-3C transformation occurring at 2200°C in the presence of TiN. At the same time, a small quantity of TiN dissolved in SiC would work to accelerate the transformation. The quantity of Ti dissolved in SiC was fairly small at 0.2wt%, as determined by the EPMA analysis, with the result that the lattice-lattice distance of SiC was not changed much.

Transformation of SiC results from rearrangement of the layer planes (caused by diffusion through the solid phase), slip of the layer planes (caused by the partial transformation), sublimation/recrystallization, and dissolution/separation.[4] As discussed earlier, activation energy associated with the 6H→3C transformation was 1373kJ/mol, determined from dependence of the transformation on temperature and time. Activation energy for coefficient of diffusion through the solid phase of SiC is well established. For example, that of Si through SiC is 697 to 912kJ/mol,[23] and that of C is 715 to 814,[23] or 592 or 1266kJ/mol,[24] the last value being for the SiC system containing 100ppm of N. Activation energy associated with sublimation of SiC is 553 to 610kJ/mol,[10,14,25] and that associated with the 3C→6H phase transformation is 495 to 661k/mol.[4,14,26,27] Activation energy for the phase transformation, determined in this study, is larger than the literature value, and it is difficult to deduce the mechanisms involved in the phase transformation from the activation energy. The larger activation energy, however, suggests that recombination of the atoms through the solid phase serves as the rate-determining step in the phase transformation process.[4]

5. Conclusions

The 6H-SiC powder containing 10 to 60mol% of TiN powder was transformed into the 3C system, when hot-pressed at 2200°C.

It is known that the 6H→3C phase transformation proceeds at a high N_2 pressure; however, it is demonstrated to proceed at 1 atm in an Ar gas atmosphere, when SiC is mixed with TiN. Dissolution of a small quantity of TiN in SiC, or dissolution of N derived from TiN in SiC is considered to be responsible for the phase transformation.

It has been confirmed that the similar phase transformation proceeds, also in the presence of other metallic nitrides, such as ZrN and VN.

References:

1) G. Orange, H. Tanaka and G. Fantozzi, Ceram. Int., 13, 159-65 (1987).
2) K. Yamada and M. Mohri, "Silicon Carbide Ceramics," edited by S. Somiya and K. Inomata, Uchida Rokaku-ho, 1988, pp.9-29.
3) H. Tanaka, K. Inomata, K. Tsukuda and A. Hagimura, Yogyo Kyokai-shi, 92, 461-65 (1984).
4) N. W. Jepps and T. F. Page, J. Cryst. Growth Charac., 7, 259-307 (1983).
5) J. Ruska, L. J. Gauckler, J. Lorenz and H. U. Rexer, J. Mater. Sci., 14, 2013-17 (1979).
6) L. Aggour, E. Fitzer and W. Weisweiler, High Temp. - High Press., 6, 73-84 (1974).
7) W. F. Knippenberg, Philips Res. Rep., 18, 161-237 (1963).
8) K. Inomata, M. Mitomo, Z. Inoue and K. Tanaka, Yogyo Kyokai-shi, 77, 130-35 (1969).
9) D. R. Hamilton, "Silicon Carbide", Edited by J. R. O'Corner and J. Smiltens, Pergamon Press, (1960) pp.43-52.
10) L. J. Kroko, J. Electro-chem. Soc., 113, 801-08 (1966).
11) F. A. Halden, "Silicon Carbide", Edited by J. R. O'Corner and J. Smiltens, Pergamon Press (1960) pp.115-23.
12) R. C. Marshall, Mater. Res. Bull., 4, S73-S84 (1969).
13) K. M. Merz, "Silicon Carbide", Edited by J. R. O'Ccorner and J. Smiltens, Pergamon Press (1960) pp.73-83.
14) K. Inomata, Z. Inoue and N. Kijima, Yogyo Kyokai-shi, 77, 313-18 (1969).
15) M. Mitomo, K. Inomata, Z. Inoue and S. Kumanomodo, Yogyo Kyokai-shi, 78, 224-28 (1969).
16) D. H. Stutz, S. Prochazka, and J. Lorenz, J. Am. Ceram. Soc., 68, 479-82 (1985).
17) R. M. William, B. N. Juterbock, S. S. Shinozaki, C. R. Peters and T. J. Whalen, Am. Ceram. Soc. Bull., 64, 1385-89 (1985).
18) S. Prochazka, "Special Ceramics 6", Brit. Ceram. Res. Assoc. (1975) pp. 171-81.
19) T. Kawamura, Mineralogical J., 4, 335-55 (1965).
20) A. Addamiano and L. S. Staikoff, J. Phys. chem. Solids, 26, 669-72 (1965).
21) R. Kieffer, E. Gugel, P. Ettmayer and A. Schmidt, Ber. Deut. Keram. Ges., 43, 621-23 (1966).
22) N. W. Jepps and T. F. Page, J. Amer. Ceram. Soc., 64, C177-78 (1981).
23) J. D. Hong, M. H. Hon and R. F. Davis, Ceramugia Int., 5, 155-60 (1979).
24) R. N. Ghoshtagore and R. L. Coble, Phy. Rev., 143, 623-26 (1966).
25) J. Drowart, G. De. Maria and M. G. Inghram, J. Chem. Phys., 29, 1015-21 (1958).
26) G. A. Bootsma, W. F. Knippenberg and G. Verspui, J. Cryst. Growth, 8, 341-53 (1971).
27) E. D. Whitney, Nature, 199, 278-80 (1963).

This article is a full translation of the article which appeared in Nippon Seramikkusu Kyokai Gakujutsu Ronbunshi (Japanese version), Vol.99, No.5, 1991.

Crystal Structure Analysis of a Low Temperature Form of $ZrTiO_4$ with a Modulated Structure

Toshiyuki Yamada, Kazuyori Urabe, Hiroyuki Ikawa and Hiromasa Shimojima

Department of Inorganic Materials, Faculty of Engineering, Tokyo Institute of Technology
12-1, Ookayama, Meguroku, Tokyo 152 Japan

A modulated structure of a low-temperature form of zirconium titanate ($ZrTiO_4$) was analyzed with an X-ray diffractometer. Superstructure spots were indexed by introducing a modulated wave vector of k=0.58a. Intensities for normal and super-structure spots measured along the a* axis were used for the calculation of electron densities. The results indicated the existence of modulation of scattering amplitude of cations as well as displactive modulation of oxygen ions. The estimated ordered arrangement of metal ions along the a-axis was Zr-Zr-Ti-Ti-Zr-Zr-.

[Received October 6, 1990; Accepted January 24, 1991]

Key-words: Zirconium titanate, Modulated structure, Crystal structure, Structure analysis, Single crystal

1. Introduction

Hafnium titanate ($HfTiO_4$) is known as a refractory material with low thermal expansion.[1-6] The crystal structure of $HfTiO_4$ was analyzed by Harari et al,[7] and found to have an α-PbO_2-type structure with the space group Pbcn.[8] Moreover, it was reported that the crystal structure of zirconium titanate ($ZrTiO_4$) is the same as $HfTiO_4$.[8,9]

The heavy dependence of the lattice constant of $ZrTiO_4$ on heat treatment used to attract interest,[10,11] which was revealed by Mchale and Roth to be caused by phase transition.[12] They also claimed that $ZrTiO_4$ is decomposed into two phases at low temperature.[13]

Ikawa et al.[14,15] pointed out that there are greater differences in properties between $HfTiO_4$ and $ZrTiO_4$ in properties than were believed earlier.[2,3,11] In addition, they[14] proposed a working hypothesis to explain the differences and proved that the properties of a $ZrTiO_4$ solid solution can be controlled on the basis of the hypothesis.

This study is part of a project to review the crystal structure of $HfTiO_4$ and $ZrTiO_4$. The single crystal of $ZrTiO_4$ was grown to measure the diffraction intensities from superstructure which appears after heat treatment, and the results were analyzed to clarify the modulated structure of low-temperature-type $ZrTiO_4$ as described below.

2. Method of Experiment

The raw powder material $ZrTiO_4$ was prepared as follows. Aqueous solutions of zirconium sulfate and titanium sulfate were made and their concentration was measured by a weight method. The solutions were then weighed out such that the molar ratio of ZrO_2 to TiO_2 was 1:1, and mixed for an hour with an appropriate amount of water. The 14% of ammonia water was added to the mixture to form a precipitate followed by further mixing for an hour. After that the precipitate was filtered by suction dried at 110°C and ground at 110°C, and calcined at 1000°C for 5 hours. The calcined powder was compacted into pellets for sintering in an electric furnace. The sintering conditions were 1600°C, 10 hours, and cooling to room temperature at a rate of 10°C/min. The pellets were pulverized to prepare $ZrTiO_4$ raw material powder.

The powder was used to grow a single crystal by a flux method reported by Sugai and Hasegawa.[16] In the method, Li_2MoO_4 and MoO_3 were adopted as flux and mixing was performed with a molar ratio of $ZrTiO_4$:Li_2MoO_4:MoO_3 =1:3:5; the mixture was heated. The heating rate from 500°C to 1300°C was 100°/h. It was held for 5hrs at 1300°C cooled down to 800°C at 0.03°C/min, and left out of the furnace for cooling.

The resulted single crystal was subjected to chemical analysis with EDX (Seiko EG&G; SED8600). Moreover, the content of Hf, an impurity in starting zirconium sulfate was measured using an ICP emission spectral analyzes(Seiko Electron; SPS 7000).

The information on the reciprocal lattice of the single crystal was obtained with a Weissenberg camera to determine a space group as well as to confirm the presence of a modulated structure. Diffraction intensity along a* axis was measured with a 4-axis automatic diffractometer (Phillips; PW-1100). In measurement, a MoKα ray monochromatized by graphite crystals was used and scanning was conducted along a* axis from 2θ of 5° to 60° at a rate of 0.05°/sec. At the same time, sdveral reflection peaks having hkl indexes with high intensity in the range of 2θ less than 70° were selected to measure their diffraction angles, and lattice constants were calculated using MoKα_1 as wavelength with a program for the method of least squares (RSLC-3[17]). The values of diffraction intensity were obtained from the weight of paper cut out according to peak profiles. The Lorentz and polarization factors of the diffraction intensities were corrected to compute $|F(hklm)|$ which underwent Fourier transformation by means of formula(1):

$$\rho(x_1, 0, 0, x_4) = \sum_h \sum_m F(h, m) \cdot \cos(h \cdot x_1 + m \cdot x_4) \quad \ldots\ldots\ldots\ldots\ldots\ldots\ldots\ldots (1)$$

where m is an index in the 4th dimension corresponding to reflection from a superstructure.

3. Experimental Results and Discussion

The single crystals prepared by the above method are needle-like rectangular parallelopipeds about 0.2×0.2×3.0mm in size growing in the direction of the c-axis with {110} face. Table 1 shows the results of compositional analysis by EDX. They are averages of two measurements with three samples. This indicates that the Zr/Ti ratio of the single crystal is about 1:1. In ICP emission spectral analysis, the concentration of Zr and Hf was measured in the raw material solution of zirconium sulfate and hafnium sulfate diluted in a certain proportion and the Hf/Zr ratio was calculated from the above values so as to ensure self-matching between both solutions. As a result, the proportion of Hf in the zirconium sulfate solution was found to be Hf/(Zr + Ti)×100=0.85atom%. This result is consistent with those of EDX analysis.

Furthermore, lattice constants determined by powder X-ray diffraction were a=0.4816(1)nm, b=0.5352(1)nm, c=0.5037(1)nm. These values were almost the same as those of low-temperature-type $ZrTiO_4$ quenched from 1000°C,[15] proving that the phase transition occured in the single crystal. The Weissenberg photograph of the single crystal was taken and all of main reflection could be indexed by the reciprocal lattice of ideal αPbO_2-type structure with the space group Pbcn, while satellite reflection with non-integral indeces was found along the a*-axis. This fact proved that the crystal has a one-dimensional modulated structure. **Figure 1** gives the schematic diagram of this diffraction pattern.

When the wave number vector of the modulation is set as

$k = 0.58a^*$

all diffraction points in the figure can be provided with four-dimensional indeces.[18] All peak in **Fig.2** were given indeces in this manner, and Fourier transformation was performed using these indeces as well as reflection intensity obtained as stated above **Table 2** lists the reflection intensity of each peak. Fourier transformation requires the phases of F(h00m). That of the main reflection can be computed from a hypothetical, ideal α-PbO_2-type structure. After processing, all signs of the main reflection proved to be positive.

According to Takagai,[19] when phase modulation coexists with intensity modulation and they can be approximated with since and cosine waves respectively, phase modulation x_n, and intensity modulation $_n$ can be expressed as follows

$$x_n = na + \frac{L\delta}{2\pi a}\sin\left(\frac{2\pi na}{L}\right) \quad \ldots\ldots\ldots\ldots (2)$$

$$f_n = f\{1 + g\cos\left(\frac{2\pi na}{L}\right)\} \quad \ldots\ldots\ldots\ldots (3)$$

where

a : lattice constant
δ : amplitude of a sine wave
L : wavelength
g : amplitude of a cosine wave

Given the intensity as

$I(\xi\ 00) = Ief^2 \mid Y(\xi) \mid^2$,

$\Psi((\xi)$ is

$$\psi(\xi) = \sum_n \{1 + g\cos(2\pi n\sigma)\} \exp[2\pi i\xi\{n + (\alpha/2\pi)\sin(2\pi n\sigma)\}] \quad \ldots\ldots\ldots\ldots\ldots\ldots (4)$$

where $\alpha=L\delta/a^2$ and $\sigma=a/L$.

The phase of satellite reflection were calculated by this formula, and those of all reflection measured this time were found to be positive.

Figure 3 shows the results of Fourier transformation with phases obtained as above. In the figure, a_4 is a vector corresponding to the space in the 4th dimension and a_1 is a cross section along the a-axis.

Since the reflection along the a*-axis and modulation

Table 1. EDX analysis of a zirconium titanate single crystal

sample	TiO_2/mol %	ZrO_2/mol %	HfO_2/mol %
$ZrTiO_4$	51.7	47.7	0.6

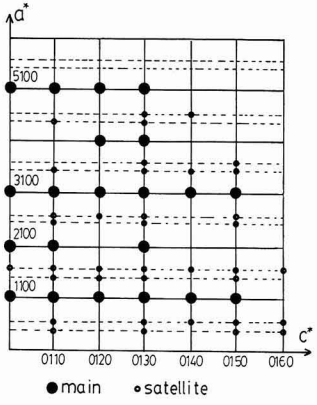

Fig. 1. Schematic representation of a reciprocal lattice for a low temperature form of zirconium titanate

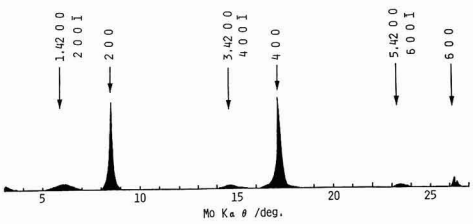

Fig. 2. X-ray diffraction pattern for a low temperature form of zirconium titanate along the a^* axis

Table 2. Peak intensities and structure factors for a low temperature form of zirconium titanate

hklm	MoKα θ/deg.	I	2Lp	|F(hklm)|
$200\bar{1}$	6.032	2127	9.368	15.068
2000	8.475	7205	6.563	33.133
$400\bar{1}$	14.630	820	3.605	15.082
4000	17.155	8930	2.984	54.705
$600\bar{1}$	23.525	206	2.002	10.144
6000	26.210	970	1.732	23.665

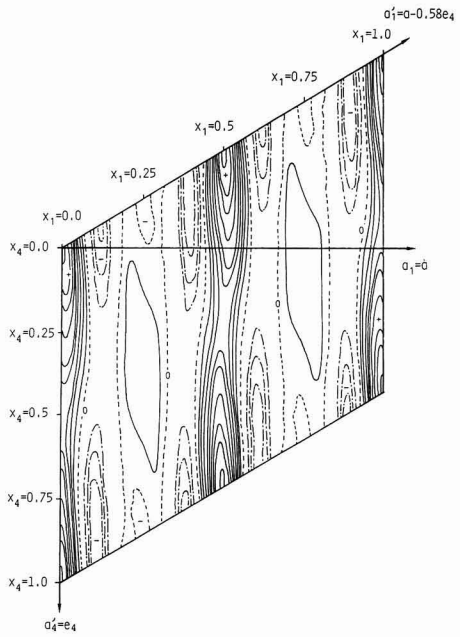

Fig. 3. Four-dimensional Fourier map for a low temperature form of zirconium titanate projected onto the a_1-a_4 plane

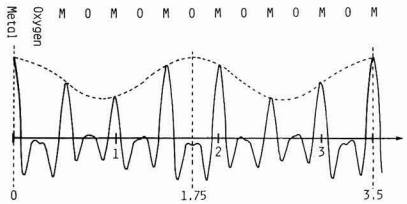

Fig. 4. One dimensional Fourier map for a low temperature form of zirconium titanate along the a-axis

appeared along the a-axis, this figure means the projection of electron density in the 4-dimensional space from the b- and c-axis directions onto the a_1-e_4 plane. However, Fourier transformation this the absolute values of electron density are meaningless. This figure shows that in the case of positive ions the modulation of scattering amplitude by electron density fluctuation occurred along with phase modulation by the displacement of atomic position, and that as for oxygen ions phase modulation occurred as well. The direction of the a_1 line ray in the 4-dimensional Fourier diagram coincides with the direction of the a-axis in **Fig.4**. Moreover, numbers along the axis in Fig.4 indicate the repetition period of a basic structure while the vertical axis does electron density. the figure reveals that low-temperature-type $ZrTiO_4$ has a non-integral modulated structure (about 1.75 times a basic period is that of modulation) as shown with the dotted line. Here the reason for the modulation of scattering power is considered to be that the random arrangement of Zr^{4+} and Ti^{4+} at a high-temperature phase shifts to regular arrangement at a low-temperature phase.

The most convenient interpretation for the distribution of electron density in Fig.4 is that positive ions are in a row along the a-axis as Ti-Ti-Zr-Ar-Ti-Ti-Zr- ....., a regular arrangement about twice the period of an α-type structure (basic structure) along the a-axis. yet in practice the arrangement does not spread the entire crystal to leave irregularities such as Zr-Zr-Ti-Ti-Zr-Ti-Ti....., which seems to result in the modulated structure.

In the next step, discussion goes to phase modulation. With regard to positive ions, the atomic position seems to deviate from that of the basic structure, and the trend is also encountered with oxygen ions. This is clear in Figs.3 and 4 showing that oxygen ions deviate to some extent from the basic position. The modulation of the of oxygen ions is considered to be deeply associated with the regular arrangement of positive ions.

4. Conclusion

The single crystal of low-temperature-type $ZrTiO_{4D}$ was synthesized to analyze its crystal structure. The results were as follows.

1) It was found that the crystal has a non-integral modulated structure in the direction of the a-axis. Additionally, the distribution of x-ray diffraction intensity along the a*-axis was measured to obtain the distribution of electron density along the a-axis by Fourier transformation.
2) the above electron density distribution detected the presence of modulation in the electron density of oxygen and positive ion sites.
3) The probable reason for this modulation was that Zr^{4+} and Ti^{4+} ions do not occupy positive ion sites at random with the same probability but align regularly along the a-axis.

Acknowledgements

The authors are grateful to Prof. M. Yamane, Tokyo Institute of Technology for his help in the use of the EDX system, Prof. Mitsuo Abe and Prof. Hiroshi Kanzaki, Tokyo Institute of Technology for their help in the use of the ICP emission spectral analyzer, and Prof. Masanori Kato, Faculty of Engineering, Tokyo Institute of Technology (now professor emeritus) and Dr. N. Ishizawa (now assistant professor, Research Laboratory of Engineering Materials, Tokyo Institute of Technology) for their help in the use of the 4-axis X-ray diffractometer.

This study was conducted at the Department of Inorganic Materials, Faculty of Engineering, Tokyo Institute of Technology. The author bless the memory of Mr.•T. yamada, one of the authors who passed away in an accident in march, 1990 after finishing this work.

References:

1) F.H. Simpson, Mater. Des. Eng., 52, 16-18 (1960).
2) R.W. Lynch and B. Moros, J. Am. Ceram. Soc., 55, 409-13 (1972).
3) R. Ruh, G.W. Hollenberg, E.G. Charles and V.A. Patel, J. Am. Ceram. Soc. 59, 405-99 (1976).
4) G.A. Carlson, J.L. Anderson, R.A. Brismeister. S.R. Skaggs and R. Rug. J. Am. Ceram. Soc., 60, 508-10 (1977).
5) S.R. Skaggs, Rev. Int. Hautes Temp. Refract., 16, 157-67 (1979).
6) L'Octet Franco-Canadian, High Temp.-High Pressures, 13, 97-103 (1981).
7) A. Harari, J.P. Bocquet, M. Huber, R. Collongues and C.R. Hebd, Seances Acad. Sci. Ser. C. 267 1316-18 (1968).
8) G. Blasse, Z. Anorg. Allg. Chem., 345, 222-24 (1966).
9) R.E. Newnham, J. Am. Ceram. Soc., 50, 216 (1967).
10) L.W. Coughanour, R.S. Roth and V.A. Deprosse, J. Res. Natl. Bur. Stand. (U.S.), 52, 37-42 (1954).
11) A. Cocco and G. Troriano, Ann. Chim. (Rome), 55, 153-63 (1965).
12) A.E. Mchale and R.S. Roth, J. Am. Ceram. Soc., 66, C18-20 (1983).

13) A.E. Mchale and R.S. Roth, J. Am. Ceram. Soc., 69, 827-32 (1986).
14) H. Ikawa, A. Iwai, K. Hiruta, H. Shimojima, K. Urabe and S. Udagawa, J. Am. Ceram. Soc., 71, 120-27 (1988).
15) H. Ikawa, H. Shimojima, K. Urabe, T. Yamada and S. Udagawa, SCIENCE OF CERAMICS, 14, 509-14 (1988).
16) T. Sugai and H. Hasegawa, Yogyo-Kyokai-Shi, 76, 429-30 (1968).
17) T. Sakurai, Universal Program System for Crystallographic Analysis, Nihon Kessho Gakkai, 99 (1967).
18) P.M. de Wolff, Acta Cryst., A30, 777-85 (1974).
19) S. Takagi, X-sen Kesshogaku II, Maruzen, 618-451 (1961).

This article is a full translation of the article which appeared in Nippon Seramikkusu Kyokai Gakujutsu Ronbunshi (Japanese version), Vol.99, No.5, 1991.

The Effects of Annealing on Surface Machining Damage of Alumina Ceramics

Yohtaro Matsuo, Toshio Ogasawara, Shiushichi Kimura, Shigemi Sato*** and Eiichi Yasuda***

Faculty of Engineering, Tokyo Institute of Technology
2-12-1, Ookayama, Meguro-ku, Tokyo 152, JAPAN
*Research Laboratory of Engineering Materials, Tokyo Institute of Technology
4259 Nagatsuta-cho, Midori-ku, Yokohama-shi, 227, JAPAN
**Material Research Laboratory, Nissan Motor Co. Ltd.
1 Natsushima-cho, Yokosuka-shi, 237, JAPAN
***NHK Spring R&D center Co. Ltd.
1 Isogo-cho, Isogo-ku, Yokohama-shi, 235, JAPAN

The grinding process induces residual stresses and scratch cracks near the surfaces of ceramic workpieces. In order to reduce the influences of the surface damage layers, the effects of annealing on the bending strength of alumina specimens ground with a #170 diamond wheel were investigated. Surface residual stresses were measured by the X-ray diffraction method and the effects of residual surface stresses on the bending strength were discussed using a simplified model. As a result, the annealing process restored the surface damage layers and bending strengths of ground alumina specimens to the initial condition. The compressive residual stress influenced the micro-cracks perpendicular to the grinding direction and consequently the bending strengths increased slightly, however they hardly influenced the deep scratch cracks parallel to the grinding direction.
[Received October 15, 1990; Accepted January 24, 1991]

Key-words: Machining damage, Alumina, Residual stress, Annealing, Crack model

1. Introduction

The grinding process of ceramics inevitably induces residual stresses and scratch cracks because it is performed by the accumulation of micro-fracture due to contacting abrasives. Kirchner et al.[1] and Yoshikawa et al.[2] have confirmed the scratch cracks occurring perpendicular to and at an angle with the surface from the bottom of grinding groove in single point grinding. **Figure 1** schematically shows such scratch cracks.[18] An abrasive grain produces a grinding groove due to micro pseudo-plastic deformation, and consequently causes median cracks parallel to the groove, radial cracks and lateral cracks developing sideward from the groove. It has been well known that these scratch cracks have a great effect on the strength of material, and much research has been done on the effect. For example, Rice et al.,[3] Tressler et al.,[4] and Cranmer et al.[5] measured the bending strength of ground SiC and Al_2O_3 materials and reported that scratch cracks caused by grinding governs the strength of material with a small grain size. Also, Mecholsky et al.,[6] Andersson et al.,[7] Rice et al.,[2] Ito,[8] Takase et al.,[9] and the authors[10] reported the relationship between grinding direction and bending strength for ground ceramics such as glass, alumina, silicon carbide, and silicon nitride. Regarding the residual stresses caused by surface grinding, though studies have been made on steels for a long time, and several reports on ceramics have recently been published. For example, Johnson-Walls et al.,[11] Tanaka et al.,[12-14] Takase et al.,[9] and Samuel et al.[15] measured the residual stresses on the ground surface of silicon nitride, alumina, and zirconia materials, and reported that a compressive residual stress field was formed at a ground surface.

Although it has been revealed that the strength of ceramic material at room temperature is impaired by grinding, the grinding of ceramics has still been performed in actual production as an effective machining process, by removing the surface damage layer in the finish-grinding process using fine abrasive grains to improve the surface condition and improve material strength due to grinding damage. However, the finish-grinding process increases the product cost. A low-cost process is required to banish the effects of grinding damage.

This paper describes the effect of annealing of alumina material with a ground surface performed to decrease the effect of scratch cracks on the bending strength of material. We also measured the residual surface stresses produced by grinding by the X-ray diffraction method, investigated the relieving behavior of residual stress due to annealing, and studied the effect of residual stress on the bending strength of material.

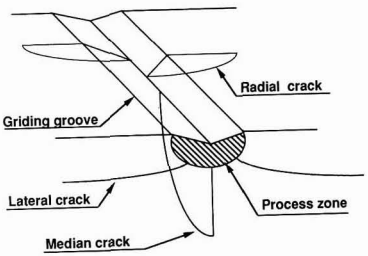

Fig. 1. Schematic drawing of the scratch cracks caused by grinding.

2. Experimental Procedure

2.1. Test Specimens and Their Preparation

The material used in the experiment was alumina compact SSA-S manufactured by Nihon Kagaku Togyo Co., Ltd. with a mean grain diameter of 2.6μm, a bulk density of 3.83g/cm^3, a purity of 99.56%, and a Young's modulus of 390GPa. The size of the specimen was 3×10×50mm (**Table 1**). Grinding was performed by using a #170 resin-bonded diamond wheel manufactured by Tokyo Diamond Co., Ltd. (200mm dia.) on a surface grinding machine (PSG-5E) manufactured by Okamoto Machine Tool Works, Ltd. Each specimen was bonded to a steel plate with an acetoacetate-base adhesive, and ground to a total depth of 200μm. The grinding conditions were a wheel velocity of 1800mm/min, a workpiece velocity of 8-10m/min, and a downfeed of 8μm (**Table 2**). Spark out was not performed, and single pass grinding was performed for one downfeed. Two grinding directions were used: one is perpendicular to the longitudinal direction of specimen (ϕ=90°) and another is parallel to it (ϕ=0°) when angle ϕ of grinding direction is defined as shown in **Fig.2.** After the grinding was completed, the specimen was allowed to stand in a desiccator at 200°C for about 2 hours to soften the adhesive, and then removed from the jig. This means that all specimens were subjected to annealing at 200°C, but the annealing treatment might have little effect. Then, the edges of the specimen were chamfered by about 20μm using a metal-bonded diamond lapping machine with a mean grain diameter of 6μm. Heat treatments were performed in the air with a heating rate of 5°C/min and a cooling rate of 2°C/min (furnace-cooled from about 300°C). The heat treatment temperatures were 1000°C, 1230°C, 1460°C, and 1580°C, and the holding time was 1 hour. Although the heat treatment above 1500°C cannot be strictly called annealing because the temperature is very close to a sintering temperature, such heat treatment is called annealing here for convenience.

2.2. Material Tests

All bending tests were made at room temperature by the four-point bending method with an upper span of 10mm and a lower span of 30mm. An Instron type universal tester was used for bending tests, with a constant cross head speed of 0.2mm/min. Fracture toughness value K1c was measured by the SEPB method with the Vickers indentation (indenting load: 20Kgf at one point) as a starter crack. The fracture toughness test was performed by the three-point bending test method with a 16mm span on a specimen cut to the half of the size specified by JIS R1601 after being subjected to the bending test. The measured K1c was 3.5±0.5MPa$\sqrt{m}$.

Table 1. Properties of alumina specimen (SSA-S).

Mean grain diameter (μm)	2.6
Bulk density (g/cm³)	3.83
Purity (%)	99.6
Young's modulus (GPa)	390
Fracture toughness (MPa$\sqrt{m}$)	3.5

Table 2. Grinding conditions.

Wheel no.	#170
Abrasive diameter (μm)	85-90
Wheel diameter (mm)	200
Wheel velocity (m/min)	1800
Workpiece velocity (m/min)	8-10
Down feed (μm)	8

2.3. Stress Measurement by X-ray Diffraction

The residual surface stresses were measured by the X-ray diffraction method. Taking the stress in the ψ scanning direction as σ_x, and the stress perpendicular to the direction as σ_y, the residual strain $\varepsilon(\psi)$ at an angle of ψ with respect to the normal of a specimen is expressed as

$$\varepsilon(\psi) = \sigma_x \sin^2\psi\,(1+\upsilon)/E - (\sigma_x+\sigma_y)\upsilon/E \quad \ldots (1)$$

(E: Young's modulus, ν: Poisson's rasio)
Expressing $\varepsilon(\psi)$ in terms of lattice space d,

$$\varepsilon(\psi) = (d(\psi)-d_0/d_0) = -\cot\theta_0 \cdot (\theta-\theta_0) \quad \ldots (2)$$

(d_0, θ_0: lattice space and diffraction angle in the distortion-less condition, respectively)
The following fundamental equation is obtained from E_{qs}.(1) and (2).

$$2\theta = -2(1+\upsilon)\cdot\tan\theta_0\cdot\sigma_x\cdot\sin^2\psi/E + 2\upsilon\tan\theta_0\cdot\sigma_x + 2\theta_0 \quad \ldots (3)$$

This equation indicates a linear relationship between 2θ and $\sin^2\psi$.
Taking the gradient of this line as M,

$$M = -2(1+\upsilon)\cdot\tan\theta_0\cdot\sigma_x/E \quad \ldots (4)$$

The residual stress σ_x is given by the following equations by using the gradient M in 2θ-$\sin^2\psi$ plot.

$$\sigma_x = K\cdot M \quad \ldots (5)$$

$$K = E\cdot\cot\theta_0/[2(1+\upsilon)] \quad \ldots (6)$$

where
K is the stress constant in the X-ray stress measurement, and depends on the physical properties of material.

In the X-ray stress measurement of alumina, the diffraction spectrum from the 220 plane (2θ=148.489°) is recommended for Cr-Kα.[16] Therefore, this diffraction plane was used in this experiment. By using the X-ray diffraction equipment in which PSPC was used for counting diffracted X-rays, the specimen was irradiated with a 4×6mm parallel beam using a Cr tube, and the residual stress was measured

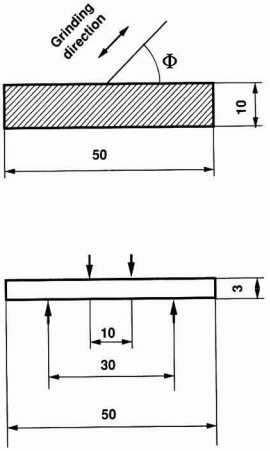

Fig. 2. Dimensions and coordinate system of the beam specimen with ground surface in four-point bending test.

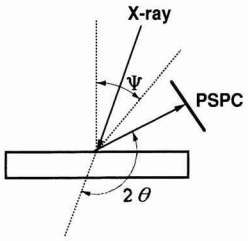

Fig. 3. Coordinate system on specimen and definition of 2θ and ψ.

Table 3. X-ray conditions for stress measurement.

Method	Parallel beam method
Characteristic X-ray	Cr-Kα
Diffraction plane	(220)
Diffraction angle	148.489°
Filter	V
Tube voltage	30 KV
Tube current	10 mA
Divergent angle	0.68°
Irradiated area	4x6 mm
PSPC present time	100 sec
ψ	0°, 10°, 20°, 30°, 40°
K (MPa/deg)	601

by scanning ψ by the parallel beam method. The outline of the measurement system is shown in **Figure 3**, and the measurement conditions in **Table 3**. For the stress constant K, a general value of K=601MPa/degree was used [14].

3. Results and Discussion

3.1. Effect of Annealing on Bending Strength and Residual Stress

Figure 4 shows the relationship between annealing temperature and bending strength at room temperature. Being not annealed, the specimen ground in the direction of ϕ=90° (perpendicular to the longitudinal direction of specimen) was found to have bending strength of about 60% that of the specimen ground in the direction of ϕ=0°. We performed bending tests of alumina specimens ground by diamond wheels with different grain sizes, and reported that the strength decreases as the abrasive size became coarser in the direction of ϕ=90°, while the strength was unchanged with the difference in grain size in the direction of ϕ-0° [10]. This means that the median cracks developing in parallel to the grinding direction, as shown in Fig.1, have a large effect, while the radial cracks have little effect.

Annealing gradually reduced the anisotropy of strength with the difference in grinding direction. The bending strength of specimen ground in the direction of ϕ=90° increased gradually up to an annealing temperature of 1000°C and rapidly at 1230°C, at which the strength was nearly equal to that of specimen ground in the direction of ϕ=0°. At an annealing temperature of 1460°C, the bending strength slightly decreased, and somewhat increased at 1580°C. For the specimen ground in the direction of ϕ=0° (longitudinal direction of specimen), the strength was highest when the specimen was not annealed, decreasing gradually up to an annealing temperature of 1460°C. At 1580°C, the strength increased slightly as with the specimen ground in the direction of ϕ=90°. **Figure 5** shows the bulk density of alumina as a function of annealing temperature. The bulk density was nearly constant up to an annealing temperature of 1000°C. At 1580°C, the density increases suddenly, indicating that densification occurs due to annealing. SEM micrography indicated that the grains grew to a mean grain diameter of about 8μm when the specimen was annealed at 1580°C. This suggests that the slight increase in strength due to annealing at 1580°C results from the change of micro-structure.

Figures 6 and **7** show the measurement results of residual surface stresses by the $\sin^2\psi$-2θ method. The ordinates represent 2θ and the abscissae $\sin^2\psi$. When the gradient is negative, the residual stress is tensile, and when positive, the stress is compressive. These figures indicate that compressive residual stresses occur on the ground surface of material, and are relieved by annealing. The measured values have good linearity, indicating that the X-ray stress

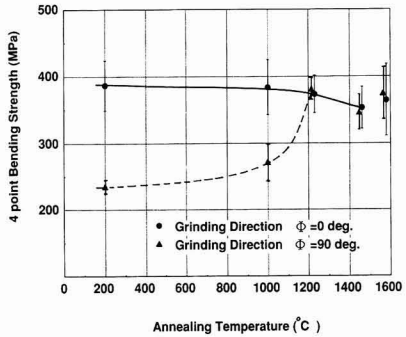

Fig. 4. Effects of annealing on four-point bending strength.

Table 4. Bending strength and Residual stress.

Annealing Temperature (℃)		200	1000	1230	1460	1580
Bending strength (MPa) *1	ø=0°	386.8 (37.2)	383.7 (41.0)	373.2 (28.0)	353.0 (31.8)	364.6 (53.4)
	ø=90	235.1 (10.2)	271.4 (27.7)	381.6 (16.1)	344.2 (26.7)	372.5 (39.4)
Density(g/cm³)		3.83	3.84	3.83	3.83	3.87
Residual stress (MPa) *2	ø=0°	-136.6 (23.0)	-103.2 (5.76)	39.99 (22.8)	-4.81 (22.9)	25.52 (73.8)
	ø=90	-236.7 (15.6)	-171.7 (4.06)	82.81 (3.99)	44.62 (1.58)	50.83 (31.3)

*1 ( ):standard deviation
*2 residual stress measured parallel to longitudinal direction

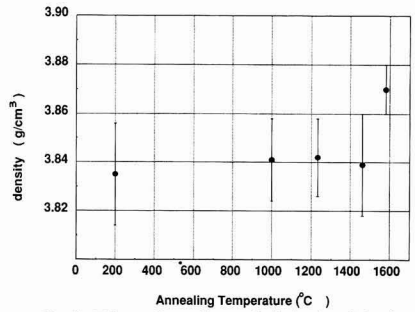

Fig. 5. Effects of annealing on bulk density of alumina.

measurement methods in highly applicable to alumina. **Figure 8** shows the relationship between residual stress and annealing temperature obtained from Figs.6 and 7. For the specimen not annealed, a compressive residual stress of about 140MPa was found in the grinding direction and that of about 240MPa perpendicular to the grinding direction; the magnitude of residual stress differs with the grinding direction. When the specimen was annealed at 1000°C, the compressive residual stress in the grinding direction was hardly changed, being about 100MPa, while that perpendicular to the grinding direction is about 170MPa, relief of residual stress being found due to annealing. When the annealing temperature is 1230°C or higher, the compressive surface stress becomes nearly zero or changes into a tensile stress of low value. This suggests that annealing at temperatures of 1230°C or higher relieves almost all residual stresses caused by grinding. This relief of residual stress and the restoration of lowered strength due to scratch cracks occur at nearly the same tempemperature. This suggests the possibility of restoration of surface damage layer promoted by the crack closing force due to residual stress.

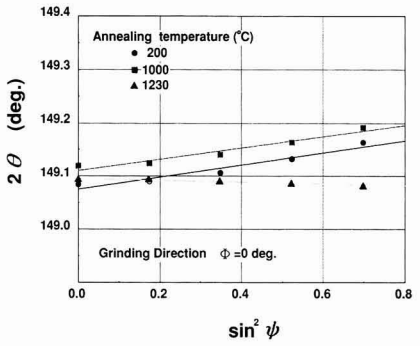

Fig. 6. $\sin^2\psi$-2θ diagram for (220) diffraction of ground alumina (grinding direction ϕ=0° deg.).

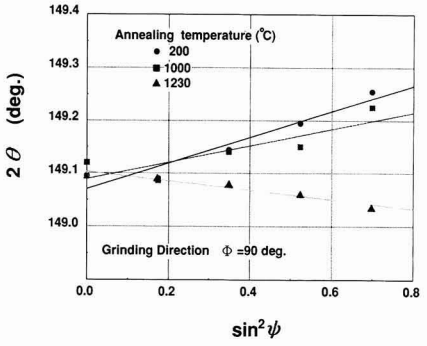

Fig. 7. $\sin^2\psi$-2θ diagram for (220) diffraction of ground alumina (grinding direction ϕ=90° deg.).

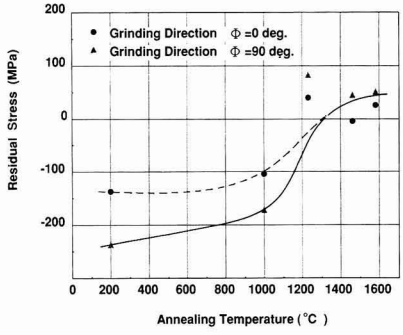

Fig. 8. Effects of annealing temperature on surface residual stress parallel to specimen axis.

3.2. Crack Model and Residual Stress

In this section, we briefly discuss the effect of residual surface stress due to grinding on the bending strength of material.

For example, residual stress distribution on ceramics due to grinding were reported by Suzuki et al.,[14] Kishimoto et al.,[17] Samuel et al.,[16] and Johnson-Walls et al..[11] The residual stress distribution is measured while the surface is gradually lapped. In this case, the residual stress is relieved due to the removal of surface, which makes it difficult to accurately measure the residual stress distribution. Generally, a field of tensile residual stress is formed in the area inside the compressive residual stress layer near the ground surface. This is because the scratch cracks are considered to be formed by tensile stress inside the area near the surface induced by the compressive residual stress due to pseudo-plastic deformation on the surface, as with the mechanism of crack formation due to static indentation. The analysis of tensile residual stresses due to indentation has been reported by many researchers. From the fact that the measured apparent fracture toughness value becomes considerably lower than the actual value in measuring fracture toughness by the CSF(Control Surface Flow) method, it is obvious that compressive residual stresses are distributed on the surface and tensile ones in the inner area. Suzuki et al.[14] reported that the depth of compressive residual stress layer caused by grinding is about 20-30μm for heavily ground (#200) alumina. Johnson-Wall et al.[11] and Samuel et al.[15] also reported nearly the same depth of compressive residual stress as a result of measurement of residual stresses on ground silicon nitride. These facts suggest that compressive residual stresses are distributed down to a depth of about 20-30μm from the surface, and tensile ones at a deeper area. The crack dimension calculated from the fracture toughness and bending strength of alumina used in this experiment is about 40-60μm for the specimen of ϕ=90° (ground perpendicularly) and about 15-25μm for the specimen of ϕ=0° (ground lengthwise). This suggests that the scratch crack is deeper than the compressive residual stress layer for ϕ=90°, while the former is shallower than the latter for ϕ=0°.

Two simple models of residual stress distribution as shown in **Figs.9(a)** and **9(b)** were assumed to consider the effect of residual stress layer on the strength of material. Model 1 represents linear stress distribution, while Model 2 stepwise distribution of compressive and tensile stresses, where a denotes the crack length and b denotes the depth of residual stress layer. A two-dimensional edge crack (shape factor Y=1.1215) was assumed as the crack shape. The stress intensity factor K_{1R} due to residual surface stress is given by the following equation approximately.[15]

$$K_{1R} = (2/\pi) \cdot \sigma_{R0} \cdot \sqrt{\pi a} \cdot h\,(b/a) \quad \ldots\ldots\ldots (7)$$

(Model 1)

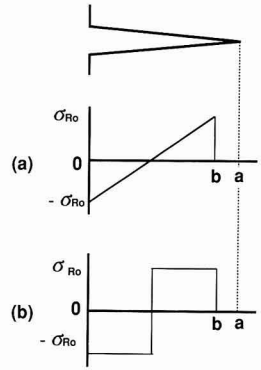

Fig. 9. Simplified residual distribution model (a) model 1 (b) model 2.

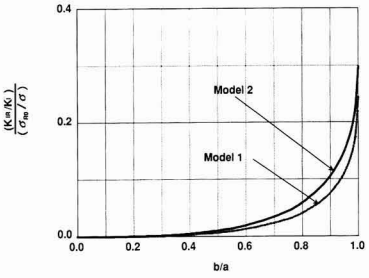

Fig. 10. Plot showing variation of $(K_{1R}/K_1)/\sigma_{R0}/\sigma)$ with (b/a). (depth of residual stress layer is deeper than crack depth).
K_{1R}: stress intensity factor by residual stress,
K_1: stress intensity factor by applied stress,
b: depth of residual stress layer,
a: crack size.

$$h\,(b/a) = 2\,(a/b)\,(1-\sqrt{1-(b/a)^2}) - \sin^{-1}(b/a)$$

(Model 2)

$$h(b/a) = 2(a/b)\,(\sin^{-1}(b/a) - 2\,\sin^{-1}\,(b/2a))$$

Taking the stress intensity factor due to tensile stress (applied stress) as K_1, the ratio of K_{1R} to K_1 is expressed as

$$K_{1R}/K_1 = (2/\pi \cdot Y) \cdot (\sigma_{R0}/\sigma) \cdot h(b/a) \quad \ldots\ldots (8)$$

The ratio of K_{1R}/K_1 becomes the maximum at b/a=1, the value being

$$K_{1R}/K_1 = 0.244 \cdot (\sigma_{R0}/\sigma) \quad \ldots\ldots\ldots\ldots (9)$$

$$K_{1R}/K_1 = 0.297 \cdot (\sigma_{R0}/\sigma) \quad \ldots\ldots\ldots\ldots (10)$$

It is found that the ratio of K_{1R}/K_1 is, even at the maximum, is merely about 25% of σ_{Ro}/σ for Model 1, and about 30% for Model 2. **Figure 10** shows the relationship between $(K_{1R}/K_1)/(\sigma_{Ro}/\sigma)$ and b/a for two models. The value of $(K_{1R}/K_1)/(\sigma_{Ro}/\sigma)$ increases suddenly as b/a approaches 1, and K_{1R} has little effect when b/a<0.9 for both models. The difference between two models that have widely differing stress distribution is small, and seems to have little effect when a>b, irrespective of the shape of residual surface stress distribution.

The case in which crack length a is shaller than residual stress layer b is considered. An analysis based on the above-described concept gives

$$K_{1R} = (2/\pi) \cdot \sigma_{R0} \cdot \sqrt{\pi\, a} \cdot h\,(b/a) \quad \ldots\ldots\ldots (11)$$

(Model 1)

$$h(b/a) = 2(a/b)$$

(Model 2)

$$h(b/a) = (\pi/2 - 2\sin^{-1}(b/2a))$$

Figure 11 shows the relationship between $(K_{1R}/K_1)/(\sigma_{Ro}/\sigma)$ and (b/a) for this case. In this figure, the value of $(K_{1R}/K_1)/(\sigma_{Ro}/\sigma)$ decreases with the increase in b/a. The increase in strength due to compressive residual stress can be expected in the region where K_{1R} value is negative, namely, where b/a=1.3 and higher for Model 1 and b/a=1.4 and higher for Model 2.

The experimental results are discussed below. Figure 8 indicates that the compressive residual stresses in the surface are gradually relieved by annealing for both ϕ=0° and ϕ=90°, and become nearly zero or are changed into a little tensile stress when the annealing temperature exceeds 1230°C. The bending strength of specimens ground in the direction of ϕ=90° increases gradually up to an annealing temperature of 1000°C, and suddenly jumps at 1230°C. This increase in strength is caused by the restoration of surface damage layer due to heat treatment; there may be little effect of residual stress. This is because the above discussion leads to the fact that the residual surface stress has little effect on the strength of material since the medican cracks are deeper than residual surface stress layer. When ϕ=0°, the crack caused by grinding has little effect on the strength of material. This suggests that the residual surface stress layer is deeper than the surface cracks. The crack depth calculated from the fracture toughness and strength is about 15-30μm. Assuming that the depth of residual stress layer is about 40μm, b/a is about 1.2-2.0. Also, assuming Model 1 as a residual stress distribution, K_{1R}/K_1 is -0.1(σ_{ro}/σ) to -0.3(σ_{ro}/σ). Where the residual stress is considered to be about -100MPa, an increase in strength of 2-10% due to compressive surface stress is expected. As seen from the data of ϕ=0°, the strength is almost unchanged up to an annealing temperature of 1000°C, and decreases slightly by about 4% at 1230°C and by about 8% at 1460°C. This is a tendency similar to the residual stress relieving behavior, and the strength has nearly the same value as that in the preceding discussion. One of the reason why the bending strength decreases even though annealing restores the surface damage layer may be the change of microstructure (such as the grains growth) due to annealing. However, microscopic observations did not reveal notable changes of microstructure, and the density was almost unchanged (as shown in Fig.5). For this reason,this decrease in strength is

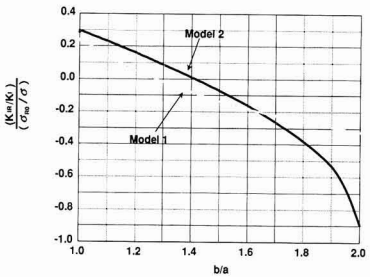

Fig. 11. Plot showing variation on $(K_{1R}/K_1)/(\sigma_{R0}/\sigma)$ with (b/a). (crack depth is deeper than that of residual stress layer).

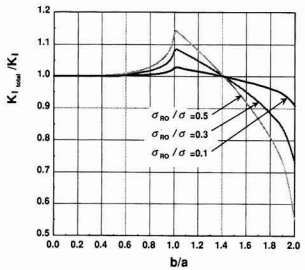

Fig. 12. Plot showing variation of (K_{total}/K_1) with (b/a) as a function of (σ_{R0}/σ_g). K_{total}: $K_{total}=K_{1R}+K_1$, b: depth of residual stress layer, and a: crack size

probably caused by the relief of compressive residual stress on the surface. **Figure 12** shows the relationship between b/a and σ_{Ro}/σ. The ordinates represent $(K_1+K_{1R})/K_1$, with the increase in this value, the strength decreases, and vice versa. This result suggests that the residual stress due to grinding has little effect on the strength unless the crack length is shorter than the compressive residual stress layer. From the above discussion, based on a simplified stress distribution model, it has been found that the residual stress due to grinding has little effect on the strength, though the stress distribution differs from the actual one; this fact agrees with the experimental result.

Although the compressive residual stresses due to grinding appears to be preferable for the above reasons, they are not necessarily so.

The results of this experiment are considered to be useful for industry. At present, finishing after rough machining is done with a grinding wheel of fine grains. For alumina, however, the surface damage layer and the strength can be restored to the initial condition by simply performing annealing treatment. In other words, the finishing of alumina to remove the surface damage layer can be replaced with annealing if there is not problem of surface roughness and accuracy.

5. Conclusions

The effect of annealing on the surface damage layer of alumina has been studied with the following conclusions.

1) The surface damage layers and strength of alumina whose strength had been decreased by scratch cracks were restored to the initial condition by annealing of alumina whose strength had been decreased by scratch cracks under adequate conditions.
2) The compressive residual stress caused by grinding influenced the micro-cracks perpendicular to the grinding direction and consequently caused a slight increase in strength. On the other hand it hardly influenced the deep scratch cracks parallel to the grinding direction.

Acknowledgments

This work was partially supported by a grant from the Industrial Technology Encouraging Council of Asahi Glass Co., Ltd. The support is gratefully acknowledged.

(Presented in The Ceramic Society of Japan 1987 Annual Meeting)

References:

1) H.P. Kirchner and E.D. Isaacson, J. Amer. Ceram. Soc., 65, 55-60 (1982)
2) M. Yoshikawa, H.Cho and K.Tokura, Yogyo-Kyokai-Shi, 95 (10), 961-69 (1987)
3) R.W. Rice, NBSspecial publication 562, 429-454 (1979)
4) R.E. Tressler, R.A. Langensiepen and R.C. Brakt, J. Amer. Ceram. Soc., 57, 226-227
5) D.C. Cranmer, R.E. Tressler and R.C. Bradt, ibid., 60, p230 (1977)
6) J.J. Mecholsky Jr., S.W. Freiman and R.W. Rice, J. Amer. Ceram. Soc., 60, 114-117 (1977)
7) C.A. Andersson and R.F. Bratton, NBS special publication 562, 463-476 (1979)
8) M.Ito, The Japan Institute of Precision Machinery/The Ceramic Society of Japan Symposium "Precision Machining of Fine Ceramics" text (1982), p.42.
9) K.Takase, H.Kako and K.Kawakami, Toyota Engineering, 35(1), 39-48 (1985)
10) Y.Matsuo, T.Ogasawara, S.Kimura and E.Yasuda, J. Soc. Mater. Sci. Japan, 36(401), 166-172 (1987)
11) D.Johnson-walls, A.G. Evans, D.B. Marshall and M.R. James, J. Amer. Ceram. Soc., 69, 44-48 (1986)
12) K.Tanaka, E.Matsui and Y.Akiba, Materials, 35, 749-754 (1986)
13) K.Tanaka, T.Kurimura, E.Matsui and Y.Akiba, J. Soc. Mater. Sci. Japan, 36, 817-822 (1987)
14) K.Suzuki, K.Tanaka, Y.Yamamoto and H.Nakagawa, J. Soc. Mater. Sci. Japan, 38, 582-588 (1989)
15) R.Samuel and S.Chandrasekar, J. Amer. Ceram. Soc., 72, 1960-1966 (1989)
16) K.Suzuki and K.Tanaka, 85th X-ray Material Strength Subcommittee Material (material No. X85-R3), (1988)
17) H.Kishimoto, A.Ueno, H.Kawasmoto and S.Kondo, Materials, 36, 810-816 (1987)
18) D.W. Richerson, "Modern Ceramic Engineering," 260-273 Marcel Dekker Inc., New York and Basel, (1982)

This article is a full translation of the article which appeared in Nippon Seramikkusu Kyokai Gakujutsu Ronbunshi (Japanese version), Vol.99, No.5, 1991.

Oxidation-Resistant Coating of TiC-SiC System on C/C Composite by Chemical Vapor Deposition

Chihiro Kawai and Tadashi Igarashi

Itami Research Laboratories, Sumitomo Electric Industries, Ltd.
1-1-1, Koya-Kita, Itami-shi, Hyogo 664, Japan

Oxidation resistance and oxidation mechanism of a carbon/carbon composite (C/C composite), on which inner layer of TiC and outer of SiC were coated by chemical vapor deposition, were investigated.
The CVD conditions used were, $TiCl_4$-CH_4-H_2 or $SiCl_4$-H_2 system, deposition temperature ranging from 1050° to 1350°C and total gas pressures ranging from 40 to 100 torr. TiC coating was 7 to 50μm thick and SiC coating was 70 to 270μm thick. The oxidation resistance of the coated C/C composite was estimated from room temperature to 1300°C in air using several heating programs.
In two layers-coating, the number of thermal cracks which generated on the surface of the coated layer decreased and the oxidation resistance improved depending on the thickness ratio of TiC to SiC coating as compared with SiC monolayer-coating. It is recognized that large compressive stresse generated in the outer layer of SiC and TiO_2 (rutile) formed along the thermal cracks in the coated layers after the oxidation.
[Received October 19, 1990; Accepted February 20, 1991]

Key-words: CVD, TiC, SiC, Oxidation, C/Ccomposite, Residual stress

1. Introduction

Carbon-fiber reinforced carbon composite (carbon/carbon composite or C/C composite) show high specific strength and high specific modulus at 1500°C or more,[1] and high fracture toughness. As such, they are attracting much attention as materials for thermal protection system and combusters for high-speed flying devices such as space planes. For the C/C composite to be used for the above purposes, it is necessary to provide them with high resistance to oxidation at high temperature in the presence of oxygen and ozone, in addition to the above mechanical properties.

Coating on the C/C composite with a SiC film by chemical vapor deposition (CVD), capable of producing deposites of thermally stable phase at high temperature, is the most common coating method to provide the composite with oxidation resistance. The CVD-coated SiC film, however, will have a number of thermal cracks, which cause the base material to be oxidized in an oxidative atmosphere at high temperature. This is attributable to a very low thermal expansion coefficient of the C/C composite ($1 \times 10^{-6}K^{-1}$ or less). In other words, the SiC film is exposed to an excessive tensile stress during the cooling process, due to the difference between the base and coating in thermal expansion coefficient. As a result, the C/C composite cannot be made sufficiently resistant to oxidation.

It is therefore essential, in order to produce a coating film free of thermal cracks, to reduce tensile stress which will be created within the film. One of the methods to attain this goal is coating with the graded C-SiC composition,[2] in which the coating composition is changed continuously from carbon at the coating-base interface (c-axis of carbon is oriented to the base) to SiC at the surfaces, in order to change thermal expansion coefficient of the coating, and thereby to reduce tensile generated at the surfaces.

In this study, an attempt was made to positively introduce compressive residual stress into the coating surfaces, in place of devising to reduce residual tensile stress. Concretely, two-layered coating of TiC and SiC was devised using TiC having a larger thermal expansion coefficient than SiC, to increase coating strength and thereby control propagation of the thermal cracks, and resistance of the coating to oxidation was investigated.

2. Experimental Procedure

2.1. CVD Conditions

The substrate was prepreg sheet of two-dimensionally woven PAN-base carbon fibers (Toreka T-300, plain fabrics of 1000 fibers), which were deposited with carbon particles by the electrophoresis method, laminated and then sintered under high pressure.[3] The C/C composite thus prepared was 25 × 12.5mm in area, 5mm thick in the lamination direction. The average thermal expansion coefficient in a temperature range from room temperature to 600°C was 0.10 to $0.15 \times 10^{-6}K^{-1}$ in the fiber direction, and 11 to $12 \times 10^{-6}K^{-1}$ in the lamination direction. The composite sheet was coated with TiC to a thickness of 7 to 50μm and then with SiC to a thickness of 70 to 270μm, where the former coating was deposited by CVD apparatus (equipped with carbon electrodes, externally heated) using a mixture of $TiCl_4$ or $SiCl_4$, CH_4 and H_2. The film thickness was estimated from the weight gain and density of the coating materials (TiC: 4.93g/cm^3, SiC: 3.21g/cm^3).[4] **Table 1** summarizes the CVD conditions.

Table 1. The CVD conditions.

Table 1. The CVD conditions.

coated materials	TiC	SiC
temperature/°C	1050	1350
total pressure/torr	60	40
gas flow rates		
$TiCl_4$/l·min^{-1}	0.34	0
$SiCl_4$/l·min^{-1}	0	0.76
CH_4/l·min^{-1}	0.25	0.40
H_2/l·min^{-1}	7.00	5.80

Table 2. The heat cycle patterns in the oxidative examination.

patterns No.	heating rate /K·min^{-1}	duration temp./°C	time/hr	cooling rate /K·min^{-1}	the number of heat cycles
1	8.5	1300	1	8.5	3
2	rapidly	1300	1	8.5	3
3	rapidly	700～1300	1～7	quench	1～5

2.2. Residual Stress in Coating Film

Residual stress (in the plane direction) in the coating film on the C/C composite was measured by the X-ray stress measurement method ($\sin^2\psi$-2θ method) with CuKα rays for the TiC-SiC film and the single-phase SiC film, for comparison. Residual stress σ is given by the following equation:[5]

$$\sigma = -\frac{E}{2(1+\nu)} \cdot \cot\theta \cdot \frac{\pi}{180} \cdot \frac{\partial(2\theta)}{\partial(\sin^2\psi)} \quad \ldots (1)$$

where, E is Young's modulus (E_{sic}: 320GPa) and υ is Poisson ratio (υ_{sic}: 0.24).[6]

2.3. Oxidation Resistance

The sample was heated in air by a siliconite furnace either at a constant or cyclic temperatures in a range from 700 to 1300°C, and the change in weight was measured to estimate its oxidation resistance. It was supported at three points by a SiC jig, to secure that the entire surfaces of the sample made contact with the atmosphere gas. Table 1 presents the heating patterns. Temperature for the oxidation tests was limited to 1300°C, because the operating temperature of the thermal protection system made using C/C composite insulators for HOPE's is 1300°C or less,[7] and the CVD-prepared SiC film was sufficiently oxidation-resistant to have a weight change of 0.1mg/cm^{2}h at 1300°C or less that the weight gain by the oxidation treatment could be regraded as that of the substrate.

The sample before and after the oxidation test was analyzed by a powder X-ray diffractometer (XRD) and X-ray microanalyzer (EPMA) to identify the product phases, by a scanning electron microscope (SEM) to observe the surface and fracture face of the coating film, and by an optical microscope of the sample's cross-section ground with diamond paste.

3. Results and Discussion

3.1. Structure of Coating Films

Figure 1 presents the SEM photograph of the fracture surface of the two-layered film consisting of the 13μm-thick TiC and 90μm-thick SiC films. Both TiC and SiC films were highly densified, and no exfoliation was detected between the films or between the substrate and the film. **Figure 2** presents the optical micrographs of the cross-sections of the C/C composite samples, coated with the 150μm-thick single-phase SiC film and 243μm-thick two-layered film (TiC film: 13μm, SiC film: 230μm). Thermal cracks were found in both types of films. Anisotropy of the C/C composite in the thermal expansion coefficient caused anisotropy in propagation of the thermal cracks, two-dimensional in the plane, and in parallel to the lamination direction only through the thickness. Most of the thermal cracks formed at the interfaces between the C/C composite substrate and the single-phase SiC film reached the coating film surfaces, whereas many thermal cracks ceased to propagate in the vicinity of the surfaces of the two-layered film. Propagation of the thermal cracks also depended on relative TiC/SiC thickness ratio, more noted in the film of higher thickness ratio. The SEM photographs of the coating film surfaces indicated that the two-layered film was smaller in thermal crack width and its number than the single-phase film, as shown in **Fig.3**, from which it was judged that the two-layered structure prevented the cracks from propagating to the film surfaces. It was found, however, that the coating films were peeled from each other, after the SiC coating was completed, when the film thickness ratio was 0.5. **Figure 4** shows the outer appearance of the exfoliated films; these films were separated, and rolled up.

3.2. Oxidation Resistance

Figure 5 shows the weight losses of the C/C composites coated with the single-phase SiC film or two-layered film

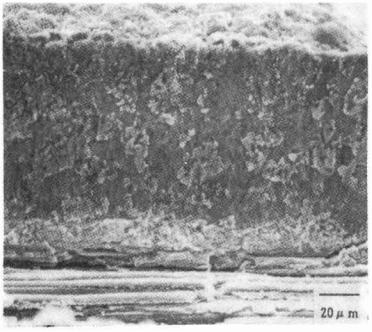

Fig. 1. The fracture surface of TiC-SiC two layers on C/C composite.

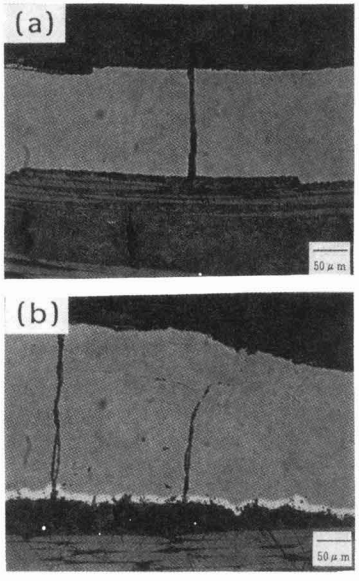

Fig. 2. The surface of the coated layers on C/C composite. (a) SiC monolayer and (b) TiC-SiC two layers.(SEM photograph).

at a constant or cyclic temperature during the oxidation treatment process. The composite coated with the single-phase film lost significant weight, irrespective of the heating patterns, and the SiC film was totally exfoliated from the substrate, resulting from oxidation loss of the C/C composite at the interfaces between the C/C composite substrate and the coating film with oxygen flowing through the thermal cracks in the film.

The two-layered coating films also lost their weights on the heating patterns 1 and 2. Extent of the weight loss depended on the TiC/SiC film thickness ratio, decreasing as the ratio increased. By contrast, essentially no weight loss was observed with the sample exposed to the heating pattern 3, where rapid heating/quenching cycles were repeated between room temperature and 1300°C, while the sample was kept at a constant temperature which would cause no oxidation, except at 1300°C. **Figure 6** shows the effects of oxidation temperature on weight change of the samples, where the C/C composite samples coated with the 15 to 17μm-thick TiC film and 250 to 260μm-thick SiC film (TiC/SiC film thickness ratio = 0.06) were heated at a constant temperature ranging from 700° to 1300°C. A weight loss was observed at 700° to 900°C, while a small weight gain was observed at 1000° to 1100°C. By contrast, no weight change was observed at 1200° to 1300°C.

It is therefore considered, based on the above results, that the sample exposed to thermal cycles loses no weight when held at 1200° to 1300°C, but loses weight during the heating or cooling period at between 400° and 1000°C, where oxidation of the C/C composite is believed to start around 400°C in air.

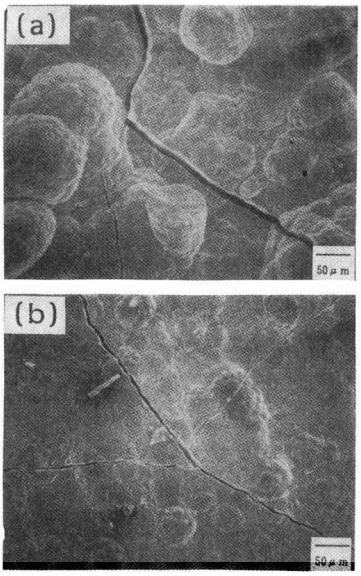

Fig. 3. The cross-sectional surfaces of the coated layers on C/C composite. (a) SiC monolayer and (b) TiC-SiC two layers.

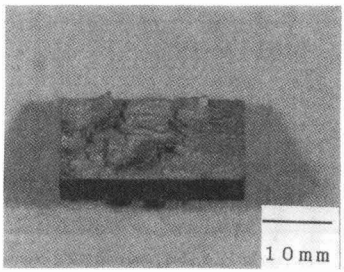

Fig. 4. The coated C/C composite with the deposition thickness ratio (TiC/SiC) of 0.5 .

3.3. Oxidation-Resistance Mechanisms of C/C Composite Coated with Two-Layer Film

(1) Increased strength of the SiC film, as a result of introduction of compressive residual stress

Figure 7 shows residual stress in the surface of the SiC film for the C/C composites coated with the single SiC film or two-layered film.

Essentially no residual stress was found in the single-phase coating film, resulting from the tensile residual stress generated during the cooling process after the film was coated, which cracked the film to release the stress. On the other hand, a compressive stress of 0.5 to 1.0GPa was found

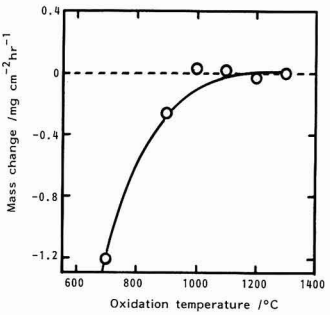

Fig. 6. Oxidation resistances of the coated C/C composites under constant temperatures.

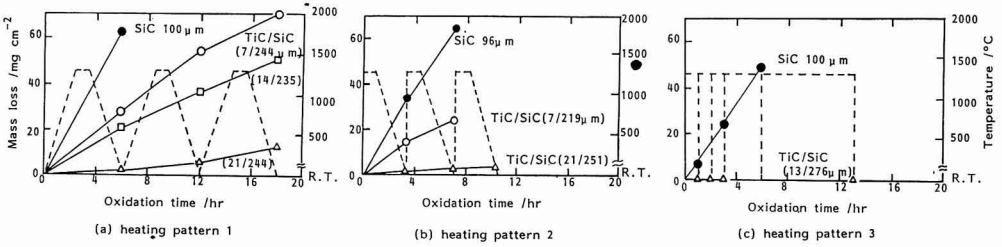

Fig. 5. Oxidation resistances of the coated C/C composites under several heat cycles.

in the SiC portion of the two-layered film, believed to be formed during the cooling process, due to difference in the thermal expansion coefficient of TiC and SiC. As shown in Fig.2, two-layered film had a smaller number of thermal cracks, some of which did not reach the coating surfaces, than the single-phase film, because of the compressive residual stress that worked to increase strength of the outer film of SiC. No definite dependence of the residual stress level on the TiC/SiC film thickness ratio is shown in Fig.7. However, the SiC film was exfoliated from the interfaces between the TiC and SiC films at a thickness ratio of 0.5, showing that these films were mutually intrusive (Fig.4), conceivably resulting from an excessive compressive stress in the surface film of SiC.

(2) Self-restoring ability

Figure 8 presents the photographs, taken by a stereomicroscope, of the two-layered coating film (TiC: 15 to 17μm-thick, SiC: 250 to 260μm), oxidation-tested at constant temperature in a range from 700° to 1300°C. No significant change was observed before and after the oxidation tests conducted at 700° to 900°C and 1200° to 1300°C. The sample tested at 1000° to 1100°C, on the other hand, had yellowish brown deposits along the thermal cracks running on the coating surfaces. **Figure 9** presents the SEM images of these deposits, which were present in such a way to fill the cracks. **Figure 10** presents the X-ray diffraction patterns of the oxidation-tested coating film surface. TiO_2 (rutile) was identified, in addition to SiO_2 believed to be the product of oxidation of SiC. Furthermore, the EPMA analysis detected no Si or C in the deposits filling the thermal cracks, but detected Ti, from which it was judged that the deposits were of TiO_2. This would be the product of the reactions between TiC and oxygen reaching the inner film through the thermal cracks during the oxidation test.

It was, therefore, considered that the weight loss observed during the treatment at 700 to 900°C resulted from the oxidation of the C/C composite with oxygen flowing to the substrate through the thermal cracks, and a small quantity of the weight gain during the treatment at 900° to 1100°C from the oxidation of part of TiC into TiO_2. In this temperature range, it was presumed that wasting by oxidation did not occur at the C/C composite substrate. This was caused by TiO_2 which filled the thermal cracks to prevent oxygen flow, the phenomenon referred to as self-restoration. Oxidation-resistance of the sample tended to increase as thickness of the TiC film increased for almost the same SiC film thickness, as shown in Fig.5, because of the increased quantity of TiO_2 formed during the oxidation test to fill the thermal cracks more.

Filling of the thermal cracks with TiO_2 was not observed in the samples treated at 700° to 900°C, because rate of TiO_2 formation was sufficiently lower at 900°C or below than at 1000°C or above. The same trends were noted in the samples treated at 1200°C to 1300°C, because of closing of the thermal cracks at these temperature levels.

It is, therefore, concluded that improved oxidation-resistance of the C/C composite substrate coated with the two-layered TiC/SiC film results from introduction of compressive residual stress to prevent propagation of the thermal cracks, and from the self-restoration by oxidation of TiC in the inner film. These effects will increase as

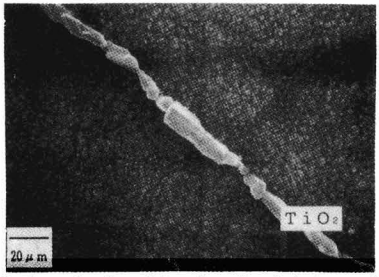

Fig. 9. The product formed along thermal cracks in the coated layer after the oxidative examination at 1100°C for 1hr.

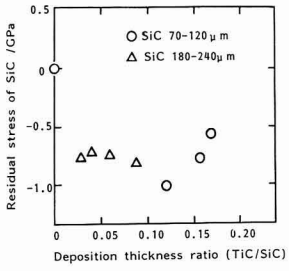

Fig. 7. Residual stress of the surface layer SiC in the coated C/C composites.

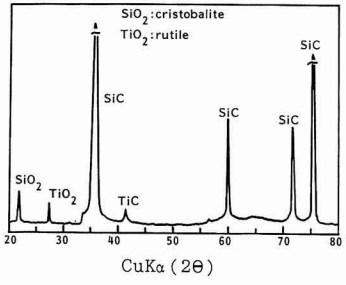

Fig. 10. X-ray diffraction pattern of the surface of the coated layer with the product in thermal cracks.

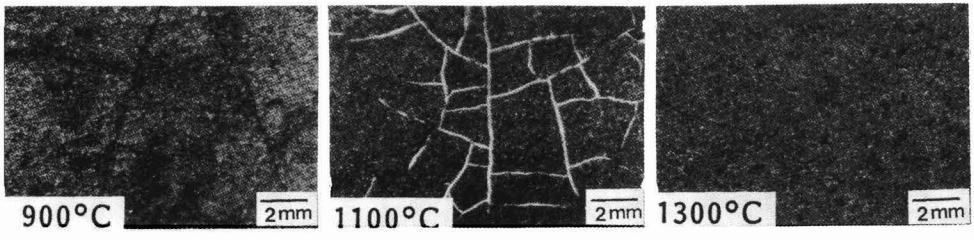

Fig. 8. The surface layers of the coated C/C composites after the oxidative examinations at 700° to 1300°C for 1hr.

thickness of the TiC film increased at the same coating film thickness.

4. Conclusions

The carbon fiver reinforced composite (C/C composite) was coated with a two-layered film (TiC and SiC films) by CVD to improve resistance to oxidation.

1) The two-layered TiC/SiC coating greatly improved the oxidation-resistance of the C/C composite at up to 1300°C in air. The effects depended on the TiC/SiC film thickness ratio, increasing as the ratio increased.
2) The two-layered coating film had a smaller number of thermal cracks than the single-phase SiC film. A compressive residual stress was found in the surface SiC films.
3) It was observed that the thermal cracks in the oxidation-treated two-layered film were filled with TiO_2, found to be formed at 1000° to 1100°C.
4) Improved oxidation-resistance of the C/C composite coated with the two-layered film resulted from a reduced number of thermal cracks and from filling of the cracks with TiO_2 to prevent oxygen from flowing to the C/C composite (self-restoration effect) at 1100°C or less, and from closing of the thermal cracks at 1200° to 1300°C.

Acknowledgements
A part of this study was performed through Special Coordination Funds of the Science and Technology Agency of Japanese Government.
(Presented to the Ceramic Society of Japan 1989 Annual Meeting (May) and Fall Symposium (October).)

References:

1) Allen J. Klein, "Carbon/;Carbon: An ultra high temperature composite" Advanced Composite, March/April (1989), 38-44.
2) C. Kawai and R. Igarashi, Third Symposium for Inclined Functional Materials Proceedings, 79-83 (1989)
3) S. Sakagami, K. Iwata, M. Kawase and S. Wakamatsu, "Carbon/Carbon Composite by Carbon Powder Sintering Method", proceedings of the First Japan International SAMPE Symposium and Exhibition, (1989) p.1166-1170.
4) G. V. Samsonov, High-Temperature Materials No.2 Properties Index, Plenum Press, New York (1964) pp.65-72.
5) "X-Ray Measurement of Stresses," edited by the Materials Society of Japan, Yoken-do, (1981) pp.54-67.
6) T. Hirai and M. Sasaki, "Silicon Carbide Ceramics," Uchida Rokaku-ho, (1988) p.56.
7) H. Yamao, HOPE Workshop Proceedings, (1989).

This article is a full translation of the article which appeared in Nippon Seramikkusu Kyokai Gakujutsu Ronbunshi (Japanese version), Vol.99, No.5, 1991.

Effect of Composition on Phase Stability under Hydrothermal Conditions and Fracture Strength of Yttria- and Ceria-Doped Tetragonal Zirconia-Alumina Composites Fabricated by HIP

Masanori Hirano, Tatsuo Matsuyama, Hiroshi Inada, Kazutaka Suzuki, Haruo Yoshida and Michihide Machida

Noritake Co., Limited, Noritake, Nishi-ku, Nagoya-shi, 451 Japan
Government Industrial Research Institute, Nagoya, 1-1, Hirate-cho, Kita-ku, Nagoya-shi, 462 Japan

The effect of alumina content and composition of tetragonal zirconia (TZP) on the fracture strength and hydrothermal stability of (Y, Ce)-TZP/Al_2O_3 composites treated by HIP at 1400° to 1600°C under 147MPa for 0.5h in Ar were studied. (Y, Ce)-TZP/Al_2O_3 composites treated by HIP at 1400°C exhibited the maximum density and maximum bending strength. The mean values of bending strength of HIPped (Y, Ce)-TZP/Al_2O_3 composites were 1800MPa for (4Y, 4Ce)-TZP/25wt%Al_2O_3 composites, 1700MPa for (2.5Y, 4Ce)-TZP/25wt%Al_2O_3 composites, and 1600MPa for (2.5Y, 5.5Ce)-TZP/25wt%Al_2O_3 composites. The phase stability of HIP treated (Y, Ce)-TZP/Al_2O_3 composites under hydrothermal conditions at 180°C and 1MPa increased with increasing alumina content. Dispersion of Al_2O_3 into (Y, Ce)-TZP was useful to enhance the bending strength, to suppress the tetragonal to monoclinic phase transformation and grain growth of zirconia and to improve the resistance to low-temperature degradation.
[Received November 15, 1990; Accepted January 24, 1991]

Key-words: (Y, Ce)-TZP/Al_2O_3 composites, Hot isostatic pressing, Bending strength, Hydrothermal aging, Phase transformation

1. Introduction

Partially stabilized zirconia has been used as a structural material because of its excellent mechanical properties. In particular, the Y_2O_3-ZrO_2 system is sintered into the tetragonal structure (Y-TZP) to exhibit a high mechanical strength.[1-3] However, it is known that Y-TZP ages and degrades at a low temperature region (200° to 400°C), notably in the presence of steam,[3-6] resulting from the gradual phase transformation of the tetragonal system, present as the metastable phase at room temperature, into the stable monoclinic phase. A number of researchers are discussing methods to improve phase stability of Y-TZP at low temperature.[7-9] Tsukuma et al. discuss that (Ce-TZP) containing CeO_2 as the stabilizing agent is stabler than Y-TZP.[10] It should be noted, however, that Ce-TZP, though sufficiently stable, is much lower in mechanical strength than Y-TZP. Zirconia ceramics are found to have improved strength when treated by hot isostatic pressing (HIP),[11,12] particularly the Y-TZP/Al_2O_3 composites whose strength can be increased to 2000MPa or more.[13,14] Sato et al. attempted to increase strength of the Ce-TZP compositions (mainly 12Ce-TZP) by HIP treatment and found that the composite of 12Ce-TZP containing 20wt% of Al_2O_3 has a strength of 620 to 760MPa.[15] The pressurelessly sintered 12Ce-TZP compositions, with Y_2O_3 or Al_2O_3 (ZY, 12(e)-TZP or(2Y, 12(e)-TZP/Al_2O_3) added are found to have a lower strength than the 12Ce-TZP sinter.[16] Thus, no Ce-TZP composition such as 12Ce-TZP with a strength of 1000MPa or more has been developed so far, unlike the Y-TZP composition. The (Y, Ce)-TZP composition containing Y_2O_3 and CeO_2 as the stabilizing agents is lower in strength, though higher in stability than the Y-TZP composition.[17,18] For the HIP-treated (Y, Ce)-TZP compositions, the (4Y, 4Ce)-TZP has a strength around 1100MPa.[18] Furthermore, the authors have HIP-treated the preliminarily sintered (Y, Ce)-TZP/Al_2O_3 composites to investigate the effects of HIP conditions on the sinter properties.[19]

In this study, we investigated the effects of alumina content and zirconia composition on mechanical strength and phase-stability of the HIP-treated (Y, Ce)-TZP/Al_2O_3 composites under hydrothermal conditions.

2. Experimental Procedure

2.1. Specimen Preparation

The zirconia powder was prepared by the hydrolysis of zirconium oxychloride ($ZrOCl_2O$-$8H_2O$), where an aqueous solution of the zirconium compound was heated at the boiling point for 48h in the presence of ammonia water (28wt%) and H_2O_2 water (30wt%). The detailed procedure is described elsewhere.[18] Various compositions of the zirconia powder thus prepared, containing Y_2O_3 and/or CeO_2 as the stabilizing agents, were mixed with α-alumina (99.99% pure, Taimei Kagaku's TM-D) in various ratios in the presence of a solvent.

Table 1 summarizes compositions and specific surface areas of zirconia powders, and **Table 2** alumina content of the composites. The powder was formed preliminarily under a pressure of 19.6MPa, pressed under an isostatic pressure of 196MPa, and then preliminarily sintered at 1350° to 1600°C for 2h in air.

2.2. HIP Treatment

The above sinter was treated in a graphite crucible with a small-size laboratory HIP apparatus equipped with a

graphite heater unit. High-purity Ar gas was used as the pressure medium. The HIP treatment was carried out for 30 min. at three temperature levels: 1400°, 1500° or 1600°C, where each sample was heated at 30°C/min to 1200°C and then at 10°C/min to a given temperature (1400°, 1500° or 1600°C). It was thus held for 30min. under a pressure of 147MPa, and then allowed to cool in the apparatus.

2.3. Analytical Procedure

Density was determined by the Archimedean method, and mechanical strength by the 3-point bending test (JIS R1601) conducted under the conditions of 30mm span and a cross-head speed of 0.5mm/min. The specimen for the bending test was 3×4×40mm in size, polished by a #140 diamond wheel. A total of 5 or more specimens were tested for each composition. The fracture face and the microstructures on the surface were observed by a scanning electron microscope (SEM, Hitachi S450). For phase stability, each specimen polished by a #140 diamond wheel was treated under cycles of the hydrothermal conditions of 180°C and 1MPa, while placed in an autoclave, for 5h for each cycle. The treated specimen was analyzed by X-ray diffractometry using the method proposed by Garvie et al.[20] to identify the surface phases and to quantitatively analyze the monoclinic phase. The treatment time is the total time for which the specimen was exposed to the hydrothermal conditions of 180°C and 1MPa.

3. Results and Discussion

3.1. Composition and Density

Figure 1 shows the effects of HIP temperature on density of the three types of (Y, Ce)-TZP/Al_2O_3 composites containing 25wt% of Al_2O_3 preliminarily sintered at 1400°C. Each composition had a high density when HIP-treated at 1400°C. Of the compositions HIP-treated at 1500°C, the (4Y, 4Ce)-TZP/Al_2O_3 composition had the same density as that treated at 1400°C; however, the (2.5Y, 4Ce)-TZP/Al_2O_3 and (2.5Y, 5.5Ce)-TZP/Al_2O_3 compositions had a slightly lower density than those treated at 1400°C. Increasing HIP temperature to 1600°C greatly decreased the density of each sample. The (4Y, 4Ce)-TZP/Al_2O_3 was less sensitive in density to HIP temperature than the other compositions. The (2.5Y, 5.5Ce)-TZP/Al_2O_3, containing a larger quantity of CeO_2, decreased in density more rapidly as HIP temperature increased, to a level lower than that of the untreated one above 1500°C. Thus, density of the sample HIP-treated at high temperature increasingly depended on zirconia content.

Figure 2 shows the effects of alumina content on density of the (4Y, 4Ce)-TZP/Al_2O_3 compositions HIP-treated at different temperature levels. The composition containing 40wt% of alumina was preliminarily sintered at 1500°C and the others at 1400°C. Relative density of each composite was calculated based on its composition using the intrinsic density levels of 6.12g/cm^3 for the (4Y, 4Ce)-TZP and 3.98g/cm^3 for alumina, the former determined from the lattice constants.[21,22] The compositions HIP-treated at 1400°C were highly densified to 99.7% or more in all alumina contents used (5wt% to 40wt%). Those HIP-treated at 1500°C were also highly densified to the same extent as above, except that containing the smallest quantity (5wt%) of alumina, whose density was slightly lower at 99.5%. Those compositions HIP-treated at 1600°C, on the other hand, had

Table 1. Composition and specific surface area of zirconia powders.

Specimen	Composition (mol%)	Specific surface area of powder (m^2/g)
Y	$3Y_2O_3$ 97ZrO_2	18
XC	$4YO_{1.5}$ 4CeO_2 92ZrO_2	21
IC	$4YO_{1.5}$ 4CeO_2 92ZrO_2	27
IIC	$2.5YO_{1.5}$ 4CeO_2 93.5ZrO_2	25
IIIC	$2.5YO_{1.5}$ 5.5CeO_2 92ZrO_2	26

Table 2. Compositions of specimens.

Material	Specimen	Composition: Co-precipitated zirconia Composition(mol%)	Co-precipitated zirconia (wt%)	Al_2O_3 (wt%)
Y-TZP	Y0	$3Y_2O_3$ 97ZrO_2	100	0
(Y,Ce)-TZP	XC0	$4YO_{1.5}$ 4CeO_2 92ZrO_2	100	0
	Y5	$3Y_2O_3$ 97ZrO_2	95	5
Y-TZP/	Y12.5	$3Y_2O_3$ 97ZrO_2	87.5	12.5
Al_2O_3	Y25	$3Y_2O_3$ 97ZrO_2	75	25
	Y40	$3Y_2O_3$ 97ZrO_2	60	40
	XC5	$4YO_{1.5}$ 4CeO_2 92ZrO_2	95	5
	XC12.5	$4YO_{1.5}$ 4CeO_2 92ZrO_2	87.5	12.5
(Y,Ce)-TZP	XC25	$4YO_{1.5}$ 4CeO_2 92ZrO_2	75	25
/Al_2O_3	XC40	$4YO_{1.5}$ 4CeO_2 92ZrO_2	60	40
	IC25	$4YO_{1.5}$ 4CeO_2 92ZrO_2	75	25
	IIC25	$2.5YO_{1.5}$ 4CeO_2 93.5ZrO_2	75	25
	IIIC25	$2.5YO_{1.5}$ 5.5CeO_2 92ZrO_2	75	25

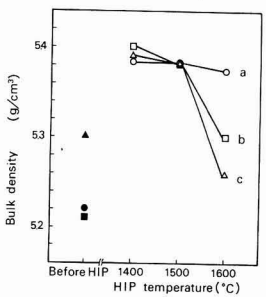

Fig. 1. Bulk density of (a) (4Y, 4Ce)-TZP/Al_2O_3 composites (IC25 specimen), (b) (2.5Y, 4Ce)-TZP/Al_2O_3 composites (IIC25 specimen), and (c) (2.5Y, 5.5Ce)-TZP/Al_2O_3 composites (IIIC25 specimen) presinterd at 1400°C for 2h, then HIPped at various temperatures for 0.5h.

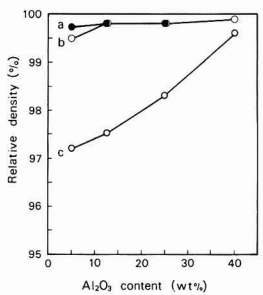

Fig. 2. Relation between alumina content and relative density of (4Y, 4Ce)-TZP/Al_2O_3 composites (XC specimen) HIPped at (a) 1400°C, (b)1500°C, and (c) 1600°c for 0.5h.

Table 3. Amount of monoclinic ZrO_2 phase on the surface for the specimens HIP treated at 1400° to 1600°C.

Specimen	Monoclinic ZrO_2 (%)		
	1400°CHIP	1500°CHIP	1600°CHIP
Y25	0	0	0
XC5	0	11	30
XC12.5	0	5	27
XC25	0	0	22
XC40	0	0	15

a much lower density than those treated at 1400° and 1500°C; density of the composition, HIP-treated at 1600°C, containing 5wt% of alumina was around 97%, whereas that of the one containing 40wt% of alumina was 99.5%. Thus, density of the composites HIP-treated at 1600°C greatly depended on alumina content; it was lower than the density of those HIP-treated at 1400°C, more notably as alumina content decreased. The X-ray diffraction analysis detected the monoclinic zirconia phase in all of the compositions HIP-treated at 1600°C. **Table 3** presents the quantity of monoclinic zirconia phase on the HIP-treated surfaces. No monoclinic phase was detected in the specimen HIP-treated at 1400°C, but it was detected in those containing small quantities of alumina HIP-treated at 1500°C. For those HIP-treated at 1600°C, the monoclinic quantity increased as alumina content decreased. It was noted, however, that no monoclinic phase was detected in the Y-TZP/Al_2O_3 even HIP-treated at 1600°C.

It was considered that the reduced density as a result of increased HIP temperature was mainly caused by the reduction of CeO_2 as the stabilizing agent into Ce_2O_3, because of CO formation derived from the carbon crucible and heater elements, with the result that the tetragonal to monoclinic phase transformation was accelerated. The results shown in Fig.2 indicated that addition of alumina worked to prevent reduction of CeO_2 as the stabilizing agent and decrease in density of zirconia, which would be caused by the tetragonal to monoclinic phase transformation. The controlled phase transformation was considered to result from the increased modulus of elasticity of the HIP treated body by the presence of alumina causing increased strain energy in the changed free energy associated with the phase transformation.

3.2. Composition, Mechanical Strength and Microstructures

3.2.1. Effects of Alumina Content

Figure 3 shows the effects of alumina content on bending strength of the HIP-treated (4Y, 4Ce)-TZP/Al_2O_3 compositions (XC specimens). Bending strength of the alumina-free (4Y, 4Ce)-TZP Hip treated at 1400°C was approximately 950MPa. The addition of 5wt% of alumina to the above composition increased bending strength by more than 25% to approximately 1200MPa. Bending strength of the HIP-treated compositions tended to increase as alumina content increased in a range used in this study (5 to 40 wt%), as shown in Fig.3.

Figure 4 shows the mirostructures of the (4Y, 4Ce)-TZP/Al_2O_3 compositions containing 12.5 and 25wt% of alumina, preliminarily sintered at 1400°C and then HIP-treated at 1400°C, where white portions representing the zirconia grains and dark portions alumina. The HIP-treated sample containing 25wt% of alumina consisted of smaller zirconia grains than the one containing 12.5wt% of alumina; the average grain sizes of the alumina-free composition and those containing 12.5 and 25wt% of alumina were 0.4, 0.35 and 0.3μm, respectively. Thus, increasing alumina content decreased size of the zirconia grains in the HIP-treated composition, indicating that alumina added to the (Y, Ce)-TZP composition worked to control growth of the zirconia grains. It is considered, based on the results of mechanical strength and microstructure, that the increased mechanical strength of the alumina-containing HIP-treated composite comes from the several favorable effects, such as (1) HIP treatment densifies the sample at a lower temperature, to remove the defects and increase relative density, (2) dispersed alumina works to control growth of the zirconia grains, and thereby to increase critical stress at which the tetragonal to monoclinic phase transformation occurs,[23] and (3) combination with alumina increases Young's modulus of the composite.

3.2.2. Effects of Stabilizing Agent Composition

Figure 5 shows the effects of HIP temperature on bending strength of the three types of (Y, Ce)-TZP/Al_2O_3 composites containing 25wt% of alumina and stabilizing agents of different compositions, preliminarily sintered at 1400°C. Bending strength of those HIP-treated at 1400°C was affected by the stabilizing agent composition to only a small extent; each sample showed the highest strength of 1900MPa. The (4Y, 4Ce)-TZP/Al_2O_3 composite fluctuated less in bending strength to have an average level of 1800MPa. The (2.5Y, 4Ce)-TZP/Al_2O_3 and (2.5Y, 5.5Ce)-

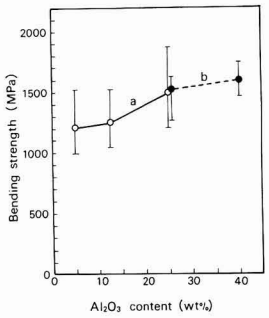

Fig. 3. Relation between alumina content and bending strength of (4Y, 4Ce)-TZP/Al_2O_3 composites(XC specimen): (a) presintered at 1400°C, then HIP treated at 1400°C; (b) presintered at 1500°C, than HIP treated at 1500°C.

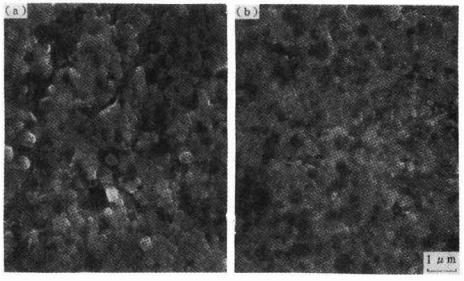

Fig. 4. SEM photographs of the polished and thermally etched surface of (a) (4Y, 4Ce)-TZP/12.5wt%Al_2O_3 composites and (b) (4Y, 4Ce)-TZP/25wt%Al_2O_3 composites HIP treated at 1400°C.

TZP/Al_2O_3 composites fluctuated more in bending strength, and their average levels were 1700 and 1600MPa, respectively. It was observed with all the samples that bending strength decreased greatly as HIP temperature increased. Those samples HIP-treated at 1500° and 1600°C had a bending strength of 1200 to 1300MPa and 700MPa or less, respectively. Decreased bending strength was more noted with the (2.5Y, 5.5Ce)-TZP/Al_2O_3 composition.

Figure 6 shows the microstructure on the fracture faces of the (2.5Y, 4Ce)-TZP and (2.5Y, 5.5Ce)-TZP composites HIP-treated at 1400° and 1600°C. Both compositions contained 25wt% of alumina. Those HIP-treated at 1400°C were highly densified to have uniform microstructures almost free of pores. Those treated at 1600°C, on the other hand, consisted of notably grown grains. The reduced bending strength of the sample treated at 1600°C, shown in Fig.5, corresponded well to the coarser microstructres shown in Fig.6, and to the reduced density shown in Fig.2, and was considered to result from growth of the zirconia grains and from the tetragonal to monoclinic phase transformation accompanying formation of the microcracks.

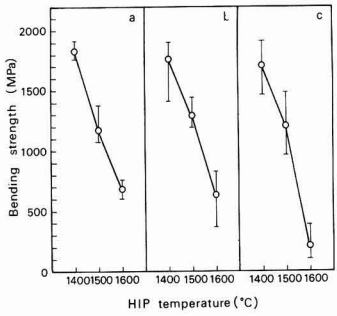

Fig. 5. Bending strength of (a) (4Y, 4Ce)-$TZP/25wt\%Al_2O_3$ composites (IC25 specimen), (b) (2.5Y, 4Ce)-$TZP/25wt\%Al_2O_3$ composites (IIC25 specimen), and (c) (2.5Y, 5.5Ce)-$TZP/25wt\%Al_2O_3$ composites (IIIC25 specimen) presintered at 1400°C for 2h, then HIP treated at various temperatures for 0.5h.

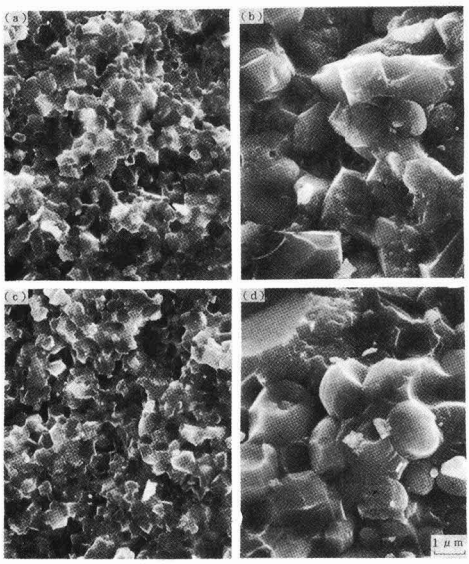

Fig. 6. SEM photographs of fracture surface of (2.5Y, 4Ce)-$TZP/25wt\%Al_2O_3$ composites HIP treated at (a) 1400°C and (b) 1600°C and (2.5Y, 5.5Ce)-$TZP/25wt\%$ Al_2O_3 composites HIP treated at (C)1400°C and (d) 1600°C.

3.3. Composition and Stability under Hydrothermal Conditions

Figure 7 shows the results of phase stability of the samples under the hydrothermal conditions of 180°C and 1MPa in an autoclave. The (Y, Ce)-TZP/Al_2O_3 compositions, preliminarily sintered at 1400°C and HIP-sintered at 1400°C, were stabler under the hydrothermal conditions, because of the controlled increase in quantity of the monoclinic phase, than the 3Y-TZP composition pressurelessly sintered at 1500°C. There was no significant difference between the HIP-treated samples containing 5wt% and 25wt% of alumina in monoclinic phase quantity, and their monoclinic phase content was not changed for hydrothermal treating time from 5 to 20h. These results indicated that the tetragonal to monoclinic phase transformation did not occur significantly in the (Y, Ce)-TZP/Al_2O_3 composition, HIP-treated at 1400°C, when it was exposed to the hydrothermal conditions in an autoclave, and that it was highly resistant to the low-temperature degradation.

Figure 8 shows the effects of alumina content on phase stability under the hydrothermal conditions of the 3Y-TZP/Al_2O_3 and (4Y, 4Ce)-TZP/Al_2O_3 compositions, preliminarily sintered at 1400°C and then HIP-treated at 1400°C. These samples were compared with each other in monoclinic ZrO_2 content, after they were treated under the hydrothermal conditions in an autoclave for 20h. The tetragonal to monoclinic phase transformation of the 3Y-TZP/Al_2O_3 and (4Y, 4Ce)-TZP/Al_2O_3 compositions was

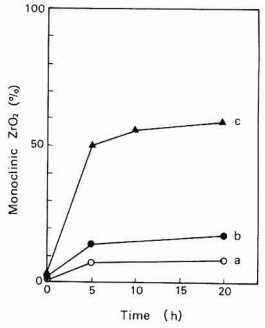

Fig. 7. Results of hydrothermal aging at 180°C and 1MPa for (a) (4Y, 4Ce)-$TZP/25wt\%Al_2O_3$ composites and (b) (4Y, 4Ce)-$TZP/5wt\%Al_2O_3$ composites fabricated by HIP treated at 1400°C and (c) 3Y-TZP fabricated by normal sintering at 1500°C.

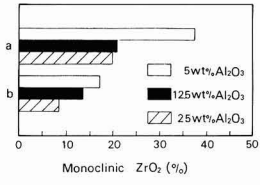

Fig. 8. Tetragonal-to-monoclinic phase transformation resulting from hydrothermal aging at 180°C and 1MPa for 20h (a) 3Y-TZP/Al_2O_3 composites and (b) (4Y, 4Ce)-TZP/Al_2O_3 composites HIP treated at 1400°C.

controlled as alumina content increased. In other words, increasing alumina content from 5wt% to 25wt% halved the monoclinic zirconia content, and thereby improved phase stability of the composite under the hydrothermal conditions.

Figure 9 shows the effects of stabilizing agent composition on phase stability of the (Y, Ce)-TZP/Al_2O_3 composite under the hydrothermal conditions. Of the three compositions tested, the (4Y, 4Ce)-TZP/Al_2O_3 had the smallest quantity of the monoclinic phase, though there was no significant difference among them. **Figure 10** shows bending strength of the composites before and after treatment under the hydrothermal conditions. Those composites pressurelessly sintered at 1500°C (3Y-TZP and (4Y, 4Ce)-TZP) lost their bending strength significantly by the hydrothermal treatment. By contrast, the (Y, Ce)-TZP/Al_2O_3 containing 25wt% of alumina, preliminarily sintered at 1400°C and HIP-treated at 1400°C, remained essentially unchanged in bending strength before and after the treatment.

It has been thus confirmed that the (Y, Ce)-TZP/Al_2O_3 composition, HIP-treated at 1400°C, is highly phase-stable such that only a very little quantity of monoclinic zirconia is transformed from the tetragonal phase, after it is exposed to the hydrothermal conditions. This conceivably results from (1) HIP treatment sufficiently densifying the sample at low temperature to almost the theoretical level, and the sinter produced consists of fine zirconia grains, (2) addition of alumina to the (Y, Ce)-TZP composition, whose tetragonal zirconia is stabler than that of the Y-TZP composition,[18] controls growth of the grains, to further stabilize the tetragonal zirconia phase, and (3) addition of alumina increases Young's modulus of the composite and changes in strain energy as part of the changes in free energy associated with the phase transformation, thereby controlling the tetragonal to monoclinic transformation.

4. Conclusions

The (Y, Ce)-TZP/Al_2O_3 composite was prepared by HIP treatment to investigate the effects of alumina content and zirconia composition on their density, bending strength and phase stability under hydrothermal conditions.

1) HIP temperature of 1400°C gave the highest bending strength; average bending strengths of the (4Y, 4Ce)-TZP, (2.5Y, 4Ce)-TZP and (2.5Y, 5.5Ce)-TZP compositions containing 25wt% of alumina were 1800, 1700 and 1600MPa.
2) Addition of alumina to the (Y, Ce)-TZP compositions controlled growth of the zirconia grains.
3) Increasing CeO_2 content sharply decreased density of the composites HIP-treated at 1600°C.
4) Addition of alumina controlled decrease in density, observed in the composites HIP-treated at 1600°C.
5) Increasing alumina content increased bending strength and phase stability under the hydrothermal conditions (180°C and 1MPa) of the HIP-treated compositions.

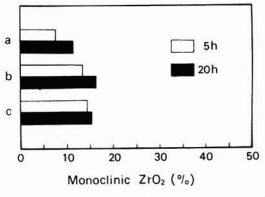

Fig. 9. Tetragonal-to-monoclinic phase transformation resulting from hydrothermal aging at 180°C and 1MPa for (a) (4Y, 4Ce)-TZP/25wt%Al_2O_3 composites, (b) (2.5Y, 4Ce)-TZP/25wt%Al_2O_3 composites and (c) (2.5Y, 5.5Ce)-TZP/25wt%Al_2O_3 composites HIP treated at 1400°C.

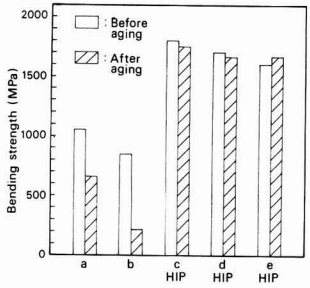

Fig. 10. Bending strength of (a) 3Y-TZP (YO specimen), (b) (4Y, 4Ce)-TZP (XCO specimen), (c) (4Y, 4Ce)-TZP/25wt%Al_2O_3 composites (IC25 specimen), (d) (2.5Y, 4Ce)-TZP/25wt%Al_2O_3 composites (IIC25 specimen), and (e) (2.5Y, 5.5Ce)-TZP/25wt%Al_2O_3 composites (IIIC25 specimen) as-prepared (sintered at 1500°C or HIP treated at 1400°C) and aged under hydrothermal conditions at 180°C and 1MPa for 100h.

Reference:

1) T.K. Guputa, J.H. Bechtold, R.C. Kuznicki, L.H. Cadoff, and B.R. Rossing, J. Mater. Sci., 12, 2421-26 (1977).
2) T.K. Guputa, F.F. Lange, and J.H. Bechtold, J. Mater. Sci., 13, 1464-70 (1978).
3) T. Tsukuma, Y. Kubota and T. Tsukidate, Yogyo Kyokai-shi, 92, 11-19 (1984).
4) K. Kobayashi, H. Kuwajima, and T. Masaki, Solid State Ion., 3-4, 489 (1981).
5) T. Sato, S. Ohtaki, and M. Shimada, J. Mater. Sci., 20, 1466-70 (1985).
6) M. Yoshimura, T. Noma, K. Kawabata and S. Somiya, Seramikkusu Ronbun-shi, 96, 265-70 (1988).
7) T. Sata and M. Shimada, Hyomen Kagaku, 10, 11-17 (1989).
8) F.F. Lange, G.L. Dunlop and B.I. Davis, J. Am. Ceram. Soc., 69, 237-40 (1986).
9) P.J. Whalen, F. Reidinger and R.F. Antrim, J. Am. Ceram. Soc., 72, 319-21 (1989).
10) K. Tsukuma, Am. Ceram. Soc. Bull., 65, 1386-89 (1986).
11) K. Tsukuma and M. Shimada, Am. Ceram. Soc. Bull., 64, 310-13 (1985).
12) T. Tatsuno and K. Homma, "Zirconia Ceramics, 5," Uchida Rokakuho, (1985), pp.27-30.
13) K. Tsukuma, K. Ueda and M. Shimada, J. Am. Ceram. Soc., 68, c-5 (1985).
14) R. Shihou, Y. Urata, T. Shiono and Y. Nishikawa, Powder and Powder Metallurgy, 37, 357-61 (1990).
15) T. Sato, T. Endo and M. Shimada, J. Am. Ceram. Soc., 72, 761-64 (1989).
16) T. Sato, T. Fukushima, T. Endo and M. Shimada, Proceedings of the International Conference on the Science of Ceramics 14, pp.843-48.
17) T. Watanabe, K. Urabe, H. Igawa and S. Udagawa, Ceramic Society of Japan Annual Meeting Proceedings, (1984) pp.463-64.
18) M. Hirano and H. Inada, Seramikkusu Ronbun-shi, 99, 124-30 (1991).
19) M. Hirano, T. Matsumoto, H. Inaka, K. Suzuki, H. Yoshida and M. Machida, Seramikkusu Ronbun-shi, 90, 191-95 (1991).

20) R.G. Garvie, and P.S. Nickolson, J. Am. Ceram. Soc., 55, 303 (1972).
21) K. Urabe, H. Ogata, H. Igawa and S. Udagawa, Ceramic Society of Japan Annual Meeting Proceedings, (1986), pp.91-92.
22) K. Urabe, K. Ogata, H. Igawa and S. Udagawa, Abstract Am. Ceram. Soc., 39th Pacific Coast Regional Meeting (1986) p.45.
23) M.V. Swain and L.R.F. Rose, J. Am. Ceram. Soc., 69, 511-18 (1986).

This article is a full translation of the article which appeared in Nippon Seramikkusu Kyokai Gakujutsu Ronbunshi (Japanese version), Vol.99, No.5, 1991.

Effects of Oxygen on Pyrolysis of Si-Ti-C-O Fibers

Toshio Shimoo*, Yoshiharu Kakehi, Masaki Sugimoto*** and Kiyohito Okamura***

*Dept. of Metallurgical Engineering, College of Engineering, University of Osaka Prefecture
4-804, Mozu-Umemachi, Sakai-Shi, 591 Japan
**Undergraduate Student, University of Osaka Prefecture, 4-804, Mozu-Umemachi, Sakai-Shi, 591 Japan
***Graduate Student, University of Osaka Prefecture, 4-804, Mozu-Umemachi, Sakai-Shi, 591 Japan

The mechanism of pyrolysis of two types of amorphous Si-Ti-C-O fibers (Tyranno fiber T-1 containing 17.8%O and T-2 containing 13.3%O) was studied in an argon atmosphere at temperatures from 1673K to 1973K. The pyrolysis rate was measured with a thermobalance, and the pyrolysis products were investigated by X-ray diffraction and TEM observation.

The amorphous fiber T-1, in which the atomic arrangement was disordered in comparison with that in T-2, evolved both SiO and CO to crystallize to β-SiC and TiC rapidly. TEM observation showed three-dimensional growth of SiC crystallites. At the same fractional decomposition of the fiber, the crystallite of T-1 was smaller than that of T-2. The pyrolysis rate was described with an Avrami-Erofeev's equation. The exponent m of this equation was 1.4 for both fibers. The rate constant *k* for T-1 was larger than that for T-2. The activation energies were 413KJ/mol for T-1 and 368KJ/mol for T-2. The pyrolytic rate was determined by the crystal growth of SiC controlled by the diffusion of carbon in the fiber.

[Received November 21, 1990; Accepted January 24, 1991]

Key-words: Si-Ti-C-O fiber(Tyranno fiber), pyrolysis, thermogravimetry, TEM, reaction mechanism, Avrami-Erofeev's equation

1. Introduction

The silicon carbide fibers were pyrolyzed at high temperature, to lose their mechanical strength significantly.[1-4] This pyrolysis is a very important problem to be solved before they are extensively used industrially, whether they are used alone or in composite with other materials. It is essential, therefore, to fully understand the mechanisms involved in the pyrolysis to effectively prevent it. However, few researchers have discussed the pyrolysis phenomena.

The authors have been determining pyrolysis rates of the Si-C-O fibers (Nippon Carbon, Nicalon)[5,6] and Si-Ti-C-O fibers (Ube Industries, Tyranno)[7], in order to investigate the mechanism of the reactions. The production process of these silicon carbide fibers consists of (1) melt spinning of the organic silicon polymer, (2) thermal oxidation in air, and (3) firing. Therefore, they invariably contain oxygen, derived from air as the atmosphere gas for the thermal oxidation curing process, though to a different extent, which causes pyrolysis of the fibers at high temperature. In other words, the pyrolysis is a heterogeneous reaction in which oxygen is removed from the fibers, accompanied by the amorphous fibers being crystallized into thermodynamically more stable β-SiC or TiC, while releasing both SiO and CO gases. Pyrolysis rate of the fibers is governed by formation and growth of the nuclei for SiC crystals, in which diffusion serves as the rate-determining step.

Thus, oxygen plays a vital role in the pyrolysis of the silicon carbide fibers. In this study, the pyrolysis of the fibers has been kinetically investigated, using two types of Si-Ti-C-O fibers of different oxygen content, to discuss the effects of oxygen on the pyrolysis rate and mechanisms.

Table 1. Various properties of Si-Ti-C-O fibers (Tyranno fibers).

fiber	heating treatment temperature T/K	composition	diameter $d/10^{-6}$m	density ρ/Mg·m^{-3}
T-1	1573	$SiTi_{0.02}C_{1.40}O_{0.64}$	8.5	2.33
T-2	1573	$SiTi_{0.02}C_{1.33}O_{0.44}$	8.5	2.38

2. Experimental Procedure

The samples used in this study were of the Si–Ti–C–O fibers (Ube Industries, Tyranno fibers) produced from polytitanocarbosilane as the precursor. **Table 1** summarizes the firing temperature, chemical compositions, diameters, and densities. Fiber T-1 was used in this study, and Fiber T-2 was the comparative sample, whose pyrolysis behavior was discussed previously.[7] Both fiber samples were fired at 1573K. As shown in the table, these fibers differed from each other mainly in oxygen content; 17.8mass% for T-1 and 13.3mass% for T-2. **Figure 1** presents the X-ray diffraction patterns of the starting fibers. Both fibers had broad diffraction lines, indicating that they were amorphous. It was also found that Sample T-1 of higher oxygen content had more irregular atomic configurations, resulting in lower density, though slightly. In this study, the major emphasis was placed on the effects of oxygen content, or different crystallinity, on pyrolysis rate of the Tyranno fibers.

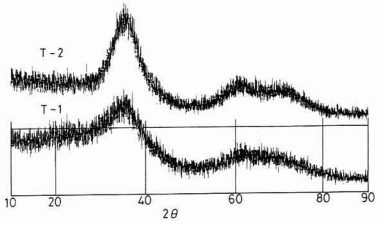

Fig. 1. X-ray diffraction patterns of original Si-Ti-C-O fibers (Tyranno fiber T-1 and T-2).

The sample fibers were pretreated with Ar at 1073K for 1h, to remove foreign materials such as the sizing agent used.

A graphite crucible (inner diameter: 26mm, height: 50mm) holding 1g of the fibers was suspended in the uniform-temperature section of a Tamman furnace after having been connected to an automatic balance (measurable limit: 100g, sensitivity: 0.1mg), to continuously monitor the pyrolysis-induced weight loss of the fiber sample. Ar gas was passed through the oven at $2.5\times10^{-5}m^3/s$ from the bottom. The empty crucible was also heated in the same manner to find the blank value, by which the weight loss curve was corrected. The heat-treated sample was analyzed by an X-ray diffractometer, chemical analysis and transmission electron microscope (TEM, JEM-2000FX).

3. Results

3.1. Pyrolysis Curve

Figure 2 presents the pyrolysis curves of Sample T-1 at varying temperature levels in a range from 1673 to 1973K, where $\Delta W/W_0$ is weight loss ratio, ΔW and W_0 being weight loss and the initial weight of the sample, respectively, determined by the thermobalance. The final weight loss rate was $\Delta W/W_0 \approx 0.32$ on average, though varying to some extent, depending on temperature level used. As shown, pyrolysis rate was greatly affected by temperature; the pyrolysis was almost completed in 0.5ks at 1973K, whereas $\Delta W/W_0$ was only 0.23 in 8.6ks at 1673K. **Figure 3** compares pyrolysis rate of Sample T-1 with that of Sample T-2, indicating that the former sample, containing a larger quantity of oxygen, was pyrolyzed faster and had a higher final weight loss ratio than the latter (the final weight loss ratio $\Delta W_f/W_0$ of the latter was approximately 0.25). The pyrolysis-induced weight loss of Tyranno fibers resulted from release of SiO and CO gases,[7] and the above results would be reasonable when considering that the presence of oxygen was the direct cause for the formation of these gases. The pyrolysis curve of a solid is generally characterized by a sigmoid shape, consisting of the (1) induction, (2) acceleration, and (3) termination regions. The induction region was not clearly observed in the pyrolysis curves shown in Figs.2 and 3 as the results of the pyrolysis at high temperature. The initial stage of the pyrolysis (decomposed fraction $X\leq0.15$) in which the Avrami-Erofeev's equation did not hold would correspond to the induction region, as discussed later.

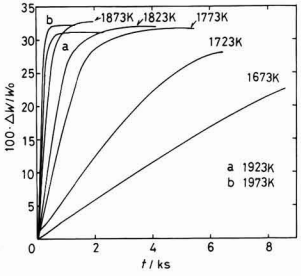

Fig. 2. Decomposition curves of fiber T-1 at various temperatures.

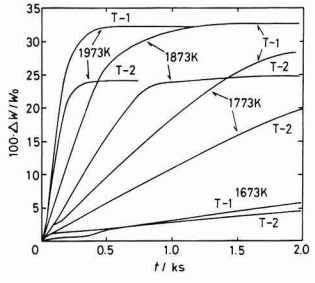

Fig. 3. Comparison of pyrolytic rate of fiber T-1 with that of T-2 at various temperatures.

3.2. Analysis of Pyrolyzed Fiber Surfaces by Scanning Electron Microscope (SEM)

Figure 4 presents the SEM photographs of the fiber surfaces, pyrolyzed at 1673 to 1973K. The fibers treated at 1673K showed almost the same outer appearance as the untreated ones, because of insufficient extent of pyrolysis (X=0.7). Those treated at 1773K or more were completely pyrolyzed. Those treated at 1773K had rough surfaces, because of the growth of the β-SiC grains. Those treated at higher temperature had more irregular surfaces, because of the accelerated growth of the grains.

3.3. X-Ray Diffraction Analysis Results

Figure 5 presents the X-ray diffraction patterns of the Tyranno fiber T-1 samples treated to different degrees; the sample pretreated at 1073K and those treated at 1873K in different times. The pretreated sample had broad X-ray diffraction patterns (indicating that it was amorphous) which were essentially the same as those of the untreated one shown in Fig.1. The pretreatment, therefore, caused no structural change. The diffraction pattern of β-SiC became sharper, i.e., crystallization proceeded with pyrolysis. The diffraction patterns of TiC were not clearly distinguished from those of β-SiC in the samples treated for up to t=0.3ks, because they were almost at the same diffraction angle. At t=1.8ks, the diffraction pattern of TiC was more intense than that of βSiC at $2\theta\approx41°$, suggesting that TiC was crystallized faster than β-SiC (thermodynamically, the former is formed easier than the latter). At t=3.6ks, in which pyrolysis was completed, the diffraction patterns of SiC (200) at $2\theta=41.3°$, TiC (200) at $2\theta=41.7°$, SiC (220) at $2\theta=59.9°$, TiC (220) at $2\theta=59.9°$, SiC (311) at $2\theta=71.7°$ and TiC (311) at $2\theta=72.0\theta$ were separated clearly from each other.[8,9]

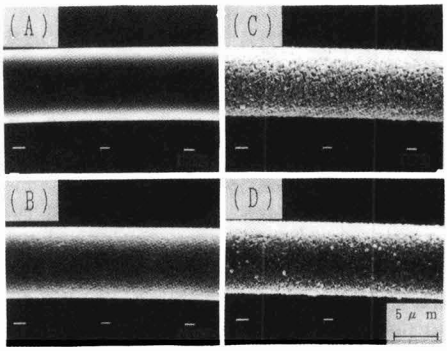

Fig. 4. SEM photographs of surface of fiber T-1 after pyrolysis at 1673K (A), 1773K (B), 1873 (C) and 1973 (D).

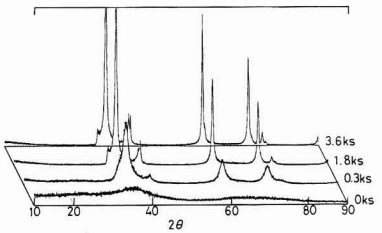

Fig. 5. X-ray diffraction patterns of Tyranno fiber T-1 heated at

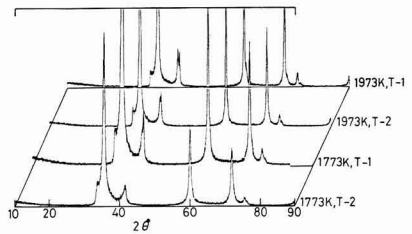

Fig. 6. Comparison of X-ray diffraction patterns of fiber T-1 with those of T-2 heated at 1773K and 1973K.

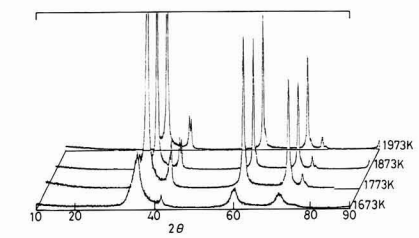

Fig. 7. X-ray diffraction patterns of fiber T-1 heated at various temperatures.

Figure 6 compares the diffraction patterns of Sample T-1 with those of T-2. As shown, each of the former patterns was sharper. Noted in particular was much better separation of the patterns of TiC in T-1; its patterns clearly appeared already at 1773K in the larger-angle side to the pattern at $2\theta=41°$. These results were in good agreement with those shown in Fig.2, which indicated that T-1 was pyrolyzed faster than T-2. The T-1's amorphous fibers were transformed faster into the crystalline β-SiC and TiC phases.

Figure 7 presents the X-ray diffraction patterns of Sample T-1 pyrolyzed at different temperature levels. The sample treated at 1673K had broad patterns, because of the incomplete pyrolysis. Increasing treatment temperature separated the diffraction patterns of β-SiC from those of TiC more clearly. This trend was particularly noted with the patterns at around $2\theta=41°$.

3.4. Pyrolysis-Induced Compositional Changes of Fibers

Figure 8 shows mole fractions of the elements that constituted the fibers, i.e., Si, Ti, C and O, changing with time at 1873K, where N_{Si}, N_{Ti}, N_C and N_O stand for mole fractions of these elements. N_o decreased, and the $(N_{Si}+N_{Ti})/N_C$ ratio moved towards unity, as pyrolysis proceeded. These results were in good agreement with the XRD and ED analysis results, indicating that the amorphous fibers were crystallized into the SiC and TiC phases by pyrolysis.

Pyrolysis of fibers of silicon carbride system is accompanied with simultaneous release of SiO and CO gases.[5-7),10)] The XRD analysis results and the others have indicated that the pyrolysis of Tyranno fibers is represented by the following formula:

$$SiTi_xC_yO_z(\text{amorphous}) \rightarrow \beta\text{–}SiC(s) + TiC(s) + SiO(g) + CO(g) \quad \ldots\ldots (1)$$

from which the following relationships will be derived:

$$(\%Si)_t \times 10^{-2} = \{(\%Si)_i \times 10^{-2} \cdot W_i - W_{SiO}{}^t \cdot (M_{Si}/M_{SiO})\}/(W_i - \Delta W_t) \quad \ldots (2)$$

$$\Delta W_t = W_{SiO}{}^t + W_{CO}{}^t \quad \ldots\ldots\ldots\ldots\ldots (3)$$

where

$(\%Si)_i$ and $(\%Si)_t$: Si content in the fiber at t=0 (initial content) and t=t

ΔW_t: weight loss of the system at t=t

$W_{SiO}{}^t$ and $W_{CO}{}^t$: quantities of SiO and CO released at t=t

W_i: initial weight of the fibers

M_{si}, $M_{si,O}$: molecular weight of Si and SiO W_i:

The W_{SiO} and W_{CO} values can be found by substituting theerved Si contents and the thermobalance analysis results into Equations (2) and (3).

Figure 9 plots the W_{SiO} and W_{CO} values against conversion X, determined by the following equation:

$$X = \Delta W_t / \Delta W_f \quad \ldots\ldots\ldots\ldots\ldots (4)$$

where, ΔW_f is the final weight loss when pyrolysis is completed (at which weight loss is no longer observed). The W_{SiO} value increased almost linearly as pyrolysis proceeded. The W_{CO} value, on the other hand, increased during the initial stage of pyrolysis, but attained a constant level after conversion X reached approximately 0.5. The relationship $W_{SiO}<W_{CO}$ held, as was the case with Sample T-2,[7)] whereas

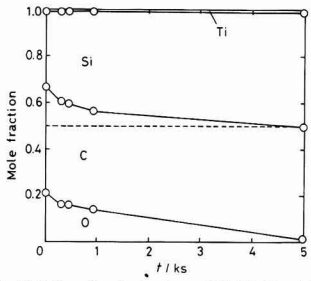

Fig. 8. Variation of mole fractions of Si, Ti, C and O in fiber T-1 heated at 1873K with time.

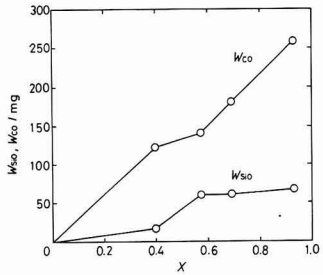

Fig. 9. Relation between mass of SiO, CO evolved and decomposed fraction of fiber T-1 heated at 1873K.

the opposite relationship $W_{SiO}>W_{CO}$ was observed with the Nicalon fibers.[5] Both Si and C diffuse through the amorphous fibers, to be crystallized into β-SiC. It is considered that oxygen present in the amorphous portions is concentrated, and released in the form of SiO and CO from the fibers. In any case, release of a gas is accompanied with the destruction of the fiber structure, and hence causes degradation of mechanical strength of the fibers.

3.5. Observation of SiC Grains by Transmission Electron Microscope

The types of samples, one pretreated at 1073K and the other pyrolyzed at 1873K, were analyzed by a transmission electron microscope (TEM), after having been crushed, to observe growth of the SiC crystallites. The TEM photographs and electron diffraction patterns of the samples are presented in **Figs.10, 11** and **12**. The electron diffraction patterns of the pretreated samples show the halo patterns characteristic of amorphous state, and correspondingly its bright field image is unclear. The diffraction patterns became clearer as the pyrolysis proceeded, and the final diffraction ring coincided with that of β-SiC. The diffraction spots of TiC were also observed. The dark-field images also showed that the SiC crystals were grown three-dimensionally.

3.6. Growth of SiC Grains

Figure 13 shows the relationship between the average SiC grain size (d), determined from the TEM photographs, and conversion of the fibers X. As shown, the grains were grown as pyrolysis proceeded. Particularly noted is the rapid grain growth in an X≥0.6 range, believed to result from coalescence of the grains. The grain size was widely varying in the above conversion range, due to the presence of both well grown grains and scarcely grown grains. Sample T-1 had a consistently smaller grain size than that of Sample T-2 throughout the progress of decomposition.

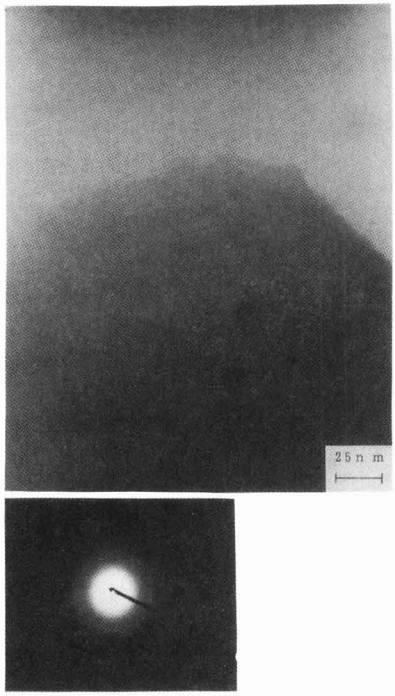

Fig. 10. TEM photograph and electron diffraction pattern of fiber T-1 heated at 1073K for 3.6ks.

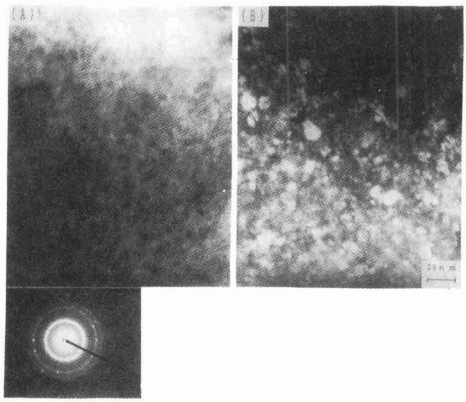

Fig. 11. TEM photograph and electron diffraction pattern of fiber T-1 heated at 1873K for 0.3ks. (A) bright field image and (B) 111 dark field image.

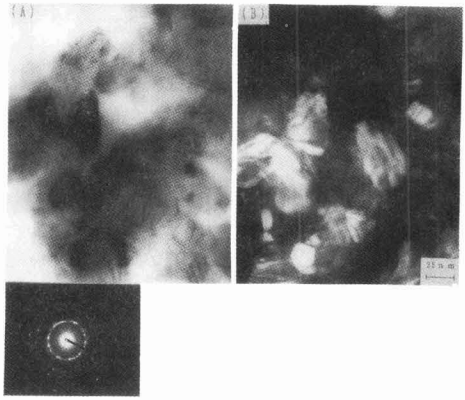

Fig. 12. TEM photograph and electron diffraction pattern of fiber T-1 heated at 1873K for 1.8ks. (A) bright field image and (B) 111 dark field image.

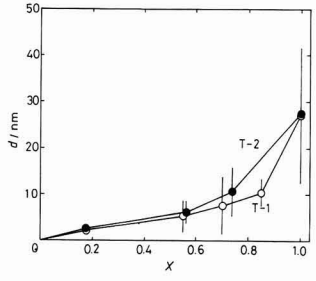

Fig. 13. Relation between particle size of SiC crystallites and decomposed fraction of fiber T-1 heated at 1873K.

4. Discussion

4.1. Analysis of Pyrolysis Rate

The pyrolysis was kinetically analyzed using the Avrami-Erofeev's equation (5),[11] as was done previously.[5-7]

$$-\ln(1-X) = k \cdot t^m \quad \ldots\ldots\ldots\ldots\ldots\ldots (5)$$

Equation (6) is derived from Equation (5):

$$\ln\{-\ln(1-X)\} = \ln k + m \cdot \ln t \quad \ldots\ldots\ldots (6)$$

where, k and m are constants, and X is conversion of the fiber sample (See Equation (4)).

Figure 14 shows the analysis of the pyrolysis results shown in Fig.2 using Equation (6). The curve for each temperature level is an almost straight line in a conversion range $0.15 \leq X \leq 0.85$. The value m, determined from the slope of each curve, was 1.2 to 1.7, with the average of m=1.4. The value m of Sample T-2 was also 1.4.[7] The initial stage of pyrolysis ($X \leq 0.15$) in which the Avrami-Erofeev's equation did not hold, or the stage of formation of the SiC nuclei. The equation was applicable to the period in which the grains grew after the nuclei formation had been completed.

Figure 15 presents the Arrhenius plot for the rate constant k, from which the activation energy of the pyrolysis of Sample T-1 was estimated to be E=413KJ/mol by the least square method. This compares with E=368KJ/mol of Sample T-2. The rate constant of T-1 was higher than that of T-2 at high temperature, though they were the same at low temperature. The above activation energy was in an energy of activation range as that associated with diffusion of C through SiC (302 to 586KJ/mol).[12-14] In other words, the above results indicated that diffusion of Si and C was necessary for the growth of the SiC grains. It is known that Si has a diffusion coefficient in SiC 10 times higher than C,[12] and rate of the diffusion process will be determined by the diffusion of C. The TEM analysis showed that the crystals were grown three-dimensionally. The Averami-Erofeev's equation may be modified, as follows, for the results after the nuclei formation was completed, i.e., those at $X \geq 0.15$:

$$-\ln(1-X) = n_o \cdot (4\pi/3) \cdot D^{3/2} \cdot t^{3/2} \quad \ldots\ldots\ldots (7)$$

where

n_o: number of nuclei in the unit volume

D: diffusion coefficient

Equation (7) gives m=1.5, in view of Equation (5), which is very close to m=1.4 as the average m value determined in this study. Pyrolysis rate of the Tyranno fiber sample T-1 was found to be governed by the growth of the SiC crystals, as was the case with Sample T-2 discussed previously.[7] The process was characterized by diffusion as the rate-determining step.

4.2. Effects of Oxygen Present in Fibers on Pyrolysis

Sample T-1, containing a larger quantity of oxygen than Sample T-2, was pyrolyzed faster, as shown in Fig.3. This phenomenon is discussed as follows.

The difference between these samples in rate of pyrolysis will be attributable to the difference in rate constant k, if the same reaction mechanisms and rate-determining step are involved in the pyrolysis process. This assumption will hold for Samples T-1 and T-2 at a high temperature region, based on the results shown in Fig.3 and 15. Rate constant k is given by the formula $k=n_o(4\pi/3)D$ 3/2D, from Equations (5) and (7). The process should have a higher n_o level to proceed faster, because D is considered to be constant. Sample T-1 consisted of consistently smaller grains than Sample T-2, as shown in Fig.13. A smaller grain size at the same conversion level means a larger number of grains present in the system. In other words, Sample T-1 will be pyrolyzed faster than T-2, because of the former's higher n_o value.

The amorphous Si-Ti-C-O fiber of more disorder atomic configuration is more distant from an equilibrium state, i.e., β-SiC and TiC crystals, and is higher in degree of supersaturation. A larger number of finer nuclei will be formed stably in a system of higher degree of supersaturation. This will account for a larger number of n_o of Sample T-1 than that of T-2, because the former sample has a more disordered atomic configuration, as shown in Fig.1.

The effects of supersaturation is more noted at higher temperature (Fig.15), because degree of supersaturation increases as temperature increases. The stable nuclei formed during the initial stage of pyrolysis will be those for TiC, because thermodynamics dictate that TiC is formed faster than β-SiC. This is backed up by the X-ray diffraction analysis results indicating that crystallization of TiC proceeds in preference to that of β-SiC, as shown in Fig.5. The authors have discussed that Tyranno fibers are pyrolyzed faster than the Ti-free Si-C-O fibers (Nicalon), because of the formation of the stable, fine nuclei for TiC.[7]

It is, therefore, concluded that pyrolysis of the amorphous silicon carbide fibers is closely related to their oxygen content and affects their mechanical strength. It is therefore necessary to prepare the samples of widely varying oxygen content, in order to further investigate behavior of the pyrolysis process.

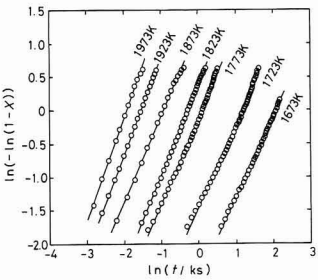

Fig. 14. Application of Avrami-Erofeev equation to data shown in Fig.2.

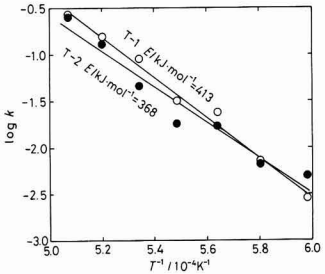

Fig. 15. Arrhenius plots for rate constant k in Avrami-Erofeev equation.

5. Conclusions

Pyrolysis of the two types of Si-Ti-C-O fibers (Tyranno fibers, T-1 and T-2) was kinetically studied at 1673 to 1973K in an Ar gas atmosphere.

1) Sample T-1, containing a larger quantity of oxygen than Sample T-2, had a more disordered atomic configuration.
2) Sample T-1 was pyrolyzed faster than Sample T-2.
3) The pyrolysis process of these fibers was characterized by the crystallization of the amorphous fibers into β-SiC and TiC, accompanied by release of SiO and CO.
4) The SiC grains were grown three-dimensionally, as revealed by the TEM analysis. Sample T-1 consisted of smaller SiC grains than Sample T-2 at the same conversion level.
5) The pyrolysis process was well represented by the Avrami-Erofeev's equation. Sample T-1 had a higher rate constant k than Sample T-2, though their index m values were the same.
6) Activation energy was 413KJ/mol with Sample T-1 and 368KJ/mol with T-2.
7) TiC was considered to be formed during the initial stage of pyrolysis. Pyrolysis at a conversion X of 0.15 or more is characterized by the growth of the SiC grains as the rate-determining step.

Acknowledgements
Part of this study was supported by a subsidy (No.02229218) from the Ministry of Education, Science and Calture.

Reference:

1) K. Okamura, M. Sato, T. Matsuzawa and Y. Hasegawa, Polym. Prepr., 25, 6-7 (1984).
2) Y. Sasaki, Y. Nishina, M. Sato and K. Okamura, J. Mater. Sci., 22, 443-448 (1987).
3) T. Yamamura, T. Ishikawa, M. Shibuya and K. Okamura, J. Mater. Sci., 23, 2589-2594.
4) D.J. Pysher, K.C. Goretta, R.S Hodder, Jr and R.E. Tressler, J. Am. Ceram. Soc., 72, 284-288 (1989).
5) S. Shimoo, M. Sugimoto, K. Okamura, J. of Japan Institute of Metals, 54, 802-808 (1990).
6) S. Shimoo, M. Sugimoto, K. Okamura, Seramikkusu Ronbun-shi, 98 (1990).
7) S. Shimoo, M. Sugimoto, K. Okamura, J. of Japan Institute of Metals, in printing.
8) JCPDS, 29-1129.
9) JCPDS, 32-1383.
10) R. Riedel, K. Strecker and G. Petzow, J. Am. Ceram. Soc., 72, 2071-2077 (1989).
11) S.F. Hulbert, J. Brit. Ceram. Soc., 6, 11-20 (1969).
12) R.N. Goshtagore and R.L. Colbe, Phys. Rev., 143, 623-626 (1966).
13) P.L. Farnsworth and R.I. Colbe, J. Am. Ceram. Soc., 49, 264-268 (1966).
14) T.L. Francis and R.L. Colbe, J. Am. Ceram. Soc., 51, 115-116 (1968).

This article is a full translation of the article which appeared in Nippon Seramikkusu Kyokai Gakujutsu Ronbunshi (Japanese version), Vol.99, No.5, 1991.

Sintering Phenomena of Si_3N_4 Bonded Ceramics Containing Al_2O_3 Particles

Yoshiyuki Yasutomi, Akio Chiba, Masahisa Sobue

Hitachi Research Laboratory, Hitachi, Ltd.,
4026 Kuji-cho, Hitachi-shi, Ibaraki, 319-12 Japan

To investigate the sintering behavior of reaction bonded ceramics containing good self-sintering ceramic powders as starting materials, Al_2O_3 and Si powder mixtures were heated to 1350°C in a 0.88MPa nitrogen gas atmosphere. Shrinkage of about 0.3% was observed for the samples containing 20 to 70vol% Al_2O_3. This value was a few times larger than that of Si_3N_4 bonded ceramics containing non-self-sintering powders such as SiC, TiN and ZrN. It was proved that the grain growth of Al_2O_3 powders by self-sintering increased the shrinkage.
TEM observation of the sintered body showed that micro-cracks were present at the grain boundaries of Al_2O_3 and Si_3N_4 grains. These cracks seemed to form due to stress of the Al_2O_3 sintering on the Si_3N_4 skeleton formed from the Si powders. This skeleton might depress the free sintering shrinkage of Al_2O_3 powders. The TEM observation also showed that Si_3N_4 grains grew epitaxially on the Al_2O_3 surface, which meant Si_3N_4 could be bonded to inorganic compounds with ionic bond character.
[Received November 27, 1990; Accepted January 24, 1991]

Key-words: Silicon nitride bonded aluminum oxide, Reaction-bonding, Near-net-shape sintering, Grain Growth

1. Introduction

Since ceramics are generally hard to process, sintering techniques required for high dimensional precision are important for their popularization. We paid attention to reaction-bonding techniques[1] utilizing Si-nitriding reaction with less dimensional changes at a sintering state, and have been developing sinterable Si_3N_4 bonded SiC[2] with high strength, conductive Si_3N_4 bonded TiN,[3] and Si_3N_4 bonded ZrN.[4] The above SiC, TiN and ZrN powders are equally inorganic compounds, stable in nitrogen at high temperatures of about 1350°C, and not changing their post-sintering particle shape. Since Si_3N_4 formed by vapor phase reaction, has a sintering mechanism to bond the particles of each inorganic compound it is known that the dimensional variation at sintering is as small as 0.1~0.3%.[5] Almost no studies have been done on the possibility of Si_3N_4-reaction-bonding ceramics of inorganic compound particles with high self-sinterability (the particles themselves get sintered through diffusion, etc. without any sintering aid).

Thus, in our current study, we have selected micro particles of Al_2O_3 (known as an inorganic compound with high self-sinterability that has a self-sintering in an atmosphere of about 1300°C), and mixed them with Si powders as reported earlier to investigate the sintering phenomena when heated in nitrogen at 1350°C.

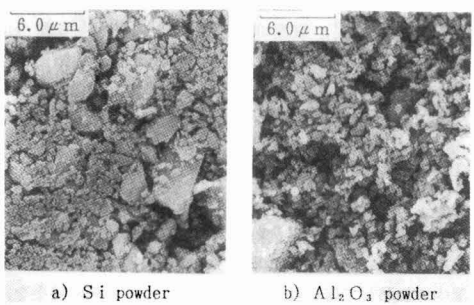

Fig. 1. Scanning electron micrographs of silicon powder and Al_2O_3 powder

2. Experiment

2.1. Method for the Preparation of Specimens

Figure 1 shows the SEM photographs of material powders used for the current experiment. The ground powders with a mean particle diameter of 0.9μm and broad grain size distribution were used as metal Si powders, and α-Al_2O_3 powders (AMS-9, 99.7% purity manufactured by Sumitomo Kagaku K.K.) with mean particle diameter of 0.5μm with narrow grain size distribution were used as self-sinterable inorganic compound particles. The formulation ratio of material Si and Al_2O_3 powders was changed and mixed in a pot mill together with ethanol and Si_3N_4 ball, when an agglomerate of Al_2O_3 was crushed and uniformly dispersed as shown in Fig.1. Then, after this mixture was dried at room temperature, thermoplastic resin of a polyethylene system was added as a molding binder for further mixing by a pressure kneader for 2h. Amount of binder was fixed to 19.4vol%. Next, the mixture thus obtained was cooled and crushed to under 10 mesh to obtain molding materials. The crushed molding materials were then pressed at 98MPa in a metal mold heated up to 140°C to prepare a molded product of 50mm in diameter and about 10mm in thickness.

Then, after a degreasing furnace was used for removing resins, the molds were heated in nitrogen gas at 0.88MPa, in a firing furnace of graphite-induction-heating type. The temperature was raised stepwisely heating under the conditions of 1100°C×20h, 1200°C×20h, 1250°C×10h, 1300°C×10h and 1350°C×10h, so that melting and evaporation due to exothermic reaction of Si could be avoided. An electric silicon carbide furnace was used for atmospheric sintering under the same heating conditions for comparison.

2.2. Evaluation of the Specific Properties

The following is a description of the test items and methods used for the sintered bodies thus obtained.

1) Relative dimensional changes at sintering.

The relative dimensional changes of the degreased bodies sintered by nitriding reaction were obtained by the following equation. The dimensions were measured by a slide calipers of 1/100mm precision.

$$\text{Relative dimensional changes at a sintering stage (\%)} = \frac{\text{Dimensions of sintered body} - \text{dimensions of dewaxed body}}{\text{Dimensions of dewaxed body}} \times 100$$

2) Bending strength

Three-point bending measurement method was applied to each sintered body for a test piece of 40×4×3mm specified by JISR1601. The test conditions were 30mm for the span of the supports and 8.33×10^{-6}m/s for cross-head speed.

3) Structure analysis

After each sintered specimen was powdered in a mortar of tungsten carbide, the substances formed were identified by powder X-ray diffraction. The micro-structures of sintered bodies were observed by SEM and transmissive electron microscopy (TEM).

4) Gas analysis

Nitrogen amount in a sintered body of single Al_2O_3 was measured, after a chemical treatment to remove O_2, by means of the thermal conductivity method using a gas analyzer LECO's Model TC-463 under a condition of 2800°C in He carrier gas.

3. Results and Discussion

3.1. Sintering Behavior of Al_2O_3 Powder Molds

Figure 2 shows the measured percent change in dimension as a result of sintering of a molded body of single Al_2O_3 powder heated in N_2 atmosphere. The values obtained when heated in air are also shown for reference. As shown in Fig.2, marked shrinkage is observed when heated in air above 1100°C, while the shrinkage is hardly recognized in the nitrogen atmosphere ranging from 1100°C to 1200°C, but occurs at a level higher than 1200°C. The magnitude of shrinkage is larger in air. The SEM photographs of the fractured surface of each specimen heat-treated to 1350°C are shown in **Fig.3**, which indicates the neck-growth at the contact between Al_2O_3 particles due to diffusion along with the growth of particles. This grain growth is responsible for the shrinkage. It is evident that the particles of specimens heated in air are larger than that heated in nitrogen. When the composition was identified by X-ray diffraction, it was found that the powders were equally composed of α-Al_2O_3 alone with no particular difference between them, but nitrogen of 48ppm was detected from the specimens heated in the nitrogen atmosphere at 1350°C by gas analysis. Thus, the reason why a dimensional variation of specimens heated in nitrogen is lower than that heated in the atmosphere is conceivably attributable to nitrogen atoms introduced at the lattice defects, thereby inhibiting the sintering.[10] It was confirmed from the above preliminary experiment that fine Al_2O_3 particles used for the current experiments was self-sinterable as their sintering advanced to some extent even in the nitrogen atmosphere at 1350°C.

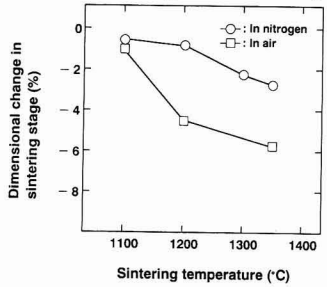

Fig. 2. Relation between sintering temperature and dimensional change in sintering stage

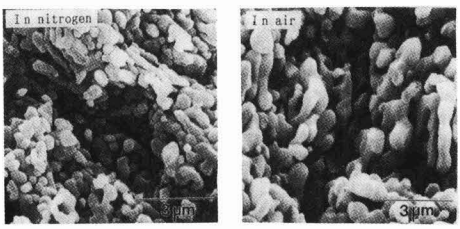

Fig. 3. SEM observation of fracture surface of Al_2O_3 sintered body heated to 1350°C in nitrogen and in air

3.2. Sintering Behavior of a Mold of Si·Al_2O_3 Powder Mixture

Figure 4 shows the particle packing density of mixture molds of Si and Al_2O_3 as well as the measurement of the relative density of sintered bodies obtained by heating them in the nitrogen atmosphere in relation to the volume fraction of Al_2O_3 powders. The relative density of the molded bodies was found to have decreased from 75% to 63% when the fraction of Al_2O_3 powders increased, but this may be attributed to fine particles of Al_2O_3 powders. The relative density of sintered bodies tended to decrease with an increase of a fraction of Al_2O_3 powders. This may be explained by a decreased packing density, and further by a less fraction of Si whose volume increases by 22% due to nitriding, for a specimen with larger amount of Al_2O_3. This tendency is similar to that of Si_3N_4 bonded ceramics which have already been reported.[3,4]

Figure 5 shows the dimensional variation of degreased bodies at sintering in relation to the volume fraction of Al_2O_3 powders. The values of the previously reported Si_3N_4 bonded ceramics are also shown for comparison. It was

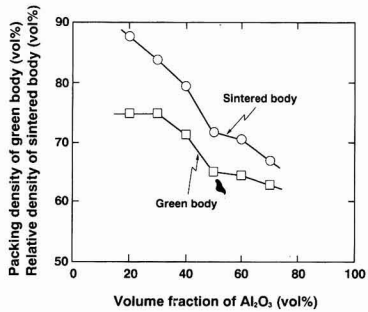

Fig. 4. Relation between volume fraction of Al_2O_3 and packing density of green body and relative density of sintered body

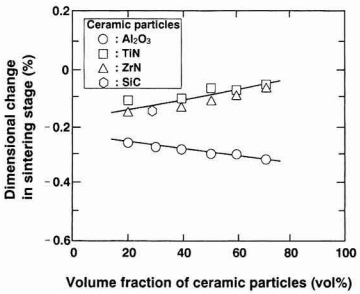

Fig. 5. Relation between volume fraction of ceramic particles and dimensional change in sintering stage

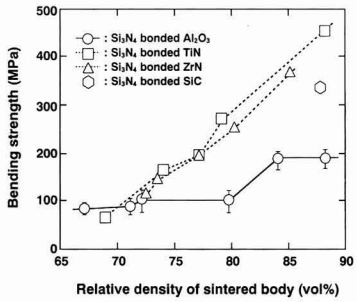

Fig. 6. Relation between relative density and bending strength of sintered body

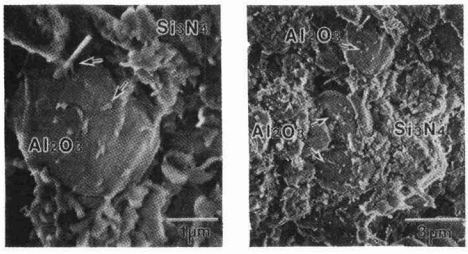

Fig. 7. SEM observation of fracture surface of Si_3N_4 bonded Al_2O_3 (Si_3N_4:Al_2O_3=80:20vol%)

found from these data that the dimensional variation at sintering of Si_3N_4 bonded ceramics with non-self-sintering property (with TiN, ZrN, and SiC) ranged from -0.15% to -0.07%, and that the shrinkage became smaller as the particle amount of ceramics increased. This shrinkage was caused by the driving force of sintering that was generated while Si was being changed into Si_3N_4. In contrast, the shrinkage tended to increase from -0.25% to -0.32% in the Si_3N_4 bonded Al_2O_3 with an increase of the volume fraction of Al_2O_3. Thus, a shrank amount of Si_3N_4 bonded Al_2O_3 larger than that of conventional Si_3N_4 bonded ceramics is probably attributable to a larger shrinkage generated by a driving force of sintering between the Al_2O_3 particles added to that of sintering during the variation from Si to Si_3N_4.

On the other hand, it is conceivable that a shrinkage ratio of Si_3N_4 bonded Al_2O_3 is smaller than that of a single Al_2O_3 in Fig.2, because 1) almost no sintering of Al_2O_3 advanced at about 1100°C where nitriding of Si started, so that a skeleton of Si_3N_4 was formed first and 2) either Si or Si_3N_4 existing between the Al_2O_3 particles inhibited the sintering of Al_2O_3.

Figure 6 shows the relationship between the relative density and the bending strength of Si_3N_4 bonded Al_2O_3. The values of the bending strength [2-4] of the previously reported Si_3N_4 bonded ceramics are also shown for comparison. Although it is clear from Fig.6 that the bending strength of each ceramic tends to increase along with an improvement of the relative density, the bending strength of Si_3N_4 bonded Al_2O_3 is apparently lower than that of other Si_3N_4 bonded ceramics even when the relative densities are comparable, the obtainable maximum bending strength was only 200MPa.

3.3. Composition Phase and Micro-structure of Si_3N_4 Bonded Al_2O_3

The X-ray diffraction patterns of sintered bodies obtained from the Si and Al_2O_3 mixture molds were compared with the JCPDS cards of known substances to identify the composition phases. As a result, the sintered bodies were composed of α, β-Si_3N_4 and the nitrides of metal Si powders, and α-Al_2O_3 and no third phase, such as compounds Si_3N_4 and Al_2O_3, was detected. Thus, the shrinkage at a sintering stage in Fig.5 is presumably not caused by the formation of third phase, but associated with the Al_2O_3 particles sintered and also with Si-nitriding.

Next, the results of observation of microstructure are shown. Highly magnified SEM photographs of the fractured surface of sintered bodies of Si_3N_4 bonded Al_2O_3 are shown in **Fig.7**, and TEM images of internal Al_2O_3 particles in **Fig.8.** The appr. 0.5μm particle diameter of α-Al_2O_3 material powder is grown as large as 2 to 3μm, and the junction between Al_2O_3 particles is also seen in Fig.8. It was confirmed from these photographs that Al_2O_3 powders were being sintered. **Figure 7** shows Al_2O_3 wrapped by fine particles of Si_3N_4, as well as Si_3N_4 particles and whisker-like substances being adhered to the surface of these particles.

Highly magnified TEM images showing the junction interface of Si_3N_4 and Al_2O_3 are given in **Fig.9**. It was found from this figure that on the (411) plane of Al_2O_3 inclined by approximately 42°C, lattice-matched (001) plane of Si_3N_4 grew.

Particles of Si_3N_4 formed by vapor phase reaction was considered to grow epitaxially on Al_2O_3 particles, as seen in the intergrain structure of Si_3N_4 bonded SiC ceramics reported previously. Thus, it was found that Si_3N_4 can be

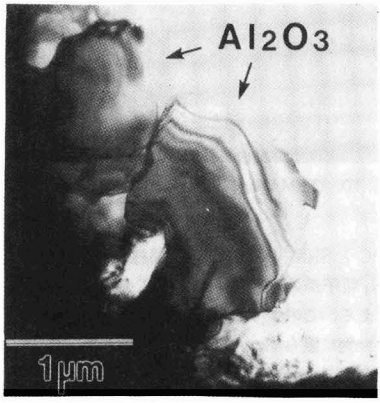

Fig. 8. TEM image of Al_2O_3 particles in the sintered body

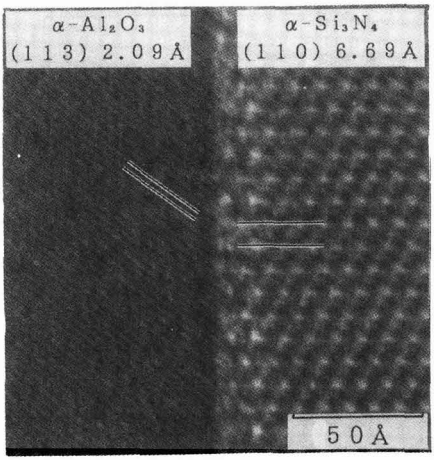

Fig. 9. High resolution TEM image showing interface between Al_2O_3 and Si_3N_4 in the sintered body

bound not necessarily to inorganic compounds with highly covalent bonding properties such as SiC, but to inorganic compounds with strongly ionic bonding properties such as Al_2O_3.

On the other hand, as shown in the low-magnified TEM images from the neighborhood of the grain boundaries of Si_3N_4 and Al_2O_3 in **Fig.10**, gaps that were not observed in the conventional Si_3N_4 bonded ceramics were seen in several spots between Al_2O_3 and Si_3N_4 particles. These gaps may partially be caused by the tensile stress between Al_2O_3 and Si_3N_4 when the dimensional shrinkage after the sintering of Al_2O_3 particles was inhibited by Si_3N_4 that had previously formed the skeleton. It is conceivable that these gaps are mainly responsible for the bending strength of Si_3N_4 bonded Al_2O_3 being lower than that of other reaction-bonding ceramics with similar sintered density.

4. Summary

1) When the molds of Al_2O_3 and Si mixture powders were heated at 1350°C in nitrogen, the complexed ceramics of Si_3N_4 bonded Al_2O_3 particles were obtained.
2) Epitaxial growth of Si_3N_4 on the surface of Al_2O_3 particles was observed, thus it was found that even an organic compound of highly ionic bonding properties can be chemically bound to Si_3N_4.
3) Since the sintering of Al_2O_3 powders with mean particle diameter of 0.5μm advanced when fired at 1350°C in nitrogen, the dimensional shrinkage at a sintering stage became larger than when the particles with no self-sintering property were used.
4) The existence of gaps was confirmed in the grain boundaries of Si_3N_4 and Al_2O_3 of the sintered bodies. It is surmised that these gaps were caused when the shrinkage due to self-sintering Al_2O_3 was constrained by the Si_3N_4 phase formed in its environment.
5) Since this micro-space becomes a notch, the bending strength of a sintered body is considered relatively small.

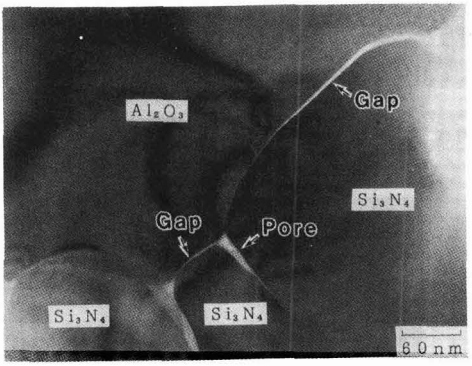

Fig. 10. TEM image of Si_3N_4 bonded Al_2O_3 c ceramics

References:

1) W.L. Wroten: Specially Bonded Silicon Carbide: Materials and Methods, 40, 83-5 (1954).
2) Y. Yasutomi, H. Kita, K. Nakamura, M. Sofue: Development of High-Strength Si_3N_4 Bonded SiC Ceramics : Nippon Seramikkusu Kyokai Gakujutsu Ronbunshi, 96, p.783-8 (1988).
3) Y. Yasutomi, K. Nakamura, M. Sofue, Y. Kubo: Development and Characterization of Electro-Conductive Si_3N_4 bonded TiN Ceramics: Nippon Seramikkusu Kyokai Gakujutsu Ronbunshi, 97, 148-54 (1989).
4) Y. Yasutomi, M. Sobue and Y. Kubo: Development and Characterization of Electro-Conductive Si_3N_4 Bonded ZrN Ceramics: Nippon Seramikkusu Kuokai Gakujutsu Ronbunshi, 97, 721-27 (1989).
5) Y. Yasutomi, M. Sobue S. Shinozaki and J. Hangas: Analyses of Microstructure and Sintering Mechanism of Si_3N_4-Bonded SiC Ceramics: Nippon Seramikkusu Kyokai Gakujutsu Ronbunshi, 98, 429-38 (1990).
6) S-T. Kwon, D-Y. Kim, T-K. Kang and D.N. Yoon: Effect of Sintering Temperature on the Densification of Al_2O_3: J. Am. Ceram. Soc., 70, C69-C70 (1987).
7) D.L. Johnson and I.B. Cutler: Diffusion Sintering II, Initial Sintering Kinetics of Alumina: J. Am. Ceram. Soc., 46, 545-50 (1963).
8) Y. Seki, S. Kose, T. Kodama, M. Kadota, T. Ogura, K. Tanimoto and I. Matsubara: Fabrication Method of Porous Alumina Compacts Containing Submicron Pores: Nippon Seramikkusu Kyokai Gakujutsu Ronbunshi, 96, 831-6 (1988).
9) S. Taruta, K. Okada and N. Otsuka: Micropore Distribution Change of Heated Powder Compacts Using Binary Alumina Powder Mixtures: Nippon Seramikkusu Kyokai Gakujutsu Ronbunshi, 98, 29-35 (1990).
10) R.L. Coble: Sintering Alumina, Effect of Atmospheres: J. Am. Ceram. Soc., 45, 123-7 (1962).

This article is a full translation of the article which appeared in Nippon Seramikkusu Kyokai Gakujutsu Ronbunshi (Japanese version), Vol.99, No.5, 1991.

Influence of Duty Factor on Wire Electro-Discharge Machining of Conductive Ceramics

Tetsuo Matsuo, Eiichi Oshima, Sadami Tomishige*, Hajime Hayakawa, Hideaki Kitao** and Toyoshige Sasaki*****

Department of Mechanical Engineering, Faculty of Engineering, Kumamoto University
2-39 Kurokami, Kumamoto-shi 860, Japan
* Kumamoto Industrial Research Institute
3-11 Higashi-mati, Kumamoto-shi 862, Japan
** Division of Mechanical Engineering, Graduate School of Engineering, Kumamoto University
2-39, Kurokami, Kumamoto-shi 860, Japan
*** Nippon Tungsten Co.
2-20 Shimizu, Fukuoka-shi, 815, Japan

Electroconductive ceramics were machined by a wire electro-discharge machining method. The machining rate and surface roughness for various pulse durations were evaluated as a function of duty factor. It is obvious that there exists an optimum duty factor from the standpoint of machining rate, and that the optimum duty factor increases with increasing pulse duration, especially in machining zirconia ceramics. But, the maximum machining rate did not depend so much upon duty factor. The machined surface roughness increased generally with an increase in duty factor. This indicates that the roughness of the machined surface did not always increase with an increase in machining rate.

Key-words: Wire EDM, Electroconductive ceramics, Duty factor, Machining rate, Surface roughness

1. Introduction

The duty factor in wire electrodischarge machining means the ratio of the net electrodischarge time to the mean time per discharge. It can be changed by changing the rest time for the specified pulse length. It is understood that with a constant pulse length, the higher the duty factor, the larger the consumed energy per unit of time and the higher the machining efficiency is expected to be. However, too short a rest time makes cooling insufficient during discharge and prevents machining dust from being discharged smoothly, causing bad discharges such as continuous arc discharges and secondary discharges due to machining debris being more likely to occur. Thus, excessively high duty factors seem rather disadvantageous. It has been reported that as the duty factor increases, with a large pulse length in ceramics machining in particular, extraordinary discharges tend to occur from local concentration of discharges due to insufficient cooling time.[1,2] While quite a few studies have been done on the effect of various factors on machining properties in the area of wire electrodischarge machining of fine ceramics, there are none on the effect of the duty factor.[1,3-10]

Carrying out wire electrodischarge machining tests with three types of ceramics -- alumina, zirconia and sialon -- we investigated by varying pulse length how machining efficiency and surface roughness varied with duty factors.

Table 1. Chemical composition and properties of work materials.

	ALUMINA-TiC		ZIRCONIA-NbC		SIALON-TiN		SKD11(Hv720)
Composition (vol.%)	Al_2O_3	TiC	ZrO_2	NbC	Sialon	TiN	Cr11.0~13.0 C 1.40~1.60 Mo,V,Mn,など
	72.5	27.5	72.5	27.5	60	40	
Density(g/cm^3)	4.24		6.52		4.0		7.87
Vickers hardness Hv	2000		1450		1550		720
Fracture toughness K_{Ic}($MN/m^{3/2}$)	5.0		7.5		5.0		16.0
Bending strength(MPa)	900		1500		850		>980
E-modulus(GPa)	400		240		336		196
Thermal conductivity(cal/cm·sec·°C)	0.04		0.01		0.06		0.18
Thermal expansion(10^{-6}/°C)	7.85		9.4		5.1		12.9
Melting point(°C)	2050	3140	2710	3610	1900	2950	1800
Electrical resistivity (R.T.) (10^{-3}·Ω·cm)	10		6.0		0.7		0.0097

2. Test Method

Table 1 shows the compositions and properties of conductive alumina, zirconia and sialon as work materials and SKD11 steel used for comparison. All samples were 10mm thick. The wire electromachining system was the FUNUC TAPE CUT MODEL. **Figure 1** shows the machining method. Machining is carried out by pulse arc discharges generated between the wire (copper, 0.25mm in dia.) and the workpiece, where the voltage and the current are measured by a system composed of a Hall element current probe and a digital oscilloscope. **Figure 2** shows some results of this measurement. With the effect of the end face taken into account, the machining rate (cut area per unit time) was obtained by measuring the time between a point with 5mm cut from the end face and a point with 30mm cut. In addition, while an override of 100% was employed in machining for alumina and zirconia, overrides 100% (D.F. 3%) to 40% (D.F. 18%) were employed for sialon to obtain optimal conditions by avoiding wire breakage.

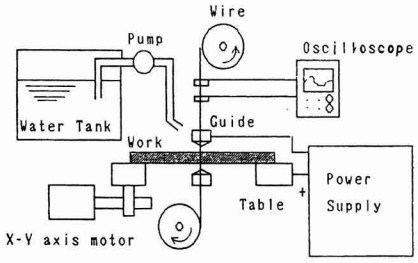

Fig. 1. Principle of the wire electro-discharge machining.

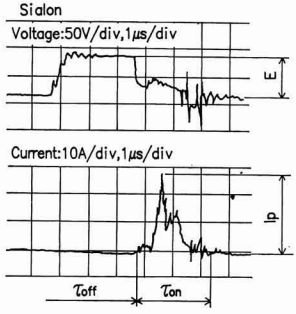

Fig. 2. Recording of electric voltage and peak current on discharging in the wire EDM.

Table 2. Wire-EDM operating conditions.

Voltage	60~80V, 100~110V
Peak current, Ip	5~30A
Pulse length, τ on	0.9~3.6 μS
Duty factor, D.F.	2.3~25.8%
Wire	ϕ0.25 Brass
Wire tension	5N
Fluid	Pure Water (6,8 l/min)

Table 2 shows the machining conditions in the test. For surface roughness, the mean roughness (Ra) was measured by using a Kosaka surface roughness meter (S3-C). To observe machined surfaces, a scanning electron microscope was used. In addition, D.F. was given by

$$\text{D.F.} = \frac{\text{Pulse length } (\tau_{on})}{\text{Pulse length } (\tau_{on}) + \text{ rest time } (\tau_{off})} \times 100\ (\%) \quad \cdots\cdots\cdots\cdots\cdots\cdots\cdots\cdots (1)$$

3. Test Results and Discussions

3.1. Machining Rates

Figure 3 shows the relation between machining rate and duty factor obtained in wire electrodischarge machining of alumina with pulse length varied against a constant peak current Ip of 22A. Evidently, irrespective of pulse length, machining rates peak at around a 7% duty factor. As the duty factor increases after the peaks, the machining rates decrease. This may be because of bad discharges due to insufficient rest times. **Figure 4** shows the results obtained with SKD11 for comparison. Here, as the duty factor increases, the machining rates rise, not reaching, with pulse length 1.2μs, a maximum at a 30% D.F. With steel, machining rates can also have a maximum. With alumina, as well as the other two ceramic samples, the limit duty factor which gives maximum machining rates is much lower than with steel.

Figure 3 shows that in a low D.F. range, a very high

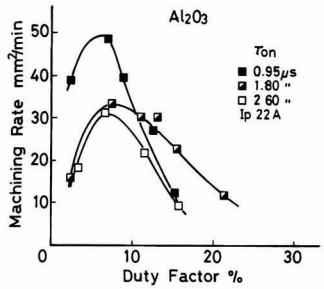

Fig. 3. Relation in cutting Al_2O_3 between duty factor and machining rate.

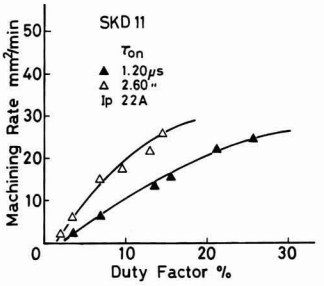

Fig. 4. Relation in cutting SKD11 steel between duty factor and machining rate.

machining rate is achieved with the shortest pulse length (0.95μs). This can be explained as follows. As shown later in **Fig.7**, with smaller pulse lengths, machining is mainly brittle fracture type removal. With larger pulse lengths or higher level of energy per discharge, it is fusion type removal. For reference, we have found that machining of zirconia which is a brittle fracture type with a pulse length of 0.95μs shifts to a fusion type as the pulse length increases under the same conditions. Thus, with a pulse length of 2.5μs, machining was a fusion type and machined surfaces showed many cracks probably caused during resolidification. These trends were also nearly the same with alumina. There are several reports on the effect of pulse length on discharge machining rates. For instance, it was discovered that with pulse lengths above a certain level in die sinking discharge machining of ZrB_2, machining rates were lower.[6] It is also reported that as the pulse length increases in die sinking discharge machining of Si_3N_4, the machining rate also increases but then levels off.[5] Thus, the effect of pulse length on machining rates is so complicated that it can not be simply defined. It was also found that the effect of pulse length on ZrO_2 wire discharge machining rates, described later, varied widely depending on whether the DF was at its upper or lower limit.

Figure 5 shows the relation between machining rate and DF obtained in wire discharge machining of zirconia. The pulse length was varied by 5 steps from 0.95 to 3.20μs. It is evident that with all pulse lengths, maximum machining rates are obtained at certain D.F. Prominent trends observed here are that with all pulse lengths, the maximum machining rates are nearly at the same level and that as the pulse length increases the curves shift rightward (or the critical D.F. rises), while high machining rate ranges increase. With the same D.F. the larger the pulse length, the longer the rest time. This possibly makes cooling more effective, while facilitating machining chip discharge.

Figure 6 shows the relation between machining rate and D.F. obtained with sialon. Also here, the machining rates peak with D.F. about 10%. Unlike for alumina and zirconia, the curves here do not show rapid drops after their peaks. This is because servo feed was adjusted with a machining stabilizer. Also, with a pulse length of 2.5μs, the machining rates are lower overall than those with the other two smaller pulse lengths. Figure 7 shows that while the machined surfaces with pulse lengths 0.9 and 1.8μs appear as a result of brittle fracture possibly due to rapid heating and cooling, that with a pulse length of 2.5μs definitely shows a result of melting removal. This proves that machining rates are higher in brittle fracture type removal; provided that the D.F. is small and there is a sufficient rest time to discharge machining chips. With a large D.F., as the machining rate rises, the discharge of machining chips increases. This naturally makes bad discharges more likely to occur, causing the machining rate to decrease rapidly. In addition, the lower machining rates in fusion type removal can also be understood from the fact that with SKD11, a material of a complete fusion type, machining rates are consistently lower than those with ceramics. These trends agree well with those with alumina and zirconia in D.F. ranges above the critical level and are opposite to those with SKD11.

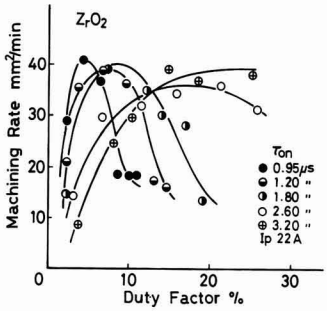

Fig. 5. Relation in cutting ZrO_2 between duty factor and machining rate.

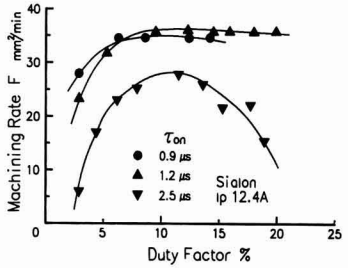

Fig. 6. Relation in cutting Sialon between duty factor and machining rate.

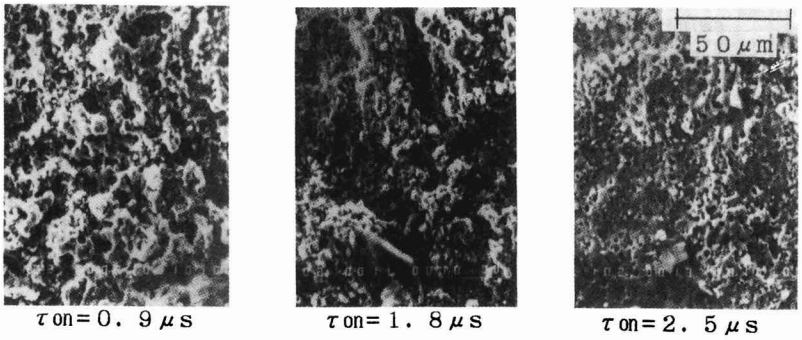

Fig. 7. SEM micrographs of cut surface of sialon.

For reference, **Fig.8** shows the relation between machining rates and D.F. obtained with the peak current value varied against a constant pulse length (1.2μs). Here, the higher the peak current value, the higher the machining rate expected. In D.F. ranges above its critical level, the machining rates with peak currents 8.8 and 12.2A are comparable. This is also because of the work of the stabilizer for adjusting servo feed mentioned earlier. Within the scope of the present test, this value seems the limit of machining rates.

In addition, the results of die sinking wire discharge tests for Si_3N_4-TiN with 20% D.F. by König et al. show that the higher the peak currents, the higher the machining rates.[3)]

3.2. Machined Surface Roughness

Figure 9 shows the relations between surface roughness and duty factor obtained in wire discharge machining of alumina and SKD11 steel. Evidently, as the duty factor rises, the surface roughness increases. With alumina here, the machined surface is particularly good with a small pulse length of 0.95μs. With SKD11 steel, as the duty factor rises, the surface roughness increases but unlike alumina, machined surfaces are worse with smaller pulse lengths. Zirconia surfaces obtained in wire discharge machining (**Fig.10**) are also worse with higher duty factors but are better with smaller pulse lengths, like the results for alumina. With alumina and zirconia, as shown above (Figs. 3 and 5), as the duty factor increased, the machining rates rose rapidly, reaching maximums with the critical duty factor. In contrast, as the duty factor increased, surface roughnesses changed slightly regardless of the critical duty factor.

Figure 11 shows the surface roughness of sialon. As the duty factor increases, surface roughness changes linearly and more mildly than with the other three materials. The surface roughness with D.F. varied against a constant pulse length (1.7μs) (**Fig.12**) also changes only a little. A close examination, however, of the surface with D.F. 18% can discover spots somewhat melted. This may be because of a shorter rest time than for the other cases. Here, unlike with alumina and zirconia, the smaller the pulse length, the greater the surface roughness. This may be because sialon contains TiN by 40%, much larger than the 25% in alumina and zirconia, which makes sialon machining more like a fusion type (as with metals) as the pulse length or supplied energy per pulse increases. This can also be understood from the fact that while the surface roughnesses for alumina and zirconia are 7 to 9 and 4 to 5μm Ra respectively, that of sialon is 1 to 2μm Ra, comparable with that of SKD11.

Various studies have recognized that generally, the higher the machining rate, the greater the surface roughness. For example, Bampa et al. have reported that as the wire machining rate with ZrB_2 increases, the surface roughness deteriorates. Similar trends have been discovered with silicon nitride, SiC and sialon.[6,7)] The results of our present study do not completely agree with such common opinions.

4. Conclusion

Studying the effect of D.F. and pulse length on the efficiency and the surface roughness obtained by wire discharge machining of alumina, zirconia, sialon and SKD11 steel, we reached the following conclusion:

1) As the duty factor rises, machining rates rise, reach peaks and then decrease. The critical D.F. which gives such maximum machining rates varies with the type of ceramics. For alumina and sialon, the critical duty fac-

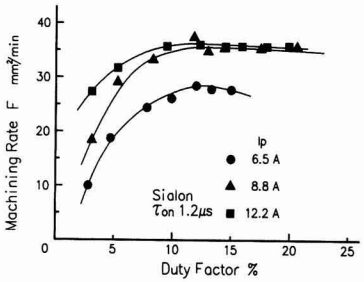

Fig. 8. Relation in cutting sialon between duty factor and machining rate.

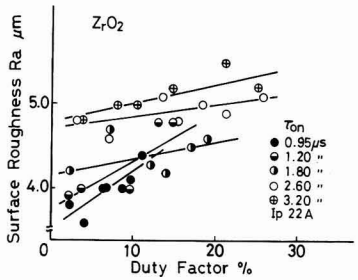

Fig 10. Relation in cutting ZrO_2 between duty factor and surface roughness.

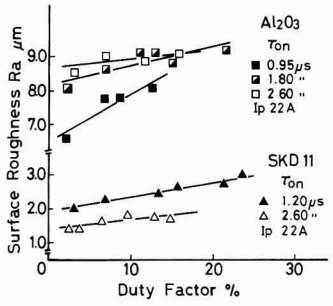

Fig. 9. Relation in cutting Al_2O_3 and SKD11 steel between duty factor and surface roughness.

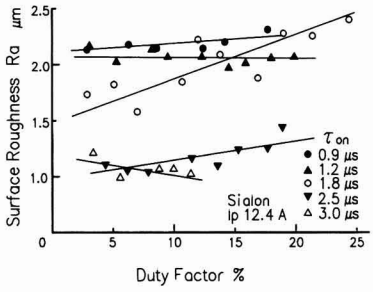

Fig. 11. Relation in cutting sialon between duty factor and surface roughness.

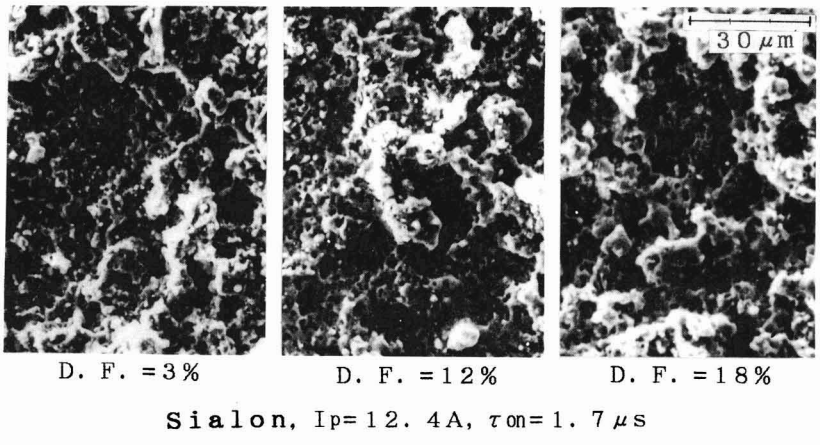

Fig. 12. SEM micrographs of cut surface of sialon.

tors are about 7 and 12% respectively regardless of pulse length. For zirconia, in the pulse length range: 0.95 to 3.20μs, the critical D.F. ranges from 4 to 20%. For SKD11 steel, there is no critical D.F. even with 30% D.F.

2) As for machining mechanisms, machining in lower pulse length ranges is a brittle fracture type. As the pulse length increases, machining turns to a fusion type. This scarcely depends on D.F. but as the D.F. increases substantially, the rest time decreases, causing machining rates to decrease due to bad discharges such as continuous arc and secondary discharges.
3) Maximum machining rates achieved with different workpiece materials are nearly the same, about 50, 40 and 35mm^2/min for alumina, zirconia and sialon respectively. These values are higher than those for SKD11. With alumina, maximum machining rates can be obtained by selecting smaller pulse lengths. With zirconia and sialon, maximum machining rates scarcely depend on pulse length.
4) Surface roughnesses obtained by wire discharge machining vary with workpiece materials. The values for alumina and zirconia are 7 to 9 and 4 to 5μm Ra. The value for sialon is 1 to 2μm Ra, which is comparable with that of SKD11. This favorable surface roughness is possible mainly because wire discharge machining of this material is a fusion type common with metals due to a higher content of conductive constituents in this material than in the other two ceramic materials. With alumina and zirconia, surface roughnesses increase linearly as the D.F. rises. With sialon, they also increase albeit moderately, proving that surface roughnesses do not quite rise proportionally to machining rates. The smaller the pulse length, the better the surface roughness with alumina and zirconia but the worse with sialon, as with SKD11.

Acknowledgements

For the present study, the wire discharge machine at Industrial Science and Technology Center, Kumamoto, was used. We sincerely thank Manager Ueda and the staff at the center, as well as student N. Kose and graduate student T. Watanabe at Kumamoto University. Mention should also be made of those concerned at Hitachi Metals Co., Ltd. and Nippon Tungsten Co., Ltd. who helped us prepare test samples.

References:

1) N. Saito, Machines and Tools, 33, 121-26 (1989).
2) T. Matsuo et al., Technical report, Engineering Dept., Kumamoto University, 38, 13-22 (1989).
3) W. König, D.F. Dauw, G. Leve, and U. Panten, Annals of CIRP, 37, 2, 623-631 (1988).
4) G.N. Leve, R. Wertheim, Annals of CIRP, 37, 1, 175-178 (1988).
5) H. Takeuchi, and E. Kamijo, Machines and Tools, 29, 4, 64-70 (1985).
6) K. Bampa, T. Sakai, and S. Okumiya, Journal of Ceramics, 94, 1, 214-23 (1986).
7) N. Saito, and N. Mori, Electromachining Engineering, 10, 30, 1-6 (1986).
8) T. Suzuki, Y. Ozaki, and T. Takawashi, Electromachining Engineering, 10, 30, 13-18 (1986).
9) M. Nakamura, K. Kubo, and T. Hirai, Journal of Ceramics, 92, 11, 54-59 (1984).
10) M. Nakamura, K. Kanayama, W. Kanematsu, and T. Hirai, Transaction of Ceramics Association, 96, 9, 901-06 (1988).

This article is a full translation of the article which appeared in Nippon Seramikkusu Kyokai Gakujutsu Ronbunshi (Japanese version), Vol.99, No.5, 1991.

Results of the Round Robin Fracture Toughness Test on Ceramics -- VAMAS Project --

Hideo Awaji, Tatsuya Yamada and Hiroshi Okuda

Japan Fine Ceramics Center
2-4-1, Mutsuno, Atsuta-ku, Nagoya 456, Japan

This report describes the results of the VAMAS international round robin test for evaluating fracture toughness of ceramics. Thirteen laboratories in Japan, France, Germany, UK, Canada, Belgium and CEC (JRC Petten) took part in the test. The values of fracture toughness obtained by the SEPB, IF and IS methods were compared with one another for gas-pressure sintered silicon nitride (GPSSN) and zirconia-alumina composites (ZAC). Also examined were indentation load dependence of fracture toughness measured by the IF and IS methods and loading rate dependence of fracture toughness by the SEPB method.

The results showed that the toughness values evaluated by the SEPB method have relatively wide scatter among the participants, suggesting some difficulty with this technique, the IS method gave the smallest scatter and the IF method the largest scatter. Fracture toughness measured by the SEPB method was dependent on the loading rate, especially for ZAC. This may have been caused by stress corrosion cracking. The values measured by the IF and IS methods apparently depended on indentation load.

[Received December 11, 1990; Accepted January 24, 1991]

Key-words: VAMAS project, Ceramics, Fracture toughness, SEPB method, IF method, IS method, Stress corrosion cracking

1. Introduction

The Versailles Project on Advanced Materials and Standards (VAMAS Project) is a project for scientific and engineering research in international cooperation, established at the Versailles Summit in 1982 to promote basic joint research on the standardization of test evaluation techniques for developing new materials like ceramics. This project has 14 groups at present, each of which is performing its own operations. Among them, the Ceramics Group is carrying out an international round robin test (RRT) for evaluating hardness, bending strength, and fracture toughness. In Japan, four organizations -- the National Research Laboratory of Metrology, Government Industrial Research Institute (Nagoya), the National Institute for Research in Inorganic Materials, and the Japan Fine Ceramics Center (JFCC) -- are performing joint experiments as well as the RRT. In addition, the VAMAS Ceramics Subcommittee (Chairman: Hiroshi Okuda), in which several researchers of private laboratories participate, has been organized to steer this project.

This report describes the results of RRT performed in 1988-89 to evaluate the fracture toughness of ceramics. This RRT was performed to clarify problems in standardizing test methods used for evaluating fracture toughness of fine ceramics. The preparation of a test plan and analysis were performed mainly by JFCC.

2. RRT Plan

Fine ceramics have great advantages of high strength at elevated temperatures, high hardness, and good corrosion resistance. However, they suffer from some disadvantages such as low fracture toughness, and their strength is heavily dependent on defects existing in the material. The problems in evaluating fracture toughness of ceramics include difficulties in preparing precracks, R-curve behavior, and stable crack growth. In this work, we clarified problems of methods for testing fracture toughness at room temperature by performing RRT to serve for standardization of fracture toughness test methods.

The test was performed by using the SEPB (Single Edge Precracked Beam),[1,2] IF (Indentation Fracture),[3] and IS (Indentation Strength)[4] methods. The SEPB method, specified in the Japanese Industrial Standards (JIS) as a fracture toughness measuring method at room temperature, has advantages of high reproducibility and small scatter. With this method, a precrack is formed by propagating a "pop-in" crack from a Vickers indentation or shallow slit by the bridge indentation method. The disadvantages of this method are that the precrack cannot be accurately read in measuring the introduced precrack from the fractured surface, and that this method is sometimes ineffective for toughened materials.[6]

The IF method, specified in JIS as a simplified method, is widely used in the industrial sector because it is simple and can be used for measuring even small specimens. However, this method has some limitations: its formula was derived from experience, the method is effective only for brittle materials in which cracks fully grow around the indentation, and the fracture toughness measured by this method is dependent on the indentation load.

The IS method is a simple method in which fracture toughness is determined from the bending strength of a specimen having Vickers indentation, with the advantage that fracture toughness can be calculated from the Young's modulus, Vickers hardness, and bending strength of the specimen so that there is no need to measure crack length. With this method, fracture toughness is analyzed by assuming that the cracks formed around the indentation grow stably as the bending load increases, until they propagate unstably at the maximum bending load. However, this method also has disadvantages: the use of semi-empirical

Table 1. List of participants

Countries	Laboratories
Belgium	•Research Center of Belgian Ceramic Industry
CEC	•Joint Research Center
France	•ENSCI (École Nationale Supérieure de Céramique Industrielle)
	•RHÔNE-POULENC
Germany	•Univrersität Karlsruhe
	•BAM (Bundesanstalt für Materialforschung und -prüfung)
U. K.	•NPL (National Physical Laboratory)
	•Harwell Laboratory
Canada	•National Research Council of Canada
Japan	•NIRIM (National Institute for Research in Inorganic Materials)
	•NRLM (National Research Laboratory of Metrology)
	•GIRIN (Government Industrial Research Institute, NAGOYA)
	•JFCC (Japan Fine Ceramics Center)

formula and dependence on indentation load.[6] Essentially, Vickers hardness shows significant indentation load dependence for ceramics.[7] This is the reason for the indentation load dependence of IF and IS methods using Vickers hardness.

In this work, we compared the values of fracture toughness obtained by these three methods by performing RRT, and also examined the indentation load dependence of fracture toughness measured by the IF and IS methods and the loading rate dependence of fracture toughness by the SEPB method. The RRT procedure was drafted by JFCC and decided after being discussed by the VAMAS subcommittee.

The specimens and the RRT procedure were sent to 23 participating laboratories, namely, 6 laboratories in the United States, 4 each in Japan and France, 3 each in the United Kingdom and Germany, and 1 each in Belgium, Canada, and CEC (Joint Research Center). Among these, 13 laboratories sent the test results, whose names are given in **Table 1**.

In Japan, the performance of RRT somewhat differs from the RRT procedure because the RRT was carried out before the international RRT. A particularly great difference in Japan is no use of the IS method.

2.1. Specimens

The specimens used in this experiment were gas-pressure sintered silicon nitride (GPSSN) and zirconia-alumina composites (ZAC). The mechanical properties of these materials are given in **Table 2**. The specimens are 3mm × 4mm × 40mm JIS bending test pieces, for which one surface (4mm-wide surface) was mirror polished with #2000 diamond wheel. Twenty polished specimens were sent to each laboratory. All twenty specimens were used for the IS method. One or two specimens that were broken in half after being subjected to the IS method were used for the IF method, and the remaining ones were used for the SEPB method.

Table 2. Mechanical properties of specimen

Properties \ Specimen	GPSSN (EC-141)	ZAC (UTZ-20)
Density [kg/m³]	3.22×10^{3}	4.9×10^{3}
Modulus of rupture [MPa]	900	1100
Young's modulus [GPa]	310	280
Hardness (HR45N)	87.2	86
Thermal expansion coefficient (R.T~800°C) [/°C]	2.8×10^{-6}	9.6×10^{-6}

2.2. IS Method

First, a Vickers indentation was put at the center of the mirror polished surface. The indentation load was 49N and 294N for GPSN, and 98N and 490N for ZAC. Ten specimens were prepared for each material. Then, a three-point bending test with a span of 30mm was made at a crosshead speed of 0.5mm/min. The value of fracture toughness was calculated by the following formula.[4]

$$K_{IC} = 0.59\,(E/H_V)^{1/8}\,(\sigma_c P_V^{1/3})^{3/4} \quad \cdots\cdots\cdots (1)$$

where,

K_{IC} : fracture toughness
E : Young's modulus
H_V : Vickers hardness
σ_c : bending strength
P_v : indentation load

2.3. SEPB Method

With the SEPB method, fracture toughness is determined by performing a bending test on a precracked specimen. For this reason, the value of fracture toughness obtained by this method may vary with the loading rate when the material is such that stress corrosion cracking is caused by moisture. In this work, we examined the loading rate dependence of fracture toughness by using two crosshead speeds of 1mm/min and 0.005mm/min.

The starter of precrack being a Vickers indentation, one indentation of 98N was used for GPSSN, and three of 196N for ZAC. Since the residual stress around the indentation affects the fracture toughness when the indentation load increases, a load as low as possible should be used. To facilitate the measurement of crack length from the fracture surface of the specimen, oil-based ink and acetone were penetrated after the introduction of precracking.

The bending test of the precracked specimen was made by the 16mm-span three-point bending method in accordance with JIS. The value of fracture toughness was calculated from Srawley's formula[8]:

$$K_{IC} = \frac{3SP}{2BW^2}\,a^{0.5}\,F(\alpha) \quad \cdots\cdots\cdots\cdots (2)$$

$$F(\alpha) = \frac{1.99 - \alpha(1-\alpha)(2.15 - 3.93\alpha + 2.7\alpha^2)}{(1+2\alpha)(1-\alpha)^{1.5}}$$

$$\alpha = a/W$$

where

S: support span

a : precrack length
W : specimen height
P : fracture load
B : specimen width.

2.4. IF Method

With the IF method, fracture toughness was determined under 98N and 196N (196N and 294N in domestic RRT) for GPSSN, and under 294N and 490N (only 294N in domestic RRT) for ZAC to examine the Vickers indentation load dependence of fracture toughness. 10 measurements were found for each load. Among many empirical formulas proposed to determine fracture toughness by using the IF method, the following formulas of Miyoshi et al.(3)[10] and Marshall and Evans (4)[3] were used.

$$K_c = 0.0264E^{0.5}P^{0.5}c^{-1.5}a \quad \ldots\ldots\ldots\ldots (3)$$

$$Kc = 0.036E^{0.4}P^{0.6}a^{0.8}c^{-1.5} \quad \ldots\ldots\ldots\ldots (4)$$

where

P : indentation load
a : half length of indentation diagonal
c : half length of crack.

Formula (3), being equivalent to that obtained by the study on standardization of fracture toughness tests conducted by the Japan Fine Ceramics Association,[9] is specified in JIS.

Table 3. The means and the standard deviations data of the fracture toughness measured by SEPB method for GPSSN and ZAC. Common CHSs are 0.005mm/min and 1.0mm/min. Other speeds are shown in parentheses.

MPam$^{1/2}$

Materials		Si_3N_4			ZAC		
CHS mm/min		0.005	1.0	others	0.005	1.0	others
PARTICIPANTS NO.	1	5.50±.276	5.64±.159		5.31±.106	6.37±.312	
	2	5.74±.24	5.44±.39		5.71±.21	5.81±.14	
	3	4.94±.41	5.16±.27		5.29±.57	5.65±.39	
	4		5.62±.13	(0.05) 5.42±.09		6.05±.34	(0.05) 6.20±.49
	5		5.62±.235	(0.01) 5.91±.313		6.10±.07	
	6		[11] 6.84±.31			[11] 7.30±.64	
	7	5.61±.159		(0.1) 5.95±.207	5.52±.130		(0.1) 6.40±.158
	8	5.61±.41	5.66±.24		5.31±.15	6.17±.22	
	9		6.42±.19	(0.08) 6.30±.08		6.56±.17	(0.08) 6.19±.12
	10	5.54±.12	5.88±.12		4.99±.27	6.27±.18	
	11	5.54±.19	5.47±.15		5.49±.18	6.29±.10	
	12	5.51±.75		(0.5) 7.11±1.88	5.22±.92		(0.5) 6.60±1.34
	13		[12] 5.72±.25	(0.05) [13] 5.70±.16		[12] 6.12±.12	(0.05) [14] 5.81±.17

[11] Span is 15mm [12] 7 specimens [13] 8 specimens [14] 6 specimens

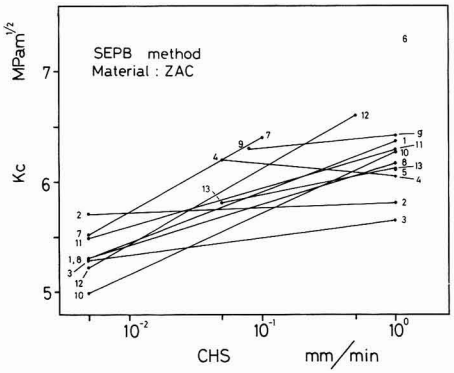

Fig. 1.. Loading rate dependence of the fracture toughness measured by SEPB method for ZAC.

3. Results and Discussion

3.1. SEPB Method

The SEPB method, developed and used in Japan, has been little known internationally, so that most participants experienced this method for the first time. The RRT was carried out in a difficult situation where each participant had to fabricate or purchase the bridge indentation jig, at much expense to the participants.

Table 3 gives the mean and standard deviation data of fracture toughness measured by the SEPB method for each participant. In this table, the participants are denoted by numbers, with no names being given.

The crosshead speeds are described by separating into 0.005mm/min and 1.0mm/min specified the RRT procedure and other speeds (the crosshead speed used is shown in parentheses). The table indicates that the standard deviations of measurements taken by each participant are relatively small and the differences between participants are also small when No.6 result is excluded, because it was obtained by the 15mm-span three-point bending test and has an extremely high values as compared with other results.

Figure 1 shows the loading rate dependence of fracture toughness for ZAC. In this figure, almost all lines have an increasing tendency. This is because an oxide-like silica causes stress corrosion cracking due to moisture in the air, and the crack grows stably. This phenomenon was observed to some extent on GPSSN containing alumina as an assistant. However, it is needless to say that tests must be made with many crosshead speeds to strictly evaluate the stress corrosion cracking property of a material.

Figure 2 compares the standard deviations of fracture toughness for ZAC at a crosshead speed of 1.0mm/min. In the figure, No.8 through No.11 data are of Japanese participants. Comparing these data, the standard deviations obtained by foreign participants are generally larger. This is because the SEPB method requires some skills, and the accuracy of jigs used in the experiment affects the deflection and length of precrack. In particular, the precrack lengths of Nos.2, 6, and 12 are great, some precrack length ratios (a/W) exceeding 0.6. In the measurement of material that

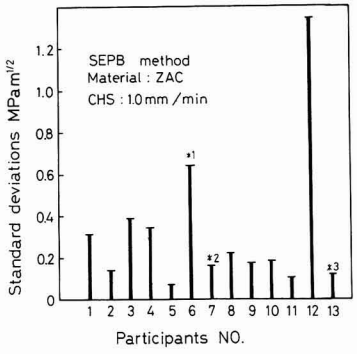

Fig. 2. Standard deviations of the fracture toughness measured by SEPB method for ZAC.

exhibits increasing R curve behavior, a value of fracture toughness higher than the actual value is obtained if the precrack is long. There is also a possibility of precrack growing stably rather than pop-in cracks. In this case, there may be a difference in the formation of process zone at the crack tip.[11]

3.2. IF Method

Table 4 gives the measurement results of fracture toughness measured by the IF method for GPSSN. Comparing the values obtained by the formula of Miyoshi et al. with those by the formula of Marshall and Evans, the former is lower than the latter, being closer to the values measured by the SEPB method. The difference in value between participants is particularly large for the indentation load of 98N. One reason for this is that the ratio of crack length to indentation diagonal length (c/a) was below 2.3 (under a load of 98N) for more than half of participants, though the ratio must be 2.3 or 2.5 and higher in order for the crack around the indentation in the IF method to be a fully growing median crack.[12]

Figure 3 shows the indentation load dependence of fracture toughness for ZAC. Almost all data indicate indentation load dependence, in which the value of fracture toughness decreases with increasing indentation load. This indentation load dependence may result from the fact that Vickers hardness depends heavily on indentation load, and this dependence somewhat differs from material to material.[7] The indentation load dependence of Vickers hardness somewhat differs from material to material, though the formulas (3) and (4) finally determined from experience include the indentation load dependence of fracture toughness.

The variation in data between participants shown in Fig.3 is very large particularly for ZAC. One reason for this is that the variation depends on the degree of mirror polishing of a specimen, and ZAC material cannot assume a satisfactory mirror surface merely by polishing. Another reason is that it is difficult to accurately determine the position of crack tip because ZAC material transmits light somewhat, so that measurement idiosyncracies are reflected by the measured values. Diamond indenter wear affects the size of indentation and the length of crack around the indentation. For example, **Figure 4**, showing the relation between the coefficient of variation (standard deviation/mean value) and the fracture toughness measured by the IF method under the indentation load of 294N for ZAC, indicates that the data with large coefficient of variation generally exhibits a high value of fracture toughness. When a worn diamond indenter is used, the variation becomes larger and the size of indentation is small, so the hardness and in turn the fracture toughness may be evaluated higher than the actual values.

Table 4. The means and the standard deviations data of the fracture toughness measured by IF method for GPSSN.
(1): Calculation by formula of Miyoshi et al.
(2): Calculation by formula of Marshall et al.

MPam$^{1/2}$

Indented Load (N)		98		196		294	
Used equations		(1)	(2)	(1)	(2)	(1)	(2)
PARTICIPANTS NO.	1	5.42±.127	5.92±.37	5.37±.175	5.86±.182		
	2	5.42±.28	5.90±.31	5.48±.20	5.96±.21		
	3	5.28±.15	5.73±.15	5.51±.12	5.98±.13		
	4	5.40±.124	5.86±.132	5.41±.090	5.87±.098		
	5	7.70±.276	8.29±.313	6.63±.327	7.17±.368		
	6	7.49±.749	8.10±.811	6.36±.417	6.88±.441		
	7	5.47±.167	5.93±.177	5.53±.303	5.94±.283		
	8			6.19±.24	6.70±.25	5.76±.16	6.23±.17
	9			5.93±.163	6.43±.177	5.70±.16	6.18±.17
	10			5.73±.19	6.21±.20	5.40±.07	5.85±.07
	11			5.70±.14	6.18±.15	5.65±.11	6.12±.12
	12	5.41±.17	5.89±.21	5.14±.11	5.60±.12		
	13	5.39±.08	5.86±.08				

3.3. IS Method

Table 5 gives the measured values of fracture toughness obtained by the IS method. This table indicates that the standard deviations of measurements and the differences between participants are very small. This may be because with the IS method, the crack length need not be measured and the fracture toughness can be calculated only from the bending strength and the hardness.

Figure 5 shows the indentation load dependence of fracture toughness measured by the IS method. The fracture toughness increases with increasing indentation load. In the figure, the data obtained by participant No.2 from a specimen annealed after indentation is included for reference. This high value of fracture toughness results from a decrease in residual stress around the indentation caused by annealing. The formula of Chantikul et al., which theoretically analyzes the effect of residual stress, becomes invalid for the specimen after annealing. This means that the IS method cannot be applied to fracture toughness tests at high temperatures.

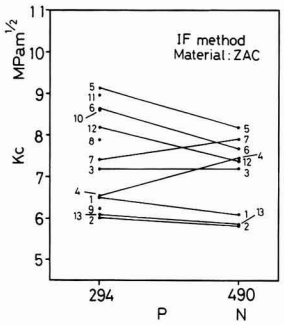

Fig. 3. Indentation load dependence of the fracture toughness by IF method for ZAC.

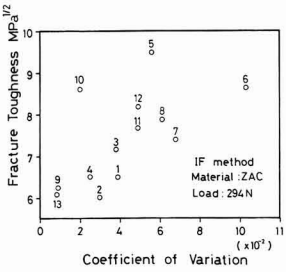

Fig .4. Relation between the mean and the coefficient of variation of the fracture toughness measured by each participant.

Table 5. The mean and the standard deviation data of the fracture toughness measured by IS method for GPSSN and ZAC.

MPam$^{1/2}$

Materials		Si_3N_4		ZAC	
Indented Load (N)		49	294	98	490
PARTICIPANTS NO.	1	5.78±.081	6.29±.149	7.00±.094	7.50±.135
	2	5.72±.12	6.31±.11	6.95±.26	7.46±.08
	3	5.61±.11	6.26±.17	6.54±.12	7.10±.08
	4	5.75±.171	6.29±.181	6.56±.101	7.30±.069
	5	5.99±.151		6.54±.180	
	6		6.54±.172		6.69±.113
	7	5.85±.175	6.40±.114	7.28±.165	7.58±.106
	8				
	9				
	10				
	11				
	12	5.99±.14	6.53±.19	7.14±.24	7.96±.29
	13	5.64±.17	6.33±.11	6.62±.18	7.59±.36

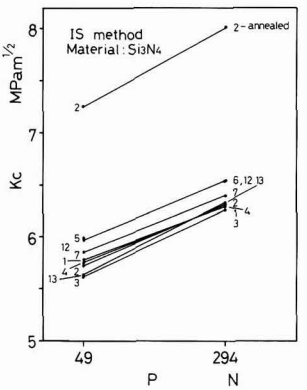

Fig. 5. Indentation load dependence of the fracture toughness measured by IS method for GPSSN.

3.4. Comparison between Test Methods

Table 6 summarizes the test results obtained by three test methods. The table indicates the range of mean fracture toughness and standard deviations, overall mean fracture toughness, standard deviations of mean values, and number of laboratories. The data of the SEPB method are for a crosshead speed of 1mm/min. The data of the IF method are under the indentation load of 196N for GPSSN and 294N for ZAC. The data of the IS method are under the indentation load of 294N for GPSSN and under 490N for ZAC. The values of fracture toughness measured by the IF method are calculated by the formula of Miyoshi et al. As seen from the table, the value obtained by the SEPB method is lowest, and the differences in overall mean values between methods are relatively small. The standard deviation of mean values for GPSSN is smallest with the IS method. The reason why very small scatter of values for GPSSN was given by the IS method having little difference between individuals is because the gas-pressure sintered silicon nitride EC-141 has small internal defects, providing uniform material property. For ZAC, even the IS method gave relatively large scatter, which suggests that it is difficult to compare the variation between test methods by using ZAC. To perform RRT, a material with a small variation in property must be chosen.

Table 6. Summary of Results

	Material GPSSN			Material ZAC		
	SEPB 1.0	IF 196N	IS 294N	SEPB 1.0	IF 294N	IS 490N
Range of mean fracture toughness .MPam$^{1/2}$	5.16 -6.42	5.14 -6.63	6.26 -6.54	5.65 -6.56	6.02 -9.15	6.69 -7.96
Range of std. deviations .±	0.12 -0.39	0.09 -0.42	0.11 -0.18	0.07 -0.39	0.05 -0.89	0.07 -0.29
Overall mean fracture toughness .MPam$^{1/2}$	5.66	5.75	6.37	6.14	7.36	7.41
Std. dev. of mean .±	0.33	0.45	0.11	0.26	1.06	0.38
Number of labs.	10	12	8	10	13	8

Some laboratories made negative comments on the SEPB method, while some praised it highly. For the SEPB method to become widely accepted, it is necessary to make accurate jigs and familliarize the measuring technique.

4. Conclusions

International RRT (for evaluating fracture toughness) was performed to provide basic data for preparing the international standards for fracture toughness tests at normal temperature. The following conclusions were reached from the analysis of variations and features of data.

1) Among the materials used, GPSSN was found to be homogeneous with few defects. This material could be used to compare variations in fracture toughness between test methods.
2) Relatively large variations found in the SEPB method for foreign laboratories may be caused by unfamiliarity with the test method. It is desirable to make the precrack forming technique more familiar.
3) The value of fracture toughness measured by the SEPB method showed significant load rate dependence on a material subject to stress corrosion cracking.
4) The IF method gave the largest scatter. The degree of scatter depends on the degree of mirror polishing of the specimen, light transmittance of the material, and wear of diamond indenter used. This method is prone to be affected by the idiosyncracies in measuring and equipment.
5) The IF method gave the smallest scatter. Although this method shows little difference between individuals, there are problems in using it at high temperature.
6) Both the IF and IS methods showed indentation load dependence.

Acknowledgments

This work was carried out with the cooperation of many laboratories in Japan and abroad. We wish to thank all laboratories participating in RRT. Also, we cordially thank the following researchers for participating in the RRT plan preparation and discussion of test results as members of the domestic VAMAS subcommittee: S. Nagai at the National Research Laboratory of Metrology, F. Wakai and M. Ito at the Government Industrial Research Institute, Nagoya, H. Tanaka at National Institute for Research in Inorganic Materials, M. Matsui at NGK Insulators, Ltd., S. Wada at Toyota Central Laboratory, K. Komeya at Toshiba Corporation (now, Yokohama National Univ.), H. Fujita at Asahi Glass Co., Ltd., and T. Nose at Nippon

Steel Corporation.
This work was carried out as part of "International Joint Research on Test Evaluation Techniques for Important New Materials," supported by Science and Technology Promotion Grants from the Science and Technology Agency.

References:

1) VAMAS Bulletin No.1.
2) T. Nose and T. Fujii, J. Am. Ceram. Soc., 71, 328-33 (1988).
3) T. Sadahiro, Journal of the Japan Institute of Metals, 45, 291-95 (1981).
4) D.B. Marshall and R.G. Evans, J. Am. Ceram. Soc., 64, pC182-83 (1981).
5) JIS R 1607 (1990).
6) H. Awaji, T. Watanabe, T. Yamada, Y. Sakaida, Tamiya, and H. Nakagawa, Transactions of the Japan Society of Mechanical Engineers, A56, 1148-53 (1990).
7) H. Awaji, Materials Testing Technology, 34, 256-62 (1989).
8) J.E. Srawley, Int. J. Fracture Mech., 12, 475-76 (1976).
9) Japan Fine Ceramics Association edit., "Study Report on Standardization of Fine Ceramics" (1988).
10) T. Miyoshi, A. Sagawa and T. Sasa, Transactions of the Japan Society of Mechanical Engineers, A51, 2489-95 (1985).
11) T. Fujii and T. Nose, IJIS International 29, 717-25 (1989).
12) K. Shinhara, Ceramics, 20, 12-18 (1986).

This article is a full translation of the article which appeared in Nippon Seramikkusu Kyokai Gakujutsu Ronbunshi (Japanese version), Vol.99, No.5, 1991.

^{29}Si MAS NMR Study on Structural Change of Silicate Ions in Tobermorite with Carbonation of ALC

Yasuhisa Ikeda, Yoshiyuki Yasuike, and Yoichi Takashima

Kashima Laboratory, Institute of Research and Innovation
1201, Takada, Kashiwa-Shi, Chiba 277, Japan

The structural change of silicate ions in 11Å tobermorite with carbonation of ALC was studied by solid-state high resolution ^{29}Si NMR spectroscopy. It was found that the tobermorite in ALC is an anomalous Al-substituted type and that the silicate ions have double chain structure with Si-O-Si bridges. In addition, it was suggested that the silicate ions in tobermorite change from the double chain structure to three-dimensional cross-linked framework with the carbonation of ALC.
[Received November 7, 1990; Accepted January 24, 1991]

Key-words: ^{29}Si NMR, ALC, Tobermorite, Carbonation, Silicate ion

1. Introduction

One of the aging problems in discussing the durability of autoclaved curing lightweight aerated concrete (ALC) is carbonation. This phenomenon of ALC involves 11Å-tobermorite (Tb), the major crystalline constituent, reacting with CO_2 in air with the presence of moisture to decompose into calcium carbonate (vaterite (V), aragonite (a) and calcite (C)), silica gel (SG) and water as follows.[1-4]

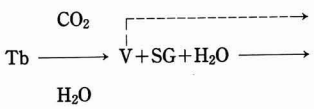

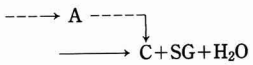

It is known that with the progress of this carbonation the bulk density of ALC increases while its porosity decreases. Moreover, drying shrinkage, a cause of cracks, is greater in the case of carbonated ALC; one reason for this is considered to be the polymerization of isolated silica gel.[5]

Until now, the decomposition process of tobermorite by carbonation has been studied on changes in crystalline substance (Tb→V, A, or C) by means of X-ray diffraction, whereas amorphous silica gel (regarded as a significant contributor to shrinkage) was not dealt with very much for its formation and polymerization, that is, as to how silicate ions composing the skeleton of tobermorite undergo a morphological change to form silica gel. This is attributed to the fact that it is difficult for conventional morphological analyses of silicate ions such as silicomolybdic acid method and trimethylsilylation method to perform accurate morphological analysis in the solid state.[6]

Lippmaa et al. conducted solid-state high resolution ^{29}Si NMR spectroscopy with various silicates, and found that there is a close relation between the morphology of silicate ions in the silicates and their ^{29}Si NMR chemical shift.[7] That is, the ^{29}Si NMR chemical shift of various silicate ions is in the range of -60 to -120ppm with the reference of tetramethylsilane (TMS), and as the polymerization degree of silicate ions rises from Q^0 (neso), Q^1 (soro), Q^2 (cyclo, ino), Q^3 (phyilo), and Q^4 (tekto) they shift to a higher magnetic field, showing that the ^{29}Si NMR method is quite effective for the morphological analysis of silicate ions. Wieker et al. studied the morphology of silicate ions in various synthetic tobermorites by the ^{29}Si NMR method, and found that 11Å-tobermorite is composed of silicate ions with a double chain structure (Q^2 and Q^3 types) and its branching site number decreases with an increase in the Ca/Si ratio.[8] Moreover, Komarneni et al. researched the morphology of silicate ions in Al-substituted tobermorites by the same method, and detected the presence of Q^2- and Q^3-type silicate ions as Wieker et al. did.[9] In addition, Ogai et al. recently coped with the structure of synthetic tobermorites and its structural change by heating, and reported that the presence mode of Q^3 is closely related to thermal structural change.[10] Further, Mitsuda reported that the silica skeleton of calcium silicate hydrates change into Q^4-type compounds by carbonation.[11]

This study describes the morphological analysis of silicate ions by the ^{29}Si NMR method, to find out how the silicate ions in tobermorite -- as the major constituent crystals governing the properties of ALC -- undergo morphological changes by carbonation.

2. Experiment

ALC used in this experiment was a commercial building material with a bulk density of 0.45 to 0.55g/cm^3 produced mainly from quartz sand and cement under saturated vapor pressure at 180°C. The carbonation of ALC was accelerated under the conditions of 20°C, 60% R.H. and 10% CO_2. The carbonation degree of carbonated ALC was obtained as follows: a sample was reacted with hydrochloric acid in a closed container with reduced pressure, and a pressure rise by the resulting CO_2 was compared with that of a carbonate (Na_2CO_3) with known chemical composition after decomposition by hydrochloric acid to determine the amount of CO_2.

The measurement of ^{29}Si NMR spectrum was conducted by a DD/MAS method with an observation frequency of 53.54MHz using JEOL JNM-GSH27T). The conditions of the measurement were: data point = 8k, spectral width =

20kHz, and number of scans = 2000 to 6000. The chemical shift of ^{29}Si NMR was measured with TMS as a reference. The identification of ALC crystal phases was carried out by powder X-ray diffraction. Additionally, the infrared (IR) spectra of samples were determined by a diffuse reflectance method with a resolving power of 4cm^{-1} and a measuring wavenumber range of 4000 to 450cm^{-1} using Perkin Elmer 1720FT-IR system.

3. Results and Discussion

Figure 1 shows the X-ray diffraction patterns of ALC without carbonation and with accelerated carbonation. The

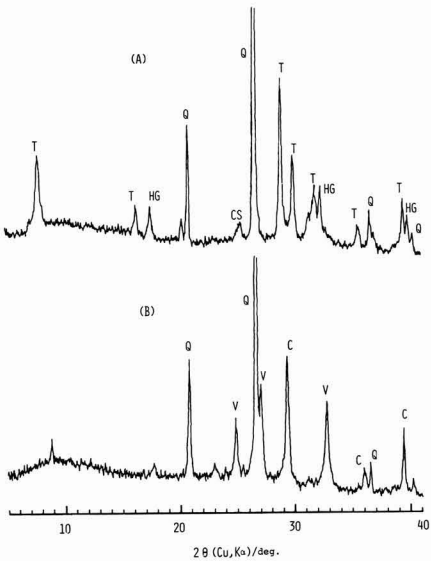

Fig. 1. X-ray diffraction patterns of non-carbonated ALC(A) and 80% carbonated ALC(B). Q: Quartz, T: 11Å tobermorite, C: Calcite, V: Vaterite, HG: Hydrogarnet, CS: Calcium sulfate.

uncarbonated ALC has 11Å-tobermorite, a major hydrate, while in the case of the carbonated ALC tobermorite is decomposed to form calcite and vaterite. In order to clarify such a decomposition process of tobermorite by the carbonation of ALC, the IR spectra of ALC of various degree of carbonation were measured and are shown in **Fig.2**. This indicates that with the progress of carbonation, an absorption peak at 877cm^{-1} and near 1450cm^{-1} increase while that near 970cm^{-1} decreases and absorption appears near 1045cm^{-1}. In the change of these IR spectra the absorption peaks at 877cm^{-1} and near 1450cm^{-1} are assigned to the absorption of ν_3 and ν_2 due to CO_3^{2-} of calcium carbonate formed by the decomposition of tobermorite, based on comparison with the measurement[12] results of IR spectra in the carbonation of C-S-H as well as those of calcium carbonate. On the other hand, spectral changes in the range of 970 to 1040cm^{-1} resemble a phenomenon in which the absorption of Si-O stretching vibration near 980cm^{-1} in C-S-H undergoes long wavenumber shift to an absorption site at 1080cm^{-1} due to silica gel with a decrease in a Ca/Si molar ratio and carbonation.[12,13] In fact, as seen from **Fig.3**, the IR spectrum of 92% carbonated ALC is almost the same as that of amorphous silica gel. These results suggest that spectral changes in the region of 970 to 1040cm^{-1} are considered to be due to the formation of silica gel by the decomposition of tobermorite.

In the next step, the morphological change of silicate ions constituting tobermorite during decomposition from tobermorite into calcium carbonate (chiefly calcite) and amorphous silica gel was investigated by measuring ^{29}Si NMR spectra of uncarbonated and 80%-carbonated ALC. The results are shown in **Fig.4** and **Table 1** with data reported by Wieker et al.[8] and Komarneni et al.[9] In Table 1, the peaks of uncarbonated ALC at −85.4 and −96.2ppm agree with those of pure tobermorite studied by Wieker et al. and of synthetic anomalous tobermorite by Komarneni et al. These peaks are considered to be assigned to Q^2 (chain middle group) and Q^3 (chain branching sites) type silicate ions respectively. Moreover, they coincide the chemical shift of xonotlite with a double chain structure. Further, Komarneni et al. found that in the anomalous tobermorite, peaks corresponding to Q^2 and Q^3 undergo lower magnetic field shift from −85 to −82ppm and from −95.7 to −91.5ppm respectively.[9] As in Table 1, Komarneni et al. attributed the peaks at −82 and −91.5ppm to Q^2 (1Al) and Q^3 (1Al).

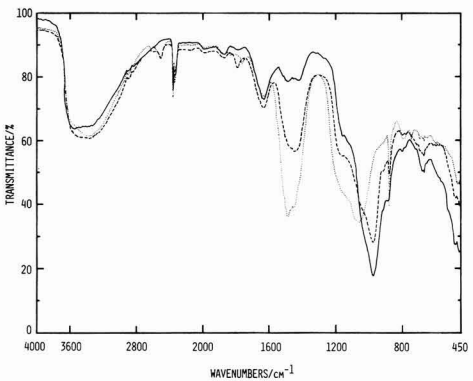

Fig. 2. IR spectra of carbonated ALC. — 3.6% carbonated ALC, -----: 47% carbonated ALC, · · · · ·: 92% carbonated ALC.

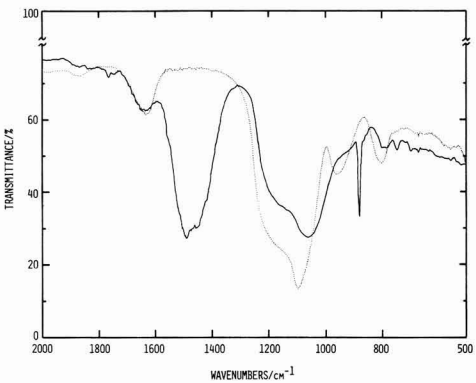

Fig. 3. IR spectra of 92% carbonated ALC and silica gel. —: 92% carbonated ALC, ·····: silica gel.

This suggests that the shoulder at −82ppm and peak at −91.7ppm of uncarbonated ALC are also attributable to Q^2 (1Al) and Q^3 (1Al) types. From the above results, it is concluded that 11Å-tobermorite in ALC is anomalous, its silicate ions have a double chain structure with Si-O-Si bridges at places, and some Si atoms are substituted with Al. Moreover, the peak at −107.4ppm coincides with the chemical shift of quartz so that it is probably ascribable to unreacted quartz sand (residual quartz) in ALC production.

In the ^{29}Si NMR spectrum of 80% carbonated ALC, peaks corresponding to Q^2- and Q^3-type silicate ions observed in uncarbonated ALC disappeared and a peak classified as a Q^4 type was observed at −102.1ppm. This indicates that with the carbonation of ALC the morphology of silicate ions composing the skeleton of tobermorite changes from a double-chain structure with Si-O-Si bridges to an irregular network structure. This morphological change is considered to correspond to the formation of amorphous silica gel during the carbonation of tobermorite. Consequently, ^{29}Si NMR measurement as adopted in this study allows further detailed investigation on the morphological change of silicate ions accompanying carbonation. The results are expected to elucidate changes in the properties of ALC by carbonation, especially the mechanism of drying shrinkage. Additionally, the method may provide keys for the elucidation of a pseudo-morphism,[2] which is a familiar phenomenon in the carbonation of tobermorite.

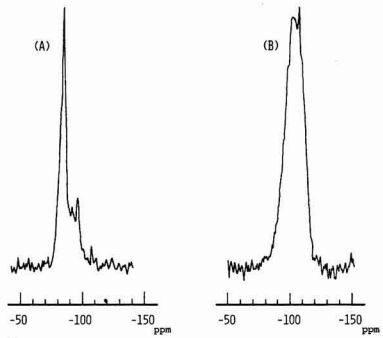

Fig. 4. ^{29}Si NMR spectra of non-carbonated ALC(A) and 80% carbonated ALC(B).

References:

1) S. Asano, Y. Kamaya, and Y. Inoue, Yogyo-Kyokai-Shi, 79, 303-311 (1971).
2) Z. Sauman, Cem. Concr. Res., 2, 541-549 (1972).
3) Z. Sauman and V. Lach, International Symposium on Autoclaved Calcium Silicate Building Products, 1-12 (1973).
4) Z. Yuping, L. Dedog, and S. Guokuang, 8th International Congress on the Chemistry of Cement, 93-98 (1986).
5) E.S. Silaenkov, Izv. Vyssh. Uchebn. Stoit. Arkhit., 18,67-70 (1975).
6) T. Yasue and Y. Arai, Sekko to Sekkai, No.212, 35-45 (1987).
7) E. Lippmaa, M. Magi, A. Samoson, G. Engelhardt, and A.R. Grimmer, J. Am. Chem. Soc., 102, 4889-4893 (1980).
8) W. Wieker, A.R. Grimmer, A. Winkler, M. magi, M. Tarmak, and E. Lippmaa, Cem. Concr. Res., 12, 333-339 (1982).
9) S. Komarneni, R. Roy, D.M. Roy, C.A. Fyfe, G.J. Kennedy, A.A. Bothner-By, J. Dadok, and A.S. Chesnick, J. Mat. Sci., 20, 4209-4214 (1985).
10) M. Ogai, Y. Ohno and T. Mitsuda, Nihon Seramikkusu Kyokai Nenkai Koen Yokoshu, 395 (1990).
11) T. Mitsuda, Seko to Sekkai, 229, 80-86 (1990).
12) K. Suzuki, N. Nishikawa and T. Hayashi, Dai 43-kai Semento Gijutsu Taikai Koenshu, 58-63 (1989).
13) K. Suzuki, N. Nishikawa and T. Hayashi, Semento Gijutsu Nenpo, 42, 36-39 (1988).

This article is a full translation of the article which appeared in Nippon Seramikkusu Kyokai Gakujutsu Ronbunshi (Japanese version), Vol.99, No.5, 1991.

Table 1. ^{29}Si NMR chemical shifts of silicate compounds.

Silicate	Starting materials	^{29}Si Chemical shifts(ppm from TMS)						Reference
		Q^0	Q^2(1 Al)	Q^2(0 Al)	Q^3(1 Al)	Q^3(0 Al)	Q^4	
Tb(Ca/Si=0.7)	Quartz + CaO	-79.7		-86.0		-96.4		8)
Tb(Ca/Si=0.8)	Quartz + CaO			-85.8		-95.9		8)
Tb(Ca/Si=0.9)	Quartz + CaO		-85*	-86.8		-97.8		8)
Tb(Ca/Si=1.0)	Quartz + CaO		-85.4*	-86.9		-97.6		8)
Tb(A)**	Quartz + CaO			-85.7		-95.7		9)
Tb(A)	Na_2SiO_3 + $FeCl_3$ + CaO			-85.7		-96.3		9)
Al-Tb(A)***	Na_2SiO_3 + $AlCl_3$ + CaO		-82.0*	-84.6	-92.0	-95.9		9)
Al-Tb(A)	Amorphous SiO_2 + kaolinite + CaO + KCl		-82.0*	-85.2	-92.0	-96.0		9)
Zonotlite				-86.8		-97.8		7)
SiO_2 (low Quartz)							-107.4	7)
SiO_2 (low cristobalite)							-109.9	7)
ALC	Silica + Cement		-82.0*	-85.4	-91.7	-96.2	-107.4	this work
Carbonated ALC	Silica + Cement						-102.1,-107.1	this work

*: Shoulder. **: Tb (A) =Anomalous tobermorite.
***: Al-Tb (A) =Anomalous Al-substituted tobermorite.

Low Resistivity Junction between $YBa_2Cu_3O_{7-x}$ Superconductor and Metals by Evaporation Method

Yutaka Takahashi and Tadatomo Suga*

Department of Precision Engineering, Faculty of Engineering University of Tokyo
7-3-1, Hongo, Bunkyo-ku, Tokyo 113, Japan
Present Address: Research Center for Advanced Science and Technology, University of Tokyo
4-6-1, Komaba, Meguro-ku, Tokyo 153, Japan

Electrical properties of an $YBa_2Cu_3O_{7-x}$/metal film/indium interface were examined by the DC four-probe technique. Contact resistance in the order of $10^{-6}\Omega\cdot cm^2$ was achieved with gold, silver and copper, while a high-resistive and non-ohmic junction was formed with indium only. Evaporation of Ib metals was highly effective in decreasing the contact resistance and such a technique will be of experimental or practical use in large current carrying applications of $YBa_2Cu_3O_{7-x}$.

[Received November 9, 1990; Accepted January 24, 1991]

Key-words: Low resistivity junction, $YBa_2Cu_3O_{7-x}$, Indium, Adhesion, Evaporated film, Gold, Silver, Copper

1. Introduction

Low resistivity junction between oxide superconductor and metal requires highly valuable techniques for both the basic experiment and practical applciation of devices. When an electrical current is applied to a superconductor through an external lead, the Joule loss occurs at the junction.

$$q = \rho_i j^2 \quad \cdots\cdots\cdots\cdots\cdots\cdots\cdots\cdots (1)$$

(ρ_i: interfacial resistivity j: electrical current density) Quench of superconductivity in the neighboring oxide superconductor at a joint area area due to the heating causes a serious damage of a sample at a high resistivity junction when an extremely large current is applied. Thus, low resistivity junction lower than $\rho_i = 10^{-5}\Omega\cdot cm^2$ is practically required.[1)]

On the other hand, since $YBa_2Cu_3O_{7-x}$ (YBCO) superconductor accomodates the oxygen stoichometry as large as x = 0 to 0.9,[2)] the superconducting properties are known to largely depend on this deficiency.[3)] Thus, it is desirable to fabricate a joint at room temperature in order that the superconducting properties prior to the process are possibly altered as oxygen is absorbed or desorbed because of heating accompanied during the process of joining with metals.

This paper reports our findings of loss resistivity interfacial electrical features of a junction of YBCO/In with an intermediate evaporated metal film. Vacuum evaporation is applied to form a metal film on YBCO, before In is joined therewith by pressure adhesion. Since this junction method is applicable to small, and larger areas, it can be used for not only bulk sintered specimens but also thin films and single crystals. The biggest advantage of th method is that it can be used easily at room temperature and in a short period of time.

2. Experimental Procedure

YBCO bulk samples used for junction were prepared by the solid state reaction method in the following manner,

1) Y_2O_3, $BaCO_3$ and CuO powders were mixed in a ratio of [Y]:[B]:[Cu] = 1:2:3.
2) The samples were calcined at 1193K for 12h.
3) The calcinated powder was ground in a ball mill and pressed into plate.
4) After the samples were sintered at 1223K for 12h and cooled in the furnace to 773K, they were retained for 48h before furnace cooling down to room temperature.

The superconducting transition temperature of these samples was about 90K, and the critical current density at 77K was 50~100 A/cm.[2]

YBCO/In joints were prepared in the following manner,

1) A pellet was cleaved by a file and divided into two parts to get an uncontaminted surface.
2) The metal (Au, Ag, or Cu) was resistive-heated in a tungsten basket in vacuum and a thin film of a few μm in thickness was evaporated on the fractured surface.
3) An In plate of 1mm in thickness (99.999% in purity manufactured by Furuuchi Kagaku K.K.) was adhered thereon, when plastic deformation amount of In was approximately 50%.

Evaporation and joint conditions are summerized in **Table 1**. The specimen joined with In and YBCO (YBCO/In film/In, specimen #7) was also prepared for comparison.

Interface resistance were measured by DC four-probe technique. The specimen was fixed to a cryostat with larger heat capacity made of copper blocks of several kg, and the atmosphere was substituted for helium to obtain better heat

Table 1. Contact characteristic.

Sample	Evaporation Condition (torr)	Contact Area (cm^2)	Contact Resistance 77K (μΩ)	Contact Resistivity 77K ($\mu\Omega\cdot cm^2$)
#1	Silver (4.0×10^{-6})	0.0550	76.1	4.18
#2	Silver (1.8×10^{-6})	0.0594	32.2	1.91
#3	Gold (2.4×10^{-6})	0.0728	70.6	5.14
#4	Gold (2.8×10^{-6})	0.1008	74.7	7.53
#5	Copper(4.0×10^{-6})	0.0416	95.0	3.95
#6	Copper(2.4×10^{-6})	0.0864	42.2	3.65
#7	Indium(2.0×10^{-6})	0.0899	1.30×10^{4}	1.16×10^{3}

conductivity. A silver paste was used for the connection of voltage terminals, while the external for electrical current were mechanically connected with the In plate using a screw.

The resistance, R, subject to the measurement in the electrode position shown in **Fig.1** is composed of the sum of In plate (R_{In}), metal film (R_f), bulk YBCO (R_{YBCO}) and the interfacial resistance such as metal film/YBCO (R_i) and In plate/metal film (R_i'). Since the metal film is several μm in thickness, it can be regarded as R_f=0. R_i' can be ignored against R as the interfacial resistance of In plate/metal film is below $3\times10^{-9}\Omega\cdot cm^2$. Thus, R is approximately expressed by the sum of three terms and R_i alone cannot be separated.

$$R = R_{In} + R_i + R_{YBCO} \quad \ldots\ldots\ldots\ldots\ldots (2)$$

In other words, since the contribution of In is estimated to be about 68μΩ at room temperature and 17μΩ at 77K when a joint area is $6\times10^{-2}cm^2$, R_{In} is compaable with R as will be shown in results of Table 1. On the other hand, R_{YBCO} occupies the great part of R in a normal conducting state.

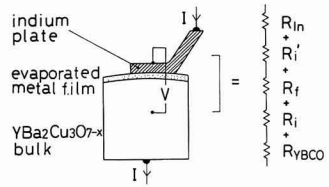

Fig. 1. Schematic diagram of the position of electrodes for four-probe method in contact resistivity measurement. A total resistance R is expressed by a sum of bulk components (R_{In}: indium plate, R_f: evaporated metal film, R_{YBCO}: YBCO bulk) and interfacial ones (R_i: YBCO/metal film, R_i': metal/film indium plate). Note that R_f and R_i' are negligibly small for R.

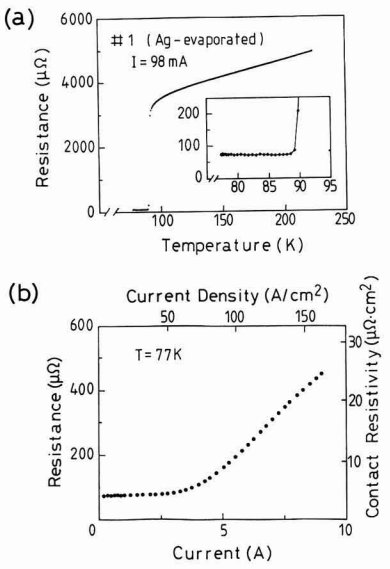

Fig. 2. (a) Temperature and (b) current dependence of resistance in YBCO/Ag film/In specimen (#1). An inset in Fig.(a) shows a magnified figure of the range of 75 to 90K.

However, the contribution dissipates in a superconducting state of a fully cooled-off specimen because of R_{YBCO} = 0.

$$R = R_{In} + R_i \qquad (T < \sim 90K) \quad \ldots\ldots\ldots (3)$$

Nonetheless, an attention has to be paid to the possibility that the contribution appears again when the electrical current density at the contact area exceeds the critical current density of YBCO.

3. Results and Discussion

3.1. Results of YBCO/Ag/In Junction

Figure 2(a) shows the temperature dependence of resistance of the YBCO/Ag/In junction (#1). R decreases linearly as the temperature lowers and drops discontinuously at about 90K. This is attributed that R_{YBCO} rapidly turns out 0 in eq.(2) corresponding to the superconducting transition of YBCO. The resistance becomes almost constant at R = 76.1μΩ down to 77K. An actual interfacial resistance R_i is lower because the measured value involves the contribution of In as mentioned in eq.(3).

$$R = R_{In} + R_i > R_i \quad \ldots\ldots\ldots\ldots\ldots\ldots (4)$$

Thus, a partial disintegration of an interfacial resistivity of YBCO/Ag is below $4.18\mu\Omega\cdot cm^2$ which is calculated from a nominal area of joining.

Figure 2(b) shows the current dependence of R at liquid nitrogen temperature in specimen #1. R is constant when a current (I) is small, while it shows a gradual increase at a region higher than 3A. This is the effect a partial disintegration of superconductivity in YBCO, and the YBCO/Ag interface is considered to be an ohmic junction. In an electrode layout of Fig.1, a local current density reaches the maximum level at junction interface, and when the level exceeds the critical current density of YBOC, there occurs resistance in the YBCO. In fact, a reduced current density divided by a contact area is in good agreement with the critical current density. As is shwon in an upper scale in Fig. 2(b).

Since heating at a junction is considerably reduced in such a low resistivity junction, it is possible to stably send an electric current of several amperes. **Figure 3** shows, for example, the change of voltage over the passage of time when a constant electrical current is continuously applied to specimen #1. The voltage increases little for I=1.00A and 3.03A as the interfacial heating is in the order of several mW, while the voltage markedly increases for I=5.03A because of the partial quench of YBCO. Joule heat is

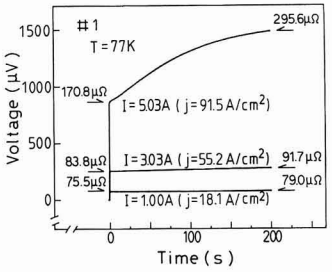

Fig. 3. Time dependence of voltage for several currents in specimen #1.

generated as the resistance occurs immediately below the interface when an electrical current exceeds its critical level. The heat is released to an outer region, but partially transferred to an inner part of a specimen thereby raising temperature. Superconductivity is disintegrated at this region and heat is generated, thus a closed loop is formed which lead to temperature rise and resistance increase in the whole system.

When oxide are characterized by much larger specific heat,[6] though they are smaller in thermal conductivity,[5] as compared with those of an alloy superconductor. Thus, the heat generated inside a thick specimen is hardly transferred to an outer region, and mostly consumed for temperature rise, although this change gradually occurs reflecting a larger heat capacity. In the measurement for 5.03A, voltage rose gradually through the above process, but tended to saturate after a balance was attained between the Joule heat generation and its dissipation outwards. In fact, an electrical current of I=5.03A was continuously applied for 30 min, but superconducting state was not completely disintegrated (quenched), (the resistance in this case jumps up to several 1000μΩ as the entire YBCO returns to a normal state, (refer to **Fig.2(a)**) and the coexisted normal and superconducting areas reached equilibrium. On the other hand, when I=10A is applied, heat release to an outer region was no longer sufficient enough to cover Joule heat, and caused an abrupt quenching.

Thus, such a problem under a large electrical current is attributable to YBCO itself, and interfacial heat generation is not predominant.

3.2. Results of YBCO/Au/In and YBCO/Cu/In Junctions

In case of Au and Cu, the same result was obtained.

1) The interfacial resistance was almost constant at 77 to 90K in the order of several $\mu\Omega cm^2$.
2) The I-V characteristics at 77K was linear, indicating an ohmic contact.

The above results are summarized in Table 1. An attempt to connect Ag and Au has been already made by various methods such as spattering, evaporation, supersonic welding, plasma arc spray, diffusion bonding, and spot welding.[7-19] An interfacial resistance is dependent on the junction methods and the presence or absence of post-annealing after junction. The values obtained by our present method are presumably included in a group of lower values obtainable by the junction methods at room temperature.

With regard to Cu, Ekin et al.[8] reported a value ρ_i=5700μΩ cm^2 at 77K, three order of magnitude larger than that the present value. Althought it is not clear whether this discrepancy is attributable to a difference between spattering and evaporation or other factors, our results revealed that Au, Ag and Cu are almost comparable as far as their interfacial resistance levels.

3.3. Results of YBCO/In Junction

As for Ib metals, an ohmic junction of several $\mu\Omega \cdot cm^2$ order was obtained, but its aspect was largely different in In being IIIb metal. **Figure 4** shows the temperature dependence and electrical current dependence of resistance in YBCO/In/In junction(#7). Resistance, R, shows semiconductive temperature dependence in Fig.4(a). It is evident that the majority of the resistance, R, is occupied by the interfacial resistance in view of the magnitude of a decrease of resistance in the neighborhood of 90K. On the other hand, Fig.4(b) shows current dependence of R at 77K was constant in a low current region, but it rapidly decreased at large current levels. (Since it is a non-ohmic junction, the interfacial resistance is meaningless unless an electrical current density is specified, a extrapolated value to $I \rightarrow$ is shown in Table 1.) Because similar results were obtained from the measurement of specimens where an In plate was directly joined to YBCO for reference, it was surmised that YBCO/In junction has non-ohmic and high resistance.

Ekin et al. conducted element analysis of In(2%Ag)/YBCO junction by Auger electron spectroscopy and found that a large amount of oxygen was contained in In.[12] Since a similar phenomenon was expected in the present specimens, the surface layer of YBCO is no longer superconductor because oxygen is withdrawn. Suzuki et al., noted that oxygen deficient YBCO is a p-type semiconductor and that the I-V properties of junction interface with metals can be expressed by the rectification theory.[19]

$$I = \alpha \{\exp(eV/k_BT) - 1\} \quad \ldots\ldots\ldots\ldots (5)$$

α: a function depending on the temperature and work function

In order to confirm validity of the equation, a constant, α, was calculated from R extrapolated to $I \rightarrow O$ in Fig.4(b). The I-V expression is replaced by the relationship between I and R which is drawn with the solid line in the figure. Decreasing of resistance is hardly in agreement with the experiment as the absolute values of electrical current is different by about one order. It is not reasonable to apply this theory as almost no rectification action was observed when the direction of current was inversed.

On the other hand, Takeuchi et al., assuming a model of the movement of oxygen that formed an oxide film with high resistance on the junction surface experimentally proved Schottky-type electrical properties in the La-Sr-Cu-O/Al system.[21] The I-V relation is expressed by

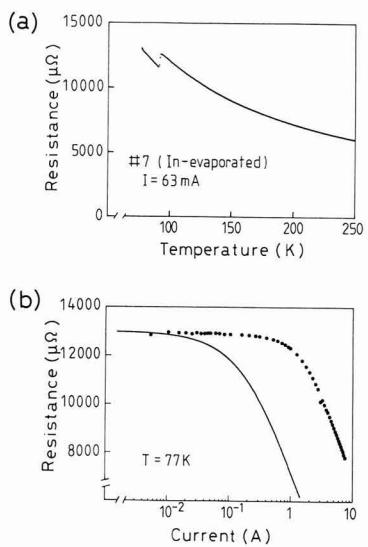

Fig. 4. (a) Temperature and (b) current dependence of resistance of YBCO/In film/In specimen (#7). A solid line in Fig.(b) shows a theoretical curve for p-type semiconductor/metal junction.

$$I = \alpha\{\exp(e\sqrt{eV/(4\pi\varepsilon d)}/k_BT) - 1\} \quad \ldots\ldots (6)$$

ε: dielectric constant of insulating phase, d: thickness of insulating phase.

The relationship is established in the YBCO/Al system as well,[22] but this model is also inappropriate as the linearity between log I-$\sqrt{V}$ was poor in the results of Fig.4(b). Deterioration of the YBCO surface and oxidation of the metal surface occur simultaneously in the junction accompanied by such a movement of oxygen. Thus, it is not easy to formulate an interfacial structure as it is quite different from the conventional models because of its complicated double-structure. It is not clear, too, whether such a difficulty is merely affected by chemical factors such as affinity with oxygen alone (Jia et al., who conducted an evaporation experiment on Yb that is a very easily oxidized metal reported that interfacial resistivity is in the order of several μΩ·cm[23]). Since it can not be denied that the formation of highly resistant interfaces in In and Al is possibly affected by the electron (band) structure of IIIb metals, further detailed investigations need to be carried out.

4. Conclusion

The junction of $YBa_2Cu_3O_{7-x}$ with In was conducted at room temperature by a simple method combined with the vacuum evaporation method, and the following electrical properties of its interface were obtained.

1) Since In is a metal that tends to be adhesive, it is possible to connect it with $YBa_2Cu_3O_{7-x}$ by mere mechanical pressing. However, it is intolerant to high electrical current transfer because of the resultant non-ohmic and high interface resistant that exhibits semiconductor-like temperature dependence (ρ_i = ~1 X 10^3μΩ·cm^2 at 77K).
2) Interfacial resistance is markedly reduced when Ib metal of several μm in thickness is evaporated in vacuum. Ohmic junction of several μΩ·cm^2 order can be obtained at 77K, and it shows little temperature dependence or constant in a range from 77 to 90K. The fact that almost similar properties were evidenced not only in noble metals such as Au and Ag with less affinity with oxygen, but also in Cu, base metal, suggests that the nature of this low resistivity junction is common to any Ib metal.

Acknowledgements

The present study was partially supported by special Coordination Funds for Promoting Science and Technology from Science and Technology Agency, Japan.

References:

1) S. Tanaka, Oyo Butsuri, 59, 647-648 (1990).
2) K. Kishio, J.Shimomura, T. Hasegawa, K. Kitazawa and K. Fueki: Jpn. J. Appl. Phys., 26, L1228-1230 (1987).
3) R.J. Cava, B. Batlogg, C.H. Chen, E.A. Rietman, S.M. Zahurak and D. Werder, Nature, 329, 423-425 (1987).
4) Y. Takahashi and T. Suga, Seramikkusu Ronbun Shi, 98, 1361-1364 (1990).
5) S.J. Hagen, Z.Z. Wang and N.P. Ong, Phys. Rev., B40, 9389-9392 (1989).
6) K. Kitazawa, T. Atake, H. Ishii, H. Sato, H. Takagi, S. Uchida, Y. Saito, K. Fueki and S. Tanaka, Jpn. J. Appl. Phys., 26, L748-750 (1987).
7) Y. Tzeng, A. Holt, R. Ely, Appl. Phys. Lett., 52, 155-156 (1988).
8) J.W. Ekin, A.J. Panson and B.A. Blankenship, Appl. Phys. Lett., 52, 331-333 (1988).
9) R. Caton, R. Selim, A.M. Buoncristiani and C.E. Byvik, Appl. Phys. Lett., 52, 1014-1016 (1988).
10) A.D. Wieck, Appl. Phys. Lett., 52, 1017-1019 (1988).
11) K. Mizushima, M. Sagoi, T. Miura and J. Yoshida, Appl. Phys. Lett., 52, 1101-1102 (1988).
12) J.W. Ekin, T.M. Larson, N.F. Bergren, A.J. Nelson, A.B. Swartzlander, L.L. Kazewrski, A.J. Panson and B.A. Blankenship, Appl. Phys. Lett., 52, 1819-1821 (1988).
13) S. Jin, M.E. Davis, T.H. Tiefel, R.B. von Dover, R.C. Sherwood, H.M. O'Bryan, G.W. Kammlott and R.A. Fastnacht, Appl. Phys. Lett., 54, 2605-2607 (1988).
14) Y. Suzuki, T. Kusaka, T. Aoyama, T. Yotsuya and S. Ogawa, Appl. Phys. Lett., 54, 666-668 (1989).
15) S. Jin, J.E. Graebner, T.H. Tiefel and G.W. Kammlott, Appl. Phys. Lett., 56, 186-188 (1990).
16) M.P. Maley, J.O. Willis, J.D. Katz, R.G. Castro and R.M. Aikin, Trans. Magn., 25, 2053-2055 (1989).
17) Y. Iye, T. Tamegai, H. Takeya and H. Takei, Jpn. J. Appl. Phys., 27, L658-660 (1988).
18) K. Mizushima, M. Sagoi, T. Miura and J. Yoshida, Jpn. J. Appl. Phys., 27, L1489-1491 (1988).
19) M. Suzuki, T. Fujii, K. Mori, K. Muto and T. Watari, Jpn. J. Appl. Phys., 27, 2003-2004 (1988).
20) J. Talvacchio, IEEE Trans. on Components, Hybrids and Manufacturing Technology, 12, 21-31 (1989).
21) K. Takeuchi, Y. Okabe, M. Kawasaki and H. Koinuma, Jpn. J. Appl. Phys., 26, L1017-1018 (1987).
22) Y. Takahashi, H. Takagi and T. Suga, Abstracts of 107th Autumn Meeting, Jpn. Inst. Metals, p.172 (1990).
23) Q.X. Jia and W.A. Anderson, J. Phys. D: Appl. Phys., 22, 1565-1567 (1989).

This article is a full translation of the article which appeared in Nippon Seramikkusu Kyokai Gakujutsu Ronbunshi (Japanese version), Vol.99, No.5, 1991.

Mechanical Properties of SiC Whisker/Al_2O_3 Composites Using Whiskers with Different Surface Roughness

Takashi Akatsu, Yasuhiro Tanabe, Shin Matsuura, Motoyuki Yamada*, Hajime Ishii, Mitsuhiro Munakata and Eiichi Yasuda

Research Laboratory of Engineering Materials, Tokyo Institute of Technology
4259, Nagatsuta-cho, Midori-ku, Yokohama-shi 227, Japan
* Corporate Research Center, Shin-Etsu Chemical Co., Ltd.
100-1, Sakato, Takatsu-ku, Kawasaki-shi 213, Japan

SiC whisker/Al_2O_3 composites containing whiskers with different surface geometries were fabricated and their mechanical properties were evaluated. The surface geometry of SiC whiskers was changed by heat treatment in an inert gas atmosphere. Composites using whiskers with a smooth surface showed higher fracture toughness K_{IC} and higher effective fracture energy γ_{eff} than those with rough surfaces. It is suggested that the smoothing of whisker surfaces leads to a decrease in frictional force at whisker/matrix interfaces and that pulling-out mechanism operate to toughen the composites.
[Received November 26, 1990; Accepted January 24, 1991]

Key-words: SiC whiskers, Composite, Surface roughness, Fracture toughness, Effective fracture energy

1. Introduction

The authors have been discussing that increased toughness of the SiC-whisker/Al_2O_3 composites results mainly from the "whisker pull-out" effects.[1,2] However, the whiskers actually pulled-out are much shorter than the original length of whiskers. It is, therefore, expected that the toughness of whisker-reinforced composites can be increased, if the latter are designed in such a way that the whiskers can be pulled out more easily.

Resistance force that works when the whiskers are pulled out comes conceivably from the chemically bonding force and frictional force at the whisker/matrix interfaces (hereinafter referred to simply as the interfaces)[3,4]. This study was carried out with special emphasis placed on frictional force working at the interfaces. A very high compressive residual stress (approximately 1GPa) acts on the whiskers in a radial direction in the SiC-whisker/Al_2O_3 composite, because of the difference between SiC and Al_2O_3 in thermal expansion coefficient,[5] from which it is judged that the normal force to interface, which yields frictional force, will be very high. It is therefore necessary to reduce the friction factor at the interfaces, in order to reduce resistance to pulling-out of the whiskers. In other words, the use of smooth whiskers promotes pulling-out of the whiskers due to reduced friction.

It is reported that SiC whiskers are changed in their shape when treated at high temperature in an inert gas atmosphere.[6]

In this study, SiC whiskers were heat treated in an Ar gas atmosphere to make their surfaces smoother, and the composites of alumina reinforced with these whiskers were prepared to assess their mechanical properties and investigate the effects of geometrical conditions at the interfaces on composite toughness.

2. Experimental Procedure

2.1. Sample Preparation

1) Starting Materials:
The SiC whiskers used in this study were Shin-Etsu Chemical's KSC-42' (average diameter: 1.1μm, average length: 35μm, catalog values) and KSC-42" (average diameter: 2.0μm, average length: 36μm, catalog values), both being of β-SiC. No significant SiO_2 layer was detected on the whisker surfaces by ESCA. The Al_2O_3 powder used as the matrix of each composite was Taimei Chemicals' Taimicron TM-100.

2) Heat Treatment of Whiskers:
The SiC whiskers, placed in a graphite crucible, were heat treated at 1900°C in an Ar gas atmosphere for 15min to 5h. The KSC-42' whiskers treated for 15 and 25min, and the KSC-42" whiskers for 15min were used to reinforce the composites.

3) Preparation of Composites:
The volume fraction of the whiskers in each composite was arranged at 20%. The composite was hot-pressed under conditions of 1750°C, 33MPa, 1h and an Ar gas atmosphere. The detailed conditions are described elsewhere.[1]

2.2. Analytical Procedure

1) Density:
Apparent density was measured by the Archimedes' method with water. It was confirmed that each sample had a relative density of 99% or more.

2) Strength:
Strength was determined by the 4-point bending test (JIS R1601). Each specimen for the bending test was prepared in such a way that the main cracks propagated in the hot-pressed direction.

3) Fracture Toughness K_{IC}:
Fracture toughness K_{IC} was determined by the 3-point bending test with a chevron notched beam.[1] The specimen was prepared in such a way that the main cracks propagated in the hot-pressed direction.

4) Effective Fracture Energy:

Effective fracture energy γ_{eff} was determined for the specimens having quasistatically propagated cracks until they were finally fractured in K_{IC} measurement.[7)]

5) Observation of Fracture Morphologies:

The fracture surfaces of the specimens tested to determine K_{IC} were analyzed by a scanning electron microscope (SEM) to observe the fracture morphologies.

3. Results and Discussion

3.1. Changed Morphologies of Whisker Surfaces

Figure 1 presents the SEM analysis results. Both KSC-42' and KSC-42" whiskers as the starting materials had rough surfaces, which were smoothened by the heat treatment; the surfaces became smoother as they were treated longer. It is accepted that a convex surface is generally higher in chemical potential than a concave surface, with the result that mass tends to transfer from a convex to a concave surface. The surface smoothened by the heat treatment conceivably resulted from the above mass transfer effects.

It was found, however, that the whiskers were grown to grains excessively when treated for 30min or more, and those whiskers treated for 15 or 25min were used to reinforce the composites. It was found by the SEM analysis that the whisker size itself was not changed much by the heat treatment. It was also confirmed by X-ray analysis that the β crystalline phase remained unchanged before and after the treatment.

3.2. Mechanical Properties

Figures 2 and 3 present the K_{IC} and γ_{eff} results. Smoothening the whisker surfaces is considered to greatly increase K_{IC} and γ_{eff} of the composite materials, assuming that the whisker properties (such as tensile strength) are not changed much by the heat treatment. In other words, it is expected that toughness of the SiC-whisker/Al_2O_3 composite can be improved, when the whiskers are designed to reduce frictional resistance at the interfaces and thereby facilitate their pulling out.

Figure 4 presents the SEM photographs of the fracture surfaces. As shown, more whiskers were pulled out when

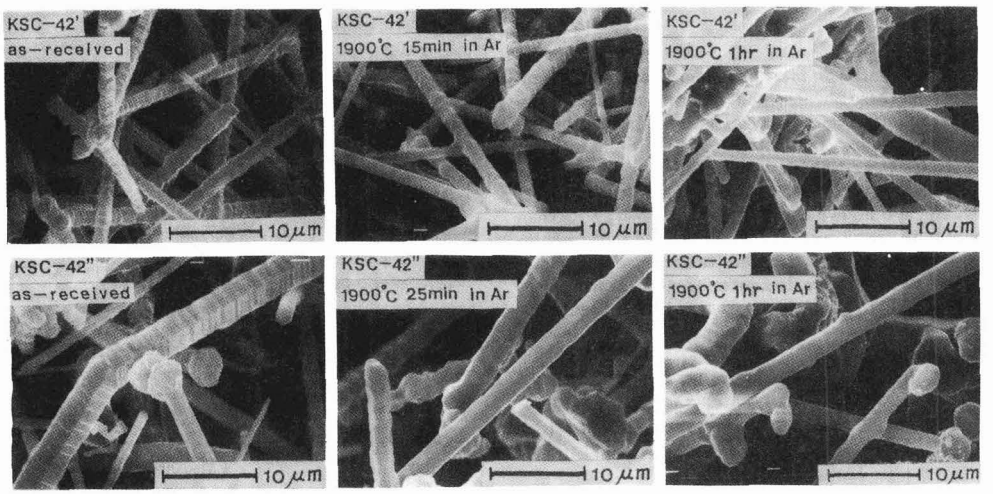

Fig. 1. SEM observations of SiC whiskers.

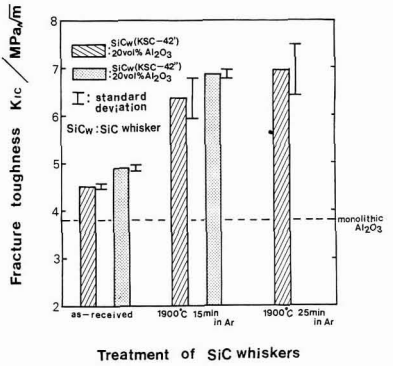

Fig. 2. Fracture toughness K_{IC} of SiC whisker 20vol%/Al_2O_3 composites.

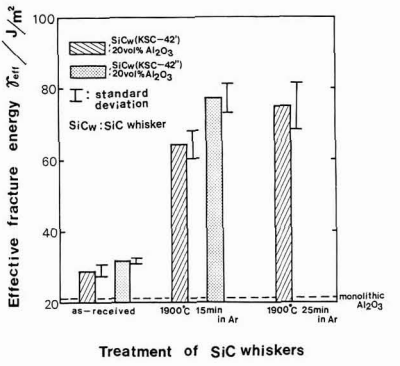

Fig. 3. Effective fracture energy γ_{eff} of SiC whisker 20vol%/Al_2O_3 composites.

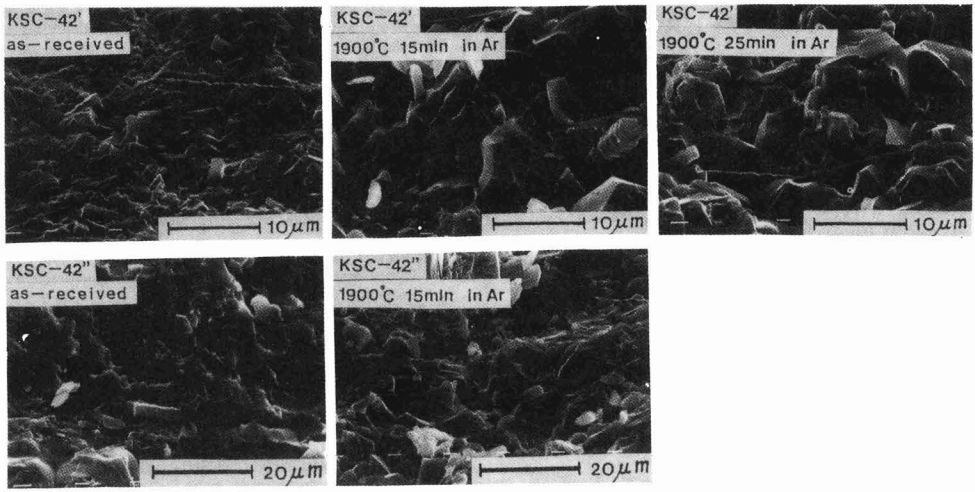

Fig. 4. Fractured surfaces of SiC whisker 20vol%/Al_2O_3 composites observed by SEM.

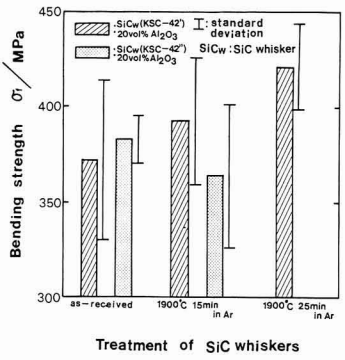

Fig. 5. Four-point bending strength σ_f of SiC whisker 20vol%/Al_2O_3 composites.

their surfaces were smoothened by the heat treatment. This feature of fractured surfaces also indicated that smoothening the whisker surfaces improved toughness greatly.

Figure 5 shows the bending strength σ_f results. In general, no significant effects of the heat treatment on bending strength were observed. The heat-treated KSC-42' whiskers seemed to give a slightly higher bending strength by heat teatment than the KSC-42" whiskers. Improved strength might be affected by improved fracture toughness K_{IC} resulting from the heat treatment of the whiskers, as predicted from linear fracture mechanics.

4. Conclusions

1) Heat treatment of SiC whiskers in an inert atmosphere smoothened the surfaces by reducing irregularities on them. The surfaces became smoother as treatment time was increased at the constant temperature.
2) The composite reinforced with the surface-smoothened SiC whiskers had a higher K_{IC} and γ_{eff} level than that reinforced with untreated whiskers. This is conceivably attributable to the enhanced "whisker pull-out" effects resulting from reduced frictional resistance at the whisker/matrix interfaces.

Acknowledgements
Part of this study was financially supported by Asahi Glass Co., Ltd.

References:

1) E. Yasuda, T. Akatsu and Y. Tanabe, Seramikkusu Ronbun-shi, 99, 52-8 (1991).
2) E. Yasuda, T. Akatsu, Y. Tanabe and Y. Matsuo, 3rd Ceramic Society of Japan Autumn Symposium Proceedings, pp.150-151, (1990).
3) T.N. Tiegs, P.F. Becher and L.A. Harris, Ceramic Microstractures '86.: Role of Interfaces., J.A. Pask and A.G. Evans eds., Material Science Research vol.21, Plenum, pp.911-917 (1988).
4) E. Yasuda, Y.Q. Wang T. Akatsu and Y. Tanabe, 9th High-Temperature Materials Basic Seminar Proceedings, pp.113-117, (1989).
5) Z. Li and R.C. Bradt, J. am. Ceram. Soc., 72, [1], 70-7 (1989).
6) A.J. Whitehead, T.F. Page and I. Higgins, Ceram. Eng. Sci. Proc., 10, [7-8], pp.986-997 (1989).
7) J. Nakayama, J. Am. Ceram. Soc., 48, 583 (1965).

This article is a full translation of the article which appeared in Nippon Seramikkusu Kyokai Gakujutsu Ronbunshi (Japanese version), Vol.99, No.5, 1991.

Information & Communications

News

Development of Synthetic Kaolinite

The Agency of Industrial Science and Technology's Industrial Research Institute (Nagoya) has established, jointly with the Research Association for Artificial Clay Synthesis Technology, a process for producing synthetic kaolinite as the starting material for various fine ceramic materials. Synthetic kaolinite as the compound of silica and alumina is given plastic properties by adding water-soluble ions or organic matter, adsorbed on or bonded to kaolinite during the curing process. The product consists of thin plate-shaped, hexagonal crystallites having a diameter of 1μm or less. Having asymmetric structures similar to those found in natural clay, it disperses well in a solvent. It also shows the desired plastic properties. It is highly white after sintering, because of smaller quantities of impurities such as iron and titanium. These favorable characteristics will make it a feasible starting material for various purposes including high-quality white porcelains, electronic ceramics (such as substrates), medical devices and catalyst carriers. The research association plans to approach a manufacturer to produce the synthetic kaolinite product, but will market it themselves. The price will be around 30,000 yen/kg.

Single Crystals of La, Ce, and B

The Science and Technology Agency's National Institute for Research in Inorganic Materials has developed a new material consisting of single crystals of lanthanum, cerium and boron useful as electron sources for various high-technological devices such as electron beam drawing units (for LSI production) and electron microscopes. The new material is lanthanum cerium boride, the crystals of which are grown by the floating zone (FZ) method. Seven parts of powdered lanthanum boride and 3 parts of powdered cerium boride are mixed, and the mixture is pressed into cylindrical shapes and fired at 1700°C. The sinters are treated by the FZ method for crystallization to produce single-crystalline cylinders 8mm in diameter and 6cm long. Lanthanum boride, used at present as an electron beam source, suffers directional slippages in the crystalline structure called subgrain boundaries, and the affected portions are not available as the beam source. The new material is completely free of these defects.

Silicon Nitride Ceramic Car Parts

Kyocera Corp. is commercially producing silicon nitride ceramic parts for turbochargers (used to improve acceleration characteristics). The part, an exhaust gas rotor roughly half the weight of conventional rotors of heat-resistant alloy, cuts acceleration response time from 1.5 to 1.0sec. Toyota Motors has decided to use the ceramic turborotors for its "Supra" cars in August, 1990. Kyocera is producing 10,000 parts/month at present; production volume will be increased the 30,000 parts/month by October, 1991, for other prospective customers.

Another ceramic part close to commercialization is the intake valve, in which the characteristics of silicon nitride will be fully exhibited, to increase revolution speed from 7,500 to 9,000rpm. Prospective markets will be worth tens of billions of yen should all existing valves be replaced by ceramic ones. Kyocera expects to increase sales of the ceramic automobile parts to 10 billion yen by 1995.

Large-Size Single Crystal Apparatus

Nichiden Kikai has developed an apparatus for growing large-size (10 to 20mm diameter) single crystals of high-purity oxides. The device is based on a modified floating zone (FZ) method and uses an oval reflection mirror condensing heat rays emitted from a halogen lamp onto the work, which is molten at max. 2150°C. The crystals can be grown at 0.2 to 20mm/h to a maximum length of 150mm. The apparatus uses no crucible to prevent contamination. The molten compositions can be controlled to produce high-purity crystals. The prospective applications of the large-size crystals include rutile type titanium oxide of high birefringence index, and materials for optical lasers, electro-optic modulators and ferroelectric devices. Price of the main body is 26.5 million yen. The company expects to sell 10 units a year to cement, glass and new material manufacturers. The optical crystal markets, now of on the order of 20 to 30 billion yen, will grow to the 100 billion yen level in 5 years.

Uniform of Sparingly Soluble Salts

A research group at Waseda University's Faculty of Engineering, led by Prof. S. Toyokura and Dr. Jivi Stabeak (present at the Czechoslovakian Academy of Science's Institutes for Inorganic Materials) has developed a process for producing uniform-size monocrystals of sparingly soluble salts based on the CDJ method (one type of reaction-crystallization method). Monodisperse microparticles, characterized by their uniform size, are attracting much attention as functional materials. The microcrystals of sparingly soluble salts, massively used as photosensitive materials, are required to be of monodisperse systems to satisfy increasing demands for higher-quality images. The reaction-crystallization process is characterized by chemical reactions between the starting materials introduced in the solution to form and separate the crystalline products. In the CDJ method, starting materials are supplied through two nozzles in jets (double-jet; hence the name CDJ) to stir the reaction solution and control crystal growth. The key to the process is optimization of the feed supply and stirring conditions. The research group has produced microcrystals of lead sulfate as part of the basic research program, and they consider the process to be applicable to the production of other monodisperse particle systems.

Organic-Inorganic Composite

Showa Technocoat has developed an organic-inorganic composite coating material sufficiently resistant to severe environments such as those found in exhaust ducts in incinerators, and started sending samples to prospective users. The common corrosion- and heat-resistant coating materials have hydroxide and ester groups. They are however not highly resistant to acids and alkalis, because of their rather weak molecule-molecule bonds. The newly developed coating material, on the other hand, has a structure similar to that of cross-linked siloxane, polymerized and cross-linked over a catalyst, in which no cross-linking agent is used. Its molecular structure is characterized by stronger molecule-molecule bonds, making it highly resistant to acids and alkalis. Having a thermal expansion coefficient close to that of stainless steel, it is free of cracks and allows no permeation, even when exposed to 260°C. The applicable areas include tanks and reactors in chemical plants, in addition to exhaust gas ducts. Applicability to salt-resistant piping for the Kansai New International Airport is also under study. The company expects to attain initial sales of 8 tons/year.

Zirconia-Base Resistance Heater Element

Shinagawa Refractory has developed a

zirconia-base resistance heater element operable at up to 2000°C in an oxidative atmosphere and a superhigh-temperature electrical oven that uses the elements. The heater element is of a composite prepared by mixing, forming, and firing a mixture of yttria-stabilized zirconia particles and fibers. It has a porous structure (porosity: 25%), in which the fibers account for 10 to 15%. Moreover, it is designed so that the lead wires can be tightly connected to the element, to solve problems resulting from thermal spalling and arc discharge between the lead and element. The element can be heated up to 2000°C at least 50 times (electricity turn-on time: 500h or more). At the same time, the company has developed related devices and materials for the superhigh-temperature electrical oven that uses these elements, including zirconia-base refractory material, electrical insulating material and automatic controlling mechanisms. Price of the heater element is 100 to 150 thousand yen for the model with platinum-rhodium terminals, and 80 to 100 thousand yen for that with lanthanum-chromite terminals. Price of the oven is 6 to 15 million yen, depending on capacity. The company is expecting initial sales of 100 million yen, and 400 to 500 million yen several years later.

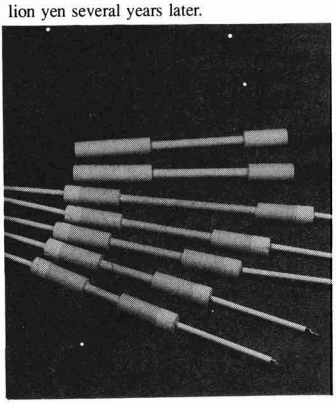

New Binder for Aluminum Nitride

Toshiba has developed an acrylic copolymer binder and applied it to the production of aluminum nitride substrate completely free from deformation during the firing process. The new binder is a copolymer of acrylic ester and methacrylate. Aluminum nitride powder and 15% of the binder are mixed into a slurry in a solvent of toluene, butanol and methyl isobutyl ketone. The slurry is then spread by the doctor blade method, while being heated to evaporate the solvents and binder, into a band-shaped green sheet. Density of the starting powder, which greatly determines shrinkage of the sinter, is 2.2g/cm^3, which is roughly 10% higher than that of the conventional one. Quantity of residual carbon after the binder is evaporated is 0.19%, which is roughly half that of the conventional amount. Toshiba applied molecular design techniques instead of traditional mechanical mixing to production of the binder in order to optimize the aluminum nitride substrate. The company plans to use this binder for aluminum nitride sinters requiring very high dimension accuracy.

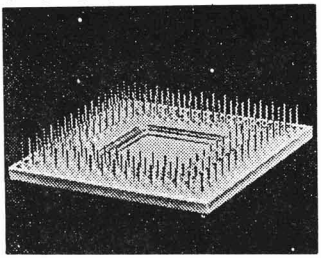

High-Temperature Thin Film Sensor

The Industrial Research Institute of Kanagawa Prefecture and Techno Seven Co. have jointly developed a technique to manufacture a high-temperature type thin film temperature sensor of 650° to 900°C without heat treatment. This development is based on electric shock chemical vapor deposition (EACVD). The resistance temperature characteristics of the sensor are a thermistor constant of 1880K at 0 to 100°C, and an initial resistance value of 141kΩ at 2.26°C. The sensor is highly stable, with a resistance variation rate of 0.16% and a temperature change of 0.1°C or less when it is left for 100 hours at 100°C. The prototype consists of a silicon substrate, bulb filament, gas σupply, and vacuum air outlet. The filament is heated to approximately 2000°C and its radiated heat causes the temperature of the silicon substrate to increase to more than 650°C. A DC current of 0.3A is applied between the filament and the substrate to produce a sort of plasma condition. Any desired temperature of the substrate is obtained by controlling the current. This results n a multicrystal silicon carbon of good quality.

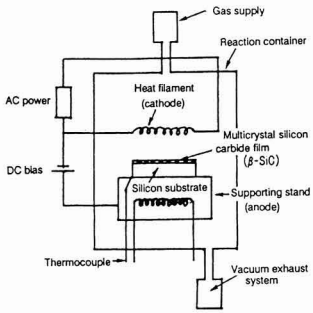

High-Precision Voltage Standard System Using Josephson Elements

Electrotechnical Laboratory has developed a new voltage standard system which can calibrate voltage at a resolution of 1.3volt/10^8 in a range from 1.4 to 1.9 volt. It is composed of 2400 to 3000 Nb superconducting elements. This high-precision standard voltage system is expected to have substantial influences on electronics industry in the field of semiconductor manufacturing, development of electronic instruments. It is composed of a container which can cool elements to the liquid helium temperature, an oscillator which can emit 94GHz waves with an accuracy of 10^{-10}. This system in an operating form is to be marketed by Advantest Co., Ltd.

Fibrous Oxide Superconductor

NRIM (National Research Institute for Metals) has developed polycrystalline fiber of Bi system superconductor. It is well known that the microorganization of a superconductor strongly affects its Jc; however, details of this fact have not yet been clarified. The achievement of NRIM may permit elucidation of this relationship which may be useful for R&D on higher Jc materials. The new technique applied the laser heating pedestal method whereby materials are heated and melted by laser beams and grow an crystal. The starting material is a superconducting bar prepared by sintering powder.

The tip of the bar is heated and melted by CO_2 laser, in which a seed crystal is contacted and pulled up to form a crystal. With this method, single phase crystal of Bi system superconductor is obtainable, and thus the Institute prepared polycrystalline Bi superconducting fiber 0.5mm in diameter.

Superconducting Flywheel

Ichinose Industry Co., Ltd., a rolling stock parts manufacturer, has developed a superconducting flywheel. The flywheel system is composed of a flywheel 40cm in diameter with a ring-shaped permanent magnet at its lower side, and 5 Y system superconducting bulk magnets which are arranged on a plate when cooled to the liquid helium temperature, the Y system magnets become superconducting magnets and levitate flywheel. A motor rotates the flywheel to store energy. For obtaining energy, the flywheel rotates a generator. This system is a prototype for demonstration tests.

A High-accuracy Method for Quantitatively Analyzing Impurity Contained in Superconductors

Governmental Industrial Research Institute, Shikoku, has developed a method to analyze impurity in superconducting oxides with high precision employing ICP. It can detect 19 elements including iron, silicon, etc. contained in superconductors with an accuracy of several micrograms.

It is indispensable to know an exact quantity impurity contained in superconductors for preparing them with good reproducibility. The newly developed technique is intended to cope with this problem.

A specimen in a liquid form is sprayed in the counter of a ring plasma at 6000 to

9000°C. When the specimen is heated sufficiently, it emits light. Analysis of the light and the intensities of its components reveals quantitative presence of elements.

Partial Cooling System for Josephson Elements

Fujitsu Laboratory Ltd. has, jointly with Shinko Electric Industry and Toyo Oxygen Co., Ltd., developed a partial cooling system for electronic elements which can be used in computer circuits boards.

A Josephson Junction element is high in switching speed at 1.5ps. However, it must be cooled to the liquid helium temperature to realize original performance. Conventionally the whole substrate on which JJ elements are mounted is cooled. If JJ elements only are to be cooled separately from general room temperature elements, such system requires a cable longer than 1m for connecting JJ elements and general elements. As a cable longer than 1m requires as much as 10ns for electrons to move through it, such system cannot be employed for a high speed computer which uses JJ elements. The newly developed partial cooling system is composed of a vacuum bottle 15cm in diameter and 70cm long to which a cable is connected. It can house a 5cm square JJ element chip, so that the JJ elements are connected to a general room temperature element with cable. Time necessary for electrons to move through the cable from JJ elements to general room temperature elements is 130ps, as the length of the cable is 2.4cm. As a result, a JJ element has to be mounted on the same PCB with general electronic devices. With this system, JJ elements can be used for those parts where high speed processing is indispensable. The clock frequency of such a computer is expected to be 1.1GHz.

Josephson Carry-select Adder

Fujitsu Laboratory has developed high speed 24 bit JJ element carry-select adder in which the minimum time required for adding is 360ps.

New Type Equipment to Fabricate Superconducting Film

National Research Institute for Metals has developed a device for fabricating superconducting oxides applying high frequency plasmas. This permits the fabrication of high-performance superconducting thin-film oxides without annealing treatments. The equipment evaporates a superconductor with a high-frequency plasma of 13.56MHz to deposit on a substrate. Deposition chamber pressure is 10 torr. The substrate is made of MgO_2. To fabricate thin-films, sintered powder of a Y system superconductor is provided by Ar gas to be evaporated. Vapor of the superconductor powder deposits on the surface of MgO maintained at 700°C to form a mirror thin-film which crystalline axes are properly arranged. Tc of the superconductor film is 91K. In the processes in which annealing is necessary reproduction of superconductors is difficult. As this new process requires no annealing treatment, superconducting films stable in their characteristics are easily obtained.

Trial Manufacture of Superconducting Energy Storage Device

EPDC has, jointly with Toshiba, developed a superconducting energy storage device (SMES), and carried out demonstration tests to obtain data on stability in performance, control system, etc. SMES aims at storage of electric power in superconducting coil to cope with sudden fluctuation in loads.

The newly developed device is has a capacity of 16KJ(4kWh). It is composed of a superconducting coil and an AC/DC converter (output 5.23kV) being connected to a 3kV transmission line.

The AC current obtained from the transmission line was stored in the superconducting coil after converted from AC to DC. When load on the transmission line fluctuates, the coil discharges electric power to stabilize the voltage level.

Bulk Magnet of Oxide Superconductor to Generate Magnetic Flux of 1.35T

Nippon Steel Corp. has developed a high temperature superconductor for bulk magnet which generates 1.35 tesla. Its Jc is 37,000A/cm^2 under 1 tesla at 77K.

It measures 42mm in diameter and 15mm thick as almost single-gained bulk.(Fig.1)

The magnetic flux was measured with afixed hole element between two specimens at 77K. In the case that a 1.5T magnetic field is impressed during cooling and then removed after cooling, the bulk showed 0.72T after 100s and 0.67T after 1000s. These values are much larger than those of Nd-Fe-B system (0.45T) magnet which has been the strongest magnet.

When two laminated superconductors are impressed with 1.5T, they indicated 1.35T after 100s. The value decreases as time posses. Fig.2 shows its change. They displayed1.28T after 2000s. It is estimated that the value will be 1.00T even after 1 year.

Now the application of the Y-Ba-Cu-O system superconductor is being expected for magnetic levitation, superconducting bearing, bulk magnet, etc.; however, it is indispensable for the Y system superconductor to show enough magnetic flux intensity with large bulk. New achievement may permit operational use of the Y system superconductor in the near future.

NSC has improved the QMG process (quench and melt growth) to fabricate Y system superconductors. The QMG process is one of melting processes for high Jc oxide superconductor manufacturing. In this process, Y-Ba-Cu-O system suprecoductor powder green is molten at 1400°C and cooled rapidly with 2 copper plates to make a plate

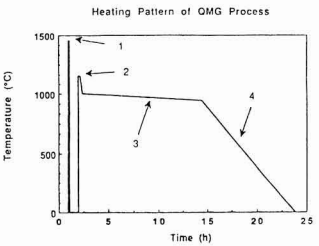

Fig. 1. Heat treatment pattern of QMG method, (1) Melt and quick cool step, (2) Partical melting step, (3) Slow cooling step, (4) Cooling step.

Photo. Bulk of superconductor which is pulling up 3kg heavy.

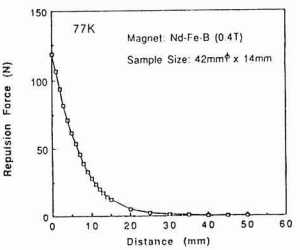

Fig. 2. Repulsion force of the bulk magnet (42mmϕ × 14mm).

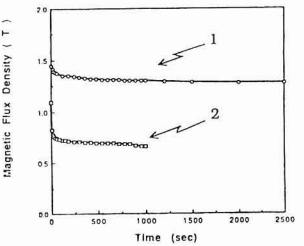

Fig. 3. Chang in magnetic flux against time elapse (1) Change in magnetic flux intensity of laminated bulk superconductor, (2) Change in magnetic flux intensity of single bulk superconductor.

precursor. This precursor is again heated to 1100°C to melt partially, then cooled with the temperature decreasing at a rate of 1°C/h. (Fig.3) With this process, the microorganism of the bulk material shows that YBa_2Cu_3Ox(123) grain size become large and a matrix is formed in which fine Y_2BaCuO_5(211) phase of several μm size is distributed uniformly.

Y System VTB Element

Prof. T. Goto, Electrical Communication University, has on an experimental basis fabricated Y system VTB, one of Josephson Junction elements. He confirmed that the test-fabricated VTB displayed JJ characteristics when the width of a groove carved was 0.08μm.

For the device, Y system superconductor thin film was fabricated on the surface of MgO substrate with sputtering. Thickness of the film was 0.3μm. On the film, a groove 0.08μm wide and 0.2μ deep was carved. When a current was applied at 4.2K, JJ characteristics generating 26μV appeared for over 300μA.

A VTB element has been made of Nb, but never an oxide superconductor.

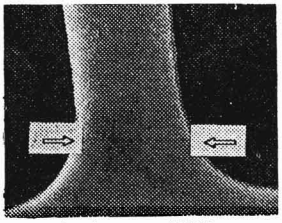

Photo. Microphotogram of VTB.

Superconducting Magnetism Shielding Device

Assoc. Prof. M. Takada, Nagaoka Technology and Science University, has, jointly with Nippon Cement Co., Ltd., developed a high-performance Bi system superconducting magnetism shielding device which can shield

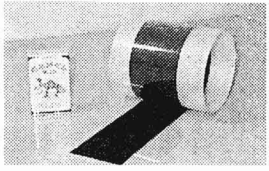

Photo. Shielding material.

24 gauss of magnetism in the direction from outside to inside, 34 gauss in the direction from inside to outside.

It is a cylindrical device for which flake superconductors were arranged like fish scales. To fabricate sheets, the plastic sheet manufacturing process for IC packaging was applied.

A conventional shield is made with superconducting powder, while the newly developed shield is made of scale-like flakes as material so that shielding power becomes larger.

Abstracts of Articles on Ceramics from the Selected Journals of the Academic Societies

The Journal of the Metal Finishing Society of Japan
Vol.42, No.1, 1991
p.84-88

Effect of Matrixes on Wear Characteristics of SiC Composite Coatings

Masayoshi NISHIRA*, Kenji YAMAGISHI* and Mamoru SUGIMOTO**

Composite coatings consisting of SiC particles codeposited into electroless nickel, electro nickel and copper matrix were produced, and their wear characteristics were examined by an abrasive wheel wear test. When the rate of deposited depth was constant, abrasion loss increased with increasing SiC particle size. Loss decreased with excessive SiC content in the deposition. It was found that the optimum rate of deposited depth lies between 60 and 80 percent. The wear characteristics of the composite coatings obtained by electroless nickel plating were better than those obtained by other platings.

Key Words : Composite Coating, Silicon Carbide, Wear

Journal of the Japan Institute Metals
Vol.55, No.1 1991
p.67-71

Measurements of Surface Acoustic Wave Propagation Velocity of Partially Stabilized Zirconia Joined to Metals

Toshio Narita* and Tatsuo Ishikawa*

Using a reflection-type acoustic microscope, surface acoustic wave (SAW) velocities were measured with a frequency of 500 MHz on the partially stabilized zirconia (PSZ) ceramics itself as well as those joined to nickel-Kovar alloy, with and without external stresses.

The relationship between SAW velocities (V_R, m/s) and tension stresses (σ, MPa) was given by the equation; $V_R = -0.21\sigma + 3270$. With this relationship, SAW velocities measured on the ceramic surface of the joint were transformed into stress and its distribution.

For the joint as-bonded, the largest tension stress of ca. 1 GPa was observed at the metal/ceramic interface and then it decreased rapidly far from the interface. With applying external load, the stress at the interface was unchanged, whereas the stress gradient tended to be steeper. After broken down the joint, a flat distribution was observed for the ceramic surface detached from the metal, showing residual stress free.

It was proposed that an acoustic microscope equipped with a minute loading unit shows considerable promise for non-destructive and localized evaluation of stress and its distribution on the ceramic surface, with and without external stresses.

Keywords: *scanning acoustic microscope, surface acoustic wave, ceramic-metal joint, partially stabilized zirconia, thermal residual stress, non-destructive evaulation, ultrasonic microspectroscopy*

Journal of the Japan Institute Metals
Vol.55 No.1 1991
p.72-78

Fatigue Crack Propagation Characteristics in SiC_p/6061-T6 Composite*

Toshiro Kobayashi**, Hiroyoshi Iwanari***, Shinji Hakamata****, Mitsuo Niinomi** and Hiroyuki Toda****

Researches and developments concerning aluminum matrix composites which are excellent in specific strength and specific modulus have been reported and applications of aluminum matrix components are expected as the structural materials of composites of automobiles and aircraft. However, there are few reports on the fatigue crack propagation characteristics which are very important for the design of structural materials. Since composites fracture in a complicated manner such as exfoliation between matrix and reinforcement or failure of reinforcements. Therefore, such properties as well as tensile strength should be evaluated for the applications of aluminum matrix composites as structural materials especially from the viewpoint of the guarantee of higher security.

The effect of volume fraction of SiC particles on the fatigue crack propagation characteristics of 6061 aluminum alloys reinforced with SiC particles (SiC_p/6061-T6 composites) manufactured by powder metallurgy process were investigated. The following results were obtained. In a higher stress intensity range, unstable fatigue crack propagation was found as the threshold stress intensity range ΔK_{th} and $\Delta K_{eff.th}$ increased with increasing content of SiC particles. However, $\Delta K_{eff.th}$ was suggested to be solely a function of the mean SiC particle size and to be independent of the volume fraction. This implies that for near-threshold crack extension, the maximum plastic zone size at the crack tip must exceed the mean SiC particle size.

Keywords: *SiC_p/6061-T6 composite, fatigue crack propagation, Paris' law, crack closure, fatigue threshold*

Journal of the Chemical Society of Japan
No.2, 1991
p.110-119

Synthesis of High-silica Zeolite Y

Akira YOSHIDA

Government Industrial Research Institute, Kyushu ; Shuku-machi, Tosu-shi 841 Japan

Zeolite Y with SiO_2/Al_2O_3 molar ratios=5.5~6.0, were synthesized from the reaction mixtures whose molar ratio were $(2.541\text{-}2.943)Na_2O\text{-}Al_2O_3\text{-}(9.81\text{-}13)SiO_2\text{-}(104.2\text{-}120.4)H_2O$, using colloidal silica, silica sol and sodium aluminate solution. The changes in chemical composition of solid and liquid phases on the course of zeolitization were analyzed by XRD, MASNMR, SEM observation, and chemical analyses. After the ageing at 25℃ for 24 h, only a small amount of silica reacted with sodium aluminate solution, and the concentration of silica in liquid phase was very low. After the heating at 99.5℃ for 1 h, ^{29}Si-MASNMR signals shifted to lower fields, and the concentration of silica species increased up to 1.2~1.6 mol/dm^3, though the concentration of aluminate ions decreased to 0.01~0.02 mol/dm^3. During the induction period, the concentrations in liquid compositions were kept at nearly constant. With decreasing Na_2O/SiO_2 molar ratio of reaction mixture, Na^+/SiO_2 ratio in liquid phase decreased. When the value of Na^+/SiO_2 in liquid phase decreased to 0.84 or less during the crystallization, spherulites of chabazite and gmelinite appeared. The changes of ^{29}Si-MASNMR signals seemingly showed the solid-solid transformation mechanism on the formation of zeolite Y. However, the XRD and chemical analyses of solid phases proved the formation of zeolite Y with SiO_2/Al_2O_3=5.985, from amorphous solid with SiO_2/Al_2O_3=7.0-7.2. These results show the liquid-solid transformation mechanism on the formation of zeolite Y.

Zairyo
Vol.40, No.449, Feb. 1991
p.178-184

Bending Strength and Fatigue Behavior of Nuclear-Grade Graphite under Impact Load

Masatoshi FUTAKAWA*, Kenji KIKUCHI**, Yasushi MUTO** and Heki SHIBATA***

The graphite components in HTR (High Temperature gas-cooled Reactor) are subjected to impact force when an earthquake occurs. It is important from a viewpoint of seismic safety design to investigate the difference between impact and nonimpact strengths.

Both bending strength and bending fatigue strength tests, therefore, were carried out under impact and nonimpact loads on two kinds of graphite materials, that is, isotropic and near-isotropic ones. The impact response analyses, in which a beam model was used by taking account of the contact behavior between the specimen and a tap, were performed to evaluate the relationships among impact energy, impact force and impact stress.

The main conclusions obtained are summarized as follows ;

(1) A beam model taking account of the contact behavior through the Hertzian theory is applicable to describe the impact behavior.

(2) The bending strength of graphite is independent of strain rate in the range 10^{-4} to 5 l/s.

(3) The strength of graphite is lower in impact fatigue than in nonimpact fatigue, irrespective of kind of graphite and specimen volume.

Key words : Impact, Bending fatigue, Bending strength, Impact response analysis, Hertzian contact stiffness

Zairyo
Vol.40, No.449, Feb. 1991
p.192-198

Time-Temperature Dependence of Flexural Strength of Unidirectional CFRP Using Pitch Based Carbon Fibers

Yasushi MIYANO*, Yukio TAKAMURA**, Megumu SUZUKI*** and Michihiro MOHRI****

The flexural fracture behavior of unidirectional CFRP laminates (X) using pitch based carbon fibers XN40, which was recently developed as high grade fiber, was investigated by three point bending test over wide ranges of temperature and strain rate. At the same time, similar experiments were carried out for two types of CFRP, M and P, in which PAN based carbon fibers M40 and pitch based carbon fibers P55S are used, respectively. By comparing the results of three types of CFRP laminates, characteristics of CFRP(X) were clarified as mentioned below ;

(1) The flexural strength of CFRP(X) as well as the others remarkably changes with temperature and strain rate. The master curves of flexural strength can be constructed for those CFRPs by using the reciprocation law between time and temperature. The time-temperature shift factors of flexural strength in respective CFRP are in quantitatively good agreement with each other.

(2) The region of reduced time is clearly divided into three parts by the mechanism of fracture for CFRP(X), that is, the micro-buckling of fibers as the initiation of fracture in the region of long reduced time, the compressive fracture of fibers in the region of medium reduced time and the tensile fracture of fibers in the region of short reduced time. In the region of long reduced time, the flexural strength of CFRP(X) is in good agreement with those of CFRP(M) and CFRP(P), which remarkably changes with reduced time. However, in the region of medium reduced time, the flexural strength of CFRP(X) shows characteristic behavior which is different from the others. The flexural strength of CFRP(X) remarkably changes with reduced time, although those of the others slightly change.

Key words : Pitch based carbon fiber, Mechanical property, Fracture behavior, CFRP, Flexural strength, Time-temperature dependence

Zairyo
Vol.40, No.449, Feb. 1991
p.217–223

Experimental Investigation and Numerical Simulation on Bending Strength of Silicon Nitride Affected by Grinding Condition

Toshihiko HOSHIDE*, Kazumasa OKUMURA** and Tatsuo INOUE*

Three-point bending tests were conducted using specimens of sintered silicon nitride ground in six types of condition, which were prescribed by the combination of the mesh-size of grinding wheel and the cutting depth. It was revealed by the Weibull statistical analysis that the stength was higher and its scatter was less in specimens ground by using a grinding wheel with larger abrasive grains. The relative estimation of residual stress induced by grinding was tried by using the indentation-flaw method to evaluate the fracture toughness simply. In this case, the crack formation resistance ratio, which was defined as the apparent fracture toughness measured on the ground surface divided by that on the surface without residual stress, was proposed to correlate the stength depending on the grinding condition. The crack formation resistance ratio became larger with an increase of strength. The tendency was ascribed to the variation of the intensity of compressive residual stress depending on the grinding condition. A simulation was carried out to discuss the dominant factor to affect the relation between the strength distribution and the grinding condition. In the analysis, the fracture mechanics model for cracks located in the region subjected to tensile stress was combined with the Monte Carlo simulation. The simulated result presented similar characteristics of the strength distribution as observed experimentally. The characteristics of the strength distribution was successfully explained by introducing the concept of superposing distinct strength distribution depending on the crack geometry.

Key words : Bending strength, Grinding condition, Weibull statistics, Fracture toughness, Monte Carlo simulation, Silicon nitride

Taikabutsu
Vol.43, No.2 1991
p.56–65

Reactivity Between BN Composite Ceramics And Molten Stainless-Steel

Keisuke Asano, Akio Ishii, and Yasushi Tsutsui

The behavior of contact angle between BN composite ceramics produced by hot press method and SUS304–steel are investigated. As a result, the following are clear.

(1) In case of Si_3N_4–BN composite systems, the contact angle of all samples decreases with increasing of the temperature, and become smaller than that of BN ceramic. It also becomes small with increasing of BN contents. It is easy to get wet for the steel as a protect layer of SiO_2 produced at the surface of ceramics becomes thin with incresing of the temperature and BN contents.

(2) In case of AlN–BN composite systems, the contact angle of all samples is bigger than that of BN ceramic. And it is not only independent of BN content, but also changeless to the temperature. It is hard to get wet for the steel as a layer of stable Al_2O_3 produced at the surface of ceramics.

key words: silicon nitride, aluminum nitride, boron nitride, composite ceramics, stainless-steel, wettability, contact angle.

Journal of the Fuel Society of Japan
Vol.70, No.2 1991
p.153-158

Current Status of River Water Heat Utilization System — Presentation of the System in Building 21 A, Okawabata River City Apartment House —

Takashi YAMADA
(Tokyo Gas Co., Ltd.)

SYNOPSIS : — A river water heat utilization system has been introduced to Building 21 A, Okawabata River City. This is a super-highrise apartment building constructed by the Housing and Urban Development Corporation at 1-chome Tsukuda, a development area on the banks of the Sumida River. This system supplies hot water by a gas absorptive heat pump, the heat sources being the water of the Sumida River for the low temperature and city gas for the driving heat.

Compared with conventional gas boiler systems, this system provides a 43% reduction in primary energy. In practical use, however,considering the additional burning when the supply water temperature becomed low and the drop of COP caused by scaled heat exchanger tubes, reduction of moderate approx. 40,000 Nm^3/year in terms of gas volume is expected.

As the heat selling project for this area is 5 Gcal/hour or less in capacity,the Heat Supply Law will not be applied and it will be operated as project incidental to the city gas project by the Tokyo Gas Company. Small-sized heat supply projects as this are named "spot heat supply" by the company. The success or failure of spot heat supply (=small-sized heat supply) depends mainly on the cut down of the equipment cost and personnel cost.

Key Words

River water utilization, Absorptive heat pump, Energy saving, Spot heat supply

Journal of the Fuel Society of Japan
Vol.70, No.2 1991
p.159-167

Recent Trend of Next Generation Ironmaking Technology

Tsutomu NOZAKI

(Ironmaking and Steelmaking Research Department, Irod and Steel Research Labs.,Kawasaki Steel Corp.)

SYNOPSIS : — Smelting reduction processes are focussed rapidly by the decrease of cokes production caused by decrement of coke oven furnaces and problems of pollution and warmness by CO_2 generation. Supporting technologies against shortness of cokes production are pulverized coal injection technique, new formed coke process and oxygen blowing through blast furnace tuyeres. Beyond these technologies, smelting reduction process is characterized by direct utilization of crude coal. This report will describe the targets and problems surrounding the smelting reduction processes, and will explain the state of the arts of the development of various smelting reduction processes, namely, Elred, CBF, HIsmelt AISI Direct Steelmaking method, Plasmasmelt, Corex and DIOS processes.

Limitation of CO_2 generation is also the big problem in the various industries. In Japan, the ratio of CO_2 generation by ironmaking and steelmaking plants is approximately 13%. Kawasaki Steel Corp has been succeeded in the developing the CO gas purification in off gas which comes from combined blowing converter. Purified CO gas is utilized as resources of C_1 chemistry and as aggitation gas of converter instead of Ar gas.

Key Words

Ironmaking technology, Off gas utilization, Smelting reduction

Journal of the Japan Institute Metals
Vol.55 No.2 1991
p.105-109

Dependence of Lattice Constants and T_c on the Oxygen Content z in $YBa_2Cu_3O_z$: from the Database*

Yuji Asada**, Etuo Nakada**,
Akimitu Miyazaki** and Tadaharu Yokokawa**

The data on lattice constants $L(a, b, c)$, T_c and oxygen content z in $YBa_2Cu_3O_z$ are retrieved from the factual database of superconducting materials, which is now being constructed in NRIM. The linear relations between $L(a, b, c)$ and z are statistically obtained with high values of correlation coefficient. Especially, the lattice constant c is highly correlated with z. These relation can be used to estimate z-values which are not described in the paper referred. The orthorhombic distortion $p(=b-a)$ is introduced to investigate the structural transformation and variation of T_c. The values of z, where phase transitions take place, are discussed. T_c drastically changes at $z1=6.75$ and $z2\sim6.5$ which are related to the structural change. We propose that T_c should be related to p rather than z.

Keywords: *database, oxygen content, $YBa_2Cu_3O_z$, lattice constant, superconducting transition temperature*

Journal of the Japan Institute Metals
Vol.55 No.2 1991
p.166-171

Effect of Additives on the Formation of $MgAl_2O_4$ from MgO and Al_2O_3*

Shinji Hirai**, Hideaki Murakami*** and Hiroshi G. Katayama**

The mixture of Al_2O_3 and MgO at a mole ratio of 1: 1, was fired between 1173 and 1623 K in air, to investigate the effects of the particle size and type of Al_2O_3, and the kind of additives on the formation rate of $MgAl_2O_4$ and, at the same time, to elucidate the mechanism of the reaction. The results are shown as follows. (1) $MgAl_2O_4$ was formed more rapidly from Al_2O_3 than from Al_2O_3. (2) The addition of CaB_4O_7, B_2O_3 and NaF accelerated the formation of $MgAl_2O_4$, but the addition of CaF_2, $CaCl_2$ and $CaCO_3$ in an amount of 1 mass% or below had little effect on this reaction. (3) With the progress of the reaction, the Al_2O_3-$MgAl_2O_4$ interface moved from the outside to the inside of Al_2O_3 particle, whereas the $MgAl_2O_4$-MgO interface moved to the outside of the particle. On the basis of this finding, the reaction rate was analyzed using the solid-diffusion controlled equation which includes a correction factor for the change of molecular volume. As a result, the apparent activation energy value was estimated to be 316 kJ/mol for the addition of 1 mass%CaB_4O_7 and 270 kJ/mol for no addition. These values were approximated by the activation energy value of the interdiffusion of Mg^{2+} and Al^{3+} within the defective MgO-Al_2O_3 spinel.

Keywords: *$MgAl_2O_4$, MgO, Al_2O_3, reaction mechanism, kinetic analysis, additive*